Model-Based Experimental Design in Electrochemistry

Hoang Viet Nguyen

Centre of Research in Electrochemical Science and Technology
Department of Chemical Engineering and Biotechnology
University of Cambridge

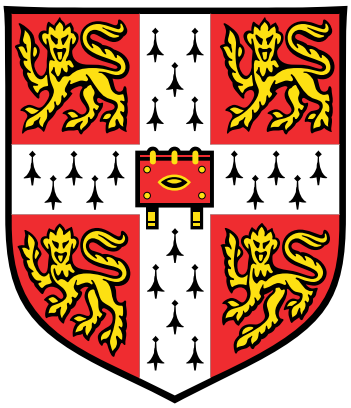

This dissertation is submitted for the degree of
Doctor of Philosophy

Trinity College

June 2017

Declaration

I hereby declare that except where specific reference is made to the work of others, the contents of this dissertation are original and have not been submitted in whole or in part for consideration for any other degree or qualification in this, or any other University. This dissertation is the result of my own work and includes nothing which is the outcome of work done in collaboration, except where specifically indicated in the text. This dissertation contains fewer than 65,000 words including appendices, bibliography, footnotes, tables and equations and has less than 150 figures.

Hoang Viet Nguyen
June 2017

Acknowledgements

First and foremost I would like to express sincere gratitude to Dr Adrian Fisher. His patience and support, both technically and logistically, help shaping this work.

I also would like to thank our collaborators for their generous supports. Specifically, Professor Frank Marken and his group from Bath University have always welcomed and treated us with great food. Many thanks to Sunyhik and Christopher for their experimental data and discussions.

I am grateful for the support from Dr Erik Birgersson and his group at NUS. He and his students taught me a great deal about the software Comsol, which is useful and forms a big part of my work. I would like to thank Dr Karthik Somansudaram for help setting up the simulation in Chapter 4.

I thank all my friends and colleagues at CREST, in particular Hongkai Ma for our fruitful collaborations in Chapter 5.

And finally and above all to my parents, I am so much indebted to you guys. Thank you gazillion times for everything!

Abstract

The following thesis applies an experimental design framework to investigate properties of electron transfer kinetics and homogeneous catalytic reactions. The approach is model-based and the classical Butler-Volmer description is chosen to describe the fundamental electrochemical reaction at a conductive interface. The methodology focuses on two significant design variables: the applied potential at the electrode and mass transport mode induced by physical arrangement.

An important problem in electrochemistry is the recovery of model parameters from output current measurements. In this work, the identifiability function is proposed as a measure of correspondence between the parameters and output variable. Under diffusion-limit conditions, plain Monte Carlo optimization shows that the function is globally non-identifiable, or equivalently the correspondence is generally non-unique. However by selecting linear voltammetry as the applied potential, the primary parameters in the Butler-Volmer description are theoretically recovered from a single set of data. The result is accomplished via applications of Sobol ranking to reduce the parameter set and a sensitivity equation to inverse these parameters.

The use of hydrodynamic tools for investigating electron transfer reactions is next considered. The work initially focuses on the rotating disk and its generalization - the rocking disk mechanism. A numerical framework is developed to analyze the latter, most notably the derivation of a Levich-like expression for the limiting current. The results are then used to compute corresponding identifiability functions for each of the above configurations. Potential effectiveness of each device in recovering kinetic parameters are straightforwardly evaluated by comparing the functional values. Furthermore, another hydrodynamic device - the rotating drum, which is highly suitable for viscous and resistive solvents, is theoretically analyzed. Combined with previous results, this rotating drum configuration shows promising potential as an alternative tool to traditional electrode arrangement.

The final chapter illustrates the combination of modulated input signal and appro-

priate mass transport regimes to express electro-catalytic effects. An AC voltammetry technique plays an important role in this approach and is discussed step-by-step from simple redox reaction to the complete EC' catalytic mechanism. A general algorithm based on forward and inverse Fourier transform functions for extracting harmonic currents from the total current is presented. The catalytic effect is evaluated and compared for three cases: macro, micro electrodes under diffusion control condition and in micro fluidic environments. Experimental data are also included to support the simulated design results.

Publications

Book Chapter

Section 1.5/Chapter 1 in Song, Cheng and Zhao: Micro Fluidics, Fundamental Devices and Applications, Wiley Interscience, 2016

Journal

C. E. Hotchen, H. V. Nguyen, A. C. Fisher, F. Marken. Hydrodynamic microgap voltammetry under couette flow conditions: Electrochemistry at a rotating drum in viscous poly-ethylene glycol (PEG). ChemPhysChem, 16, 2015

S. D. Ahn, K. Somasundaram, H. V. Nguyen, E. Birgersson, J. Y. Lee, X. Gao, A. C. Fisher, P. E. Frith, F. Marken. Hydrodynamic Voltammetry at a Rocking Disc Electrode: Theory versus Experiment. Electrochimica Acta, 188, 2016

Peng Song, Hongkai Ma, Luwen Meng, Yian Wang, Hoang Viet Nguyen, Nathan S. Lawrence and Adrian C. Fisher. Fourier transform large amplitude alternating current voltammetry investigations of the split wave phenomenon in electrocatalytic mechanisms. PCCP, 19, 2017

In Preparation

H. K. Ma, H. V. Nguyen, A. C. Fisher. Elicitation of homogeneous self-catalytic effects inside channel electrodes via Fourier Transform large amplitude voltammetry

Contents

List of Figures

List of Tables

Nomenclature

Physical Symbols

F	Faraday Constant
R	Boltzmann Constant
T_0	Room Temperature

Greek Symbols

α	Butler-Volmer Charge Transfer Coefficient
ν	Solution Dynamic Viscosity
ω	Number of revolution per second or minute
ρ	Solution Density

Mathematical Symbols

ϕ/E	Electrical Potential
$\triangle E$	Sinusoidal Signal Amplitude
$\underline{v}$	Velocity Vector Field
A	Electrode Geometric Area
c	Species Solution Concentration
C_{dl}	Butler-Volmer Double Layer Specific Capacitance
D	Generic Diffusion Coefficient
D_R/D_O	Diffusivity of Reduced/Oxidized Species

E	Applied Potential
E_0	Butler-Volmer Equilibrium Potential/Formal Potential
f	Rotation Frequency
FD/FE	Finite Difference/Finite Element
G	Gibbs Free Energy
h_c/d_c or d	Channel Height/Width
I_c	Capacitive Current
I_f	Faradaic Current
I_{lim}	Levich Limiting Current
J	Species Flux
k_0	Butler-Volmer Kinetic Constant
$k_{EC}/k_{EC'}$	Homogeneous Kinetic Constant in EC/EC' mechanism
k_f/k_b	Butler-Volmer Forward/Backward Kinetic
n	Number of Electrons transferred in a Redox reaction
ODE/PDE	Ordinary/Partial Differential Equation
R_u	Butler-Volmer Uncompensated Resistance
t	Time
V_f	Volumetric Flow Rate
v_{scan}	Voltage Scan Rate
x_e/w_e	Electrode Length/Width

Chapter 1

Introduction

Thanks to the recent advances in computational power, the use of model based experimental design (MBED) has become ubiquitous in almost every field of science and engineering. Primary advantages of using this approach include an improved understanding of experimental measurements (e.g. qualitative and/or quantitative insights into underpinning physical mechanism in place) and supporting the design of additional experiments.

The general practice of MBED is briefly summarized in Figure 1 [4]. The methodology can be divided into two main stages. The first stage is concerned with the selection of models to describe the physical process. Model discrimination is a critical step in this stage. After a realistic mathematical model is selected, it is subjected to several experimental designs in the subsequent stage. Often a major aim of such experiments is to extract the accurate parameters of a proposed model. This process usually involves regression of parameters and computations of relevant statistical metrics from existing data. Finally, the final model will be validated against newly acquired information before being implemented in further applications.

In the second stage of the experimental design procedure, the issue of identifiability becomes significant. This concept essentially expresses the direct correspondence between model's measurable outputs and its parameter inputs. A model structure, with high identifiability characteristics, implies that parameters are theoretically estimable with higher precision. In addition, the choice of model inputs or controlled variables significantly influences the identifiability outcome. In complex and non-linear models however, the interaction among parameters may lead to non-identifiability, no matter how well-designed the controlled variables are. Therefore, smaller group(s) of parameters should be carefully selected to improve the regression procedure and statistical

test.

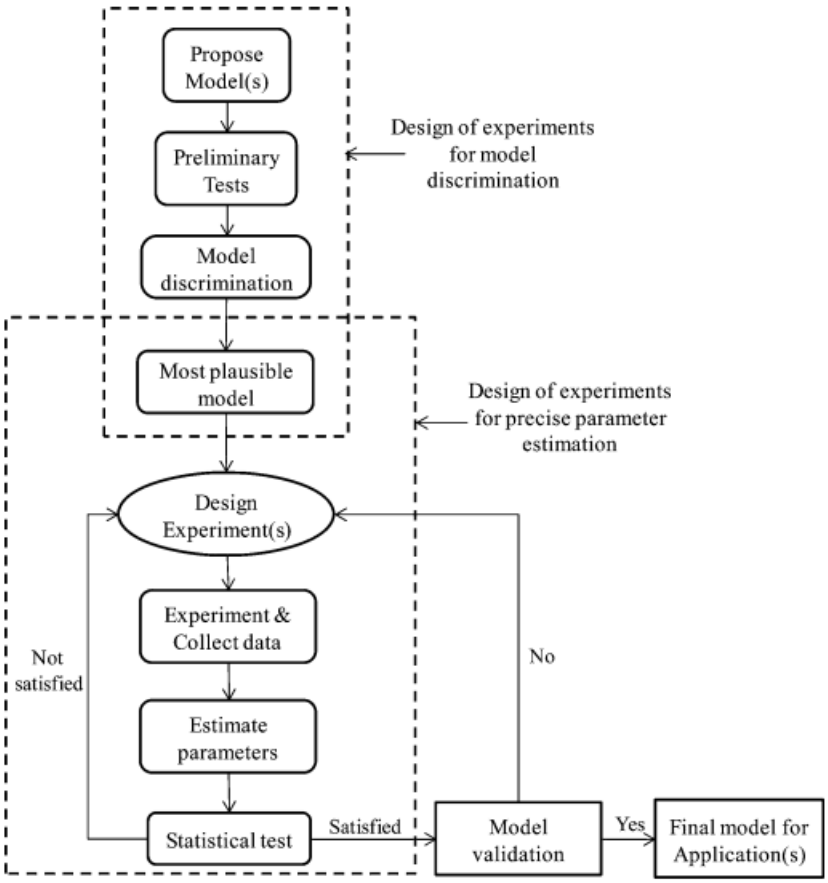

Figure 1: A schematic diagram of model based experimental design (MBED) framework

In an electrochemical context, experimental design involve two primary factors: i) the applied voltage at electrical interface and ii) the physical cell arrangement to conduct measurements. The overall aim of this thesis is to investigate the role of these components on the identifiability of a specific electrochemical model, namely in this case the classical Butler-Volmer description (Section 1.2). In addition, the implication of identifiability is not just limited to problems of parameter regression and statistics, but also the ability to elicit the underlying physical and chemical aspects of the physical process. Such an ability can be accomplished via applications of appropriate voltage-based waveforms, and in combination with micro-fluidic device - a novel way of conducting electrochemical measurements. Before going into further details, the following sections serve as a review of relevant literature and topics which are extensively covered in this work.

1.1 Electrochemistry Fundamentals

Electrochemistry is a branch of physical chemistry studying chemical reactions induced by electrical effects [2]. The field encompasses a wide range of phenomena and industrial applications. Examples of large scale applications include electroplating of metals and the production of aluminium, chlorine and the corrosion-protection of materials [5]. In addition, operations of many important technological devices are based on electrochemical principles such as energy storage (e.g. Lithium-ion batteries and super capacitors [6][7]) and generators (i.e. dye sensitized solar and fuel cells [8][9]). In chemical analysis, electrochemical-based sensors have gained popularity due to its ability to detect very low concentration ($\sim \mu M$) and its reusability [10–12]. Another well-known example is the glucose sensor; these sensors are used for personal point of care with annual sale amounting to millions of dollars [13].

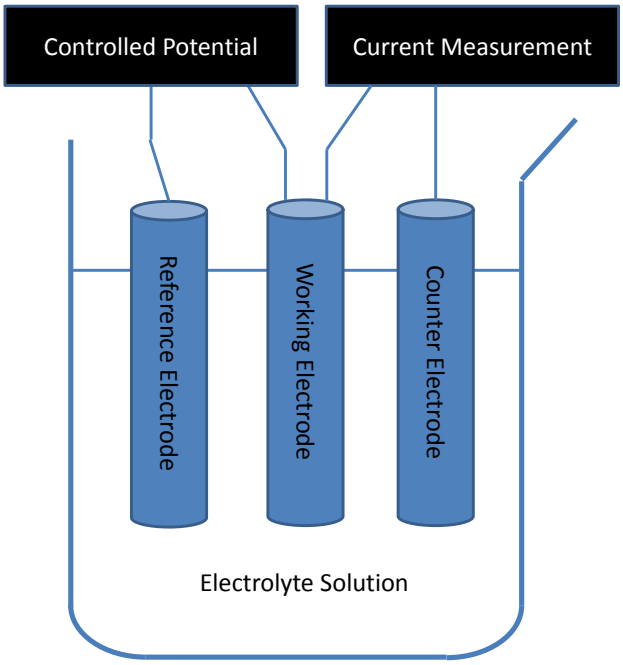

Figure 2: A schematic diagram for the three electrode system used to conduct electrochemical measurements

The most basic example of an electrochemical reaction is the generic redox process:

$$O + ne^- \leftrightarrows R \tag{1.1}$$

Reaction 1.1 involves the transfer of electrons between a reductive/oxidative pair (R/O) and a conductive surface, e.g. an electrode. Common electrodes are often traditional metals such as gold or platinum, however carbon-based surfaces are now becoming popular [14, 15]. In practice, the charge transfer reaction is conducted by using a three-electrode system (Figure 2). An external input is applied to the working electrode and the resulting output is measured. If the input is a varying potential, the output is a current. This technique is often called potentiometry or voltammetry. On the other hand, in the galvanostatic mode, a constant current is applied at the working electrode and a potential is then recorded, although this technique is far less common in chemical analysis. Generally speaking, counter electrodes should have a large surface area so that reaction 1.1, of the working electrode, is not limited by the complementary reaction occuring at the counter itself. In addition, the reference electrode should have a low impedance and be maintained at a constant potential.

For any given redox pair R/O, there is an associated equilibrium potential E_0 (relative to reference electrode) at which there is no current flow. Therefore, at that potential, the rates of oxidation and reduction balance, and no current flows to the external circuit.

The electron transfer step is quantum-mechanical in nature [16]. Physically, this type of process involves the electron tunnelling phenomenon between electrolyte molecules and the conductive surface. Therefore, the process depends on the distance between these objects, meaning that the molecules must be around the surface (e.g. at a few $\mathring{A}$). Secondly, the thermodynamics must be favourable for the reaction to occur (Figure 3). Considering the Fermi level E_F of a metal surface, if that level is raised to one above the LUMO (lowest unoccupied molecular orbital) of the analyte, then the electron is thermodynamically transferred from the metal to the molecule, i.e. a reductive reaction. On the other hand, if the Fermi level is depressed below the analyte's HOMO (highest occupied molecular orbital), then oxidation is favoured. Furthermore, the act of raising or depressing E_F can be effectively achieved by an applying external voltage to the conductive electrode.

There are two primary ways for electrolytes to interact with conductors. The first method is to adsorb directly the species onto the surface. The adsorption can be

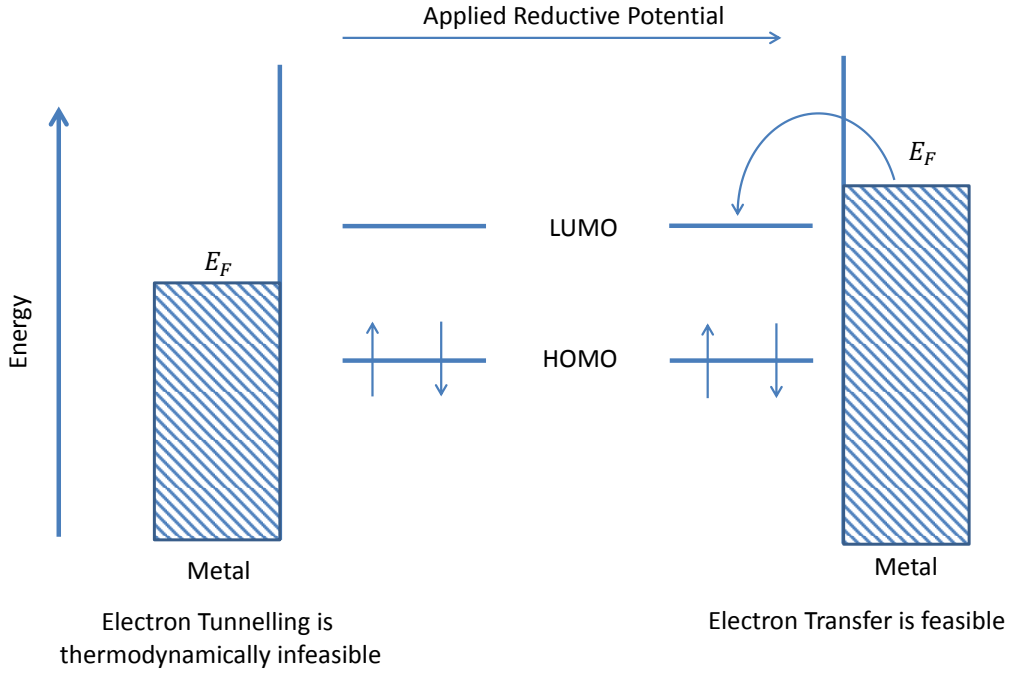

Figure 3: Electron transfer mechanism between a metal surface and electroactive species. In this diagram, the analyte receives electrons from metal and is reduced

either physisorption or chemisorption. In the second method, electrolytes freely move inside the medium and the electron transfer is divided into the following sub-steps (Figure 4): (1) R is transported to electrode's neighbourhood, (2) O is then formed and transported away and the process repeats. In the delineation above, some means of mass transport is required. The following subsections review major mass transport mechanisms encoutered within solution.

1.1.1 Diffusion

Transport by diffusion occurs due to uneven spatial distribution of chemical concentration. Thus, without external restrictions, a species tends to move from regions of higher concentrations to low. The driving force here is the concentration gradient as expressed by Fick's first law:

$$J_R = -D_R \nabla c_R \tag{1.2}$$

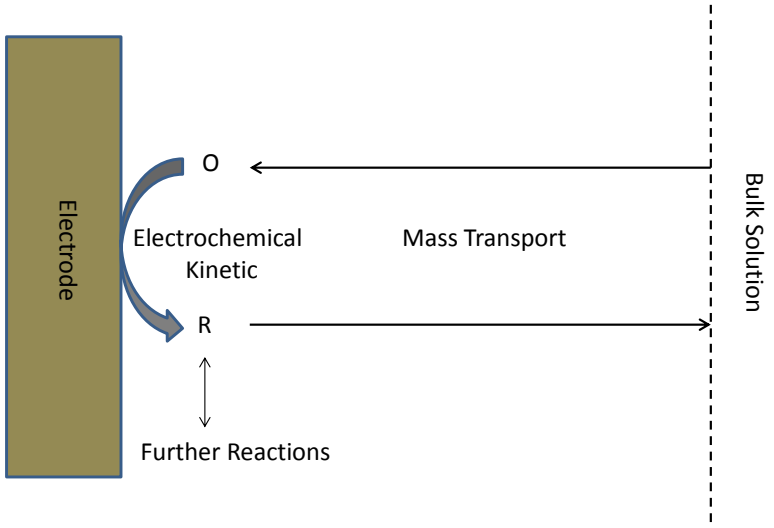

Figure 4: Basic steps in an electrochemical reaction. Species are transported to the electrode, followed by electron tunnelling under a favourable thermodynamic potential and the product is then transported away

where J_R the flux, D_R the species diffusivity and the ∇c_R the concentration gradient with respect to space coordinates. Diffusivity has a complex dependence on solute sizes, solution properties and temperature, as expressed via the Stoke-Einstein relation [17]. For a general time-dependent diffusional process, applying the mass balance to a fixed control volume (Figure 5) leads to the well-known Fick's second law:

$$\frac{\partial c_R}{\partial t} = \nabla.(D_R \nabla c_R) \tag{1.3}$$

With the appropriate initial and boundary conditions, Equation 1.3 is completely solved for the concentration evolution. Relation 1.3 holds well for low concentrations of solute since the majority of the medium can be taken as stationary relative to solute molecules' movement. At higher concentrations, the more general Stefan-Maxwell equation should be used to account for the relative motion between solute and solvent molecules [18].

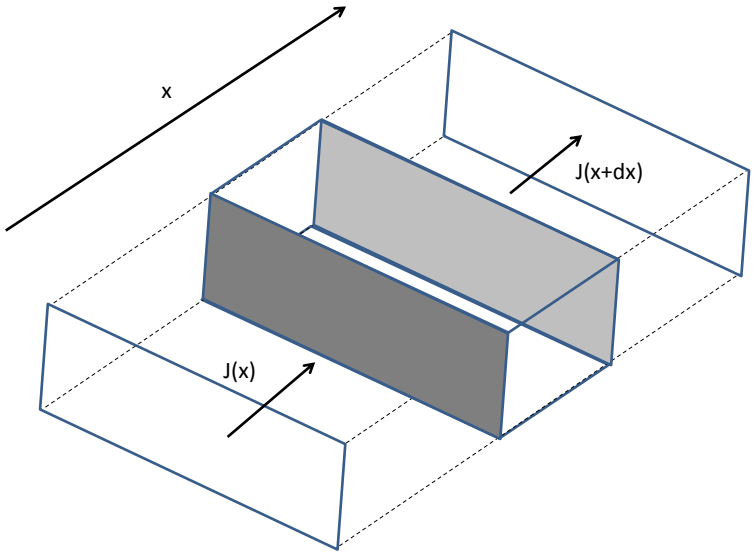

Figure 5: Mass balance under pure diffusion conditions with the denoted control volume, leading to the diffusion equation

1.1.2 Convection

Convection refers to the movement of a material inside a medium caused by mechanical forces. There are two types of convection: natural and forced. Natural convection often arises due to density differences within the bulk solution. Such effects are uncontrollable and difficult to analyze. Forced convection, by contrast, is significantly larger and often designed to be more controllable. This effect can be induced via pumping or stirring of the solution. To take into account effects of convection, the original diffusion equation is modified to:

$$\frac{\partial c_R}{\partial t} = D_R \nabla^2 c_R - \underline{v}.\nabla c_R \tag{1.4}$$

whereas the second term on the RHS accounts for convective flux. Because fluxes caused by forced convection is usually much higher than those by natural convection, one can safely neglect the latter in analysis. Finally, the velocity field $\underline{v}$ is generally computable from the Navier-Stoke equations , subjecting to certain restrictions [19, 20]. It is further evident that the concentration field c_R, which is responsible for mass transport phenomena, and the velocity field $\underline{v}$ can be calculated independently of each

other. This fact is advantageous and is exploited in later chapters of this work.

1.1.3 Electrostatic Migration

If the electrolyte species is charged and an electric field is present, then mass transport can also be induced via electrostatic interactions. Migratory fluxes are primarily dependent on species ionic charge z, the potential gradient $\nabla\phi$, mobility factor u and potential difference between the solid (e.g. electrode) and solvent phase $\phi = \phi_{\mathrm{S}} - \phi_{\mathrm{L}}$:

$$J_M \propto zuc_R\nabla\phi \tag{1.5}$$

Fortunately, the complexity caused by electrostatic migrations can be suppressed by adding an excess amount of electro-inactive electrolyte [21, 22]. For example, to study redox reaction of ferro/ferri cyanide in aqueous solution:

$$Fe(CN)^{3-}_{6(aq)} + e^- \leftrightarrows Fe(CN)^{4-}_{6(aq)} \tag{1.6}$$

one often adds excess amounts of supporting inert such as KCl, KNO_3, *etc.* to the prepared solution. Consequently, migration fluxes are mainly due to supporting species and those due to electroactive species can thus be ignored. The addition of supporting electrolyte has another beneficial effect. This helps to reduce the potential gradient $\nabla\phi$ between the two phases and therefore J_M (Equation 1.5) also becomes smaller.

However, in some cases, the addition of supporting electrolytes is not desirable because of side reactions or damage to the samples, especially sensitive biological compounds. Also, the effect of migration flux can be considered mathematically, albeit additional complications may arise in the analysis [23, 24]. All the above mass-transport processes can be summarized in the general Poisson-Nernst-Planck equation [25]:

$$\frac{\partial c_R}{\partial t} = \nabla.N_R + r_R \tag{1.7}$$

$$N_R = -D_R\nabla c_R + vc_R - zuFc_R\nabla\phi$$

where r_R is the rate of consumption or generation of the species due to chemical reactions. The factor N_R therefore accounts for the possible modes of mass transport discussed above.

1.2 Kinetic Models of Electrochemical Reactions

To apply the experimental design procedure to study of electrochemical reactions, it is necessary to have a rate law for the elementary process 1.1. This section reviews the two most commonly used models in the literature: Butler-Volmer [26] and the Marcus-Hush [27].

In general, the electron transfer rate is assumed to be first order with respect to the reactant and product concentration at the electrode surface (corresponding to coordinate $x = 0$):

$$\frac{I_f}{nFA} = k_f(c_R)_{x=0} - k_b(c_O)_{x=0} \tag{1.8}$$

where terms $k_f(c_R)_{x=0}$ and $k_b(c_O)_{x=0}$ are respectively referred to as the anodic and cathodic currents. Faradaic current I_f accounts for the number of electrons n being exchanged, A is taken as the geometric area. and the parameter F denotes the Faradaic constant.

Both Butler-Volmer and Marcus-Hush models focus on deriving the forward and backward rate constants k_f and k_b. A detailed derivation can be found in many excellent references and only the main points are summarized here for both cases. For Butler-Volmer description, Transition State theory states that (Figure 6):

$$k \propto \exp(\frac{-\triangle G}{RT}) \tag{1.9}$$

The applied potential E changes the relative positions of the curves, hence accelerating or decelerating the reactions. Linerization of free energy curves around the operating point leads to:

$$\triangle G_f(E) = \triangle G_f(E_0) - (1-\alpha)F(E - E_0)$$

$$\triangle G_b(E) = \triangle G_b(E_0) + \alpha F(E - E_0)$$

The transfer coefficient α represents the similarity between the transition state and the product. A value closer to 1 signifies that the transition state lies closer to product state and vice versa. Since at the equilibrium potential E_0, $k_f = k_b = k_0$, the rates

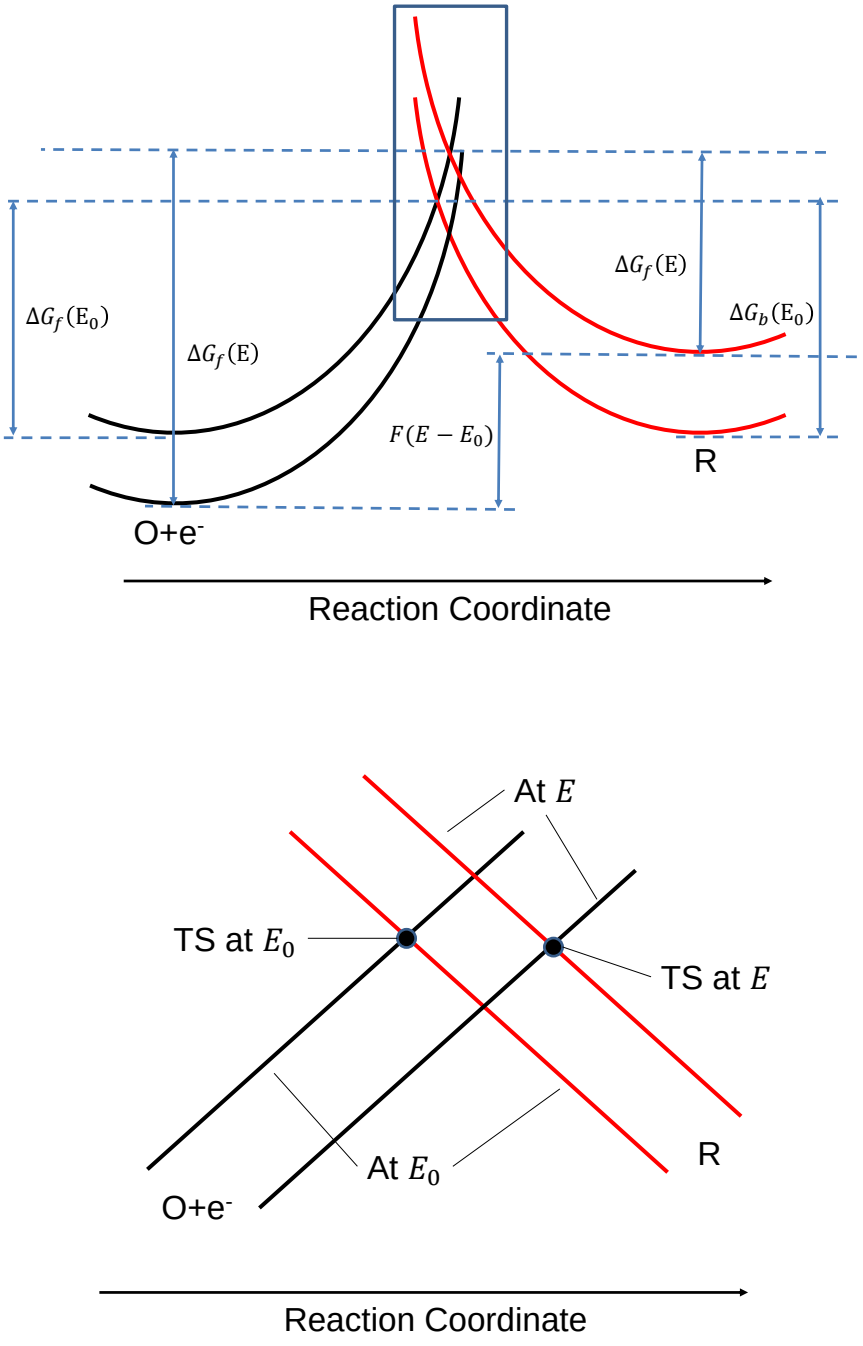

Figure 6: The Transition State theory applied to the simple electron transfer reaction. The Gibbs free energies vary with the potential (top) and the corresponding transition state (inside the rectangle) shifts closer to the product side if a favourable potential is applied (bottom)

are therefore as follows:

$$k_f = k_0 \exp(\frac{(1-\alpha)nF(E-E_0)}{RT_0}) \tag{1.10}$$

$$k_b = k_0 \exp(\frac{-\alpha nF(E-E_0)}{RT_0}) \tag{1.11}$$

If mass transport gradient does not exist, then Equation 1.8 assumes a simpler form:

$$\frac{I_f}{nFA} = i_0(\exp(\frac{(1-\alpha)nF(E-E_0)}{RT_0}) - \exp(\frac{-\alpha nF(E-E_0)}{RT_0})) \tag{1.12}$$

where the constant i_0 is called the equilibrium exchange current density (i.e. the anodic or cathodic current at $E = E_0$). Linearization of 1.12 leads to the Tafel equation which is frequently used to extract i_0. Furthermore because $i_0 = nFk_0$, kinetic constant k_0 can also be estimated from i_0.

In Butler-Volmer kinetics, there are three important factors: the rate constant at equilbrium k_0, the dimensionless transfer coefficient α and the equilibrium potential E_0. If the reaction is very fast (typically $k_0 \geq 10\, cm/s$), then an instant equilibrium is established and the species behave in a classical manner predicted by the Nernst equation [28]:

$$\frac{c_R}{c_O} = \exp(-\frac{nF(E-E_0)}{RT_0}) \tag{1.13}$$

The above equation implies that under Nernstian conditions, the recovery of parameters k_0 and α from the current output is not possible. In other words, the parameter set (k_0, α, E_0) become non-identifiable at this limit. This subject is discussed further in Chapter 3 of the work.

The Marcus-Hush formulation refines the Butler-Volmer model for the electron transfer process. Theoretical studies show that this step proceeds via either an inner-sphere or outer-sphere mechanism [29]. Whilst the latter only involves the direct electron exchange between two species (e.g. the metal surface and electrolyte molecules) via quantum mechanical tunnelling, the former includes significant changes in molecular geometries and desolvation processes to facilitate such exchanges.

Under Marcus-Hush formulation, the corresponding anodic and cathodic rates are derived as follows [30]. Essentially, this model has 4 parameters (k_0, λ and γ and E_0)

compared to 3 (k_0,α and E_0) of Butler-Volmer. The parameters λ and γ represent intrinsic chemical properties of the reaction along with the external potential θ.

$$k_f^{MH} = k_0 \frac{I_f(\theta, \Lambda, \gamma)}{I_f(0, \Lambda, \gamma)} \tag{1.14}$$

$$k_b^{MH} = k_0 \frac{I_b(\theta, \Lambda, \gamma)}{I_b(0, \Lambda, \gamma)} \tag{1.15}$$

$$\Lambda = \frac{\lambda F}{RT_0} \tag{1.16}$$

$$\theta = \frac{nF(E - E_0)}{RT_0} \tag{1.17}$$

$$\frac{\triangle G_{red/ox}(\varepsilon)}{RT} = \frac{\Lambda}{4}(1 \pm \frac{\theta + \varepsilon}{\Lambda})^2 + \gamma \frac{\theta + \varepsilon}{4}(1 - (\frac{\theta + \varepsilon}{\Lambda})^2) + \frac{\Lambda}{16}\gamma^2 \tag{1.18}$$

for each energy value ε, the activation energies for the reductive and oxidate states is calculated by Eyring equations 1.9. Therefore the total activation energies are summations across all energy continuum in a metal electrode (i.e. $I(\theta, \Lambda, \gamma)$'s are integrations of the Eyring expressions) [31].

In Marcus-Hush, the first additional parameter $\lambda = \lambda_i + \lambda_o$ is the total reorganization energy required to distort the reactant's molecular arrangements (λ_i) and the solvation shell (λ_o). These organization energies respectively correspond to the inner-sphere and outer-sphere electron transfer mechanisms (Figure 7). In a outer-sphere mechanism, the electron transfer takes place between two separate and intact chemical entities, however the outer structures of these species are reorganized to facilitate the electron exchange. On the other hand, a chemical bridge (e.g. bridging ligands) is formed between the oxidative and reductive species during inner-sphere electron transfers.

The second dimensionless parameter γ accounts for the asymmetry of the vibration force constants between the oxidative and reductive species. The symmetric Marcus-Hush model corresponds to $\gamma = 0$. In this case, it is evident from Eyring expressions 1.18 that activation energies of the redox couple are parabolic and independent of γ (Figure 8 [32]). Since both curves have the same curvature or shape at all potentials, their corresponding intramolecular force constants are also the same. In addition, at equilibrium potential E_0, the transition state energy lies symmetrically between reactant and product configurations. Therefore the symmetric Marcus-Hush model is

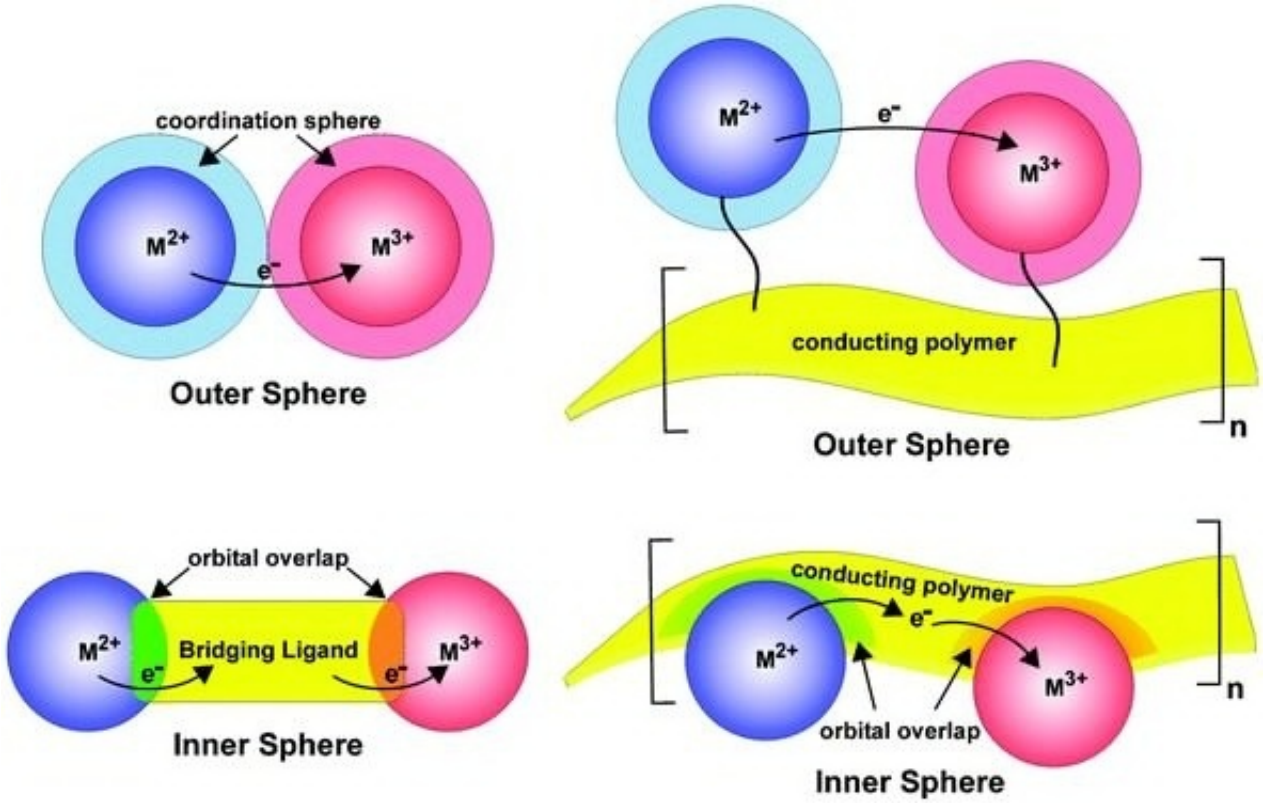

Figure 7: A molecular picture of the outer and inner sphere electron transfer reactions

equivalent to Butler-Volmer formulation at $\alpha = 0.5$. The asymmetric transition state corresponds to the case $\gamma < 0$ or $\gamma > 0$. When $\gamma > 0$, the transition state lies closer to the oxidative state because the force constant corresponding to that state is stronger and vice versa.

To compare the Butler-Volmer and Marcus-Hush models, the literature focuses on two aspects, i) the numerical differences in current responses derived from each model for an elementary redox couple and ii) the individual model's ability to fit the experimental data. In the first aspect, by applying various pulse signals, the currents are shown numerically to be similar under both slow and fast kinetic regimes k_0 and large limits of λ [33]. However, they tend to diverge as the total reorganization energy decreases. Under special circumstances, a current peak-split was predicted for Butler-Volmer, but not observed in Marcus-Hush.

In terms of data-fitting capability, Butler-Volmer appears to be both a simpler and better choice. Using square-wave voltammetry, experimental data for Europium (III) reaction was satisfactorily described by the 3 parameter model [34]. A thorough

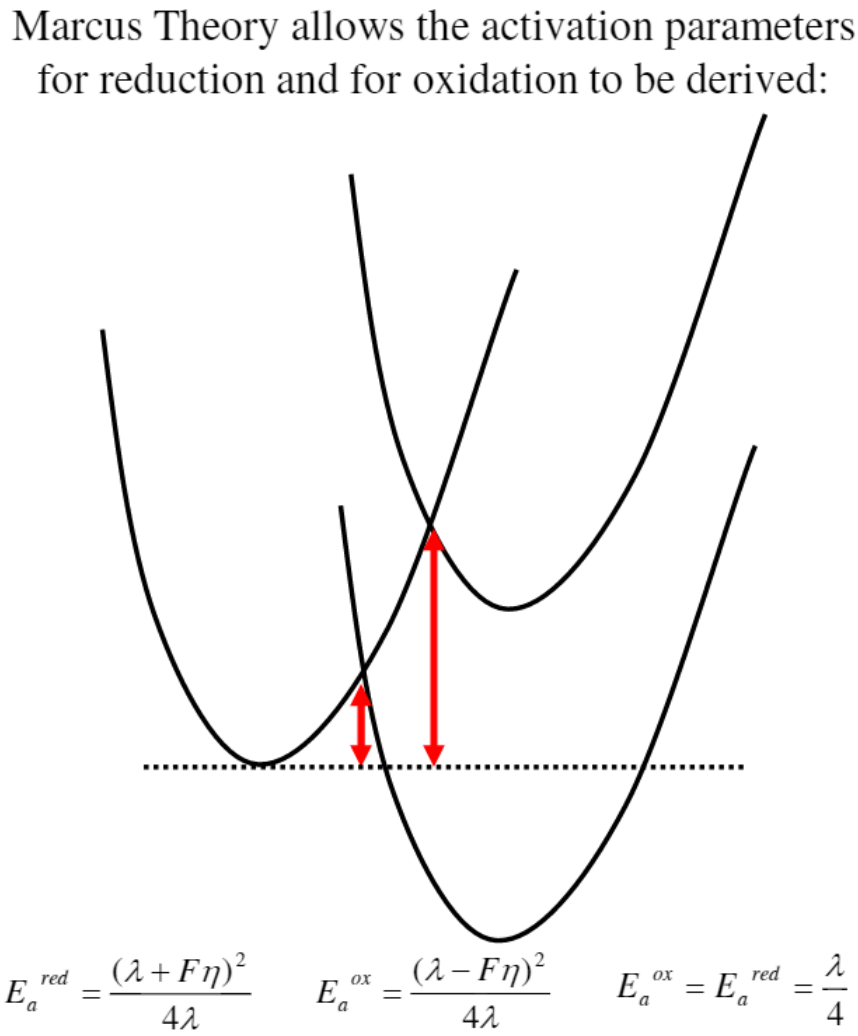

Figure 8: Parabolic potential energies of reactant (left) and product (right) in Marcus model. Activation energies are now functions of the total reorganization energy λ

and critical review of Marcus-Hush-Chidsey model concluded that for a few selected single electron transfers, the symmetric formulation ($\gamma = 0$) exhibits the inability to fit real voltammetric measurements [35]. Conversely, data can be fitted well with Butler-Volmer kinetics using the symmetric transfer coefficient ($\alpha = 0.5$). Nevertheless, the refined asymmetric Marcus-Hush formulation was observed to produce similar responses to those of Butler-Volmer, even under significantly non-symmetric α as large as 0.6 [36]. Finally, reductions of 2-Nitrotoluene and 1-Nitrobutane at gold electrodes in ionic liquids were well described by both models [37].

Physicochemically, it is evident that Marcus-Hush is a more sophisticated model; however for practical purposes, the Butler-Volmer formulation is often satisfactory

as a first approximation. The main benefits of Butler-Volmer are the relative ease in computation and better flexibility in data fitting, which by contrast often requires more complex versions for the Marcus-Hush apporach. Therefore, Butler-Volmer model is subsequently assumed throughout this thesis without further justifications.

1.3 Voltammetric Techniques

Since the electrode potential is an important thermodynamic factor in driving heterogeneous electron reactions, its selection must be carefully considered in the design of electrochemical experiments. The first and simplest class of voltammetry is the single potential step. In this technique, the voltage is raised rapidly from well below to well above E_0, consequently pushing the reaction in one direction. Under diffusion control, the induced current follows the Cottrell relation [2]:

$$i(t) = \frac{nFAC_R^{bulk}\sqrt{D_R}}{\sqrt{\pi t}} \tag{1.19}$$

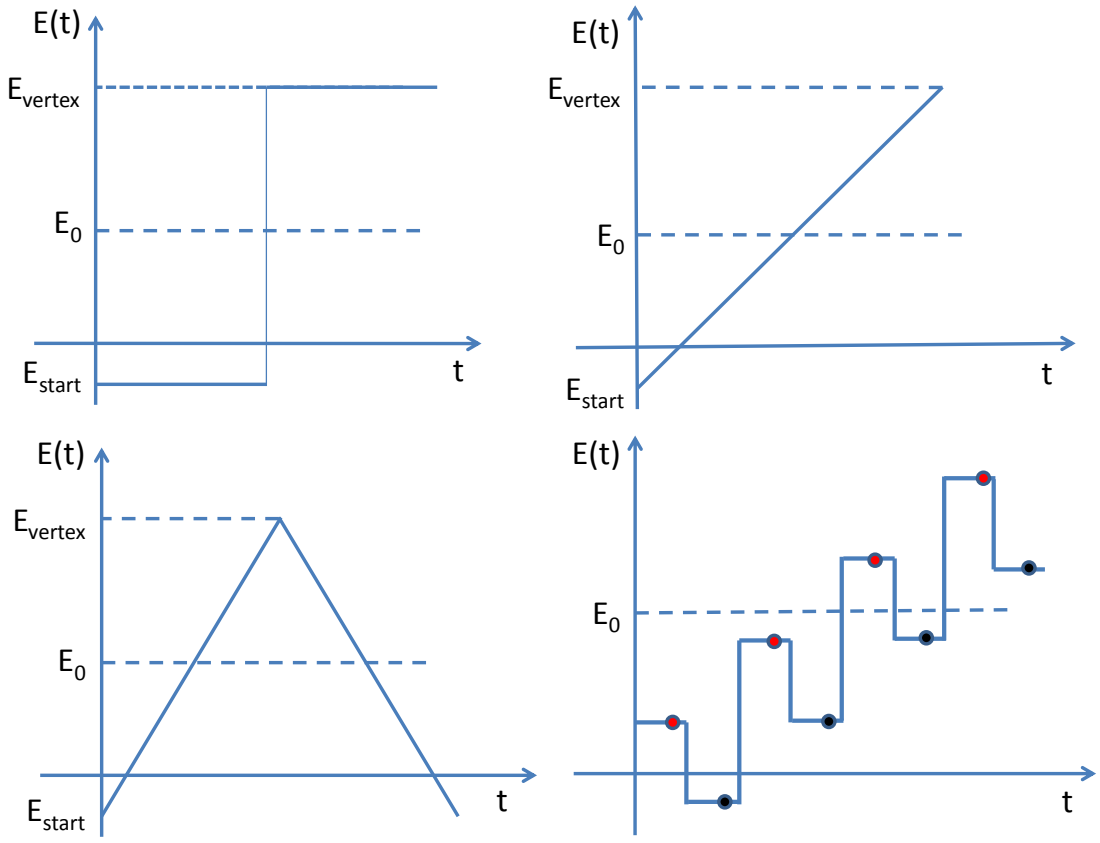

Figure 9: Common voltammetric signals (left to right, top to bottom): Potential Step, Linear Sweep, Cyclic (composing of forward and backward linear sweeps) and Square Wave (reverse pulses)

Simply stated, the current first spikes to a large value and then varies as the inverse

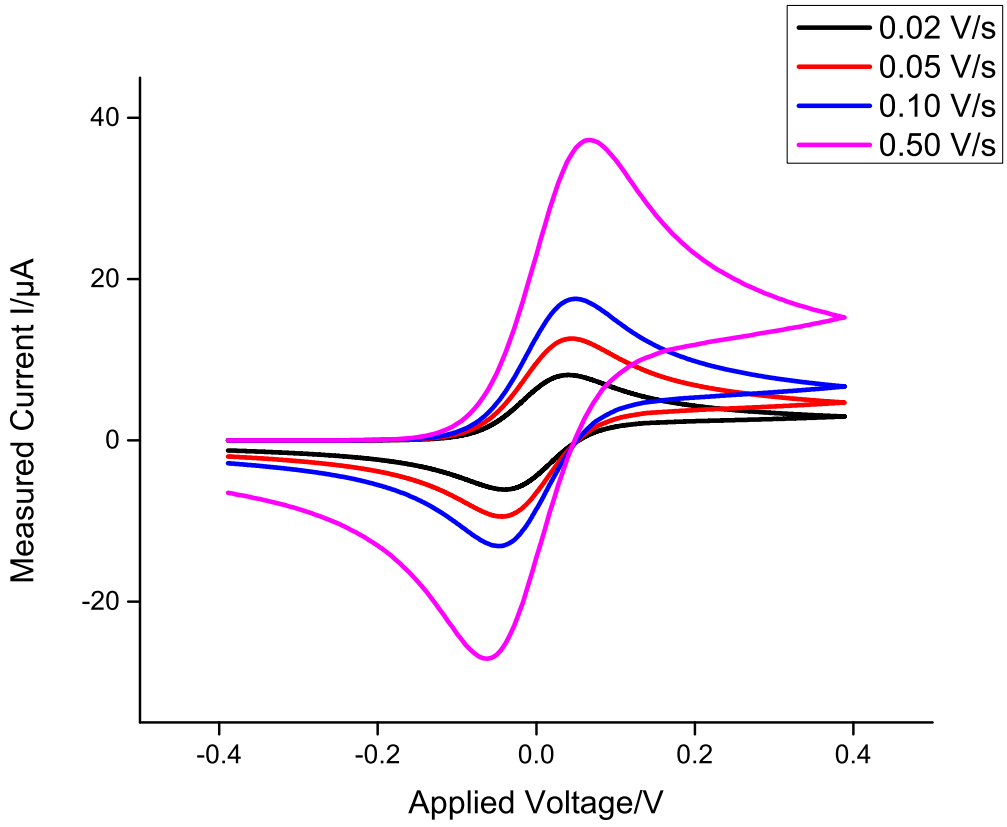

Figure 10: Typical voltammograms for cyclic voltammetry experiments at increasing scan voltage rates for reversible electron transfer reactions. Higher scan rate progressively causes larger peak current

square root of time. The large spike in current is attributed to instant conversion of reactants just above the electrode surface. Afterwards, the fresh reactants from the bulk take more and more time to diffuse towards the electrode surface. The species flux consequently decreases and so does the current. In practice, Equation 1.19 is applied in a short time period and particularly useful for estimating species diffusivity D_R.

In the second class of voltammetry, which is by far the most popular, the potential is moderated in a linear fashion by fixing a scan rate (Figure 9). They can be either linear sweep or cyclic voltammetry. As a consequence, the reaction is induced more slowly, leading to a completely different response. A typical current-voltage graph for linear sweep voltammetry is shown in Figure 10. When the voltage is considerably below E_0, small electrochemical conversions are induced and results in small currents

(according to Butler-Volmer relation 1.8). As larger voltage is applied, the reactant above the electrode is gradually depleted and replaced by fresh supply from the bulk. Therefore, a diffusion layer in which there exists a concentration gradient between the electrode and bulk is formed. At potential well above E_0, the electron transfer reaction is very fast. However, the diffusion layer also becomes thick enough so that the whole process is now mass-transport limited. Consequently, the current first rises but then drops to form a peak as in Figure 10. Furthermore, at higher scan rates, the potential is varied more quickly. At the same time, the diffusion layer stays comparatively thin to the lower scan rate cases. Therefore, the current tends to be larger for at larger voltage scan rates.

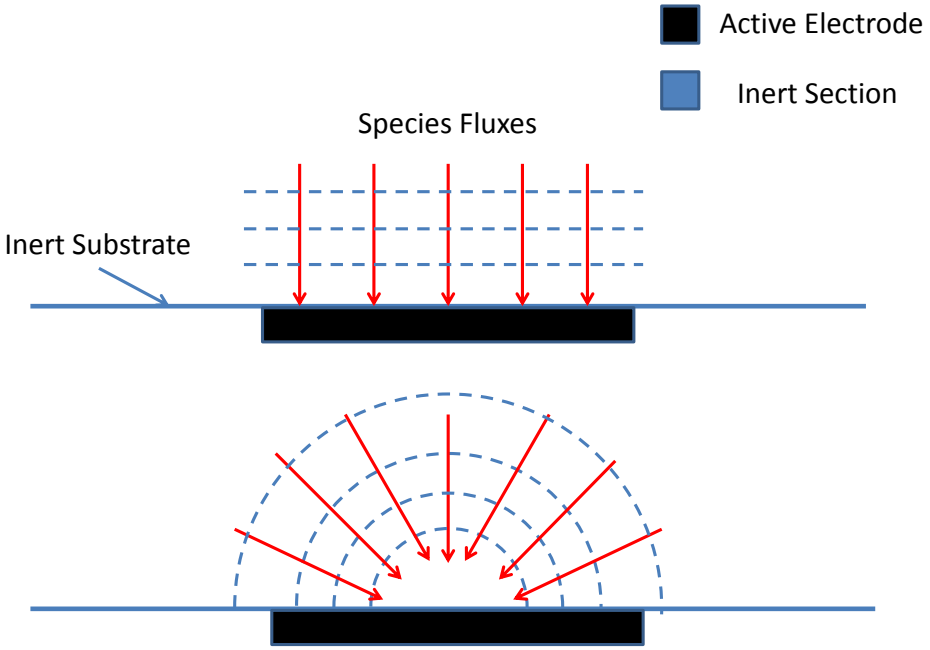

Figure 11: Differences between macro (top) and micro (bottom) electrodes. For inert and non-porous substrates (e.g. glass, polymer), there is no chemical fluxes (red arrows). For micro electrodes, the fluxes are largest at the edges and become smaller towards the centre

The Faradaic current I_f depends to a large extent on the diffusional behaviour of species flux, which is in turn influenced by the electrode dimension (Figure 11). This dimension could be broadly categorized into macro and micro sizes. For a circular

disk of diameter d_e, a macro electrode corresponds to $d_e \geq 100\,\mu m$. Micro electrodes often has $d_e \sim 1 - 10\,\mu m$ and nano spheres have $d_e \sim 100\,nm$.

For large electrodes, the species flux tends to follow uniformly straight lines. Consequently, the diffusion layer grows in mono direction orthogonal to the substrate surface (ignoring small variation around edges). The diffusion layer size is estimated by the expression $\sim (Dt)^{1/2}$, in which D is the diffusivity and t is the elapsed time for the diffusion process. If d_e is much larger than $(Dt)^{1/2}$ then macro behavior is observed. Generally, macro electrodes tend to exhibit the mass transport limitation behavior as shown in Figure 10 above.

Conversely a micro-electrode-based diffusion layer is now circular and completely covers the electrode surface. The fluxes are now dependent on position: they are greatest around the edge due to plentiful supply of reactants and smaller towards the centre. Because micro electrodes have higher fluxes than their macro counterpart, the current is less limited by diffusion. In fact, under reasonably slow scan rates, a pseudo steady state is achieved - a behavior demonstrated in later chapters of this work.

Although many of electrochemical measurements are still conducted under the diffusion control regime, hydrodynamics-based techniques have also become popular. A primary reason for applying these techniques is the ability to control the diffusion layer's thickness (Figure 12). In the diffusion mode, this layer keeps growing with time and subsequently leads to a drop in measured current; however when forced convection is present, the layer is not permanently attached and grows over the surface as before. Instead due to the flow or rotation, fresh electrolytes are brought to the surface, reacts and forms a new diffusion layer. This layer is then swiftly swept away and the process repeats. Hence over time, the thickness becomes constant and the current reaches a limiting value which is typically dependent on hydrodynamic variables. Furthermore, by varying these variables, this layer can be altered, leading to an even larger limiting current.

Figure 13 depicts two devices which are commonly used to conduct electrochemical studies under flow condition. The first device is the channel electrode, which is essentially a rectangular channel with a single or multiple electrodes embedded on the sides. The electrolyte solution is then forced over the static electrode. The other device is the rotating disk electrode which conveys the flow by regularly rotating a cylinder submerged inside a solution.

As discussed earlier, due to the constant size of the diffusion layer, the current reaches a pseudo limiting value in linear sweep voltammetry. Early work has inves-

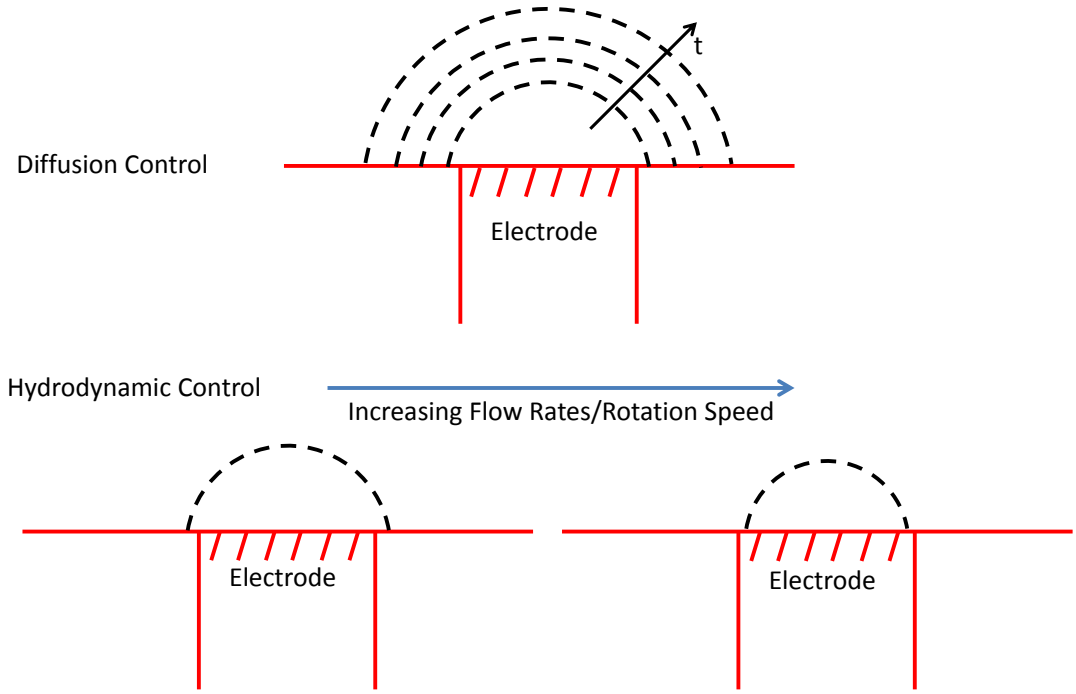

Figure 12: Mass transport under diffusion (top) and hydrodynamic (bottom) controls. The black curves denote the diffusion layer. The size of such layer is changed by varying hydrodynamic variables

tigated explicit dependence between this limiting current I_{lim} and the hydrodynamic factors, known as the Levich expressions [38, 39]. For the devices above, these corresponding expressions are:

$$I_{lim}^{CE} = 0.925nFc_{R0}w_e x_e^{2/3} D_R^{2/3} (4V_f/h_c^2 d)^{1/3} \tag{1.20}$$

$$I_{lim}^{RDE} = 0.62nFAc_{R0} D_R^{2/3} \omega^{1/2} \nu^{-1/6} \tag{1.21}$$

in which V_f is the solution flow rate across the channel and ν is the solution dynamic viscosity. Since the electroactive species are often present in minute amounts compared to the solution volume, the viscosity is essentially the same as that of the solvent. Furthermore, if either V_f or ω is increased, the respective currents also increase. An important assumption in deriving Equations 1.20 and 1.21 is the flow laminarity,

e.g. it is possible to deterministically solve for the flow profile from Navier-Stoke equations. Under turbulent regimes, these equations serve as first order approximations rather than exact results. Another critical assumption is that the time scale for mass transport is much larger than that of fluid dynamics. This is usually achieved when the hydrodynamic flow reaches a steady state profile as seen in Figure 13.

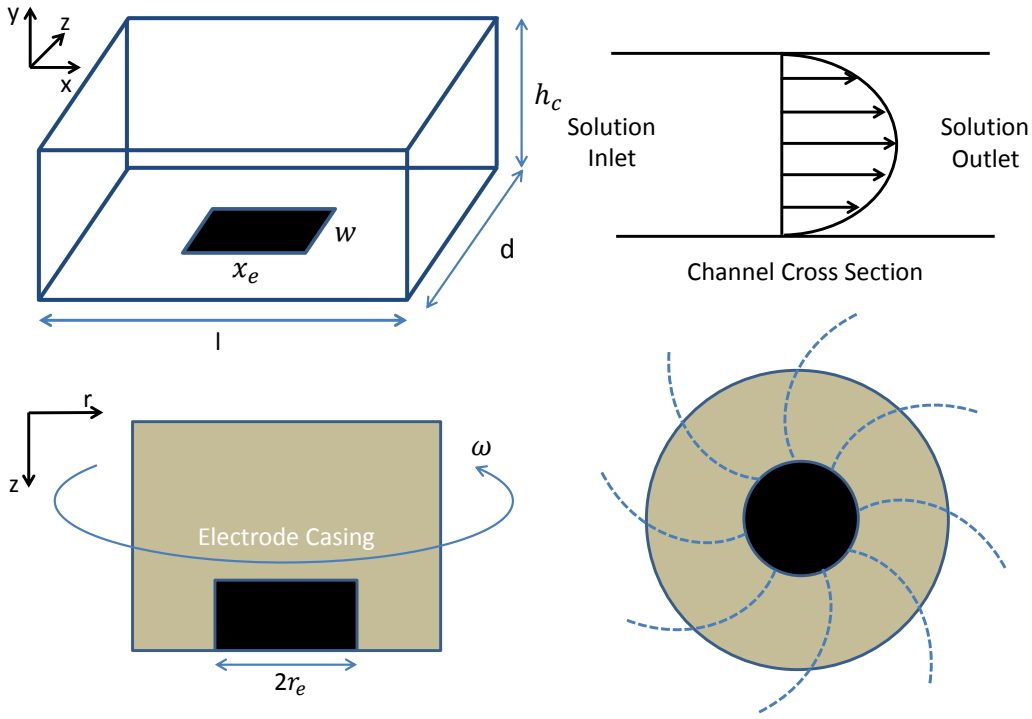

Figure 13: Channel Electrode (top) and Rotating Disk electrode (RDE) (bottom) with the corresponding dimensions. Electroactive areas are colored black. Typical steady flow profile for each device is indicated. Parabolic profile is often observed for channel electrode while swirling flow (top down view) applies to RDE. In both cases, the Reynold number is sufficiently small so that distinct, laminar fluid structures are ensured

Neglecting the background signal, the current recorded from linear sweep voltammetry composes of two parts. The first component is due to the pure charge transfer reaction and is thus associated with I_f (Equation 1.8). The second component I_c arises due to charging and discharging of the electrical double layer [40]. This layer is formed above the electrode to counter the imbalance of charge which occurs very close to the surface. The presence of this double layer and the potential gradient causes the capacitive current to flow to and away from the electrode, in the similar manner as a

normal capacitor charges and discharges.

Since exact details of the double layer are generally not accessible and dynamically changing throughout experiments, the capacitive current I_c is usually viewed as extra complication and leads to difficulty in extracting I_f. Furthermore, both linear sweeps and cyclic techniques are not always reliable methods to separate these two components from each other. In principle, the capacitive current can be reduced by either i) using a small electrode area, which effectively reduces its total capacitance or ii) decreasing the potential gradient, which is achieved via reduction of the scan rates.

A popular technique which helps to eliminate the capacitive component from electrochemical signals is Square Wave voltammetry [41] (Figure 9). In this method, the potential is stepped up and down but follows the same path of the linear sweep. The backward currents (black dots) are then subtracted from the forward ones (red dots). This subtraction effectively eliminates I_c at each time point and thus only the difference between Faradaic currents is recorded. Theoretical foundations for chemical analysis were also well established [42, 43]. Square Wave techniques have been applied to diverse problems, ranging from diagnostic bio-sensors (e.g. antigens, DNA, human hormone, etc.) to environmental sensing (e.g. heavy metals and arsenic compounds) and analysis of food ingredients [44]. In electroanalysis, the technique is used to investigate electron transfer processes at liquid/liquid interface and characterize surface-bound reactions [45].

A more general class of voltammetry, termed AC voltammetry, is also popular. In this method, a sinusoidal perturbation of different frequencies are superimposed on to the linear input (Figure 14) [46]. Several important arguments for the technique were put forward by Bond et al. [47]. Firstly, from a mathematical point of view, the technique is more fundamental in comparison to Square Wave or other similar waveforms. This conclusion stems from the fact that periodic and well-behaved functions can be decomposed into Fourier series of sins and cosines [48]. The effects of different transient waveforms were compared numerically and at low sinusoidal amplitude all responses are inherently similar when being expressed in the frequency domain [49]. Furthermore, the output from a typical AC experiment does not just contain the usual aperiodic DC component, but additional currents called harmonics (Figure 15). Because the 2^{nd} and higher harmonics are theoretically less influenced by capacitive currents (Section 5.1), they are analytically valuable. In other words, a single experiment carried out with AC signals generate a vast amount of data, which can then be used for many purposes. Finally, to enhance harmonics higher than 4^{th}

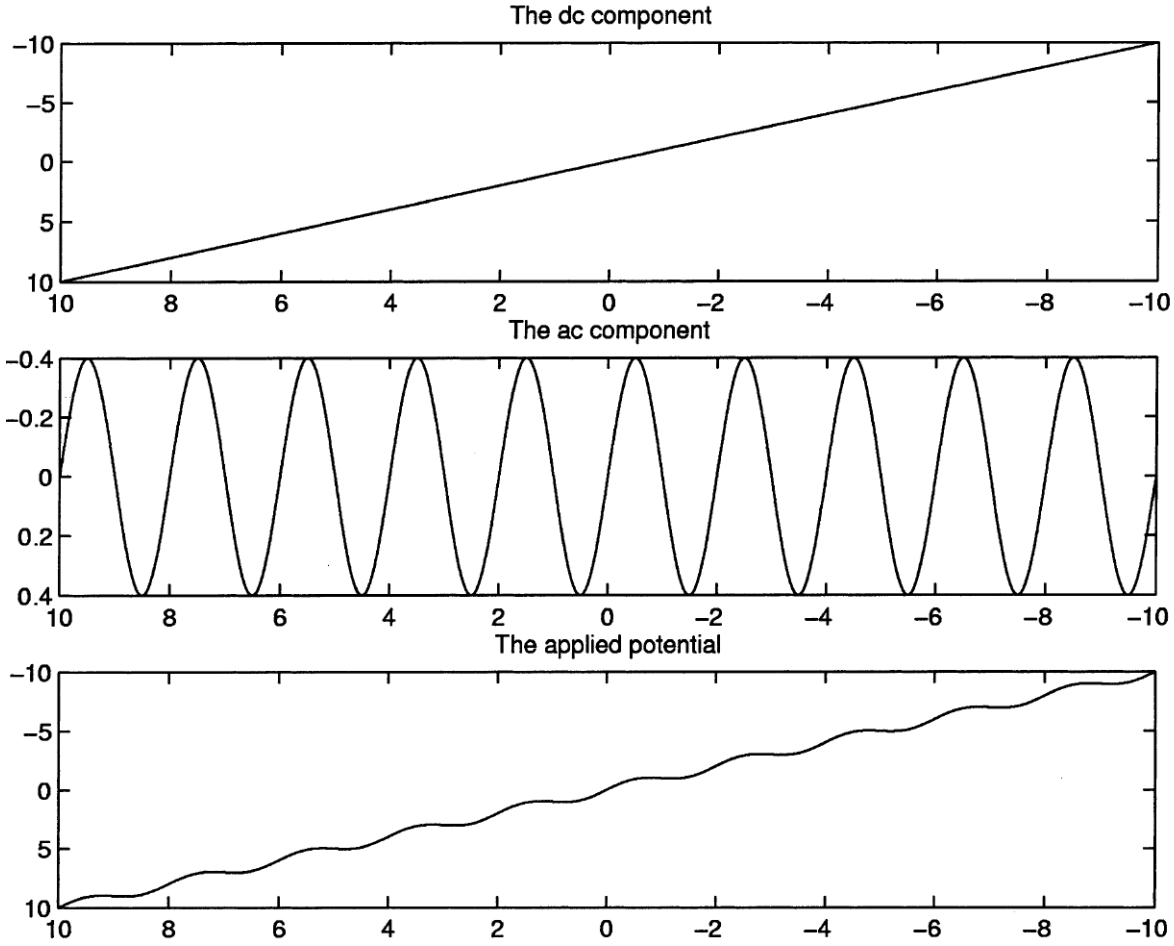

Figure 14: In AC voltammetry, the potential is formed by addition of a sin-wave function on a linear sweep

and eliminate the influence of background effects, sinusoidal perturbations with large amplitude were employed [50].

In electroanalysis, AC voltammetry is most commonly applied to estimate parameters involved with electron transfer reactions, typically the equilibrium kinetics and uncompensated solution resistance. The AC harmonics offer a simultaneous evaluation of these parameters as well as the discrimination of slow kinetics and high resistances [51]. A heuristic, pattern-recognition algorithm to estimate electrode kinetic for electroactive pair ferro/ferri-cyanide in highly resistive organic solvent was developed [52, 53]. This is accomplished by i) selecting the (higher) harmonics most sensitive to desired parameters and ii) systematically varying the parameters until a satisfactory agreement between numerical and experimental harmonics is achieved. Similar works were also carried out to investigate ferrocene oxidation at a glassy carbon electrode

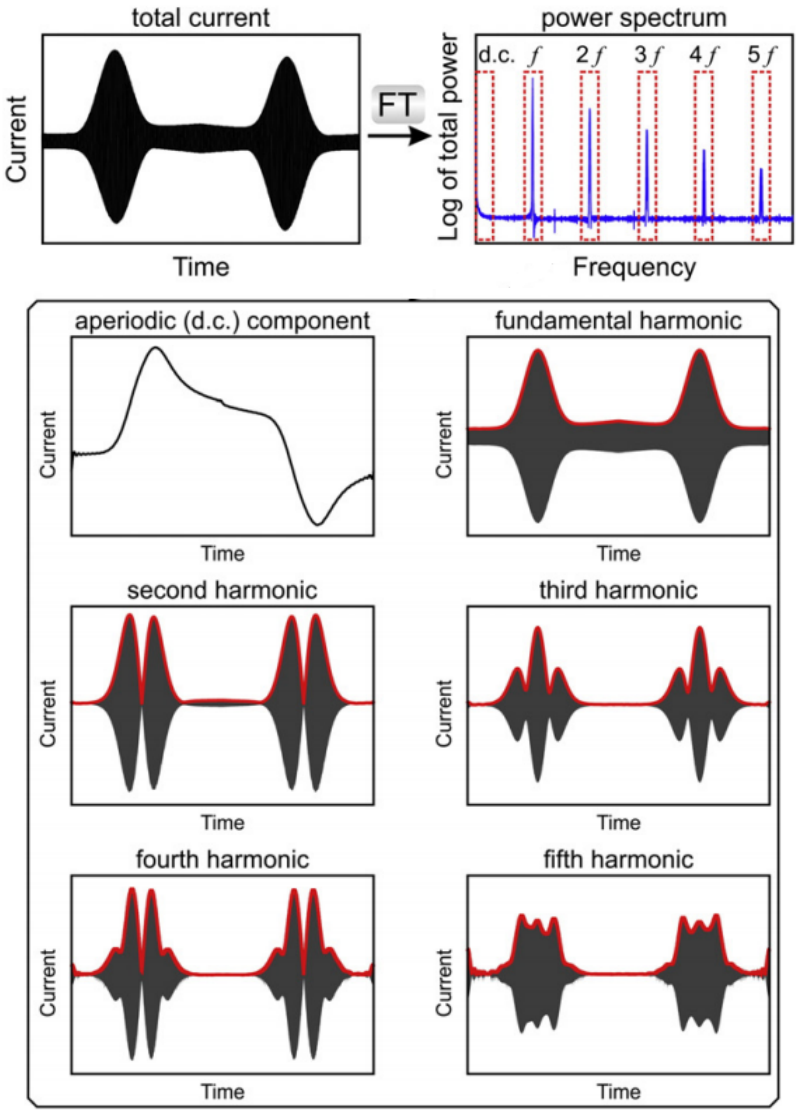

Figure 15: A typical AC voltammogram (top) and the extracted aperiodic (dc)/harmonic current (bottom). A Fourier transform is applied to the AC current to reveal the frequency spectrum

in acetone nitrile [54] and tetracyanoquinodimethane in ionic liquid [55] using various conductive materials. Both studies reveal that the interested reactions are reversible or close to reversible limits. An automated version of the above method was recently introduced using a combination between the simulation suite *MONASH* and simplex optimization toolbox NimRod [56, 57].

Another important application of AC voltammetry is to evaluate coupled homogenous kinetics. Single redox reaction sometimes does not occur alone, but is followed

by other reactions in bulk medium. A simple example is the EC mechanism:

$$R \leftrightarrow O\,(E)$$

$$O \overset{k_{EC}}{\rightarrow} P\,(C)$$

In this scheme, the reactant is first electrochemically converted to products, which then decays irreversibly to electrochemically nonreactive final product P. The presence of coupled kinetics changes the appearance of the voltammogram (Figure 16). As the homogeneous kinetics increases, more O is readily converted to P, which leaves little starting material for the backward scan. Consequently, the backward peak becomes noticeably smaller in comparison to forward peak at high k_{EC}.

The above mechanism was applied to the study of tungsten complex $[W(CO)_2(dpe)_2]^+$ (dpe = 1,2-diphenylphosphinoethane) cis to trans isomerization [58]. Although the reaction is rapid at room temperature, a range of kinetic values were obtained by fitting experimental data to multiple harmonics generated from numerical solutions. It was also observed that the resolution of chemical kinetics became better as higher frequencies are applied. A more complicated mechanism, involving catalytic reactions was studied by [59]:

$$R \leftrightarrow O + e^-$$

$$O + X \overset{k_1}{\rightarrow} R + X^+$$

$$O + X^+ \overset{k_2}{\rightarrow} R + X^{2+}$$

here X denotes mediator (ascorbic acid in this case) and R is Ferrocenemethanol ($C_{11}H_{12}FeO$). From simulation results, it is noted that if $k_2 \gg k_1$ (i.e. the second reaction is the limiting step) and the electron transfer is fast, the obtained harmonics are independent of the presence or absence of these catalytic steps. Under a fast heterogeneous transfer step, the species concentrations at the electrode interface are governed by the Nernst relation 1.13. In addition, since the magnitudes of harmonics are primarily determined by the these concentrations, the presence of catalytic steps do not influence those harmonics.

A similar mechanism, termed EC', is particularly relevant for glucose sensors, and

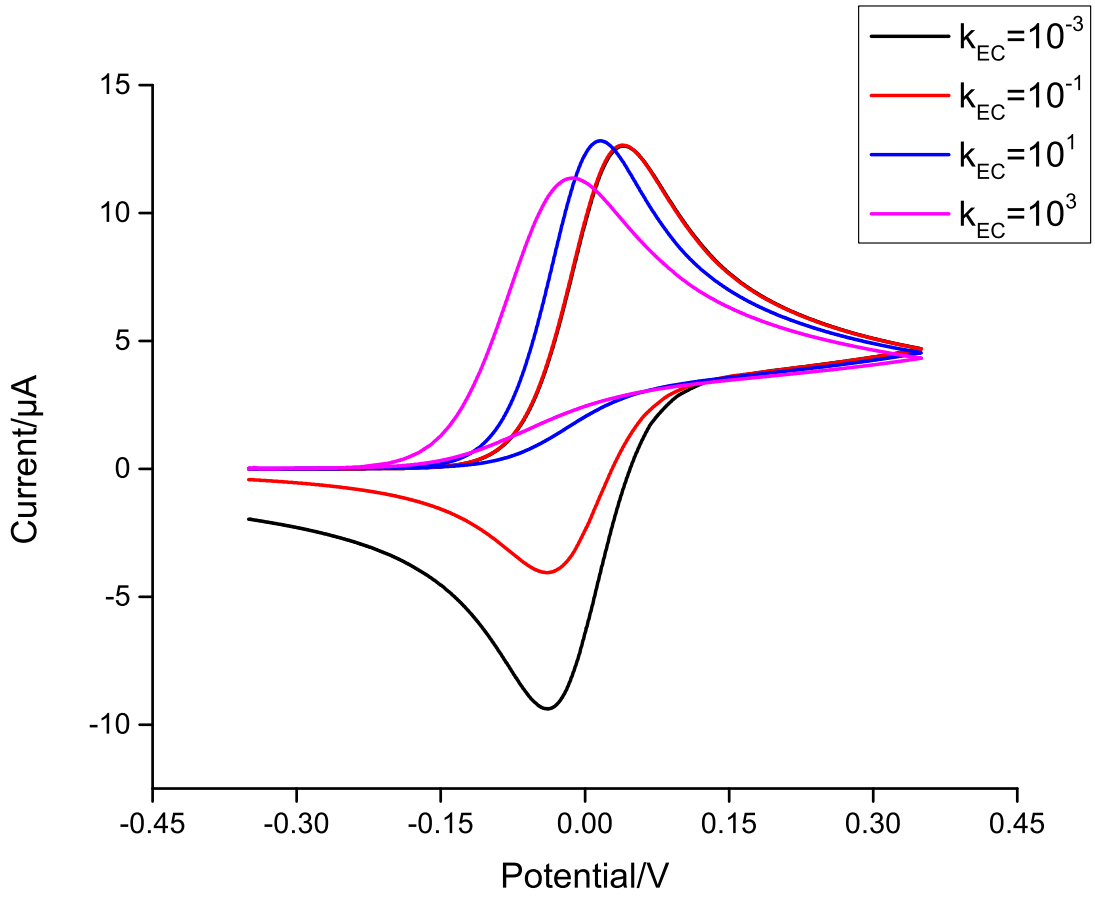

Figure 16: Cyclic voltammograms for EC mechanism under different reaction constants k_{EC} (largest value: purple and smallest value: black). As the reaction constant k_{EC} increases, the backward peak becomes smaller because the oxidative species is consumed more quickly by the homogenous reaction

the simplified scheme is described as follows [60]:

$$2FcR \rightleftarrows 2FcR^{+} + 2e^{-} \tag{1.22}$$

$$Enz + 2FcR^{+} \rightarrow Enz^{2+} + 2FcR \tag{1.23}$$

$$Glucose + Enz^{2+} \rightarrow Enz + P \tag{1.24}$$

Here the catalytic reactions are 1.23 and 1.24 which respectively regenerate elec-

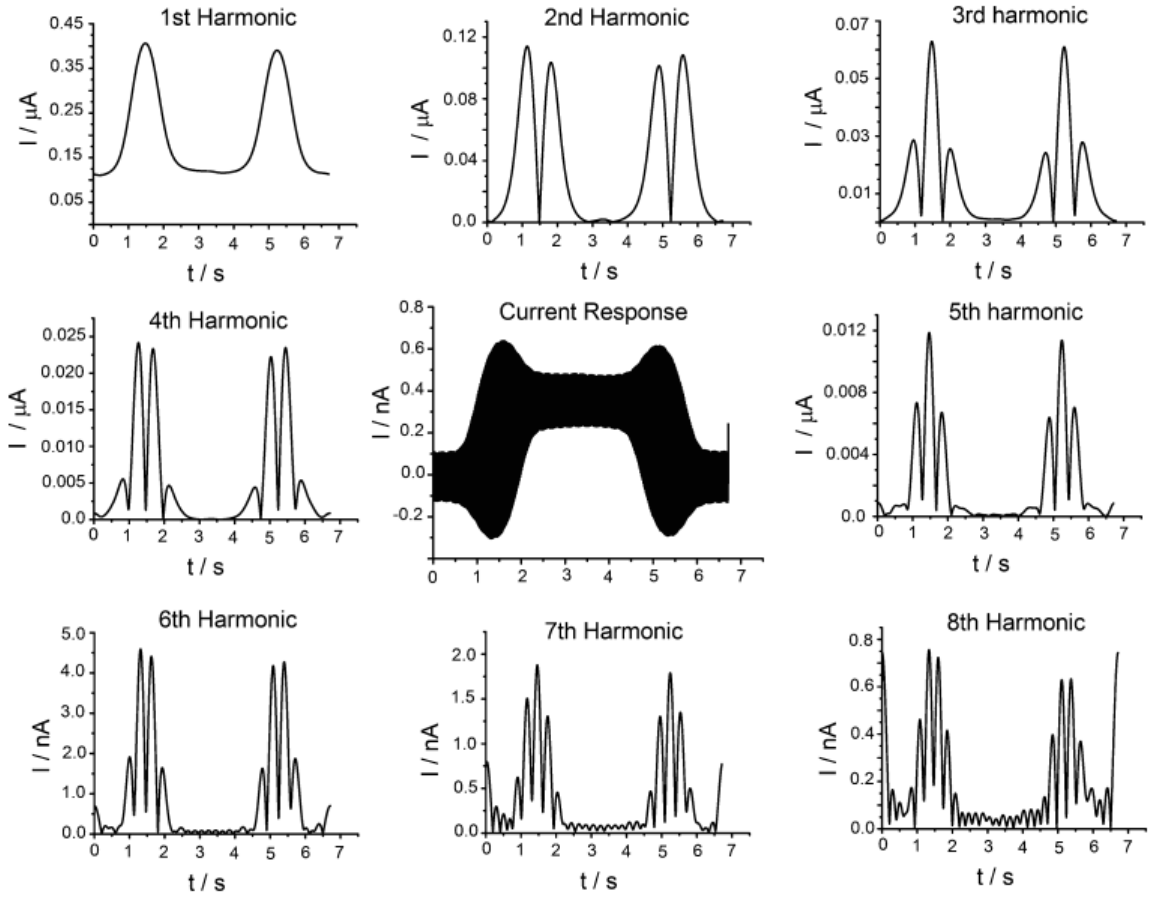

Figure 17: Total current (center) and extracted 1^{st} to 8^{th} harmonics in large amplitude AC voltammetry experiment using Au/Pt channel electrodes

troactive species FcR and the enzymes Enz. By making certain assumptions such as i) a fast heterogeneous step ii) fast and irreversible catalytic reactions and iii) an excessive amount of $Glucose$ is present relative to Enz so that the turn-over rate of Ezn is kept essentially constant, it is possible to calibrate the measured current with respect to the concentration of glucose [61]. The EC' mechanism is of great interest due to its promising applications in detecting sulphide species in oil and gas wells. Micro reactor systems for sensing sulphide-based species were developed using the traditional cyclic voltammetry and channel electrodes [62]. The possibility of harvesting energy from this mechanism using current-controlled (galvanostatic) technique was initially proposed by Cooper [63]. Despite extensive works, applications and benefits of AC technique to analysis of this mechanism has not been reported in literature.

Combination between hydrodynamic devices and sinusoidal waveform to study

electrochemical reactions is a relatively new research area. The dependence of harmonic peak heights on flow rate inside a channel was first investigated by Matthews [64] (Figure 17). It was concluded that for a simple and reversible redox couple, the peaks of higher harmonics are independent of flow rates and they converge towards the same values under diffusion controlled conditions. In addition, as higher frequencies were applied, these peaks tend to be constant versus $V_f^{1/3}$ rather than increase linearly as expressed in Levich relation 1.20. Furthermore, an estimation of double layer capacitance is feasible by using the fundamental charging current, which corresponds to the magnitude of the base-line in the 1^{st} harmonic (Equation 5.7). 2^{nd} and higher harmonics are also demonstrated to be less sensitive to rotation rate under rotating electrode [65]. Using this observation, kinetic parameters of the redox couples $[Ru(NH_3)_6]^{3+/2+}$ and $[Fe(CN)_6]^{3-/4-}$ at glassy carbon/platinum electrodes are evaluated.

1.4 Numerical Modeling in Electrochemistry

In any model-based approach, numerical solution plays a critical role. A primary motivation for using this method is exact analytical results are often limited in scope and/or not available. Cheaper computing costs and reliable programming recipes also motivate the interest in applying the methodology to complex problems.

In the field of electrochemistry, numerical methods have been extensively applied, especially to the solution of mass transport equations. Though each method differs slightly in detail, these procedures share the same underlying steps [66]:

1. Propose a physical model and corresponding conservative equations
2. Discretize the problem, which leads to finite number of unknowns
3. Solve the equation system
4. Post-process the result and derive the desired values

The oldest and perhaps simplest method is Finite Difference (FD). In this approach, the modeling domain is divided into discrete nodes (Figure 18). From conservative equations (mass, energy or momentum balances), one requires solving for the corresponding field variables (concentration or temperature) at these nodes. Using Taylor expansions, these equations are then discretized and the field values at neighbourhood nodes are related [67]. To close the problem, boundary conditions, being either Dirichlet (fixed constant) or Neumann (fixed flux), are supplied and lead to a system of equations. Routine solution methods are then applied (step 3 above) and the process is repeated until convergence or other conditions are satisfied.

Because FD is simple both in terms of concept and implementation, it has been the method of choice for practitioners both in electrochemistry and other areas such as biology and finance [68, 69]. A fast and reliable simulation methods for macro electrode, which rely on implicit time formulation was proposed by [70–72]. The method is general and allows for coupling between any homogenous and electron transfer reactions.

Theory for electrochemical responses at micro electrodes was developed by [73, 74]. A digital procedure for computing such responses, using the "Alternating Direction Implicit" (ADI) approach was implemented in [75]. Performance comparisons of major methods for micro disk, namely ADI, "Fully Implicit Finite Difference" (FIFD) and the use of Ritch Myer coefficients (FIRM) were thoroughly reviewed by Gavaghan [76, 77].

For some biological compounds, low supporting electrolytes are required to main-

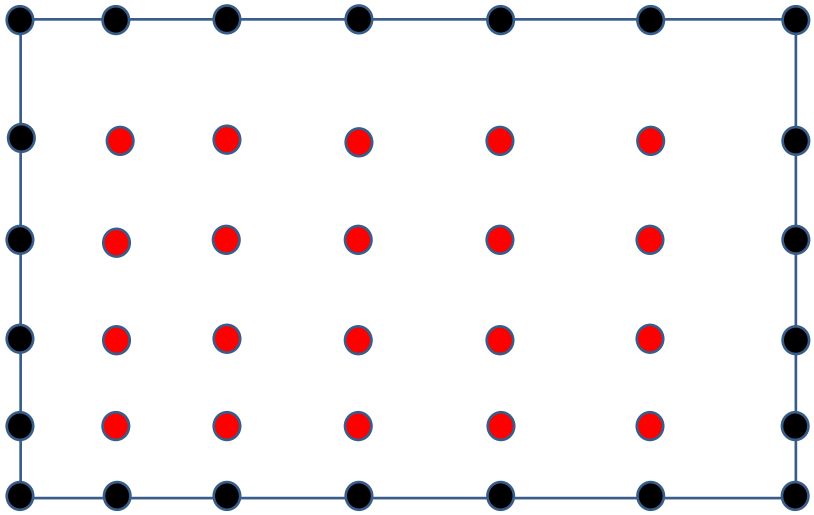

Figure 18: In FD, solution process proceeds by breaking down the modeling domain into discrete points. Boundary nodes are colored black and interior ones are red

tain their integrity. Under such circumstance, the effects of migration flux (Equation 1.5) should be taken into account. A number of studies have been reported in this direction. The zero-field approximation commonly applied in those studies was critically evaluated by Dickinson et al. [24]. Threshold concentrations of supporting electrolyte which produce the diffusional cyclic voltammogram for a given redox system were estimated in Compton et al. [23]. Using potential step voltammetry, stripping of Thalium ion at micro-sized spherical particles was studied [78]. In addition, the same technique was applied to chronoamperometry of strong acids and deviations from the usual Cottrell behavior were noted at low amounts of salt [79].

For periodic structures, a common modeling approach is the use of diffusion-domain unit cell. An interesting problem reported the investigation of the anisotropic electrochemical behaviour of highly ordered pyrolytic graphite (HOPG) surface [30]. Several advantages of carbon-based electrodes are reviewed in Reference [80]. Flat structures such as 2D graphene are open to chemical and physical modifications as well as formed into other geometries such as single wall or multiple walls tube [81]. The edge plane in HOPG is much more electrochemically active (i.e. having higher k_0) than those of

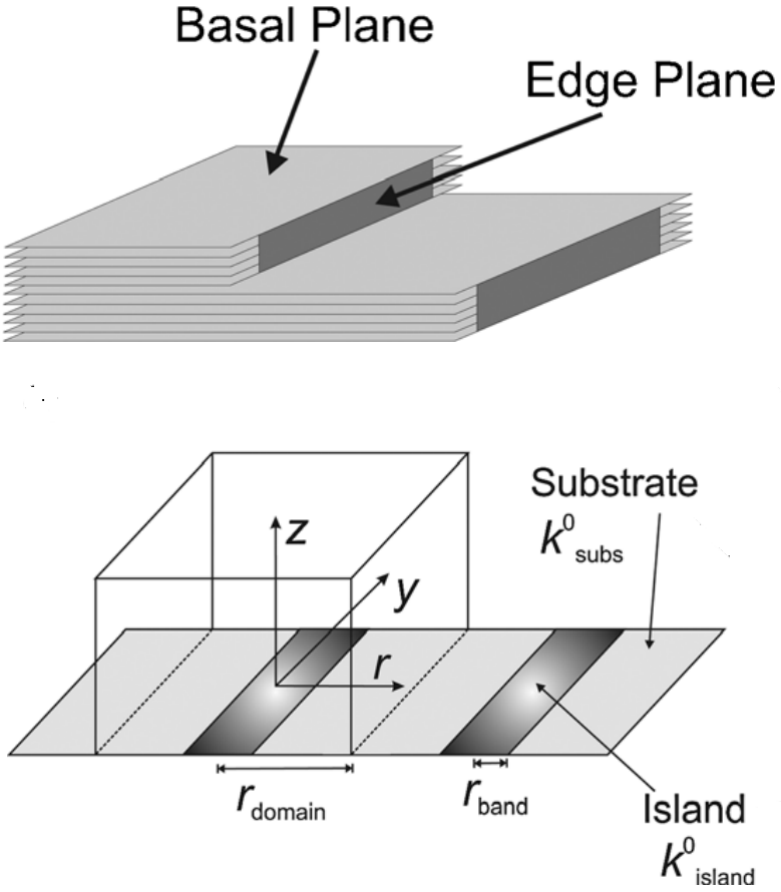

Figure 19: HOPG structures with electrochemically slow (basal) and highly active (edge) planes (top). The structure is modelled by a series of flat band electrodes and computational domain is also indicated (bottom)

large and flatter planes (Figure 19). This structure is modelled after a series of band electrodes and voltammetric responses are then studied as functions of geometrical surface coverage [82]. A very similar line of work, involving partially blocked electrode (PBE) surfaces was also investigated [83, 84]. The behaviour of porous electroactive structures was approximated by stacking layers of homogenous spherical electrodes on top of each other [85].

Though the above problems predominantly consider diffusion-controlled processes, FD were also applied to flow conditions. For example, FD models of electrochemiluminescent (ECL) activated processes inside micro-fluidic channel were demonstrated by Qui [86], showing the dependence of ECL intensity on hydrodynamic flow rates and cell geometry such as in generator/collector configurations. However, a drawback of FD is limited applicability to complex shapes. The Finite Element (FE) method

elegantly addresses this problem though the formulation is considerably more sophisticated than FD. Instead of dividing the domain into points, FE discretize it into smaller elements (Figure 20). The final solution is then approximated as polynomial combination of the field values at element's nodes and shape functions. The FE approach involves an integration across the elements and regions as opposed to the local approximation in FD. Furthermore, boundary conditions are naturally accounted for during the integration process. Thanks to improvements in mathematical formulation and computer power, FE has become a standard analysis tool in many areas such as structural/fluid mechanics, heat transport and soil erosion. Its strength lies in the flexibility to generate any mesh structure and adaptability to shapes with different curvatures [87].

Simulation of two dimensional inlaid-electrodes were considered by various authors [88, 89] (Figure 21). The main difficulty is the presence of a singularity point at the interface between electrode surfaces and substrate layers as the flux increases from almost 0 to a large finite value across this point. A common solution to this problem is appropriate mesh refinement without incurring excessive computational cost. The uses of protruded or recessed electrodes remove such singularity issue because boundary conditions are now compatible at the inter facial point. The effects of protrusion heights and recession depths on current responses were compared to that of inlaid disks using simulations [90, 91]. While there is no significant difference due to recession effects, a similar protrusion height leads to a considerable increase in current.

The subject of adaptive mesh refinement has been considered by many authors [92]. The underlying principle behind this approach is straightforward: if errors in some elements exceed certain tolerances, these elements are then locally refined to achieve better solutions. A series of work [93–95] simulate the current of inlaid disk under both diffusion and flow control for simple redox reaction as well as non-linear homogeneous kinetics (such as EC', ECE and $EC2E$). An obvious issue with this approach comparing to the fixed-mesh approach is generally higher computational expense.

Microfluidic devices have become increasingly popular in chemical applications. The main reasons are due to small sizes, ease for maintenance, higher mass transfer rates and lower production costs compared to traditionally larger devices. Because there is a presence of flow, numerical solutions to convection-diffusion equation are required (Equation 1.4). The methodology for channel electrode with 2D and partially 3D models were first demonstrated by Stevens [96, 97]. This work considers the

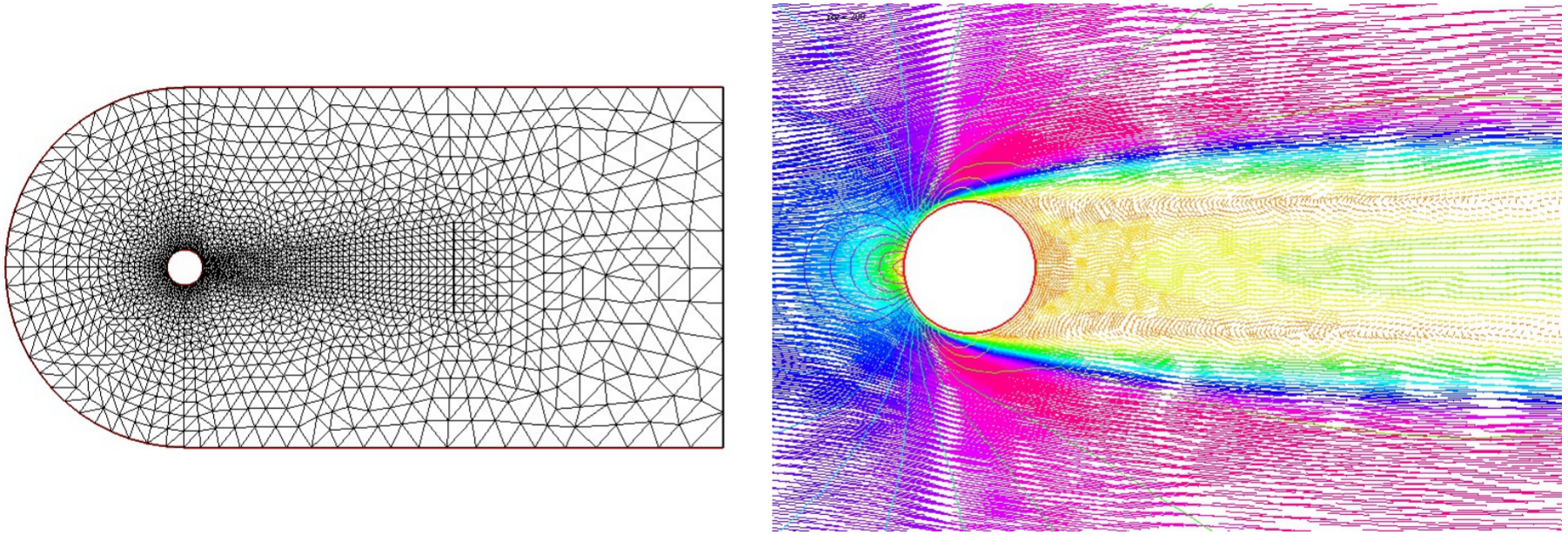

Figure 3.10: Mesh and the velocity and pressure at Reynolds 200

Figure 20: In FE, the solution region is meshed into smaller elements (left). The example shows an unstructured triangular mesh for 2D problems and the computed steady-state velocity profiles around a cylinder (right). The main flow is from left to right of page

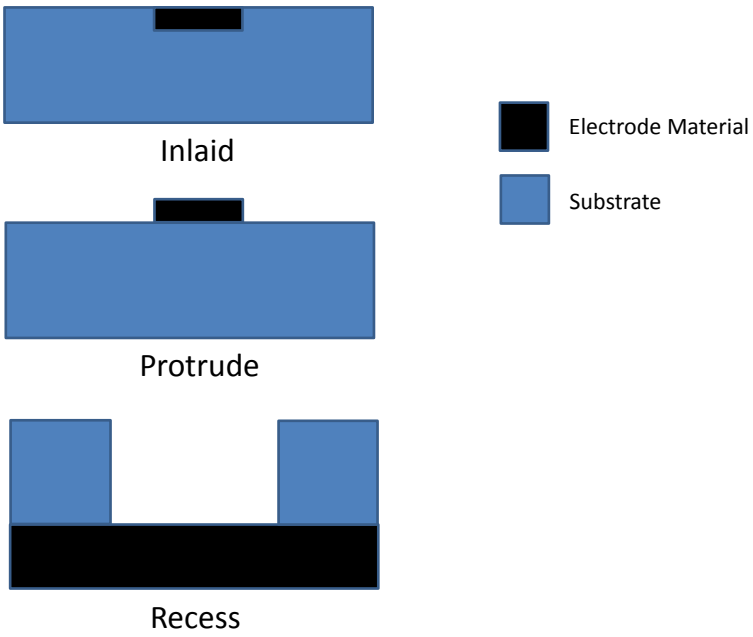

Figure 21: Due to the fabrication process, the final electrode can take many configuaration including inlaid, protrude or recess

effects of fast chemical reactions, which is a step beyond previous FD works. FE was subsequently applied to study hydro modulation effects, notably the modulations of the inlet pressure and periodical oscillations of electrode disk, taking into account the time-variant nature of the fluid flow from Navier-Stoke equations [98]. Other complex problems, such as reaction profile imaging or voltammetric responses resulting from ion-transfer across two immiscible flows in a confluence reactor was tackled by Henley [66].

Besides FD and FE, other numerical methods are available to solve partial differential equations describing the mass transport effect. Finite volume (FV) for solving diffusion equations was proposed by Feldberg [99]. The method was earlier applied to diffusional heat transport and solution of Navier-Stoke equations [100]. Essentially in FV, conservative equations are written for control volumes surrounding individual nodes. A much less common method is Lattice-Boltzmann. Implementations and consistency with previous results in FD and FE were documented by Du [101, 102]. Interestingly, solutions to the problem of particle sizing and tracking were explored via a 3D Lattice-Boltzmann model [103].

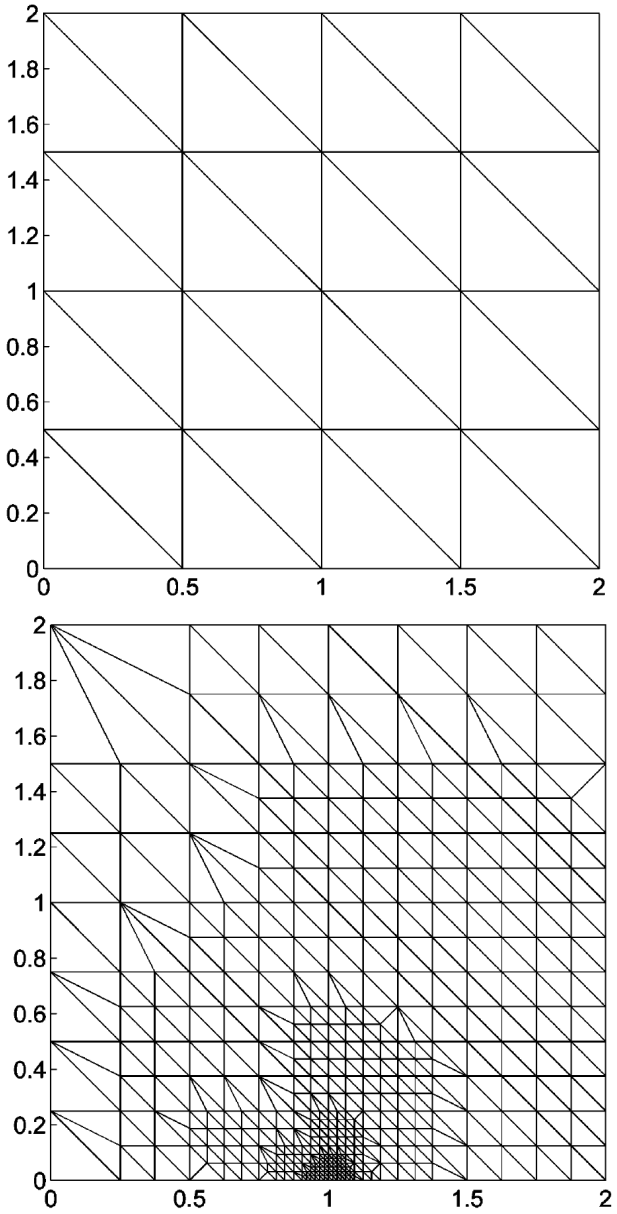

Figure 22: An example of adaptive mesh refinement for an inlaid disk. The starting mesh (top) is locally refined around the singular point 1 until convergent tolerance is achieved (bottom)

Nowadays there is a wide selection of numerical implementations for the above methods in many programming languages. Because of its mathematical simplicity, most of FD codes can be implemented in-house. For FE or FV, implementations are considerable more complex and although in-house codes are possible, significant focus has been shifted to commercial software. Open source code or proprietary packages

offers automatic generation of geometry, meshing, solutions, post-processing as well as visual graphics. In addition, they are able to couple and solve multiphysics problems thanks to extensive and well-developed physics modules.

With commercial codes, the user concentrates on physical understanding of the problem and solution prototype rather than mathematical details. Thus it tends to require less time and labour to solve a problem. However, the software cannot completely substitute the user's role. Since these methods are very general, in order to obtain good solutions it still requires certain inputs from end users, such as the mesh refinement and selection of suitable physics interfaces.

1.5 Identifiability in Experimental Design

The subject of model identifiability has one of its origins from biological sciences. Because typical models in this subject often have many parameters and limited observable outputs, it is reasonable to determine whether these parameters can be uniquely determined given the output information [104].

To form a more concrete discussion, consider the generic dynamic model expressed in equations 1.25-1.27:

$$f(\dot{x}(t), x(t), u(t), \theta, t) = 0 \tag{1.25}$$

$$x(t_0) = x_0 \tag{1.26}$$

$$y = h(x(t), u(t), \theta) \tag{1.27}$$

System 1.25 represents the collections of ordinary differential equations, partial differential equations or the general Differential Algebraic Equations which describe the time evolution of the physical system under investigation. Condition 1.26 is the starting or initial condition for the field variables x. The final equation 1.27 links the model variables to a response (or responses) y which is observable or measurable. Note that both x and u can be vectors. In addition, one may have controllable variables $u(t)$ and the parameter vector $\theta = (\theta_1, \theta_2, ..., \theta_p)$ which might not be completely known at the time. The function h is assumed to be an analytical and can be strongly non-linear. Though y can also be a vector of responses (i.e. multiple outputs), for simplicity at the moment assuming that y is a single observable and the data set is thus in the form of a time series $y_m = y(t_0 \leq t \leq t_f)$.

The concept of structural identifiability is proposed by [105] using the integral:

$$V(\theta) = \int_{t_o}^{t_f} (y(\theta, u) - y_m)^T W_y (y(\theta, u) - y_m) dt \tag{1.28}$$

where W_y is the weighting vector (taken to be unit vector for simplicity). 1.28 measures the differences or losses between model response and measured data for a given set of θ. The system 1.25-1.27 is locally identifiable if there is θ_0 at which $V(\theta)$ attains a minimum. If the local optimum is also the global one, then the structure is declared to be globally identifiable.

Another similar definition was suggested in [106], for two sets of parameters lying within the their respective bounds, the distance between them is computed as :

$$\Phi_{\theta,\theta^*} = (\theta - \theta^*)^T W_\theta (\theta - \theta^*) \tag{1.29}$$

and the corresponding distance between two resulted responses are:

$$\Phi_y = \int_{t_o}^{t_f} (y(\theta, u) - y(\theta^*, u))^T W_y (y(\theta, u) - y(\theta^*, u)) dt \tag{1.30}$$

From matrix theory and by definition, $\Phi_y \geq 0$ for any pair (θ, θ^*). Now given to small abitrary values ε_y and ε_θ, the trajectory $y(\theta, u)$ is globally identifiable if $max_{arg\,(\theta,\theta^*)}\, \Phi_{\theta,\theta^*} \leq \epsilon_\theta$ subjecting to condition that $\Phi_y \leq \varepsilon_y$. Although the definition is more complicated, the basic intuition is the model response is globally identifiable if and only if for the same control and starting conditions, the two parameter sets need to produce non-overlying responses (i.e. $\Phi_y > 0$). In other words, if $\varepsilon_y = 0$ (thus forcing $\Phi_y = 0$) then the necessary condition for identifiability is $\Phi_{\theta,\theta^*} = 0$ or equivalently $\theta = \theta^*$.

From a practical point of view, the above definitions are rather complicated. A significantly more straightforward alternative was given by [107]:

$$y(x, u, \theta_1) = y(x, u, \theta_2) \leftrightarrow \theta_1 = \theta_2 \tag{1.31}$$

Equation 1.31 represents the fact that if under the same starting condition and controlled variables, there is only a single set of parameters corresponding to each possible response. In other words, the model is identifiable if and only if the stated correspondence is 1 to 1.

Assessment of model identifiability has been a challenging subject in the literature. Detailed studies for linear structure were carried out in [108] and others. However, since a large number of models in engineering and science are non-linear, the previous results had limited implications. To deal with non-linearity, a popular approach is partial linearization of the equations so that techniques developed for linear analysis are applicable. The main drawback however is that any result only has local significance and identifiability of the original model cannot be proven definitely. Approaches to tackle general non-linear model were proposed (for example based on Taylor or generating-series expansions) [109], but so far they suffer from either limited scope (e.g. moderate models with a few parameters and state responses) or demanding

computational resources [107, 109].

Another important topic associated with identifiability is parameter estimability. Due to interactions (e.g. correlations) among the parameters, they can be structurally identifiable but poorly estimable. Consequently a large portion of experimental design literature was dedicated to development of methods which aim to i) minimize the correlations and ii) improve the precision of parameter estimates. These methods often require computation of sensitivity vectors or matrices, which measure rates of change with respect to one parameter while keeping others constant:

$$S_\theta = \frac{\partial y}{\partial \theta} = [\frac{\partial y}{\partial \theta_1}, \frac{\partial y}{\partial \theta_2}, ..., \frac{\partial y}{\partial \theta_p}] \tag{1.32}$$

If a derivative in 1.32 is a linear combination of any other derivatives, then the group of involved parameters is clearly not estimable. From an optimization perspective, each gradient represents a search direction in each dimension θ_i, therefore if they are not all independent then it is not possible to estimate all of them at once. An elegant approach is to calculate the rank of Fisher Information Matrix (FIM) [110] and if this rank is less than p then all the parameters are not estimatable. The matrix condition number, expressed by ratio between the largest and smallest eigenvalues yields similar information [111]. However, these methods alone does not guarantee accurate parameter estimates as actual magnitudes of sensitivity elements in S_θ also matter. For example, even if $\partial y/\partial \theta_i$ is linearly independent from the rest but its numerical value is small then the search step in dimension θ_i is also small and this does not lead to useful results. A similar method is based on A, D and E (i.e. alphabetical) optimal design criterion which concerns with different scalar measurements of the FIM [112]. An improved version of these methods, relying on multi objective optimization (MOO) was presented by Maheshwari et al. [4]. The $AMOO$, $DMOO$ or $EMOO$ considers the Pareto optimal front for two objectives: minimum correlation and maximum information measures and select appropriate points on the curve as the experimental conditions. A comprehensive review of the alphabetical designs and their applications in biology and engineering was given by Franceschini [113].

If the whole parameter set is not estimable, then a sensible approach is to select a subset of them and perform estimability tests above. It can be seen that the computational cost grows in a worst-case scenario as C_p^k where $k = 1, 2, ..., p$. For large p, this combinatorial approach quickly becomes infeasible. Another promising approach is parameter ranking, which orders parameters according to their influences

on the model outputs. It is straightforward that the most important sub-sets are the ones containing most significant parameters and estimability procedure should be applied to them first. By combining orthogonolisation algorithm [114] and ranking the result using minimum square errors, the ability to identify subset of parameters for estimation was demonstrated [115]. Without reference to experimental data, a similar method was proposed using the Monte Carlo method [116]. However, since the method is Monte Carlo based, computational cost is scaled with the number of model calls. A conceptually simpler and more intuitive approach to determine parameter influence was based on the ANOVA framework and developed by Sobol [117]. Two numbers of particular interest are "Total" and "First Order" sensitivity indicies. The latter index accounts for the parameter's own contribution towards output variance whilst the former includes both individual and correlational effects between parameters. Unfortunately, higher indicies are cumbersome to calculate and consequently do not contain useful interpretations [118]. The method is also Monte-Carlo based and has been applied to pharmacological model [119], biochemical network [120], heat dissipation in battery [121] and design of engineering compressor [122]. Improvements in accuracy and convergence of these indicies were also achieved using quasi random sampling [117]. Further reductions in computational cost were achieved via the use of meta-models analytically linking explanatory variables with model outputs, though such constructions are not always feasible [118].

In electrochemistry, both the subjects of identifiability and estimability were recently explored. Identifiability of simple electrochemical system was examined by employing highly modulated waveforms [123]. The same approach was earlier applied to study of reaction-diffusion system [124]. Both works proposed an identifiability test which utilizes the simplified definition 1.31. However, related topics such as parameter selection and discussion of estimability were not pursued, which renders the investigation somewhat incomplete. Identifiability studies were earlier applied to surface-bounded Volmer-Heyrovsky mechanisms by using impedance spectroscopy [125]. The results indicate minor improvements in parameter identification, which is in line with conclusions from Vikhansky [123].

1.6 Parameter Estimation and Bayesian Statistics

In the final phase of an experimental design iteration, it is often necessary to carry out a parameter estimation procedure. The main purpose of this step is to provide the best possible fit between theoretical predictions and collected data. This section reviews major classes of optimization methods and their relevant applications.

Optimization search plays an important role in many areas, ranging from chemical production to economic consumption of resources [126, 127]. Considering a generic formulation of an optimization problem:

$$min\, H(x) \tag{1.33}$$

subjecting to conditions:

$$F(x) = 0 \tag{1.34}$$

$$G(x) \leq 0 \tag{1.35}$$

$$x^L \leq x \leq x^U \tag{1.36}$$

Each equation in 1.34, 1.35 and 1.36 can be a single or set of equations, and optimizing variables x can be a scalar or a vector of numbers. Methods in optimization can be broadly divided into two classes: deterministic and stochastic. Deterministic approaches generally require at least the information of first order gradient with respect to x (quasi-Newton) or even second order derivatives (Newton methods) [128]. Thus a clear disadvantage of deterministic approaches is when it is difficult or expensive to compute those derivatives. However, gradient-based methods are very good at locating local optimum and theoretically faster than any other methods. The reason for its speed is because the search direction is always in the steepest direction with respect to function contours (Figure 23) [129]. Finally, in order to find a global optimum using gradient-based search, multiple starting points are usually required.

Conversely, gradient-less approaches do not require gradient information. In these methods, one first searches for a few directions which improve values of $H(x)$ [130–132]. New search directions are then generated by linear combinations of the best available directions. The approach resembles the famous simplex algorithm which was developed

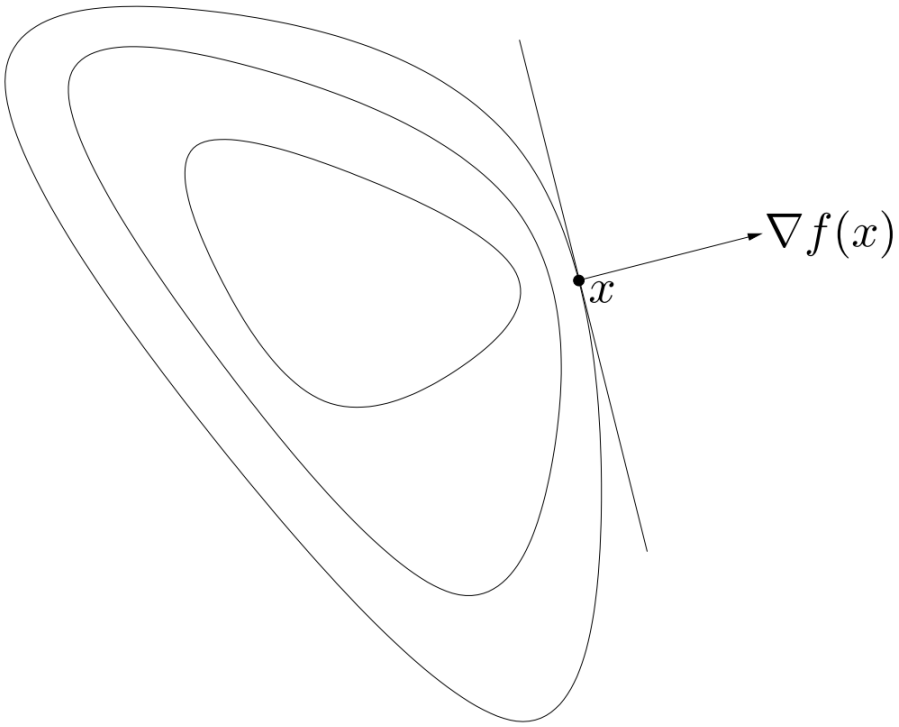

Figure 23: Principle of gradient search: the direction is in the steepest direction, i.e. orthogonal to the contour map

to globally optimize linear objectives and constraints of variables [133]. However, some obvious drawbacks are i) many functional evaluations are required and ii) some new search directions are often inefficient in comparison to gradient approaches.

Stochastic methods are mathematically simpler than deterministic counterparts. They are based heavily on the generation of random numbers and concept of acceptance probability. Starting with Monte Carlo optimization, one simply generates multiple points lying inside a hypercube defined by the bounds 1.36 then check for satisfaction of 1.34 , 1.35 and select the optimal value from 1.33. However, the "curse of dimensions" renders Monte Carlo method impossible for problems with many variables [134, 135]. Inspired by thermodynamic cooling of materials, "Simulated Annealing" method (Figure 24) was proposed [136–138]. In simulated annealing, one starts with a point (or collection of points) and begins to explore the region around them. If a newly found neighbor satisfies the acceptance probability, it is appended to the list and the current worst performing member will be discarded. Critical issues with simulated annealing are usually the choices of acceptance probability and movement directions

around a given point . However, the ideas in simulated annealing are fairly general and a host of genetic or evolutionary algorithms [135, 139] were also based on this concept. In general, stochastic search is often employed to quickly survey landscape of the objective function and yields information on possible bounds of the global optimum, especially in problems where deterministic methods are not directly applicable.

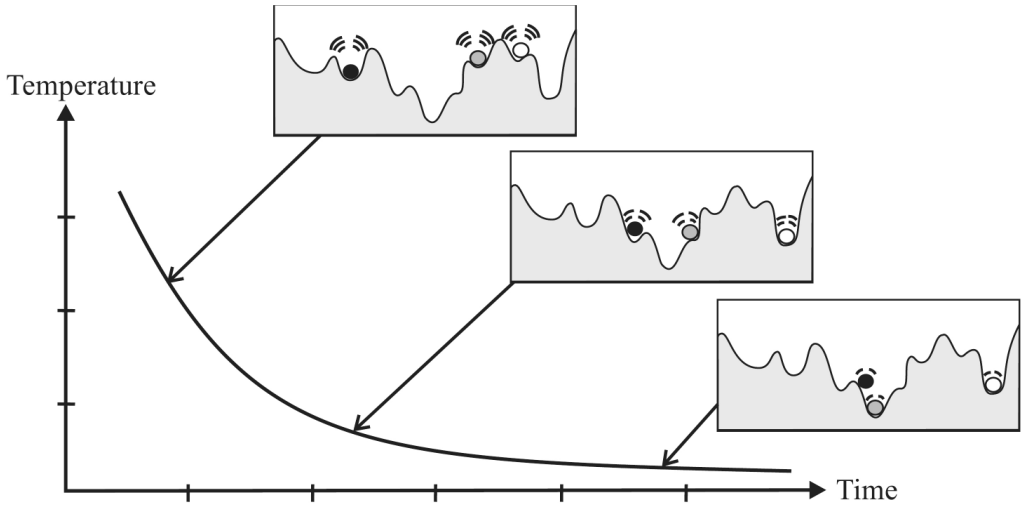

Figure 24: The objective is optimized as the temperature cools using simulated annealing algorithm. In this example, global minimum (i.e. the lowest valley) is slowly approached by two artificial neural networks

In parameter estimation, a set of scalars within hypercube space 1.36 are searched in order to minimize the measure between measured and model data (for example Equation 1.28). The parameters of a given model become x in the above formulation. In addition, there are usually no additional constraints between parameters since they are assumed to be independent of each other. Therefore constraints 1.34 and 1.35 are ignored.

Solutions to problems of estimating parameters have been well-developed. Gradient-based approach is implemented via the use of "Sensitivity Equations" . In this approach, the gradient of model response with respect to each parameter is described by another set of ODEs. The method thus allows computation of such gradients with high degree of accuracy and results in better estimation of local solutions in comparison to simple Finite Difference approximations [140, 141]. Problems in reaction engineering and petroleum reservoir management were solved by extending the approach to PDEs [142]. Sensitivity equation approach was also adapted to fit a multi-parametric charging/discharging models for polymer fuel cells [143] and Li-Ion batteries [144], with

excellent results obtained for both case studies. Notably both works chose to employ Levenberg-Marquardt, a well-known quasi-Newton method [145] which only requires first derivative information. Levenberg-Marquardt is also employed in commercial packages such as $Matlab^{®}$ for non-linear fitting routine [**?**].

Parameter estimation results provide a point estimate and a reasonable agreement between model and data. In addition, one may want to obtain statistical distributions of these parameters. In other words, it is useful to find out about mean values or credible intervals of the fitting parameters. These problems are addressed via the use of Bayesian frameworks. Bayesian theorem in continuous form is define by the following formula [146, 147]:

$$\pi(\theta|data) = p(data|\theta)\, p(\theta) / \int p(data|\theta) p(\theta) d\theta \tag{1.37}$$

where the function $p(.)$ is the probability density of the variable θ. The denominator in 1.37 is considered constant due to integration across all possible space of the parameter set θ. Consequentially, the relation is rewritten as:

$$\pi(\theta|data) \propto p(data|\theta)\, p(\theta) \tag{1.38}$$

Factor $p(\theta)$ is termed a prior probability distribution, or simply "prior". In essence, the prior contains all the knowledge about the parameter space before the inclusion of data. For example, a uniform distribution is interpreted as a uninformed prior because all the values within the range have the same probability of occurrence. The posterior-probability $\pi(\theta|data)$ is computed from RHS 1.38 (up to a constant) and reveals the "corrected" or "informed" distribution $after$ inclusion of data. It is noted that the choice of priors significantly affects posterior outcomes. For example, if the parameter distribution is expected to be single-modal then a sensible prior is the normal distribution (i.e. a single-modal distribution itself) instead of the uninformed flat distribution. In addition, the term $p(data|\theta)$ is called the likelihood probability. In the simplest form, the likelihood is expressed as a normally distributed function of square errors between the data and model responses. Thus the aim of minimizing the difference is equivalent to maximizing the likelihood function. As a consequence, parameter estimation should be carried out prior to Bayesian computations so as to provide a sensible starting point for computing sub-optimal likelihood probability.

A popular method to compute the distribution $\pi(\theta|data)$ is Monte Carlo Markov Chain (MCMC). Each version of MCMC fundamentally comprises of two parts: Monte

Carlo involving repetitive model calculations, and Markov Chain which generates new parameter sets from the previous ones via the transition probability matrix. The new set of parameter is also rejected or accepted by calculating the probability of acceptance. Properties of Markov chain in general ensures that the true posterior is approximated given a sufficient chain length. Metropolis-Hasting algorithm - the simplest version of MCMC is in fact based on simulated annealing. More sophisticated (e.g. slice sampler, Gibbs sampler or Multistage Gibbs samplers) have been proposed, but require additional knowledge which is unique to problems at hand [148].

Arrival time of weakly interacting muon particles is modeled by adaptive Metropolis-Hasting algorithm [149]. The plain version of Metropolis-Hasting is applied to estimate parameters in Li-Ion battery model and reduce computational time by proposing a meta model based on the most significant parameter [150]. Capacity loss due to regular discharge and formations of solid electrolyte interface is also modeled via combination of Bayesian Monte Carlo and exponential functions [151]. A number of case studies in reaction engineering such as esterification and hydrogenation processes using both original and adaptive versions of Metropolis-Hasting are documented in [152]. MCMC is also applied to quantitative models exploring effects of parameter distributions on cardiological beat-to-beat variations [153]. Other examples involving election pooling, population toxicokinetics and surveys of babies births and deaths are outlined in [146].

1.7 Thesis Outline

The thesis is structured as follows. Chapter 2 details Finite Difference approach and illustrates this methodology with results from the literature. There are two main benefits of doing so. Firstly, it provides the basic foundation of numerical methodology. Second, the method is then readily applicable to different inquiries of the Butler-Volmer model in the following chapters.

Chapter 3 focuses on the use of Monte Carlo sampling to study identifiability, sensitivity analysis and computational statistics problems. For Butler-Volmer model, the identifiability function conveniently reveals the compensation effects among the parameters. In addition, the influence of individual parameter on the model output is assessed by the Sobol analysis. This parameter ranking serves to simplify the model formulation and assists subsequent steps in parameter optimization and Bayesian calculation. Another goal here is to demonstrate some advantages of this stochastic approach, which is intuitively simple and amendable to different applications.

Chapter 4 studies the role of hydrodynamics on model identifiability. A new configuration - the rocking disk, is introduced, analyzed and compared with the more common rotating disk. A special factor involving hydrodynamic devices is the computation of fluid flow. The chapter also introduces and applies the simulation software *Comsol Multiphysics*®, which is highly suitable for solving transport equations and investigating advanced hydrodynamic voltammetries.

The final chapter illustrates the application of fundamental harmonic signals to identify the effect of homogeneous self-catalytic reactions. The work builds up on the background of AC (or Fast Fourier Transform) voltammetry, which is a very recent electrochemical technique. Finally, AC signals are then combined with the mechanical factor, namely the parabolic flow inside a micro-channel to permit the resolution of catalytic effects at lower harmonic components.

As a whole, the work demonstrates the application of an experimental design procedure to an electrochemical model. The two major design variables: applied voltage and mode of mass-transport, are utilized to study properties of heterogeneous electron transfer and homogeneous chemical reactions.

Chapter 2

Numerical Solution of Redox Processes

This chapter introduces a numerical approach for solving the mass tranport equation coupled with redox reaction in a stagnant electrolyte. The approach is based on Finite Difference (FD), which is the most popular method to this type of problem in electrochemistry literature. There are two motivations behind the application of FD in this work: firstly, since most electrochemical measurements are carried out in solution and stagnant conditions, then any experimental design scheme should have a reliable mechanism for solving the diffusion equation. In addition, by developing the methodology, useful insights, which are applicable to not only FD but also FE in subsequent chapters, are gained. Secondly, the work here also lays the foundation for further investigations in Chapter 3 on different topics of parameter identification.

There are many excellent references that comprehensively describe the mathematical foundations of FD [154, 155], thus such details are not repeated here for practical reasons. Only important results about the FD method are noted when relevant. A comprehensive survey of the generalized FD method and its related electrochemical simulation algorithms was outlined by Britz [156].

2.1 Diffusional Transport in One Dimension

This section discusses the diffusion equation in one dimension. Although this is a simplified form, the subject is particularly relevant to any redox processes at macro electrodes (Figure 11). Furthermore, the solution process in higher dimensions can be easily generalized from that in one dimension. First considering the simple redox E reaction:

$$O \leftrightarrow R + e^- \tag{2.1}$$

and the one-dimensional PDEs (Equation 1.3) with isotropic diffusion coefficients:

$$\frac{\partial c_R}{\partial t} = D_R \frac{\partial^2 c_R}{\partial x^2} \tag{2.2}$$

$$\frac{\partial c_O}{\partial t} = D_O \frac{\partial^2 c_O}{\partial x^2} \tag{2.3}$$

subject to boundary conditions:

$$t = 0,\ c_R = c_{R0},\ c_O = c_{O0} \tag{2.4}$$

$$t > 0,\ x \to \infty,\ c_R = c_{R0},\ c_O = c_{O0} \tag{2.5}$$

$$t > 0,\ D_R(\frac{\partial c_R}{\partial x})_{x=0} = -D_O(\frac{\partial c_O}{\partial x})_{x=0} = k_f(c_R)_{x=0} - k_b(c_O)_{x=0} \tag{2.6}$$

where k_f and k_b is defined as:

$$k_f = k_0 exp(\frac{(1-\alpha)F(E-E_0)}{RT_0}) \tag{2.7}$$

$$k_b = k_0 exp(\frac{-\alpha F(E-E_0)}{RT_0}) \tag{2.8}$$

and E is applied electrode potential.

Equations 2.2 and 2.3 describe the diffusion of each species over time and space domain. Equation 2.4 states the initial conditions and condition. Relation 2.5 imposes that the concentrations maintain their initial bulk values very far from the electrode. Relation 2.6 expresses the Butler-Volmer electrode kinetics. In addition, the solution

is well-supported, meaning that migration fluxes are ignored. The Faradaic current is calculated by expression 2.9:

$$I_f = FAD_R(\frac{\partial c_R}{\partial x})_{x=0} \tag{2.9}$$

During voltammetric measurements, there is also presence of the capacitive current, which is calculated by the expression:

$$I_c = C_{dl}A\frac{dE}{dt} \tag{2.10}$$

where C_{dl} is the approximate capacitance of the double layer. The total current is the sum of the Faradaic and capactive currents:

$$I = I_f + I_c \tag{2.11}$$

Subsequent sections also assume a negligible capacitance or $C_{dl} = 0$. Therefore, the total current is effectively due to the charge-transfer Faradaic component.

For the set of equations 2.2-2.11, the solutions are generally approached by numerical methods. Closed form solutions exist for simple cases such as linear sweep/cyclic voltammetries and reversible electron transfer, though their expressions are complicated and numerical steps are still required to fully evaluate these expressions [157, 158].

2.2 Spatial Meshing and Grid Structure

As previously discussed, an important step in FD is the discretization of the space domain. From 2.5, it is clearly not possible and necessary to cover very large x. To approximately represent this semi-infinite boundary condition, a diffusion length scales is often used. This length scale is straightforwardly estimated from dimensional analysis [156]:

$$l_{dif} \sim (max(D_R, D_O)\, t)^{1/2} \tag{2.12}$$

To be conservative, a value of $6\, l_{dif}$ is often recommended in the literature and this convention is followed here. The bounded simulation region is illustrated in Figure 25.

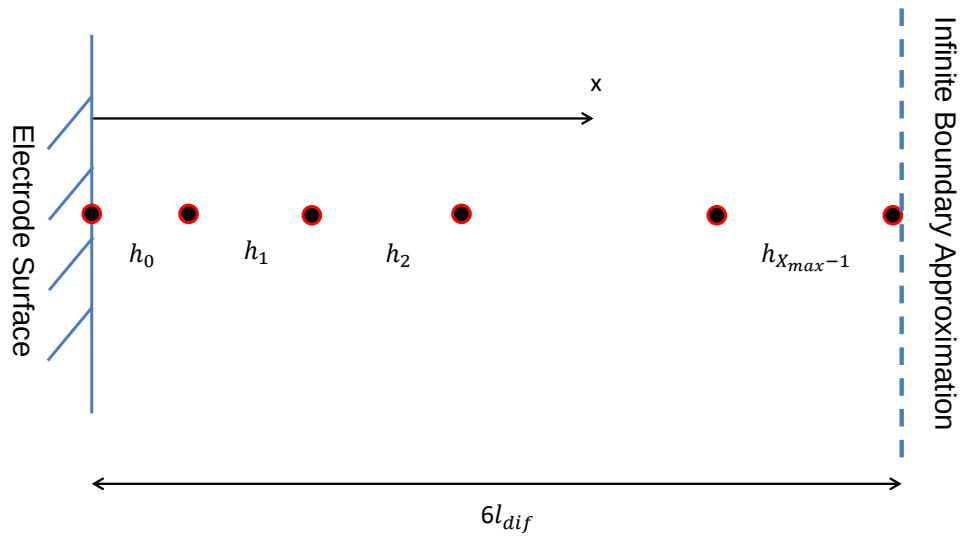

Figure 25: Modeling region for 1D diffusion. The region is broken down into discrete nodes

Next the spatial derivative needs to be discretised as a function of node points. A simple but effective apporoach is the Taylor series expansions. For a given node $0 < i < X_{max} - 1$ in the domain, forward and backward applications of the Taylor

formular result in the following:

$$c_{i+1} = c_i + h_i(\frac{\partial c}{\partial x})_i + h_i^2(\frac{\partial^2 c}{\partial x^2})_i \tag{2.13}$$

$$c_{i-1} = c_i - h_{i-1}(\frac{\partial c}{\partial x})_i + h_{i-1}^2(\frac{\partial^2 c}{\partial x^2})_i \tag{2.14}$$

and the first and second derivatives are solved for, which results in the well-known three point approximations:

$$(\frac{\partial c}{\partial x})_i = \frac{h_{i-1}^2 c_{i+1} - (h_{i-1}^2 - h_i^2)c_i - h_i^2 c_{i-1}}{h_{i-1}h_i(h_{i-1} + h_i)} \tag{2.15}$$

$$(\frac{\partial^2 c}{\partial x^2})_i = 2\frac{h_{i-1}c_{i+1} - (h_{i-1} + h_i)c_i + h_i c_{i-1}}{h_{i-1}h_i(h_{i-1} + h_i)} \tag{2.16}$$

In Equations 2.15 and 2.16, variable c stand for both c_R and c_O to avoid repetitions. By Taylor-expanding to include more points around c_i, the derivatives 2.15 and 2.16 can be approximated with more terms (e.g. four-point approximation [159]). To completely specify the grid, the values of h_i would be required. An exponential mesh is most commonly used, and has the following structure:

$$h_{i+1} = f\, h_i,\ i = 1, 2, ... \tag{2.17}$$

that is the distance between each node increases geometrically. Note that $f = 1$ leads to an equal spacing or the common regular mesh. The smallest spacing h_0 and spatial exponent $f > 1$ can then be freely specified. However, a requirement is that the points must completely cover the supposed domain and the number of points X_{max} should satisfy the condition:

$$h_0 + h_1 + ... + h_{X_{max}-1} \geq 6l_{dif}$$

or using 2.17, this can be written as:

$$h_0\frac{f^{X_{max}} - 1}{f - 1} \geq 6l_{dif}$$

and for given values of h_0 and f, X_{max} can be straightforwardly solved as:

$$X_{max} \sim log(\frac{6l_{dif}}{h_0/(f-1)})/log(f)$$

As a general rule, small spacings are placed where the maximum gradient occurs, and larger spacings are where the condition is constant. For the above example, more nodes would be placed around the electrode surface (small h_0) and less points are needed near the semi-infinite boundary because the concentrations stay constant at bulk values. Hence the major benefit of an exponential mesh is its economical value: cell points are placed where large gradients occur and reduced where the gradients become negligible.

The grid in Figure 25 is static, meaning that once h_i and f are specifed, they are kept the same throughout the simulation course. On the other hand, an adaptive grid allows intermediate modifications of h_i, which is highly relevent for short time scale processes (e.g. very fast chemical reactions). However for simple linear diffusion, a static grid is known to be sufficient and adequate for the solution process by careful selection of the variables h_0 and f.

2.3 Temporal Discretization

Since the diffusion process evolves with time, temporal expressions in Equations 2.2 and 2.3 also need to be discretized. The simplest formula is the first order approximation:

$$\frac{dc_i}{dt} \simeq \frac{c_i^{t+dt} - c_i^t}{dt} \tag{2.18}$$

Fundamentally, there are two types of formulations with respect to time. If all the concentrations are made known in the spatial derivatives, then this results in explicit formulation:

$$\frac{c_i^{t+dt} - c_i^t}{dt} = 2D\,\frac{h_{i-1}c_{i+1}^t - (h_{i-1}+h_i)c_i^t + h_i c_{i-1}^t}{h_{i-1}h_i(h_{i-1}+h_i)} \tag{2.19}$$

It is evident that there is only one unknown in 2.19, which can be easily determined. Implicit formulations are more complex and depend on the choice of time step, which contains known concentration values for all but one terms:

$$\frac{c_i^{t+dt} - c_i^t}{dt} = 2D\,\frac{h_{i-1}c_{i+1}^{t+dt} - (h_{i-1}+h_i)c_i^{t+dt} + h_i c_{i-1}^{t+dt}}{h_{i-1}h_i(h_{i-1}+h_i)} \tag{2.20}$$

By moving the unknowns in Equation 2.20 to left hand side (LHS):

$$-\gamma_i c_{i+1}^{t+dt} + (1+\gamma_i+\alpha_i)c_i^{t+dt} - \alpha_i c_{i-1}^{t+dt} = c_i^t,\ i = 1, 2, ..., X_{max} - 1 \tag{2.21}$$

$$\alpha_i = \frac{2Ddt}{h_{i-1}(h_{i-1}+h_i)}$$

$$\gamma_i = \frac{2Ddt}{h_i(h_{i-1}+h_i)}$$

Equation 2.21 is the system of equations associating the node values from the current (unknown) to the previous (known) time level. To model the diffusion of two species, $2X_{max}$ variables need to be solved at each time step. This implies that implicit methods are more computationally expensive. Figure 26 summarizes the main differences between the two methods.

As with space derivative, it is also possible to approximate the time derivative with more terms. The most generalized approach is the use of Ritchmyer coefficients [160],

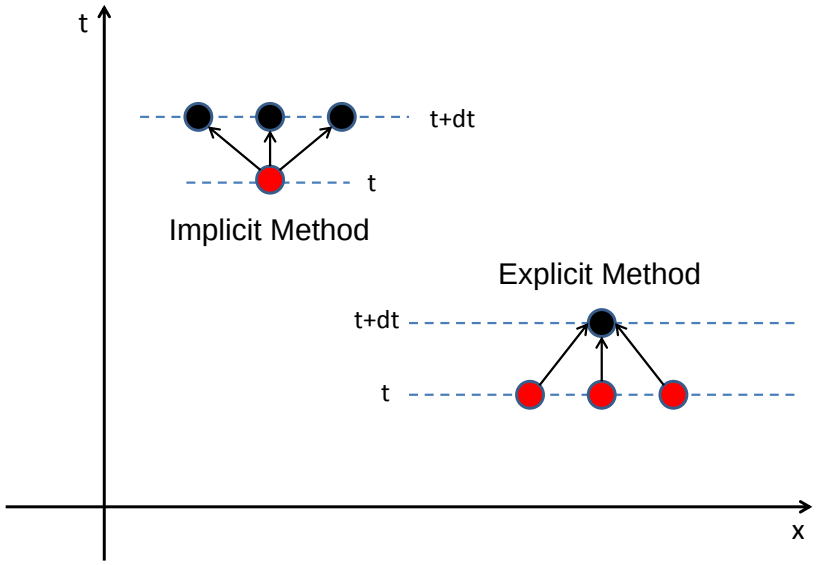

Figure 26: Comparisons between Explicit and Implicit formulations. Implicit method generally has more unknowns than explicit one, thus usually requiring more solution effort

in which the time derivative is expressed as:

$$\frac{dc_i}{dt} \simeq \frac{1}{dt} \sum_{0}^{m} a_i c_{m-i} \tag{2.22}$$

where m denotes the time level. Level m is the current level (i.e. containing the unknowns) and $m - i$ corresponds to earlier time steps and concentrations at these levels are all known. Coefficients a_i associated with each level are constants and pre-calculated in the literature (Table 1) [161]. It is further recognized that the level 2 corresponds to Equation 2.18.

Implicit and explicit methods differ significantly in terms of numerical stability. A numerical solution is mathematically stable if its value remain bounded or finite at all times. Explicit methods usually place restriction on the time step $\triangle t$ and minimum

Level	a_0	a_1	a_2	a_3	a_4	a_5
2	1	-1	-	-	-	-
3	3/2	-2	1/2	-	-	-
5	25/12	-4	3	$-4/3$	1/4	-
6	137/60	-5	5	$-10/3$	5/4	$-1/5$
7	147/60	-6	15/2	$-20/3$	15/4	1/6

Table 1: The Ritchmyer Coeffcients for discretization of time derivative (Equation 2.22)

spatial spacing h such that the following condition must be satisfied:

$$\frac{D \triangle t}{h^2} \sim 1 \tag{2.23}$$

The implicit method on the other hand does not require such condition in order to be mathematically stable. This fact implies that one can choose finer spacings and larger time steps in implicit calculations, which results in better accuracy and shorter simulation time.

There are many ways to discretise space and time, which implies that the same problem can be solved in many ways. The diminishing return argument applies here since convergence and accuracy are concerned. Firstly, since computational results are largely affected by the grid quality, it is usually better to refine the grid than using more point approximations. A similar argument applies to the choice of time derivative. Though it is possible to use more levels in Ritchmyer approximation, a reasonable small time step and level 2 approximation were observed to be the most common combination in the literature.

Finally, it is noted that both implicit and explicit formulations have their strengths and weaknesses and the final choice is mostly problem dependent. Although implicit formulations often offer higher accuracy/shorter computational time and are therefore favored in most cases, explicit methods are a much simpler and more effective approach to very non-linear problems.

2.4 Treatment of Boundary Conditions

Equation 2.5 represents Dirichlet or the essential boundary condition. To satisfy this, the nodal values are forced to be equal to the fixed constant. In the discrete domain, this condition reads as follows:

$$c_{R,X_{max}} = c_{R0},\ c_{O,X_{max}} = c_{O0} \tag{2.24}$$

On the other hand, the boundary condition at the electrode is classified as Neumann type since it involves a first order derivative. In FD, this derivative is simply discretized to link the associated nodes to those in the domain. For the current case at each time step, the applied potential $E(t)$ is assumed to be known. Furthermore, the forward and backward rates k_f and k_b are also known if k_0 and α are completely specified. A simple first order approximation of space derivative leads to:

$$D_R \frac{c_{R,1} - c_{R,0}}{h_0} = k_f c_{R,0} - k_b c_{O,0} \tag{2.25}$$

$$-D_O \frac{c_{O,1} - c_{O,0}}{h_0} = k_f c_{R,0} - k_b c_{O,0} \tag{2.26}$$

Combining Equations 2.24, 2.26 and discrete transport equations (2.19 or 2.20) derived in section 2.3, evolution of species concentration at every time point can be solved. Faradaic current is then computed from Butler-Volmer kinetics (Equation 2.6) once respective values at the electrode boundary are known.

2.5 Overview of Numerical Solutions

In numerical methods, the following generic system of equations is often encountered:

$$F(x) = 0 \tag{2.27}$$

where $F(x)$ are the functions and x are vector of multi-variate unknowns. If all F is made up of linear combinations of the variable x, then 2.27 is a linear system. Numerical solutions in this case have been well developed. The two main approaches are direct and iterative solvers. These methods are briefly discussed below. Elaborate details are found in excellent references [162, 163].

Direct methods are generally based on the method of "Lower-Upper" decomposition (LU decomposition). By rewriting Equation 2.27 specifically for linear equations:

$$Ax = b \tag{2.28}$$

In 2.28, A is the matrix containing the coeffients and b is the vector containing the known values. If the matrix A is non-singular, then LU decomposition essentially transforms A into the product of two matrices:

$$A = LU \tag{2.29}$$

where vector L is the lower-triangular matrix (i.e zero elements above the main diagonal) and U is the upper-triangular matrix (i.e. zero elements below the main diagonal). The solution x is then found by solving two sets of equations:

$$Ly = b$$

$$Ux = y$$

Due to special structures of L and U, these two equation sets can be solved easily by simple back-substitution scheme. In fact, the solution is very fast when A is a "tri-diagonal" matrix because the decomposition step 2.29 is almost instant in time. Direct methods are usually the fastest way to solve linear equations. However, these approaches require memory storage capacity during computation steps. Thus the computation becomes prohibitively expensive if there are many variables (e.g. a few millions) are to be solved.

Iterative methods on the other hand require less memory and are adaptable to multi-million variables cases. A major drawback is the amount of iteration time required in order to achieve certain convergences. Iterative methods usually start with an initial guess x_0 and progressively updates this guess until a reasonable closeness $Ax \sim b$ is achieved. Well-known methods are "Gauss-Seidel" and "Successive Over Relaxation" [164].

If the system $F(x)$ is non-linear, then the solution process is more complex. The most common approach is Newton-Raphson. Applying Taylor expansion to the equation functions:

$$F(x + \delta x) = F(x) + J(x)(\delta x) \tag{2.30}$$

where $J(x)$ is the Jacobian (i.e. the first derivative of the equation function with respect to the variables). Thus in order to approach the correct solution, the following update is required $x \to x + \delta x$ and δx is the solution to the following:

$$J(x)\delta x = -F(x) \tag{2.31}$$

Equation 2.31 is effectively another system of linear equations and previous solution methods then apply. As with iterative methods, the solution process starts with an initial guess and Equation 2.31 is repeated until satisfactory convergences are achieved. Furthermore, convergence of Newton-Raphson scheme depends to a large extent on the quality of the initial guess.

2.6 Two Dimensional Simulation and ADI Method

If the electrode size becomes sufficiently small, the fluxes are no longer unidirectional, which result in a multi-dimensional diffusion equation (Equation 2.32). Figure 27 shows the geometrical setup and reduced simulation domain. The electro-active material is colored red and supporting insulators (such as glass) is blue. For a disk, rotational symmetry reduces the problem from three to two dimensions (i.e. there is no dependence on angular position φ). The diffusional mass transport equation becomes:

$$\frac{\partial c}{\partial t} = D\left(\frac{\partial^2 c}{\partial r^2} + \frac{1}{r}\frac{\partial c}{\partial r} + \frac{\partial^2 c}{\partial z^2}\right) \tag{2.32}$$

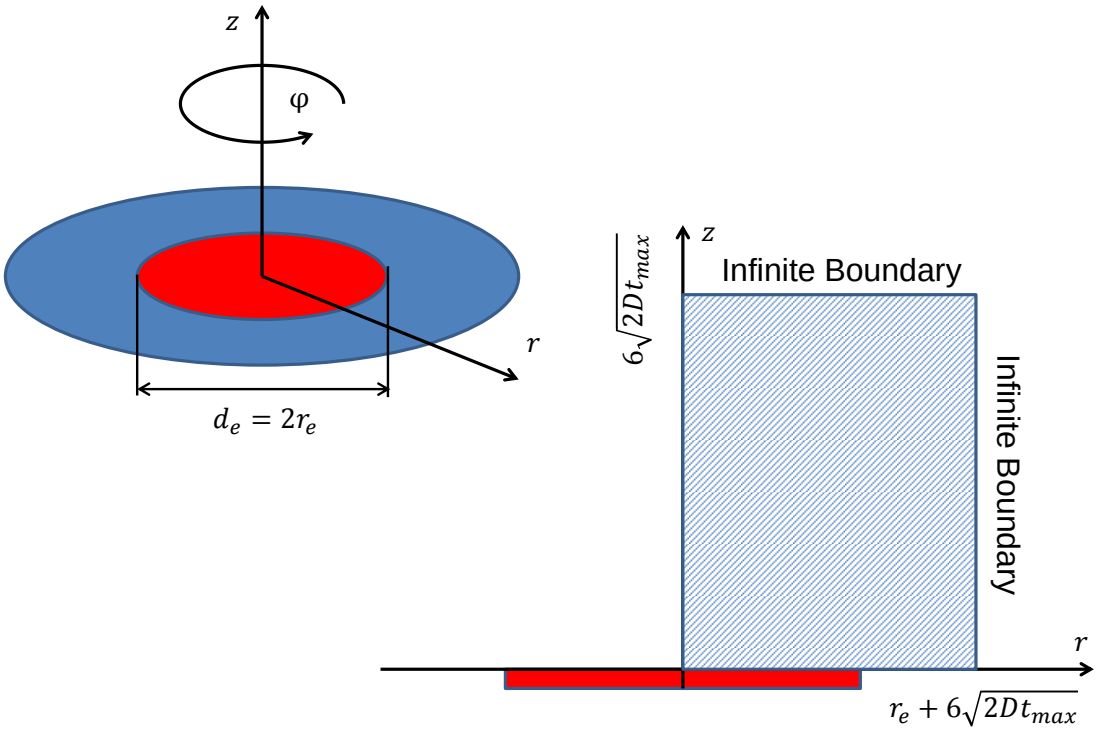

Figure 27: Geometrical representation of micro disc (top left) and the reduced rectilinear simulation domain with the boundaries (hatched)

Boundary conditions are summarized in Table 2. As before, the infinite boundaries are approximated by $z_{max} = 6\,(2\,max(D_O, D_R)t_{max})^{1/2}$ and $r_{max} = r_e + 6\,(2\,max(D_O, D_R)t_{max})^{1/2}$

Infinte Boundaries ($z = z_{max}$, $r = r_{max}$)	$c_O = c_{O0}, c_R = c_{R0}$
Electrode Surface ($z = 0$, red region)	B-V Kinetics
Insulating Substrate ($z = 0$, blue region)	No Flux
Symmetry Plane at $r = 0$ (vertical line)	No Flux

Table 2: Boundary conditions associated with micro disk problem. The boundaries are shown in Figure 27

respectively. Using the exponential mesh, this domain is divided as shown in Figure 28. The smallest spacing is placed around the electrode edge ($r = 1$) and expanded exponentially towards the main bulk (r, $z \to \infty$) and the central axis at $r = 0$. The reason for doing so is to take into account the presence of the singularity point at the edge - where there is a big change in species flux.

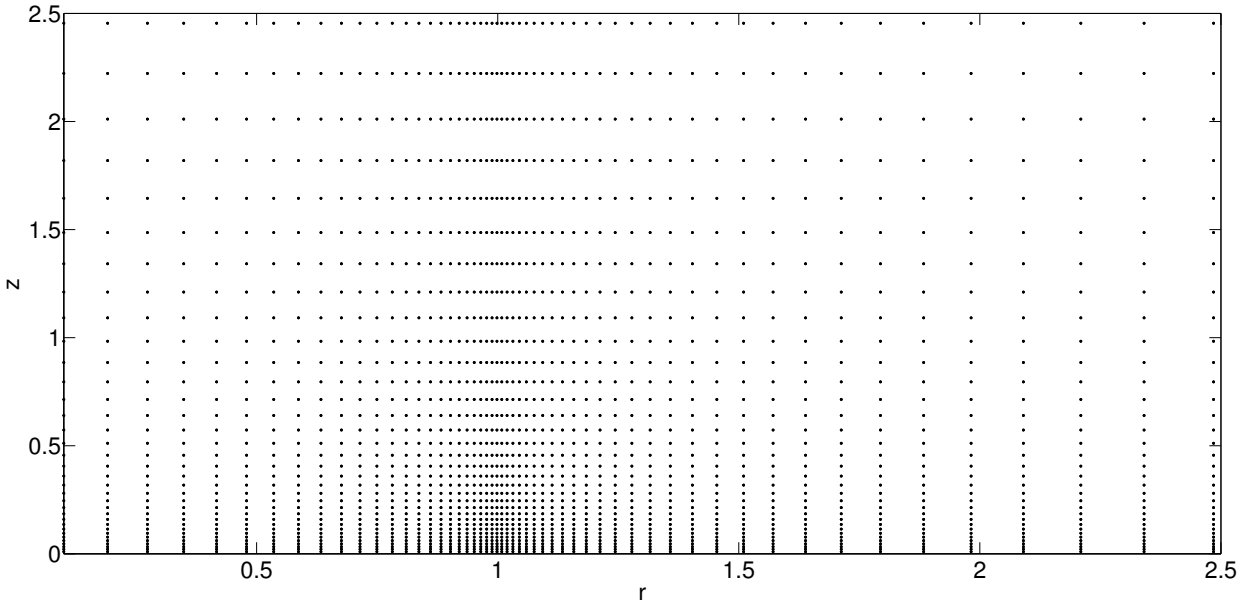

Figure 28: A typical 2D polar-coordinate grid for FD simulations of micro disk electrode. The grid is concentrated around the electrode edge ($r = 1$) and becomes sparser towards the bulk. The axis scales are non-dimensional for demonstration purposes

Applying three-point formulations (Equations 2.15 and 2.16) (note the indicies i, j corresponds respectively to dimensions r, z):

$$\frac{1}{r}\frac{\partial c_{i,j}}{\partial r} = \frac{1}{\sum h_i}\frac{h_{i-1}^2 c_{i+1,j} - (h_{i-1}^2 - h_i^2)c_{i,j} - h_i^2 c_{i-1,j}}{h_{i-1}h_i(h_{i-1} + h_i)}$$

$$\frac{\partial^2 c_{i,j}}{\partial r^2} = 2\frac{h_{i-1}c_{i+1,j} - (h_{i-1}+h_i)c_{i,j} + h_i c_{i-1,j}}{h_{i-1}h_i(h_{i-1}+h_i)}$$

$$\frac{\partial^2 c_{i,j}}{\partial z^2} = 2\frac{k_{j-1}c_{i,j+1} - (k_{j-1}+k_j)c_{i,j} + k_j c_{i,j-1}}{k_{j-1}k_j(k_{j-1}+k_j)} \tag{2.33}$$

Define the spatial differential operator to simplify the equation notation [76, 77]:

$$L_r c_{i,j} = (\frac{1}{r}\frac{\partial}{\partial r} + \frac{\partial^2}{\partial r^2})c_{i,j}$$

$$L_z c_{i,j} = (\frac{\partial^2}{\partial z^2})c_{i,j} \tag{2.34}$$

By including the temporal differential operator $L_t = \partial/\partial t$, the 2.32 is casted:

$$L_t(c_{i,j}) = L_r(c_{i,j}) + L_z(c_{i,j}) \tag{2.35}$$

A simple 1^{st} order approximation (or 2-level Ritchmyer) for LHS is:

$$\frac{c_{i,j}^{t+dt} - c_{i,j}^{t}}{dt} = L_r^{()}c_{i,j} + L_z c_{i,j}^{()}$$

where the brackets () above the operators indicate either implicit or explicit formulations. Explicit calculations are straightforward:

$$\frac{c_{i,j}^{t+dt} - c_{i,j}^{t}}{dt} = L_r^{t}c_{i,j} + L_z c_{i,j}^{t} \tag{2.36}$$

Implicit calculations are not as simple. If a method like the 1D case is applied, then one obtains:

$$\frac{c_{i,j}^{t+dt} - c_{i,j}^{t}}{dt} = L_r^{t+dt}c_{i,j} + L_z c_{i,j}^{t+dt} \tag{2.37}$$

In Equation 2.37, there are 1 known and 5 unknowns because there are 3 unknowns in r direction and extra 2 unknowns in z direction. The system of equations is still solvable, but is significantly more complicated comparing to the 1D case.

In electrochemistry, a useful approach to solving the 2D diffusion equations is Alternating Direction Implicit (ADI) [30]. ADI belongs to a more general class commonly referred to as "Operator Splitting" methods. Instead of solving the whole problem at once, the problem is split into smaller sub-problems based on individual operators in the original equation [165, 166]. From Equation 2.35, it is noted that the

concentration evolution is essentially driven by diffusions in 2 directions (r and z), thus considering the following splitting scheme:

$$\frac{c_{i,j}^{t+dt/2} - c_{i,j}^{t}}{dt/2} = L_r^{t+dt/2} c_{i,j} + L_z c_{i,j}^{t} \tag{2.38}$$

$$\frac{c_{i,j}^{t+dt} - c_{i,j}^{t+dt/2}}{dt/2} = L_r^{t+dt/2} c_{i,j} + L_z c_{i,j}^{t+dt} \tag{2.39}$$

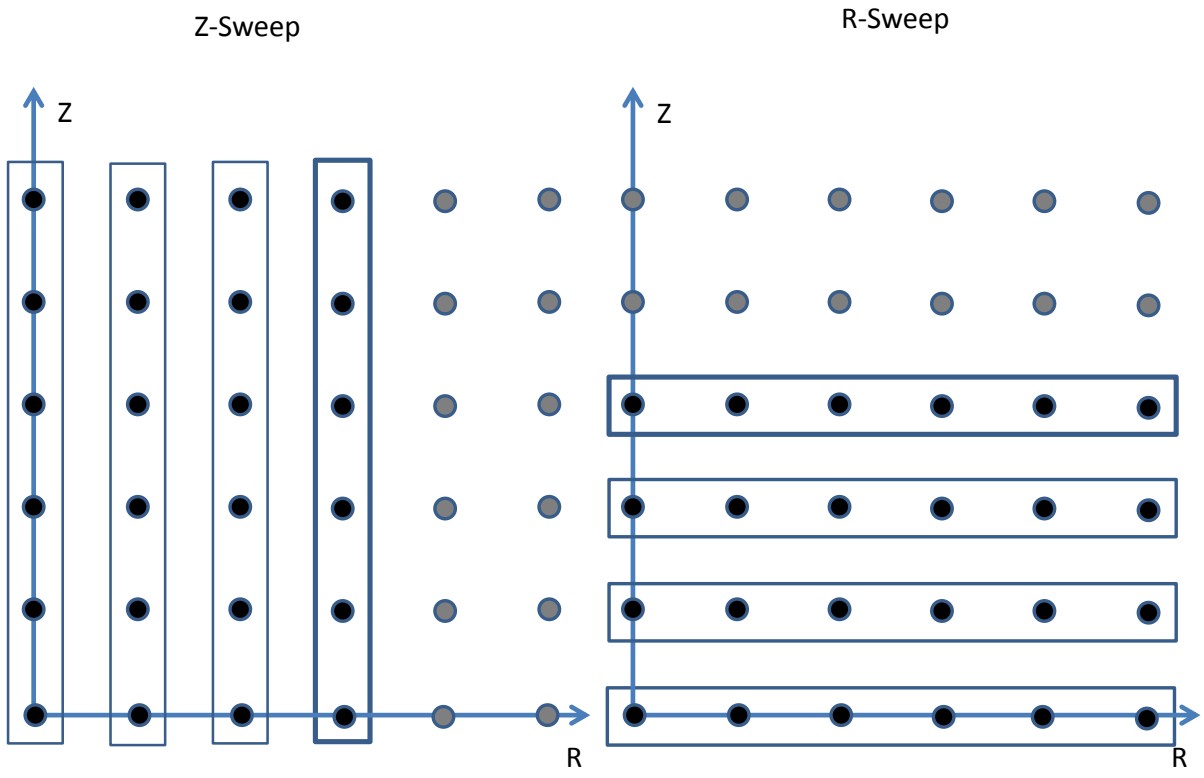

Figure 29: The Alternating Direction Implicit (ADI) in 2D. Nodes in thin-lined rectangles were already solved and those in thick-lined rectangles are currently being solved. Grey nodes are unsolved variables. For each time iteration, all the nodes in Z direction are first solved, the results are then used to solve for nodes in R direction

The original equation has been split into two sub-problems with respect to L_r and L_z respectively. In Equation 2.38, the known concentrations at time t are used to implicitly solve for the diffusion operator in r direction (i.e. r-sweep). Note here

that the time is incremented by $dt/2$. Similarly in Equation 2.39, concentrations at $t + dt/2$ are then used to solve for the diffusion operator in z direction (z-sweep) and complete the full time step dt (see Figure 29). In fact, the idea of operator splitting is also applicable to $1D$ case, but it is more interesting and useful for higher dimensions. The total error of this splitting scheme is $E_{splitting} + E_{discretization}$. The first component $E_{splitting}$ is due to errors in solving each set 2.38 and 2.39 whilst $E_{discretizing}$ is the error associated with space and time discretization schemes. Thus these errors can be both reduced by employing a sufficiently small time step and appropriate spatial meshing. Finally, the order of splitting mathematically does not affect the convergence and final solutions. Using ADI, the current problem is reduced to solving a series of 1D equations in each spatial dimension. In addition, the ADI scheme above is unconditionally stable in 2D but not generally in 3D. Due to its advantageous mathematical and numerical properties, the method has been widely applied in electrochemistry literature.

2.7 Some Numerical Results

This section illustrates some important results in electrochemistry using a FD approach. A major goal is to demonstrate that the methods and algorithms discussed in earlier sections are robust. This is accomplished by solving a number of interesting and well-known problems in the literature.

All the code in this work were written in C++ and $Matlab^{®}$. A partial reason for using $Matlab^{®}$ is due to its robust linear equation solver as well as the ease in manipulating matrices. A strong advantage of C++ is the speed of execution. However, for additional purposes (linear algebra, optimization, etc.), the use of C++ requires external libraries. All of the programs were executed on a Windows work station with Intel Core i7 and 16GB RAM.

First consider simple linear sweep voltammetry in which the applied voltage is varied as:

$$E = E_{start} + v_{scan}t,\ 0 < t < t_{scan} \tag{2.40}$$

$$t_{scan} = (E_{vertex} - E_{scan})/v_{scan} \tag{2.41}$$

For a cyclic voltammetry, a backward scan potential is then included:

$$E = E_{vertex} - v_{scan}(t - t_{max}),\ t_{scan} < t < 2t_{scan} \tag{2.42}$$

In addition, the capacitive current is computed as:

$$I_c^{dc} = C_{dl}Av_{scan},\ 0 < t < t_{max} \tag{2.43}$$

$$I_c^{dc} = C_{dl}A(-v_{scan}),\ t_{max} < t < 2t_{max} \tag{2.44}$$

is the time taken for a complete forward sweep. Parameter setting for the simulation is listed in Table 3 and Figure 30 shows the theoretical response at a macro electrode for very fast electrochemical kinetics (i.e. large k_0). In Table 3, diffusion coefficients of both reduced and oxidized species are assumed to be equal. However, this simplifying assumption is easily modified to account for different diffusivities. Furthermore, the diffusion coefficients in water differ from species to one another but commonly used chemicals are known to have those values lying within the range $10^{-6} - 10^{-5}\,cm^2/s$.

Exact values generally depend on solution temperatures, solvent molecules, chemical structures and the ambient surroundings. To approach fast kinetics regime, a sufficiently large value of k_0 is assumed ($0.1\,m/s$ in this case). It is noted that a precise value of k_0 is not important and any larger value would lead to virtually the same result. This is because a fast kinetics would lead to Nernst relation 1.13 which is independent of both α and k_0, the current is therefore not sensitive to these parameters.

Parameter Name	Notation	Numerical Value	Units
Diffusion Coefficient	D_R	$9 * 10^{-10}$	m^2/s
Diffusion Coefficient	D_O	$9 * 10^{-10}$	m^2/s
Electrochemical Kinetics	k_0	0.1	m/s
Charge Transfer Coefficient	α	0.55	–
Equilibrium Potential	E_0	0.2	V
Electrode Area	A	10^{-2}	cm^2
Specific Capacitance	C_{dl}	0	$\mu A/cm^2$
Scan Rate	v_{scan}	0.1	V/s
Starting Potential	E_{start}	-0.2	V
Finishing Potential	E_{vertex}	0.6	V
Bulk Concentration	c_{R0}	1	mol/m^3
Bulk Concentration	c_{O0}	0	mol/m^3
Smallest Spacing	h_0	10^{-7}	m
Spatial Exponential Factor	f	1.05	–
Number of Time Steps	–	2^{10}	–

Table 3: Parameters for simulations of macro disk (Figures 30 and 31)

Spatial grid parameters are listed in the last three rows of the Table 3. A small spacing is chosen for h_0. The value is selected per the diffusion layer estimate ($\sim 10^{-4}(m)$) and the smallest spacing of the order $10^{-7}(m)$ should therefore ensure good convergences to a high degree of accuracy (as confirmed in Figure 30). A rather conservative space expansion (f =1.05) is chosen, but higher values such as 1.1 or 1.2 yield exactly identical results. This fact underlines the importance of choosing correct mesh configuration in order to obtain adequate convergence.

The current and voltage in the Figure 30 above is non-dimensionalized by the following expression:

$$J = \frac{I_{total}}{(nF)^{3/2}/(RT_0)^{1/2} A D_R^{1/2} c_{R0} v_{scan}^{1/2}} \tag{2.45}$$

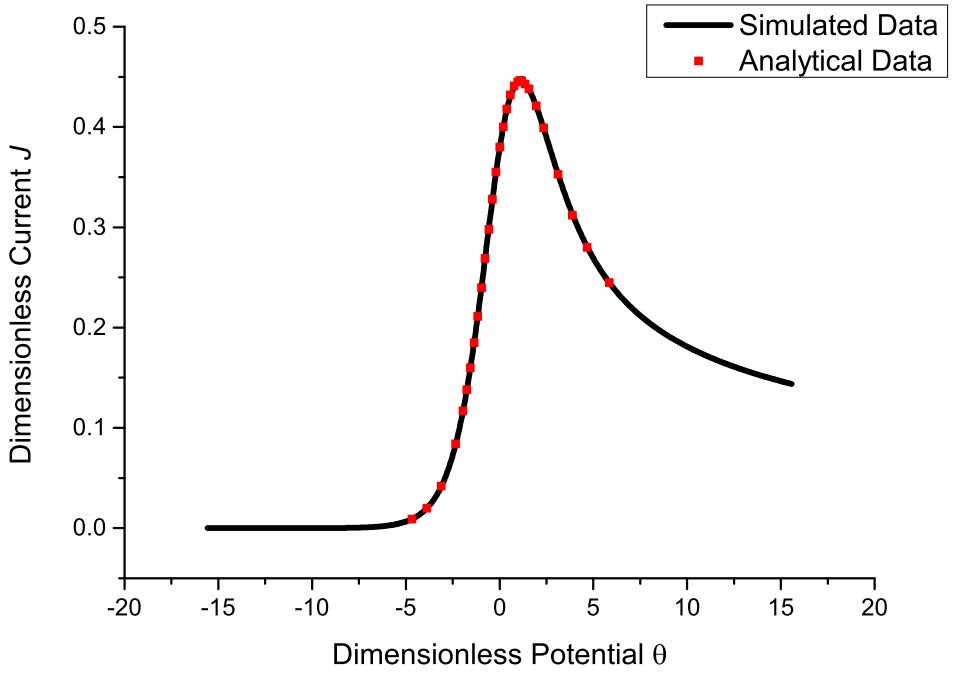

Figure 30: Dimensionless current versus dimensionless potential for a macro electrode under fast reversible kinetics. The corresponding dimensionless expressions are given by Equations 2.45 and 2.46 respectively. At $\theta = 0$, the dimensional potential $E = E_0$. The analytical values are extracted from tables in Reference [1]

$$\theta = \frac{nF}{RT_0}(E - E_0) \tag{2.46}$$

At the peak potential, the Randles-Sevcik relation holds:

$$J_p = \frac{I_p}{(nF)^{3/2}/(RT_0)^{1/2} A D_R^{1/2} c_{R0} v_{scan}^{1/2}} = 0.446 \tag{2.47}$$

This relation is analytically valuable since by measuring the peak current, information about diffusion coefficient of the species can be derived. In addition, because the expression involves species concentration, this forms the basis of many electrochemical sensors.

It is straightforward to confirm that diffusion at this electrode should follow macro behaviour by dimensional analysis. Firstly, the corresponding diameter d_e assuming a

disk shape is:

$$d_e \sim (4/\pi.10^{-6})^{1/2} \sim 0.001(m) \tag{2.48}$$

which is obviously not in the micro range. In addition, over the course of the experiment, which lasts about $t_{max} = (E_{vertex} - E_{start})/v_{scan} = 8\,(s)$, the size of the diffusion layer over the electrode surface is approximately:

$$l_{dif} \sim ((9 * 10^{-10}).8)^{1/2} \sim 0.0001(m) \tag{2.49}$$

Thus the diffusion later is still fairly thin compared to the electrode dimension. Even at significantly slower scan rates such as $0.01\,V/s$ or even $0.001V/s$, diffusion layer is still either smaller or just comparable to the electrode dimension. This fact ensures that for most practical situations, the above electrode is considered to be large.

The simulation result can be qualitatively explained as follows. At voltage significantly less than E_0, no oxidation (Equation 2.1) occurs and and the solution is mainly composed of the reductive species R. As the potential becomes higher, more reactions occur which translates into the rising current. At the electrode surface, species R starts being depleted and a mass-transfer gradient is gradually established. At potentials significantly above E_0, the whole process becomes mass transport controlled and thus current drops because the amount of fresh species R that move towards the electrode surface is reduced significantly.

The effect of reaction kinetics on the voltammogram is next considered. By varying k_0 and keeping the rest of the parameters the same, Figure 31 is obtained. Each voltammogram now includes forward and backward waves. In a typical cyclic voltammogram, there are two peaks. The forward peak associates with oxidation $R \rightarrow O + e^-$ whilst the backward peak is attributed to the reduction $O + e^- \rightarrow R$. For the case of $k_0 = 1\,cm/s$, the locations of these peaks are indicated by dotted lines in Figure 31. Because kinetics of $1\,cm/s$ still results in reversible reaction, the relation 2.47 still holds. At slower kinetic rates, the separation between peaks broadens and the peak size decreases. Using the reversible reaction (Figure 30) as the reference, this observation is explained as follows. For smaller k_0, Butler-Volmer relation (Equation 2.6) requires a larger thermodynamic factor to drive the same rates of reactions. Therefore, a larger potential is needed compared to the fast kinetic case, and the peak is shifted accordingly. In addition, the peak size is also smaller because the reaction rates are reduced.

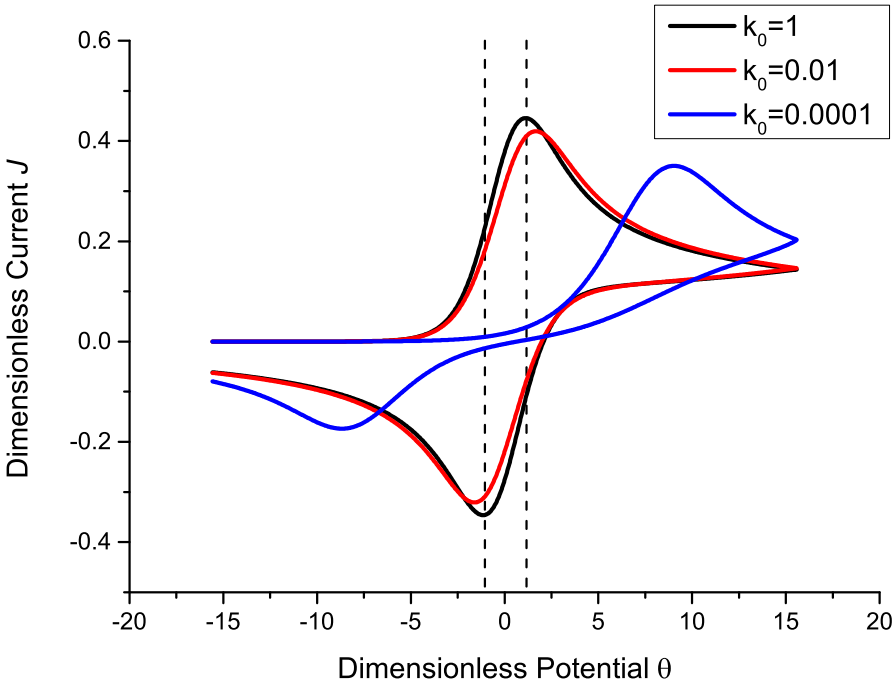

Figure 31: Cyclic voltammograms at different electrochemical reaction rates. For $k_0 = 1\,cm/s$, the potential gap is constant and independent of the scan rate . At much slower kinetics, the gap becomes larger and potential dependent [2] (All the dimensionless expressions are the same as before)

The next discussion focuses on micro disk electrodes. As previously noted, ADI is applied to solve the angular symmetric 2D diffusion equation 2.32. The setting is listed in Table 4. Before proceeding to the results, there are a few technical notes. Firstly in the simulation, dimensionless spacings dR and dZ are scaled with respect to the disk radius r_e. Secondly, the Faradaic current is now computed from the integral:

$$I_f = 2\pi F \int_0^{r_e} D(\frac{\partial c}{\partial z})_{z=0} r dr \tag{2.50}$$

to account for multi-directional variations of the fluxes. Expression 2.50 is computed at each time step using the simple Trapezoidal rule [167]. The derivative at $z = 0$ is approximated by the simple two-point formula and a fine meshing (small spacings and spatial exponential factor) ensures adequate convergence.

A classical problem in the literature is the simulation of amperometric response at micro electrodes. In amperometry, the potential is held at a constant value such that

Parameter Name	Notation	Numerical Value	Units
Diffusion Coefficient	D_R, D_O	10^{-9}	m^2/s
Electrochemical Kinetics	k_0	0.1	m/s
Charge Transfer Coefficient	α	0.60	–
Equilibrium Potential	E_0	0.2	V
Disk Radius	r_e	10	μm
Scan Rates	v_{scan}	0.1 and 0.005	V/s
Dimensionless Spacing in r direction	dR	10^{-6}	–
Dimensionless Spacing in z direction	dZ	10^{-6}	–
Spatial Exponential Factor	f	1.05	–

Table 4: Parameter settings for micro disk simulation. The disk radius is $10\,\mu m$. The dimensionless potential starts and ends at -20 and 20 respectively. The bulk concentrations for reduced and oxidized species are the same as in Table 3

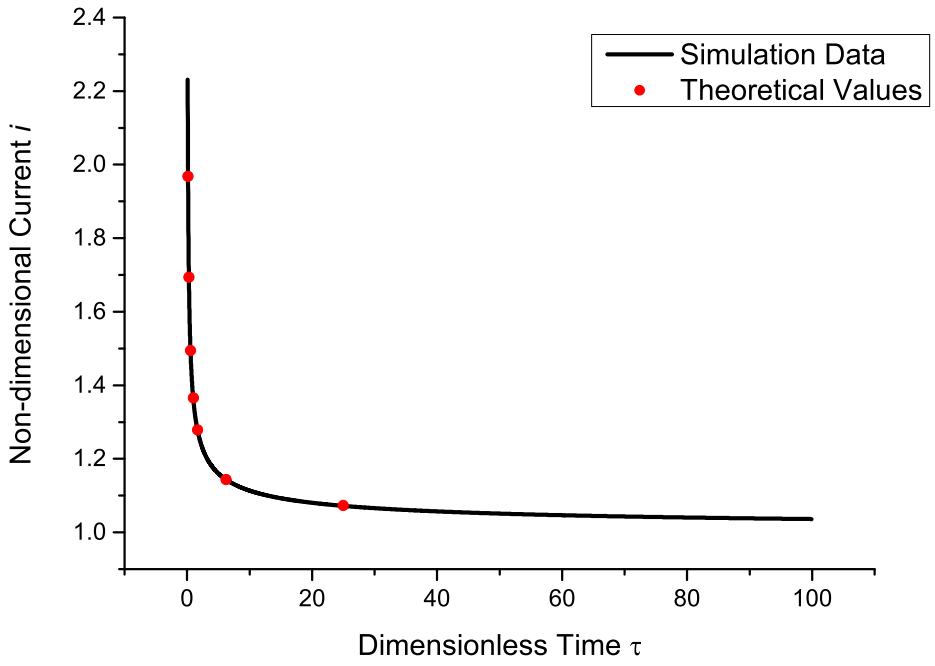

Figure 32: Amperometric response at a micro disk. Comparison between the simulation data (continuous line) and theoretical points (red dots) (Reference [3]) shows good agreement. Current and time are normalized respectively by Equations 2.51 and 2.52

complete oxidation (or reduction) is induced at the electrode surface. For the current case, a value of $0.6\,(V)$ is chosen, which is well above the equilibrium E_0. Furthermore,

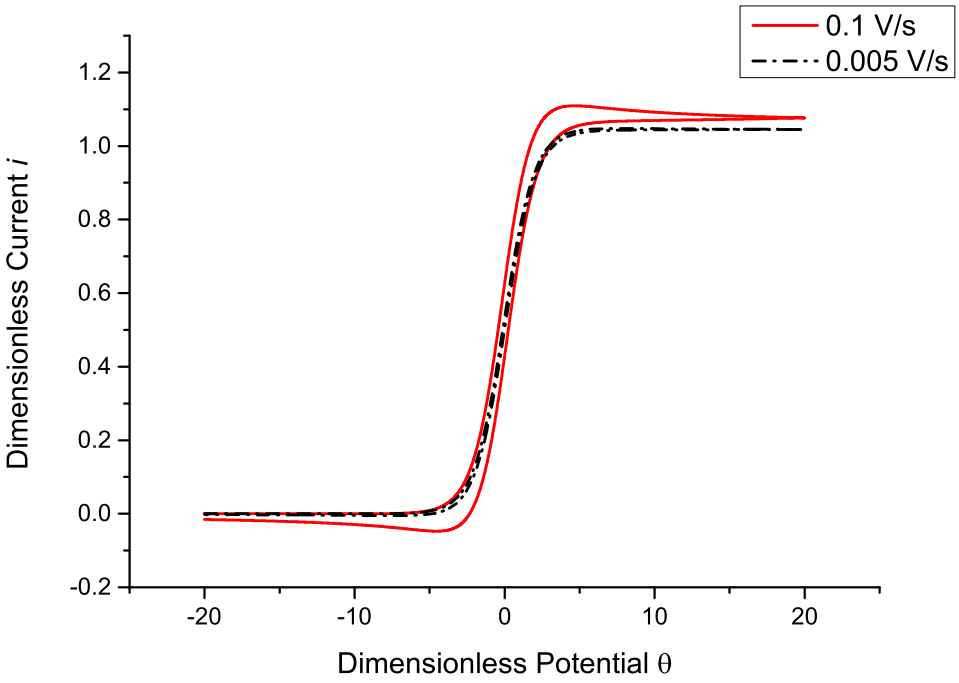

Figure 33: Dimensionless current versus dimensionless potential at two different scan rates (100 and $5\,mV/s$). A flatter and more steady state response is obtained at the slower scan rate. Dimensionless current and potential are given by expressions 2.51 and 2.46

it is customary to non-dimensionlize the current as follows:

$$i = \frac{I_{total}}{4FD_R c_{R0} r_e} \tag{2.51}$$

and the dimensionless time is expressed as:

$$\tau = \frac{Dt}{r_e^2} \tag{2.52}$$

Figure 32 compares the simuled current with theoretical data. An expression relating i and τ developed by [3] is widely used as the benchmark comparison for diffrerent numerical methods. As the time becomes large, it is shown that the dimensionless current approches 1 and the current is said to reach a limiting value I_{ss}:

$$I_{ss} = 4FD_R c_{R0} r_e \tag{2.53}$$

Equation 2.53 is useful in analytical chemistry because this relation can be used to determine either the diffusion coefficient D_R or bulk concentration c_{R0}. Anotherway of approaching the steady state current is by performing cyclic voltammetries as shown in Figure 33. Two scan rates 0.1 and $0.005\,V/s$ are used to demonstrate the principles. At high scan rates, the current response shows a peak similar to that of a macro electrode, but the feature is significantly less sharp. This is because the small electrode sizes considerably enhance fluxes towards the electrode surface and it is therefore possible to sustain high reaction rates. At small scan rates, the current shape follows the classic sigmoidal behavior. Theoretically as the scan rates becomes infinitely small, a steady state (Equation 2.53) is achieved [73]. In practice, values such as 5 or $1\,mV/s$ are usually sufficient to induce such behaviour.

It is also instructive to estimate the size of the steady state current from Expression 2.53:

$$I_{ss} \sim 4.96485 \frac{C}{mol}\, 10^{-9} \frac{m^2}{s}\, 1 \frac{mol}{m^3}\, 10^{-5} m \sim 4\,nA$$

which is much smaller in comparison to that of a macro electrode (typically in order of μA). This magnitude is nevertheless still significantly larger than the non-Faradaic component, which is estimated from Expression 2.10 as:

$$C_{dl} A v_{scan} \sim 100 \frac{\mu F}{cm^2}\, (\pi\, 10^{-6}) cm^2\, 0.005 \frac{V}{s} \sim 1.6\, 10^{-3}\, nA$$

assuming a relatively large double layer capacitance ($100\,\mu F/cm^2$). This fact confirms that for micro electrodes, capacitive currents can be safely ignored during analysis. Furthermore, computational time in 2D is also noted to be significantly more than that of one dimensional calculations (e.g. several minutes vs several seconds).

Thirdly, spherical-shaped electrodes are not so commonly encoutered at micro sizes. They are more often encountered in problems dealing with nano particles ($r_e \sim 50\,nm$). Because spherical electrodes also have the rotational symmetry around centre axis, the problem is again reduced to 2D. This effect may also be seen when we transform the equation from spherical to cylindrical coordinates and integrate along the z-axis. Therefore, the solution process described for a micro-disk is also applicable for spherical nano-electrodes. A mapping complication arises when modelling curved electrode surfaces. In theory, FD formulation can be adapted to any curvature that can be analytically expressed [154, 155]. For spherical shapes, a simple discretization is shown in Figure 34. Structurally, the red circular boundary is broken down into

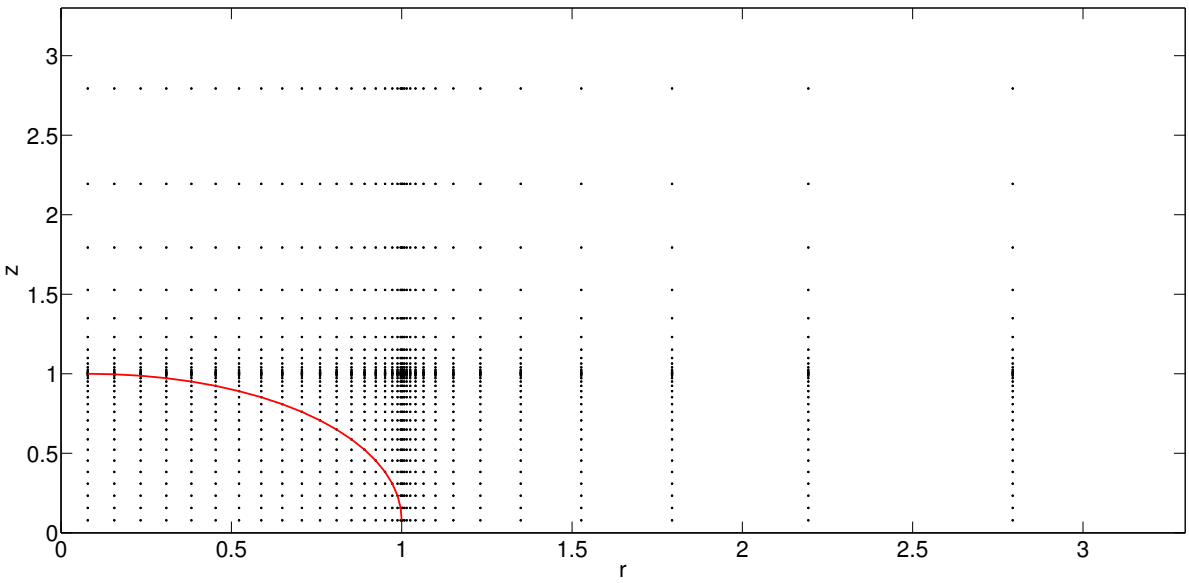

Figure 34: Meshing for spherical electrode. The boundary is coloured in red and only points on and outside the surface of the sphere are considered in the calculations

discrete points and the expanding mesh is then applied at each of these locations.

To illustrate the method, an amperometric calculation for spherical electrodes is performed. For an ultra small hemi-spheres, the current can be written as the sum of two components [2]:

$$I^{hemi-sphere} = \frac{\pi}{2}(FD_R c_{Ro} r_e) + I_{Macro}$$

where I_{Macro} is the Cotrellian response 1.19 at a macro electrode. Over a long period of time, this component tends to 0, leaving out the limiting current of $(\pi/2)FD_R c_{R0} r_e$ as shown in Figure 35. Finally,nano-spheres expectedly behaves in the same way as micro disks, which can be validated by linearly-swept cyclic voltammetry measurements..

Beside the basic E mechanism, it is interesting to consider additional homogenous reactions. The following section focuses on the EC' mechanism, which is schematically depicted in Figure 36. Initially the solution contains only substrate S and reductive form R. At the electrode surface, R is oxidized to O, which reacts with S to reform R and in-active products. It was briefly discussed in chapter 1 that EC' mechanism plays an important role in operating principles of Glucose sensors. However, the interest in studying the mechanism remains strong because of its potential application

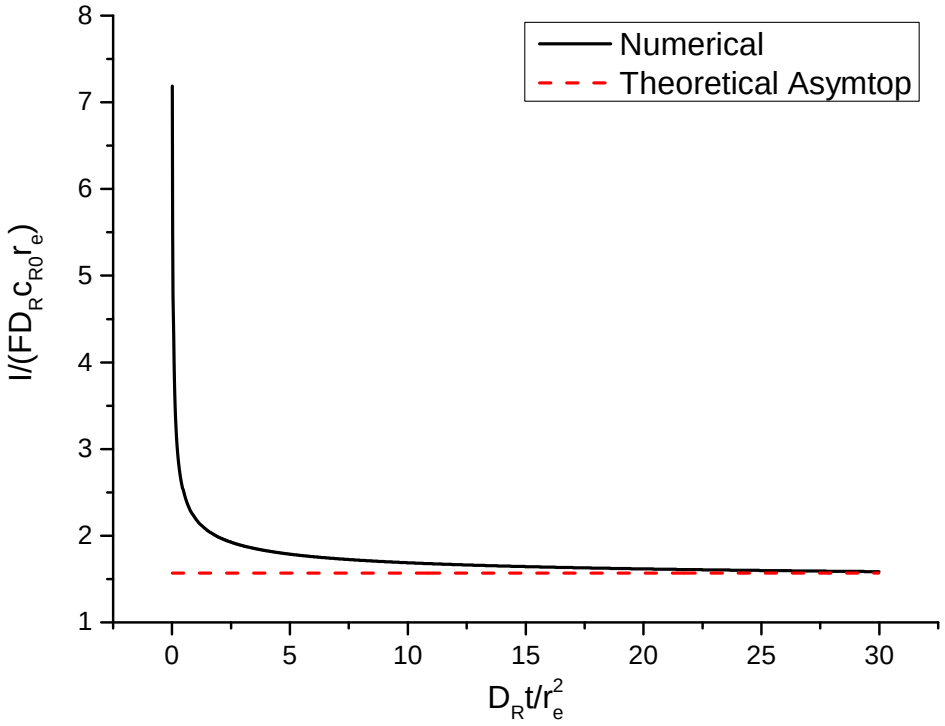

Figure 35: Limiting current at a sub micron or nano spherical electrode. The asymtope (at approximately $\pi/2 \simeq 1.57$) is colored in red

in detection of Hydrogen Sulphide (H_2S) in oil wells. Essentially, H_2S plays the role of substrate S in Figure 36 whilst the electrochemical pairs can be $Fe(CN)_6^{2-}/Fe(CN)_6^{3-}$ compounds in aqueous solutions.

Parameter Name	Notation	Value	Units
Diffusion Coefficients	D_R, D_O	10^{-5}	cm^2/s
Substrate Diffusion Coefficient	D_s	10^{-5}	cm^2/s
Initial Electroactive Concentrations	c_{R0}, c_{O0}	2, 0	mol/m^3
Initial Substrate Concentrations	c_{S0}	2	mol/m^3
Electrode Area	A	0.01	cm^2
Homogenous Reaction Rate	$k_{EC'}$	$5 * 10^5$	$M^{-1}s^{-1}$
Smallest Spacing	h_0	10^{-6}	m
Spatial Exponential Factor	f	1.05	–
Time Step	dt	0.001	s
Electrochemical Kinetics	k_0	0.1	cm/s

Table 5: Parameters settings for EC' calculations in Figures 30 and 38

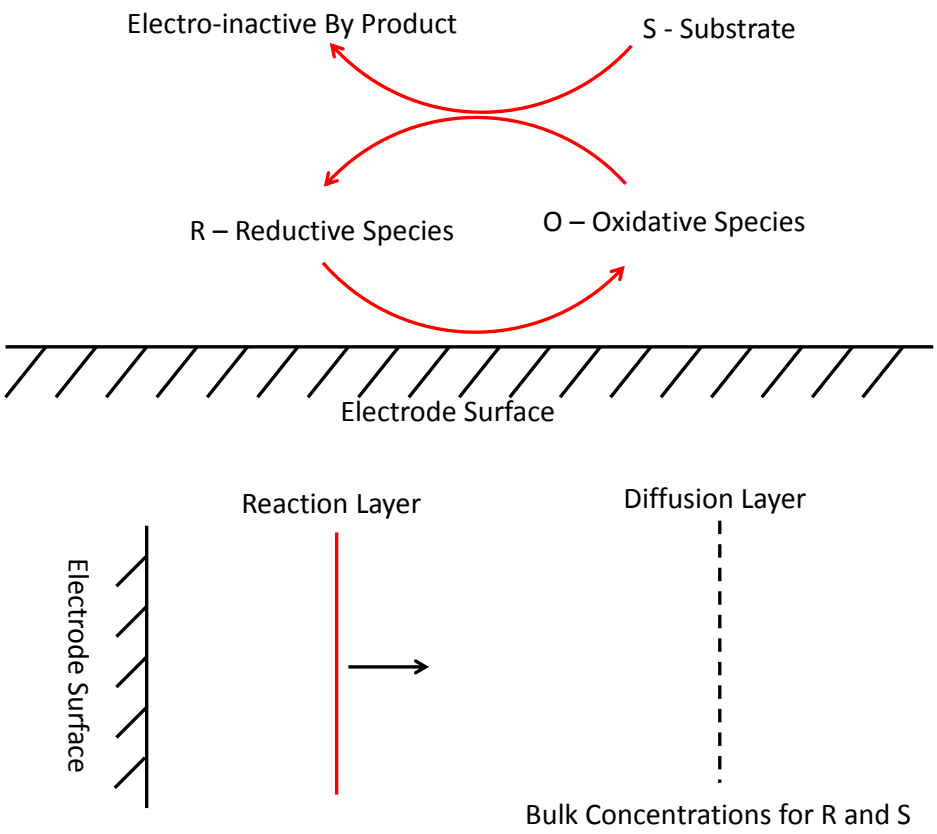

Figure 36: A schematic reaction pathway for an EC' mechanism (top) and the origin of pre-wave phenomenon in the forward sweep of cyclic voltammetry as a result of shifting of the reaction layer (bottom)

Another interesting aspect of the EC' mechanism is the introduction of a second-order term into the mass transport equation, which results in non-linear equations and requires Newton-Raphson methods to solve the mechanisms. Preliminary calculations for EC' mechanisms are illustrated below. These parameters are summarized in Table 5. One-dimensional transport equations are employed for several reasons: Firstly, they simplify computational efforts; Secondly, they resemble the experimental conditions because macro electrodes are commonly used; Thirdly, useful intuition into the process are gained before more complex calculations are performed; Finally, reversible electrochemical kinetics are assumed and the solution-based reaction is instantaneous and irreversible at high $k_{EC'}$ rates.

Figure 37 shows the effect of varying scan rates on the voltammograms [62]. Note that both the current and the potential are normalized by Equations 2.45 and 2.46. At

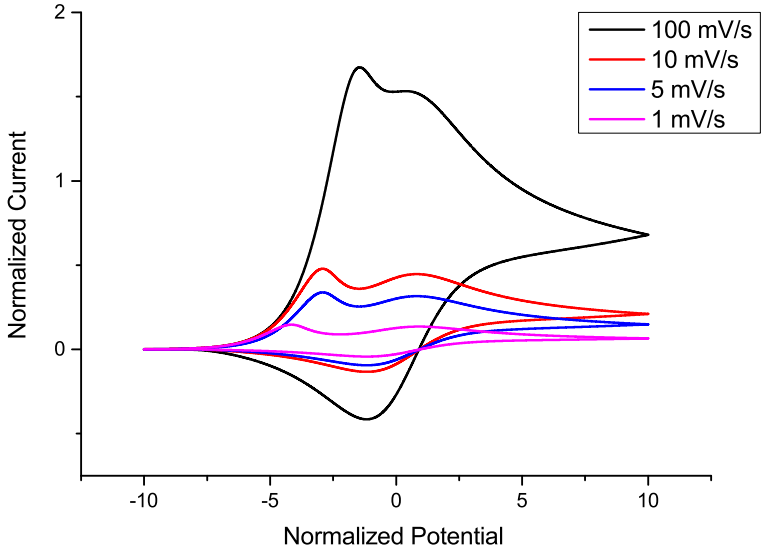

Figure 37: Increasing scan rates lead to an increase in measured currents. Notice that there are two peaks in the voltammograms. The first peak corresponds to pre-wave effect and the second is the usual redox reaction

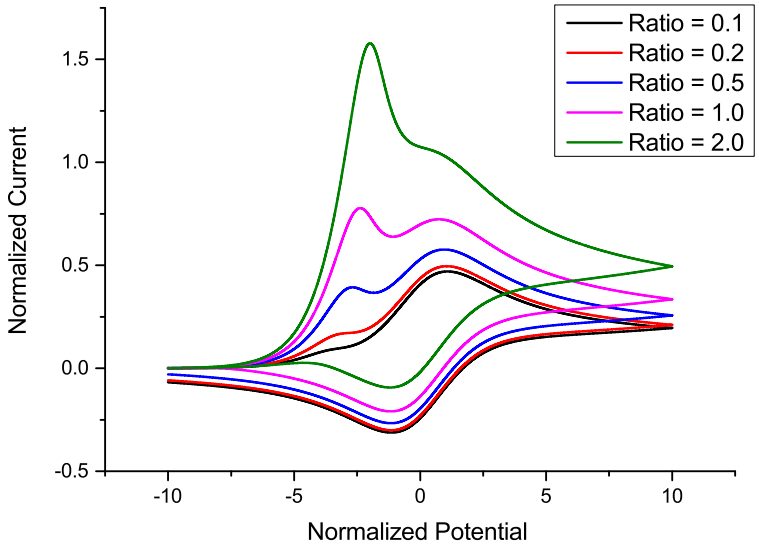

Figure 38: Effects of changing concentration ratios between substrate and electrolytes. The more S is present, the higher the pre-wave peak

higher scan rates, the scanning time is now smaller, therefore the size of the diffusion layer, which is proportional to $t^{1/2}$, also becomes smaller . A smaller diffusion layer also leads to an increase of electroactive species flux and consequentially higher currents. Thus in conclusion, a higher scan rate induces a larger current.

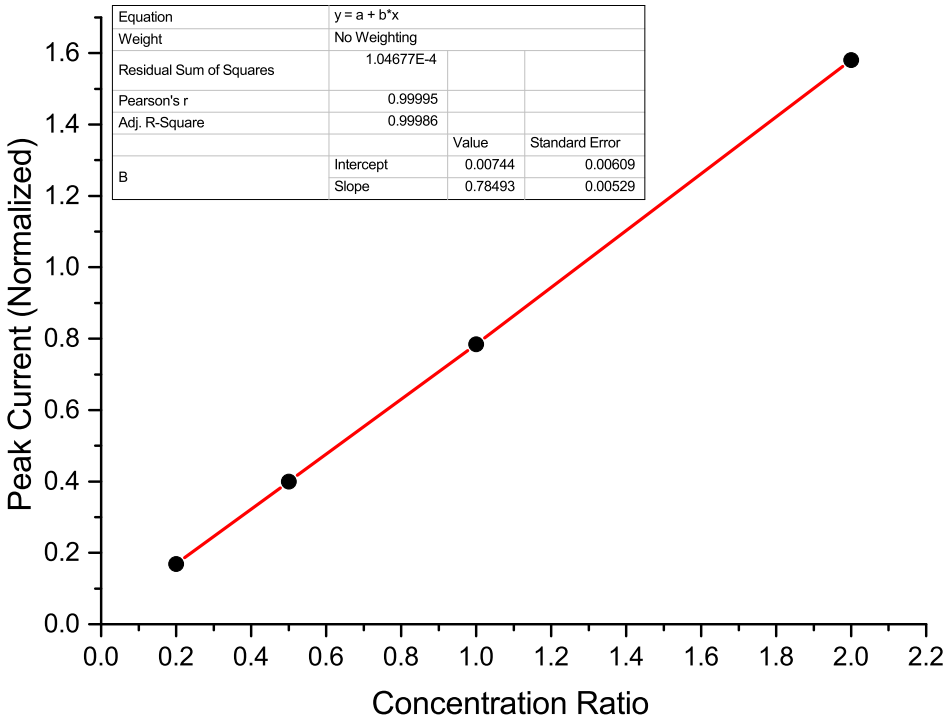

Figure 39: Pre-wave peak currents versus the concentration ratios c_{S0}/c_{R0} shows a linear relationship in Figure 38. Below ratio of 0.2, it is difficult to distinguish the pre-wave in the voltammogram

An additional interesting feature is the presence of a "pre-wave" peak before the usual peak (around the dimensionless potential 1). This fact can be reasoned by referring to the bottom figure in 36. At very high $k_{EC'}$, species R is re-formed at a much closer distance to the electrode surface. Between the reaction layer and usual diffusion layer (i.e. without EC'), the concetration of R remains essentially constant at the bulk value. The "pre-wave" current initially rises because there is initially plentiful supply of S inside the reaction layer, which quickly regenerates R and thus produces more current. However, after some time, S is depleted at the position of reaction layer and it takes sometimes for the transport of S into the reaction layer.

The regeneration of R becomes slower and the reaction layer shifts right due to mass-transport limitation. As a consequence, the current falls and a peak is formed.

To investigate the effect of substrate concentration, the scan rate is fixed at $25\,mV/s$. Calculations are then performed at different ratios of c_{S0}/c_{R0} and the results are presented in Figure 38. An observable trend is a rise in concetration ratio would lead to an increase in pre-wave current peak. Furthermore, as S increases, the pre-wave tends to shift right. This is due to the fact that a higher substrate concentration sustains the reaction layer position for longer, which decreases pre-wave occurrence at later potentials (as opposed for lower c_{S0} concentrations).

Because the pre-wave is dependent on substrate level, a strong correlation is expected between these variables (Figure 39). Note that the size of the other peaks are also influenced by the presence of S, but less pronounced comparing to the first one. Finally because the relationship is linear [168], these measurements are useful as a sensing method for the substrate. However the method becomes ineffective at very low substrate concentrations due to diminishing pre-wave magnitude.

2.8 Chapter Conclusion

This chapter described the basic numerical approach, namely FD, to the solution of diffusion equation coupled with electrochemical Butler-Volmer kinetics. Important aspects of FD, such as explicit/implicit time derivatives, mesh generation and linear solvers were discussed. These discussions are however not only limited to FD but applied to FE in later chapters.

The FD approach is then applied to several basic problems considering macro and micro electrodes. Good agreement between numerical data and analytical solutions is demonstrated for both cases. FD can also be extended to more complex curvature boundaries, as in the case of semi-hemispherical electrode. Finally, 2^{nd} order homogeneous kinetics case is considered. Since the PDEs are highly non-linear, the Newton-Raphson is considered to solve the problem. An interesting phenomenon, referred to as the pre-wave, is demonstrated and important physical insights for its origin discussed. This phenomenon is the subject of further investigation in Chapter 5.

Chapter 3 employs the linear sweep voltammetry as an experimental design factor to investigate different aspects of the Butler-Volmer model. This work requires repetitive computation of the model for diffusion transport coupled with electrochemical kinetics, thus FD method developed so far is useful. By using an extended version of the Butler-Volmer formulation, the investigation aims to identify the most significant parameters and then estimate them as accurately as possible. In addition, Monte Carlo approach is flexibly employed to different problems of optimization and multi-dimensional intergrations.

Chapter 3

Parameter Identifiability and Estimation of Redox processes under Diffusion Control

This chapter introduces the concept of identifiability measure and applies it to electrochemistry context. Special emphasis is placed on interpretations of the result, which have important implication for subsequent sections in the chapter. The extent of the investigation is however not limited to identifiability study but also encompasses parameter ranking, selection and estimation. Since the topics of estimability and estimation share virtually the same mathematical framework, this work focuses on the study of the later for practical reasons.

The following work presents a theoretical case study in which the traditional linear sweep and cyclic voltammetric techniques are heavily utilized as an experimental design variable. The work aims to determine whether this voltammetry method can adequately retrieve electron transfer kinetic information instead of employing more conceptually complex voltage designs. Furthermore, because these techniques are so commonly used, the results of this study provide a useful theoretical foundation for such practice. It is also intuitively clear that any other synthetic signal should include linear sweep and/or cyclic voltammetry, since these signal are readily available in most experimental equipments and effective at inducing redox reaction.

The chapter is structured as follows. First the Butler-Volmer formulation, from the previous chapter, is extended to account for two additional parameters: uncompensated resistance and double layer capacitance. The identifiability calculation is

then applied to this model to observe the potential compensating effects among the model parameters. By carefully selecting other experimental variables and applying global sensitivity analysis, the intrinsic electron transfer kinetic, equilibrium potential and double layer capacitance are determined as the most significant parameters in the model. To complement this result, it is shown that the first two of these parameters along with the charge transfer coefficient can be reliably estimated without the detailed knowledge of the third one. In addition, Monte Carlo Markov Chain (MCMC) statistical calculations demonstrate that the mean values for those parameters fall respectively within 4% (for k_0) and less than 1% (for α and E_0) of the assumed true values.

3.1 The extended Butler-Volmer Model

Throughout the chapter, a one-dimensional model is assumed. The system of equations can be shown compactly via Equations 3.1 and 3.2 for the redox transfer $O + e \leftrightarrow R$. The spatial operator represents second order differentation $L_x = \partial^2/\partial x^2$:

$$\frac{\partial c_i}{\partial t} = D_i L_x c_i,\ i = R, O \tag{3.1}$$

$$I_f/FA = D_R(\frac{\partial c_R}{\partial x})_{x=0} = -D_O(\frac{\partial c_O}{\partial x})_{x=0} = k_f(c_R)_{x=0} - k_b(c_O)_{x=0} \tag{3.2}$$

where the forward and backward rates k_f and k_b are defined as in Equations 1.10 and 1.11. The model has three major parameters: k_0, α and E_0. In addition to these three parameters, the total current I (or the model output) is influenced by double layer capacitance C_{dl} according to Equation 2.11. In general, the exact value of C_{dl} is unknown and it usually varies throughout the voltammetric experiments and in some cases exhibits potential-dependent behaviour.

Extra complication is caused by the uncompensated solution resistance R_u. This resistance is mainly due to the solution between the working and reference/counter electrodes, with other resistances (e.g. metal contacts) being negligible. The presence of R_u leads to losses of the driving potential, and thus requires the rates k_f and k_b to be modified as follows:

$$k_f = k_0 exp(\frac{(1-\alpha)F(E - E_0 - IR_u)}{RT_0}) \tag{3.3}$$

$$k_b = k_0 exp(\frac{-\alpha F(E - E_0 - IR_u)}{RT_0}) \tag{3.4}$$

Dielectric polarization within the solution also leads to extra losses, which is attributed to the potential difference between solid and fluid phase [24, 30]. In addition, it can be seen that the gradient of this potential is associated with electrostatic migration fluxes (Equation 1.5). As remarked earlier, this phenomenon is important at low supporting electrolyte concentrations . It is assumed in this chapter that the solution is well-supported, hence the potential loss caused by ion migrations can be safely ignored.

Considering Equations 3.1,3.2, 3.3 and 3.4 along with the boundary conditions 2.4 and 2.5, it is evident that additional non-linearity is introduced by the "Ohmic drop"

component IR_u. Because the total current $I = I_f + I_c$ now appears in the exponential term, this fact discourages the application of fully implicit formulations. This is the case because these formulations are compactly expressed as:

$$\frac{c^{t+dt} - c^t}{dt} = DL_x c^{t+dt} \tag{3.5}$$

where the operator L_x is approximated by second or higher order finite difference formular. The set of equations 3.5 at each concentration point i is then coupled with non-linear boundary condition at the electrode surface. A general solution approach is the Newton-Raphson, which can be used to determine species concentrations and the total current simultaneously. A major drawback is the exact computation of the Jacobian matrix, which is cumbersome and expensive in this case.

A straightforward way of dealing with the non-linearity in this case is to use an explicit formulation. In the current case, the concentration at a new point in time is directly computed by Equation 3.6:

$$\frac{c_i^{t+dt} - c_i^t}{dt} = D_i L_x c_i^t \tag{3.6}$$

Thus the only unknown after solving Equation 3.6 is the total current I. Ultimately, this is the only non-linear equation to be solved. Multiplying both sides by nFA, Equation 3.2 now assumes a generalized form::

$$I_f = f(I_f) \tag{3.7}$$

where I_c is known at each potential point (Equation 2.10).

A simple method to solve Equation 3.7 uses a binary (or bisection) search method. It belongs to a class of interval searches which is a discrete version of the Newton-Raphson. Some other well-known related methods include the Regula-Falsi Method or Secant Method [162]. The bisection search is described in Algorithm 3.1. In general, the bisection search works by reducing the interval size by half at each iteration. It guarantees to converge quickly if the initial interval $[a, b]$ is well chosen to contain the exact root of the equation. This requirement also implies that $f(a)\, f(b) < 0$.

To easily implement Algorithm 3.1, Equation 3.7 is re-arranged:

$$I_f - f(I_f) = 0$$

and treat the LHS as the function f in the Algorithm. A summary of parameters

in the simulation is given in Table 6. The maximum number of iterations for the "Binary Search" algorithm is set to 50. This value was observed to yield satisfactory convergence in trial runs.

Algorithm 3.1 Binary search for solution of $f(x) = 0$ where x lies inside a known interval $[a, b]$

```
Initialize guess x → (a + b)/2
Initialize Iteration → 1
while Convergence not satisfied or Maximum Iteration not reached do
  Calculate f(x)
  Calculate f(a)
  Calculate f(b)
  if f(x) * f(a) < 0 then
    b = x
  else
    a = x
  end if
  Recalculate x → (a + b)/2
  Check the convergence. If satisfied then BREAK
  Increment Iteration → Iteration + 1
  Check whether Maximum Iteration has been reached
end while
Return x
```

Name	Value	Units	Parameter Type
D_R	$7.6 * 10^{-6}$	cm^2/s	Physical Constant
D_O	$7.6 * 10^{-6}$	cm^2/s	Physical Constant
k_0	0.001	m/s	Butler-Volmer Parameter
α	0.5	$-$	Butler-Volmer Parameter
E_0	0.2	V	Butler-Volmer Parameter
C_{dl}	0	$\mu F/cm^2$	Butler-Volmer Parameter
R_u	$0 - 1000$	Ω	Butler-Volmer Parameter
T_0	298	K	Controlled Variable
v_{scan}	0.1	V/s	Controlled Variable
A	0.01	cm^2	Controlled Variable
E_{start}	-0.2	V	Controlled Variable
E_{vertex}	0.6	V	Controlled Variable
c_{R0}, c_{O0}	1, 0	mM	Species Bulk Concentrations

Table 6: Summary of parameter values for simulations with uncompensated resistance. The controlled parameters are kept the same throughout this chapter

To illustrate the explicit method, two calculations are compared and shown in Figure 40. The red curve agrees very well with the previous implicit calculations in Figure 30. In the explicit method, a larger number of time steps are required in order to maintain numerical stability. Equation 2.23 requires the non-dimensional value $D_R \triangle t/(\triangle x)^2 \sim 1$. When a smaller grid size is employed, the time step is correspondingly decreased. Therefore, the computing times for the curves are considerably larger for the red curve. Finally, from a numerical stand point, the black curve reasonably approximates the red curve for most constraints since around the peak region, the difference between the two curves is around 1%.

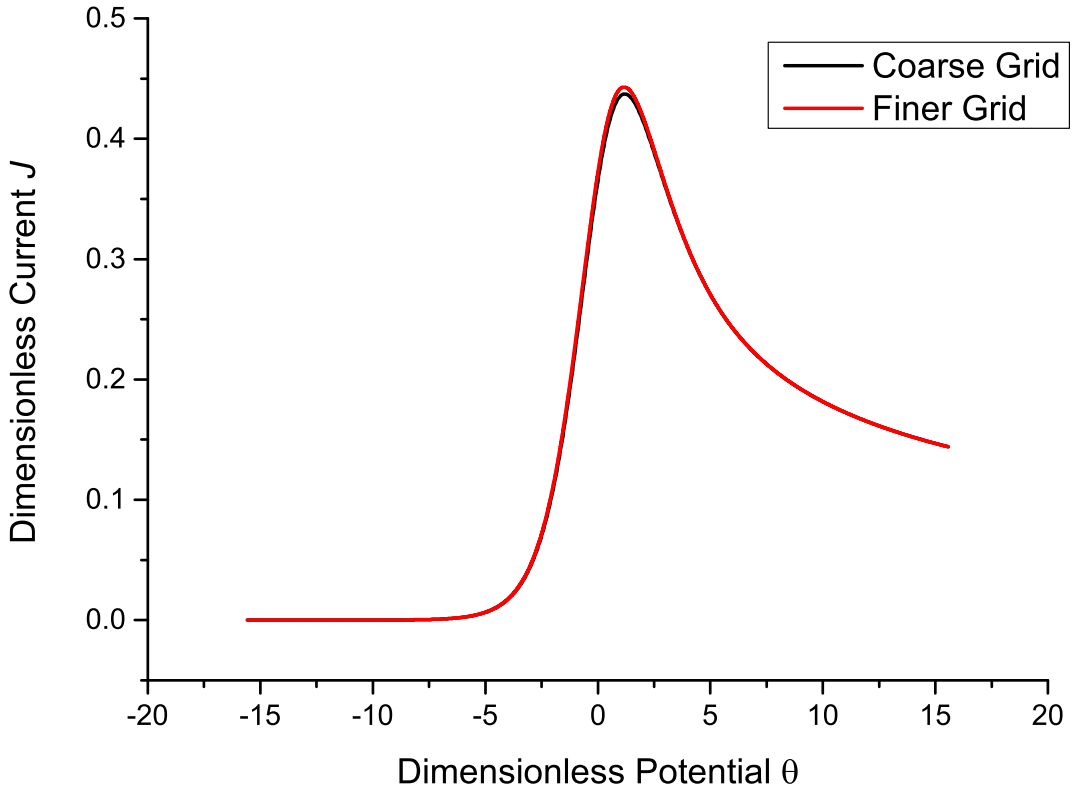

Figure 40: Explicit calculations at two different grid sizes (coarse (black) vs fine (red)). The more accurate result (red) requires more number of time steps (2^{20} in comparison to 2^{16} of the black curve). The red and black curves agree to within 0.67% and 1% of the implicit calculations in Chapter 2 respectively. The current and potential are normalized according to Equations 2.45 and 2.46

The effects of increasing resistance are shown in Figure 41. The Butler-Volmer

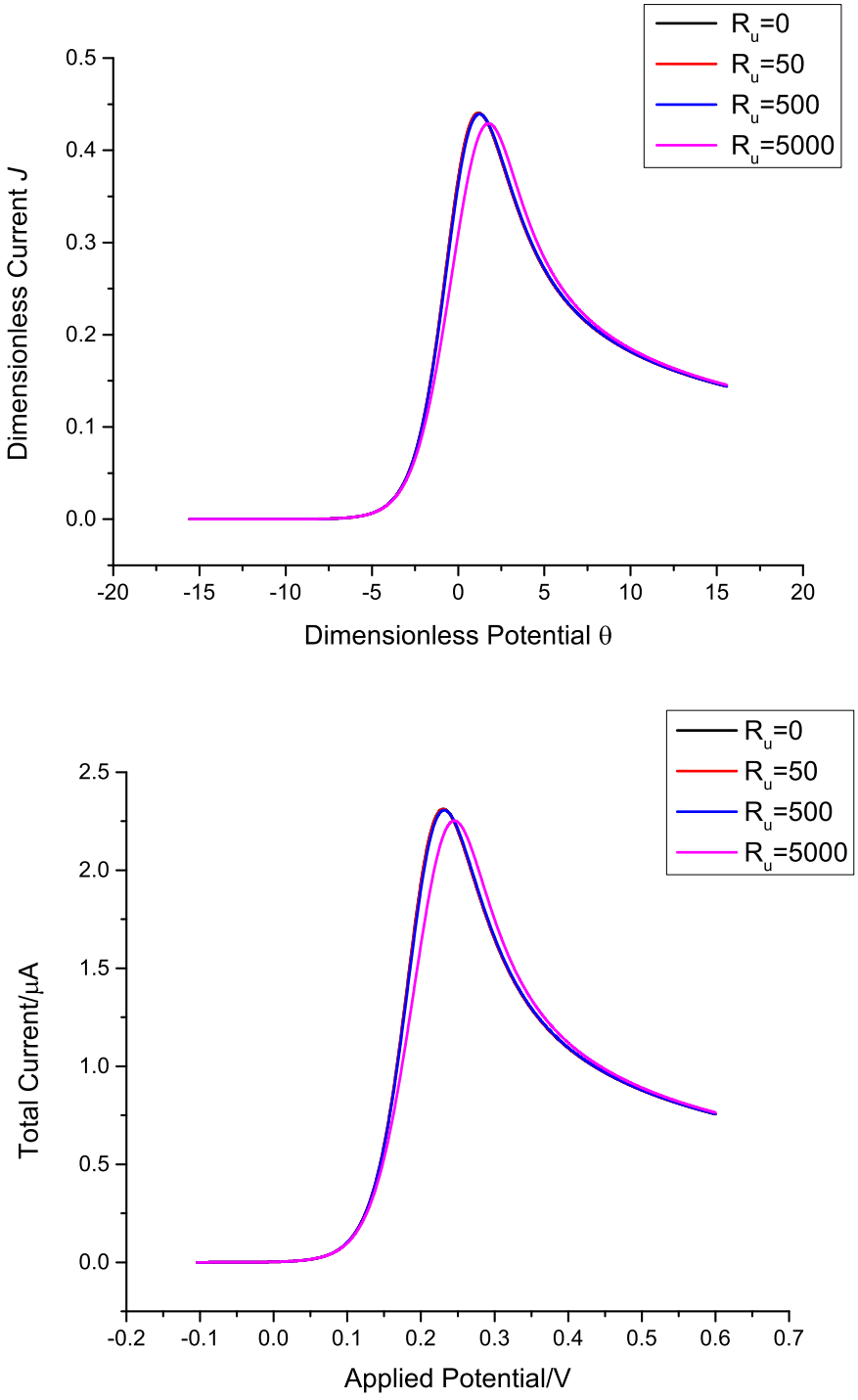

Figure 41: Effect of uncompensated resistance on linear sweep voltammetries. For small resistances ($50 - 500$ Ohm), the current response does not change significantly. For larger resistances (e.g. 5000 Ohm), the peak current starts to decrease and shifts right to compensate for a decrease in reaction kinetics. Data are presented in dimensionless (top) and dimensional format (bottom)

parameters are kept constant and R_u is increased between $50 - 5000$. A rising uncompensated resistance leads to an additional loss in the applied potential, which requires a larger oxidative potential to drive the reaction. The peak therefore shifts rightward to compensate for such effects. In addition, since the exponents in Equations 3.3 and 3.4 are now smaller in comparison to the zero resistance case, resulting in a smaller current and peak height. However, the effect is only significant at very large resistances, suggesting that higher resistances do not significantly influence the current output.

From the dimensional current (bottom Figure 41), a direct way of reducing the effect of Ohmic drop IR_u is to reduce the current I. This is in fact achieved by employing an electrode area $A = 0.01\, cm^2$, which is small enough to reduce the potential loss, but is still sufficiently big so that the macro electrode conditions still apply. A qualitative reason is given as follows. Considering the expression for the effective overpotential:

$$\eta = (E - E_0) - IR_u$$

If $R_u = 500\,\Omega$ and $I \sim 2\,(\mu A)$, the Ohmic drop is in the order of $10^{-3}\,V$. This component becomes significant when E is close to E_0, but under that condition, the current is still relatively small since the exponents in Butler-Volmer expression are also small. Thus under this experimental design condition, the effect of solution resistance on the current is negligible in the range $0 - 500\,\Omega$. Having developed a robust computation method for the extended Butler-Volmer formulation, the subject of identifiability is discussed next.

3.2 Identifiability Measure for Model Parameters

Section 1.5 of chapter 1 introduces the basic concepts in identifiability. One of the early definitions (Equation 1.28) defines identifiability with respect to data. This concept captures the idea of identifiability and estimability altogether. Another way of defining identifiability without referencing to external data was proposed by other authors [106] [124]. This definition is more intuitive and used in this work. Applying this definition to Butler-Volmer model, the model is identifiable if and only if the following equality occurs:

$$I(\theta_1, u) = I(\theta_2, u) \leftrightarrow \theta_1 = \theta_2 \tag{3.8}$$

,that is if the same current response is obtained then the underlying sets (θ, u) must be the same. Vectors θ and u denote the parameter set and experimental variables respectively:

$$\theta = [D_R, D_O, k_0, \alpha, E_0, R_u, C_{dl}] \tag{3.9}$$

$$u = [T_0, v_{scan}, A] \tag{3.10}$$

The electrode area is usually fixed, and since a homogenous temperature is assumed, the most significant variable in the relation is the scan rate $u = [v_{scan}]$. The identifiability problem was earlier studied using highly modulated signals. The results show aninvariance to the waveforms (e.g. triangular,sawtooth, square) being used [123]. In addition, it was concluded that a single set of data is not sufficient enough to allow all parameters in θ to be uniquely estimated. It also highlights the issue of parameter compensation in which groups of parameters compensate each other (due to non-linear interaction) and result in similar current responses $I's$.

The major aim of this section is to show that the model is not globally identifiable under linear sweep voltammetry. From a mathematical perspective, a locally non-identifiable model is desired. The problem is formulated as an optimization function, i.e. identifiability test:

$$max_{\theta_1,\theta_2} H(\theta_1, \theta_2) = \eta^2 = \frac{(\theta_1 - \theta_2)^2}{(I(\theta_1, u) - I(\theta_2, u))^2} \tag{3.11}$$

where optimizing variables are the pairs (θ_1, θ_2). The interpretation of 3.11 is as

follows. Assuming finite maximal η^* (or the identifiability number) exists, the following inequality applies:

$$|\theta_1\text{-}\theta_2| \leq \eta^* |I(\theta_1, u) - I(\theta_2, u)| \tag{3.12}$$

Equation 3.12 measures changes in the total current caused by the differences in parameter sets. If two different sets lead to very similar response, then a consequentially large η^* reflects the non-identifiability of the model. The larger it is, the less unique the model parameters are. Therefore one expects η^* to be as small as possible for a highly identifiable system. In addition, η^* generally depends not only on the model structure but also the experimental variables u.

Algorithm 3.2 Monte Carlo sampling for optimization of Identifiability function $H(\theta_1, \theta_2)$

```
Initialize Iteration → 1
Initialize h_sol → 0
while Maximum Iteration not reached do
  Generate a matrix of random number between 0 and 1 with size N_Parameter x 2.
  Each column corresponds to a parameter set
  Convert each column into parameter set values
  Calculate the corresponding Identifiability function h_new
  if h_new > h_sol then
    h_sol = h_new
    Update the new pair as the current solution
  end if
  Increment Iteration → Iteration + 1
  Check whether Maximum Iteration has been reached
end while
Output the value h_sol and solution pair
```

To optimize the function 3.11, previous work used semi-gradient approaches such as the Simultaneous Pertubation Stochastic Approximation (SPSA). SPSA approximates the gradient of $H(\theta_1, \theta_2)$ using a simple first order finite difference formula and is a semi-gradient approach. For each specific problem, SPSA requires tuning of parameters to ensure good performance. This work opts to use Monte Carlo sampling. In this approach, many pairs of (θ_1, θ_2) are generated and $H(\theta_1, \theta_2)$ is computed. The largest value of all is kept as the final solution. For complicated functions, the optimal value may become trapped in the local solution; the Monte Carlo method reduces the likelihood of this occurrence by searching the proximity of the global optimum [148].

The generic algorithm is described in Algorithm 3.2.

Parameters	Upper Bound	Lower Bound	Units
D_R	10^{-5}	10^{-6}	cm^2/s
D_O	10^{-5}	10^{-6}	cm^2/s
k_0	0.1	0.0001	cm/s
α	0.7	0.3	–
E_0	0.4	0.1	V
R_u	1000	0.1	Ω
C_{dl}	50	0.1	$\mu F/cm^2$

Table 7: Upper and lower bounds for each model parameter. These are typical values for experiments conducted in aqueous solution. Electrode area is fixed at $0.01\,cm^2$

Each model parameter in Table 6 is bounded, with the lower and upper values given in Table 7. The diffusivity, however needs to be adjusted, according to the solvent being used and the suggested range, which is likely applicable to aqueous solutions. The function $rand()$ is used to generate random numbers uniformly distributed between $(0, 1)$. The dimensionless number is then converted to the corresponding dimensional parameter. The current is again non-dimensionalized by dividing by I_p (Equation 2.47) before being used to compute the identifiability function H. In addition, the sampling is done in log space instead of linear space of parameters. The reason is that log sampling tends to spread out the parameter values more evenly in search space than linear sampling. Calculations are performed for linear sweep experiment with the same controlled variables in Table 6. The maximum number of iterations in Algorithm 3.2 is set to 500. 10 runs are performed and the best of 7 are ranked in the decreasing order as shown in Table 8.

From the first row of Table 8, compensating effects among parameters are clearly evident. The first set has low intrinsic reaction rate k_0 and higher resistance R_u, thus producing a lower current response with respect to reversible limits. However, the same output can also be achieved by having a larger formal potential E_0 in the second set. Consequently, the two currents are numerically similar although the two sets are significantly different. It can be concluded that there are interactions among k_0, R_u and E_0, causing the non-identifiability in the current outputs.

To summarize, the role of identifiability measure is to discover potential compensating interactions among parameters. This is accomplished by running the Algorithm 3.2 and examining the sets corresponding to the maximum of function $H(\theta)$. This brute force approach becomes less effective for large and non-linear model. Furthermore,

Sample No.	H	η^*	Parameter Sets
1	1.67	1.29	$[1.50*10^{-6}, 1.15*10^{-6}, 2.86*10^{-4}, 0.415, 0.102, 727, 7.22*10^{-7}]$ $[9.03*10^{-6}, 1.07*10^{-6}, 1.55*10^{-3}, 0.38, 0.165, 132, 1.6*10^{-6}]$
2	1.11	1.05	$[1.37*10^{-6}, 1.83*10^{-6}, 1.43*10^{-2}, 0.459, 0.125, 2.83, 2.12*10^{-7}]$ $[5.42*10^{-6}, 1.87*10^{-6}, 1.09*10^{-2}, 0.532, 0.144, 8.54, 2.01*10^{-6}]$
3	0.80	0.85	$[7.62*10^{-6}, 1.11*10^{-6}, 3.74*10^{-3}, 0.328, 0.378, 249, 6.61*10^{-6}]$ $[2.18*10^{-6}, 1.17*10^{-6}, 2.9*10^{-3}, 0.363, 0.369, 45, 1.1*10^{-6}]$
4	0.77	0.88	$[1.15*10^{-6}, 1.88*10^{-6}, 5.03*10^{-3}, 0.578, 0.137, 9.69, 3.76*10^{-7}]$ $[9.39*10^{-6}, 1.98*10^{-6}, 1.14*10^{-2}, 0.411, 0.171, 3.32, 3.15*10^{-6}]$
5	0.67	0.82	$[1.92*10^{-6}, 1.43*10^{-6}, 1*10^{-4}, 0.381, 0.215, 305, 1.3*10^{-7}]$ $[8.03*10^{-6}, 1.35*10^{-6}, 3.17*10^{-2}, 0.591, 0.357, 0.354, 2.3*10^{-6}]$
6	0.5	0.7	$[1.79*10^{-6}, 2.38*10^{-6}, 4.32*10^{-2}, 0.312, 0.159, 162, 2.15*10^{-6}]$ $[1.81*10^{-6}, 1.93*10^{-6}, 2.82*10^{-2}, 0.495, 0.173, 0.278, 48.9*10^{-6}]$
7	0.45	0.67	$[5.26*10^{-6}, 3.66*10^{-6}, 4.14*10^{-3}, 0.467, 0.174, 0.434, 20.9*10^{-6}]$ $[1*10^{-6}, 3.71*10^{-6}, 2.53*10^{-2}, 0.31, 0.168, 44.5, 1.13*10^{-6}]$

Table 8: Maximum value of identifiability function H, the corresponding number η^* and respective dimensional parameter sets using a scan rate of $100\,mV/s$. The orders in each set are $[D_O, D_R, k_0, \alpha, E_0, R_u, C_{dl}]$

the correlated parameter pairs are not evident from the calculation results.

The next section introduces a method which determines the subset of parameters having a the most influence on the model output. By focusing on this aspect, highly correlated but non-important parameters are excluded from the model details, which further simplifies subsequent analysis (e.g. parameter estimation). Theoretical foundation of this approach is based on Sobol sensitivity indices.

3.3 Sobol Global Sensitivity Analysis

Sobol's approach is based on the analysis of variance (ANOVA) framework. In this approach, the importance of a parameter is assessed based on its contribution to the variance of the output variable. The larger the contribution, the more important the parameter becomes, and effort will be directed by the toward studying this parameter. The basic theory and details of the proof were provided in the seminal work by Sobol [117]. The objectives of this section are: i) to summarize the basic notionsand equations, ii) to apply the method to the generalized Butler-Volmer model, and iii) to illustrate the results and their respective interpretations.

Assuming a vector $x = [x_1, x_2, ..., x_i, ..., x_N]$ consisting of N variables. Each variables x_i, $i = 1, 2, ..., N$ has its own probability distribution. To simplify the work, it is assumed that all the variables are uniformly distributed inside the interval $[0, 1]$. Numbers distribute inside other intervals $[a, b]$ can be directly sampled from $[0, 1]$ using a linear mapping as in Equation 3.13:

$$U_{[a,b]} = (1 - U_{[0,1]})\, a + U_{[0,1]}\, b \tag{3.13}$$

The choice for uniform distributions are conservative and un-informed, therefore if more exact distributions are known then they should be applied. If x is a model input, the output is then computed via the general function:

$$f(x) \equiv f(x_1, x_2, ..., x_N) \tag{3.14}$$

Because the variables are statistically distributed, so is the value of function f in Equation 3.14. Consequently the mean f_0 and variance D of $f(x)$ exist which implies that the following decomposition theoretically applies:

$$f(x) = f_0 + \sum_i f_i(x_i) + \sum_{i<j} f_{i,j}(x_i, x_j) + ... + f_{1,2,...,N}(x_1, x_2, ..., x_N) \tag{3.15}$$

such that each combinatorial function f_i, $f_{i,j}$, $f_{i,j,k}$, *etc.* has a zero mean. Each of those function will have corresponding variances D_i, $D_{i,j}$, *etc.* The following relation then applies:

$$D = \sum_i D_i + \sum_{i,j} D_{i,j} + ... + D_{1,2,...,N} \tag{3.16}$$

The first order sensitivity index for variable x_i is defined as follows:

$$SI_i = D_i/D \tag{3.17}$$

which is simply due to the first order term D_i. The total sensitivity index is however includes all other interactions with other parameters and D_i itself:

$$SI_i^{Total} = (D_i + \sum D_{i,j} + \sum D_{i,j,k} + D_{1,2,...,N})/D \tag{3.18}$$

The major objective of the Sobol analysis to calculate the indicies S_i and S_i^{Total} for each model variable x_i. To simplify the notation, the complementary vector is defined as:

$$x_{-i} = [x_1, x_2, x_{i-1}..., x_{i+1}, x_N] \tag{3.19}$$

in which the variable x_i is deleted from the original vector x. Thus $x = [x_{-i}, x_i]$ and $x^{'} = [x_{-i}, x_i^{'}]$ in which $x_i^{'}$ is sampled from the same distribution as x_i. Using the above notation, the Sobol formula states:

$$D_i^{Total} = \frac{1}{2}\int (f(x_{-i}, x_i) - f(x_{-i}, x_i^{'}))^2 dx dx_i^{'} \tag{3.20}$$

and a similar can be written for the complimentary variance $D_{-i}^{Total} = D - D_i^{Total}$:

$$D_{-i}^{Total} = \frac{1}{2}\int (f(x_{-i}, x_i) - f(x_{-i}^{'}, x_i))^2 dx dx_{-i} \tag{3.21}$$

In Equation 3.20, only the variation of x_i is taken into account, whilst relation 3.21 only counts the contribution of all variables except x_i. Finally, the total index D_i^{Total} is directly computed and then $S_i^{Total} = D_i^{Total}/D$ and from 3.21 as $S_i = 1 - D_{-i}^{Total}/D$.

In general, numerical methods are employed to calculate 3.20 and 3.21 since analytical solutions are not viable. This work employs the simple and highly efficient Monte Carlo integration. The main reason for choosing the Monte Carlo approach is because the integration of a multi-dimensional problem poses significant challenges to traditional numerical methods such as trapezoidal rule or Gaussian quadratures. Monte Carlo numerical approximations are listed below for the mean (Equation 3.22), variance (Equation 3.23), and indicies $D's$ (Equations 3.24 and 3.25):

$$f_0 \cong \frac{1}{N_{sample}} \sum_{1}^{N_{sample}} f(x) \tag{3.22}$$

$$D \cong \frac{1}{N_{sample}} \sum_{1}^{N_{sample}} f^2(x) - f_0^2 \tag{3.23}$$

$$D_i^{Total} \cong \frac{1}{2N_{sample}} \sum_{1}^{N_{sample}} (f(x_{-i}, x_i) - f(x_{-i}, x_i^{'}))^2 \tag{3.24}$$

$$D_{-i}^{Total} \cong \frac{1}{2N_{sample}} \sum_{1}^{N_{sample}} (f(x_{-i}^{'}, x_i) - f(x_{-i}, x_i))^2 \tag{3.25}$$

The basic Monte Carlo integration converges fairly slow and the error varies with $1/N_{sample}^{1/2}$, therefore a large number of samples is required to guarantee a good approximation of the true integral value. The Quasi-Monte Carlo approach aims to improve the convergence by using an improved sampling of the variables based on their distributions. Intuitively, by considering the hypercube space $[0,1]^N$, a good sampling procedure spreads out the vector point x as uniformly as possible. A uniform distribution of a set of sampling points leads to the cancellation of errors in the summation and results in more accurate approximations. Figure 42 compares a result from Quasi-Monte Carlo sampling to that of the usual brute force (uniform) sampling.

There are three common quasi Monte Carlo methods: Halton and Sobol sets and Linear Hypercube Sampling (LHS). The Sobol sequence construction involves a base 2 number system. It has successive partitions and reorders the points. A Halton sequence is like Sobol sampling in terms of construction, but instead uses prime-based numbers. The LHS method, tends to be less effective than the former approaches for producing random sequences with minimal discrepancy. In this work, the Sobol sequence sampling is preferred. Computation of Sensitivity Indices (SI) of the First Order, and the Total for each parameter is summarized in Algorithm 3.3. Note that for dimensional variables, the random numbers in each column generated should be converted respectively before calculating the functional value $f(x)$. For Butler-Volmer kinetics, Sobol analysis is carried out with $N_{sample} = 1000$ and $N_{run} = 5$ and the indicies are presented in Table 9. Time points are sampled at $1/4{*}t_{max}$, $1/2{*}t_{max}$, $3/4{*}$ t_{max} and t_{max} in a forward linear sweep to calculate the indicies D_i^{Total}, D_{-i}^{Total} and the results are subsequently averaged.

The following discussion focuses on the set $[k_0, \alpha, E_0, R_u, C_{dl}]$. Considering the top half of Table 9, which computes contributions of individual parameters, and taking into account the current components I_f and I_c, one can rank the set in the following order $[E_0, k_0, \alpha, R_u]$ and $[C_{dl}]$. As a whole, the order of importance would be

Sample No.	D_O	D_R	k_0	α	E_0	R_u	C_{dl}
1	$3.66 * 10^{-2}$	$1.16 * 10^{-1}$	$5.54 * 10^{-2}$	$5.04 * 10^{-3}$	$2.48 * 10^{-1}$	$4.67 * 10^{-6}$	$2.37 * 10^{-2}$
2	$3.53 * 10^{-2}$	$1.16 * 10^{-1}$	$5.27 * 10^{-2}$	$5.86 * 10^{-3}$	$2.30 * 10^{-1}$	$5.28 * 10^{-6}$	$2.20 * 10^{-2}$
3	$3.00 * 10^{-2}$	$1.09 * 10^{-1}$	$5.58 * 10^{-2}$	$5.44 * 10^{-3}$	$2.34 * 10^{-1}$	$8.17 * 10^{-6}$	$2.30 * 10^{-2}$
4	$3.45 * 10^{-2}$	$1.14 * 10^{-1}$	$5.54 * 10^{-2}$	$5.76 * 10^{-3}$	$2.62 * 10^{-1}$	$6.28 * 10^{-6}$	$2.20 * 10^{-2}$
5	$2.67 * 10^{-2}$	$1.11 * 10^{-1}$	$6.26 * 10^{-2}$	$7.15 * 10^{-3}$	$2.23 * 10^{-1}$	$7.17 * 10^{-6}$	$2.26 * 10^{-2}$
1	$6.31 * 10^{-1}$	$6.42 * 10^{-1}$	$5.65 * 10^{-1}$	$5.56 * 10^{-1}$	$7.67 * 10^{-1}$	$5.52 * 10^{-1}$	$5.59 * 10^{-1}$
2	$6.32 * 10^{-1}$	$6.72 * 10^{-1}$	$5.86 * 10^{-1}$	$5.66 * 10^{-1}$	$7.45 * 10^{-1}$	$5.70 * 10^{-1}$	$5.88 * 10^{-1}$
3	$6.20 * 10^{-1}$	$6.20 * 10^{-1}$	$5.67 * 10^{-1}$	$5.45 * 10^{-1}$	$7.80 * 10^{-1}$	$5.41 * 10^{-1}$	$5.52 * 10^{-1}$
4	$5.92 * 10^{-1}$	$5.89 * 10^{-1}$	$5.26 * 10^{-1}$	$4.87 * 10^{-1}$	$7.65 * 10^{-1}$	$4.91 * 10^{-1}$	$5.29 * 10^{-1}$
5	$6.30 * 10^{-1}$	$6.58 * 10^{-1}$	$5.74 * 10^{-1}$	$5.57 * 10^{-1}$	$7.70 * 10^{-1}$	$5.56 * 10^{-1}$	$5.76 * 10^{-1}$

Table 9: Sobol Sentivity Indicies: First Order (top table) and Total (bottom table). Since the current dynamically changes with time, computations are carried out at 4 different time points $t = 1/4 * t_{max}$, $1/2 * t_{max}$, $3/4 * t_{max}$ and t_{max}. These values are then averaged out and shown in the corresponding columns.

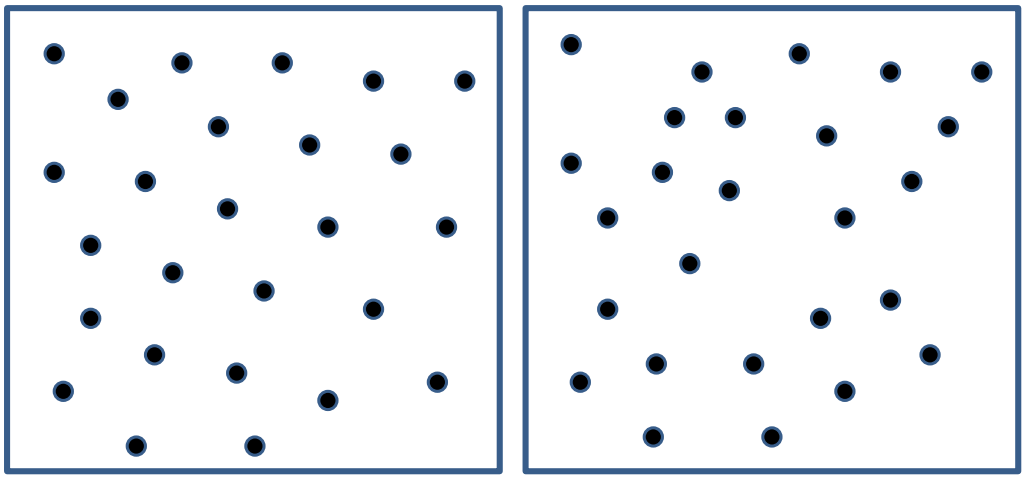

Figure 42: Quasi Monte Carlo (left) versus uniform brute force sampling (right). Brute force methods often lead to clumping, large clusters of points, and sparse regions; while quasi-Monte Carlo methods tends to spread points more uniformly across space.

$[E_0, k_0, C_{dl}, \alpha, R_u]$. The ranking complements a priory insights into the model. Firstly the total current are composed of I_f and I_c. In addition, the magnitude of I_f is primarily dependent on k_0 and thermodynamic equilibrium potential E_0. On the other hand, capacitive current I_c is largely influenced by C_{dl}. Therefore, the output I should be affected mainly by these three parameters.

The first order sensitivity index of α is less than that of both k_0 and E_0. By referring to Figure 6, it is clear that changing α in the range $[0, 1]$ effectively moves the transition state of the redox reaction only in the horizontal direction. However, such horizontal movement does not directly affect the generation of Faradaic component. On the other hand, k_0 directly influences the current magnitude because this parameter represents the intrinsic reaction rate at the formal potential. Furthermore, the relative position between the transition state and product, which also affects the Faradaic current, is decided by the magnitude of E_0. Therefore, k_0 and E_0 should have a larger influence on I_f than α, which is reflected in their relative values of the first order indices.

Algorithm 3.3 The general algorithm for calculating $SI^{First\,Order}$ and SI^{Total} using Sobol sequencing

Initialize N_{Sample}
Generate matrix of size $(N_{\text{Parameter}}, 2 * N_{\text{Sample}})$ using Sobol sequence function
for $i = 1 : 2 : 2 * N_{\text{Sample}} - 1$ **do**
  Select every two columns from the matrix and form two vectors of parameters from these columns
  Pick either of the columns and calculate the functional values $f(x)$
  Accummulate the value $f(x)$ to variable Sum and $f^2(x)$ to variable $SumofSquare$

  for Each Parameter **do**
    Replace the Parameter in the first vector with the corresponding value from the second and form a new vector
    Calculate the new function $f(x_{\text{new}})$
    Calculate the first variance $1/2 * (f(x) - f(x_{\text{new}}))^2$
    Accummulate the previously calculated value to $FirstVarianceSum$
    Keep the Parameter and replace the others in the first vector with corresponding values from the second and form a new vector
    Calculate the new function $f(x_{\text{new}})$
    Calculate the second variance sum $1/2 * (f(x) - f(x_{\text{new}}))^2$
    Accummulate the previous calculated value to $SecondVarianceSum$
  end for
end for
Calculate the mean $f_0 \rightarrow Sum/N_{\text{Sample}}$
Calculate the variance $D \rightarrow SumofSquare/N_{\text{Sample}}$
Calculate the first order index $SI^{\text{First Order}} \rightarrow FirstVarianceSum/D$
Calculate the total index $SI^{\text{Total}} \rightarrow 1 - SecondVarianceSum/D$
Post processing sensitivity indicies and plot in column diagram

Because the first order index for R_u is considerably smaller than other indices, this parameter is interpreted as insignificant in comparison to other parameters. Consequently under this circumstance, R_u can be ignored from the model formulation. Furthermore the insignificant effect of R_u was confirmed in Figure 41, but this applies to only moderate range $R_u < 1000\,\Omega$ (Table 7). Had a larger upper bound been chosen (e.g. $5000\,\Omega$), R_u would have had a more significant influence on the output and the corresponding 1^{st} order index would have become larger. In addition, the elimination of R_u is not entirely theoretical but relies on a careful design of experiments. Firstly, a sufficient amount of supporting electrolytes would help reduce the solution resistance. Secondly, a reasonably small size electrode was used, thus the current magnitude is smaller and Ohmic drop IR_u becomes negligible.

From the bottom half of Table 9, it is clear that there is a strong interaction between parameters because their numerical values are considerably larger than the corresponding first-order counterparts. However, it is not possible at this stage to infer exactly which pairwise interactions are most significant.

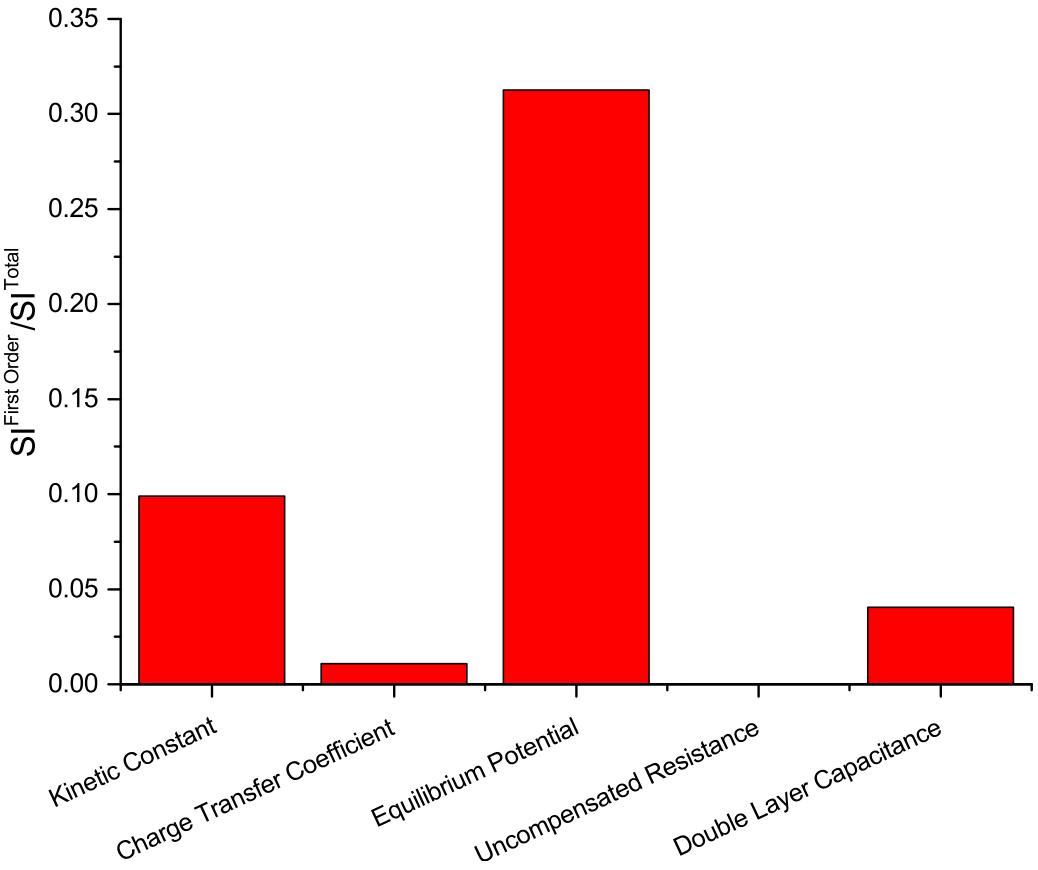

Figure 43: The ratio of $SI^{First\,Order}/SI^{Total}$ as another useful index to decide and rank the parameters in a given model. For Butler-Volmer, the orders are $[E_0, k_0, C_{dl}, \alpha, R_u]$, the same as concluded from Table. The ratio for the uncompensated resistance is virtually zero, thus indicating this parameter's insignificance in the model (Table 9)

The previous ranking of parameters can also be obtained by calculating the respective ratio between the first order and the total indices. A larger ratio implies that the parameters contribute more to the index than its interaction components, and therefore assumes a higher ranking. Figure 43 plots the ratio for each parameter and numerical comparisons reveal the same parameter ranking as discussed above. As a cautionary note, the sensitivity indices should not be viewed as absolute quantities,

but rather serve as measures of relative importance of the associated parameters in each model.

To summarize, this section illustrates the application of Sobol sensitivity analysis to Butler-Volmer model. The main outcomes are i) ranking of the parameter set and ii) elimination of the solution resistance. The second result was aided by experimental choices of adding supporting electrolytes and using small electrode areas. In post-analysis, the most significant parameter set is determined to be $[E_0, k_0, C_{dl}, \alpha]$. However, at this point any existing correlations are not known. Despite this fact, as the next section shows, these parameters are still estimable.

3.4 Sensitivity Equation Approach for Parameter Inversion

This section continues the analysis from section 3.3 above, with the aim to determine the parameters in the $[E_0, k_0, C_{dl}, \alpha]$ set. The work chose to by-pass the estimability study and proceed towards the estimation process for two practical reasons. Firstly, practitioners are often more interested in the latter than the former. Secondly, as fundamental mathematics shows, they two share similar framework. In addition, since the current parameter set is small, these parameters are expected to be all estimable.

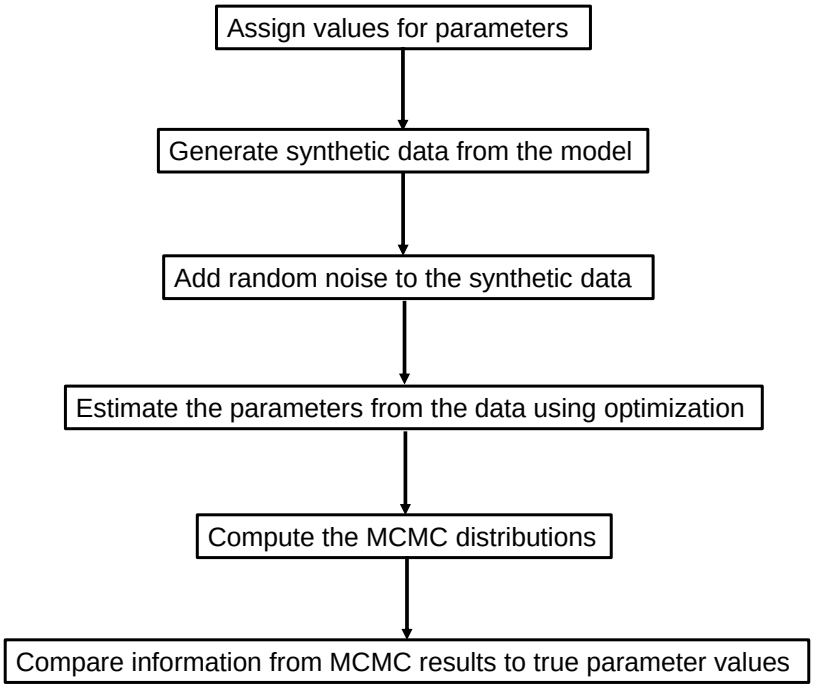

Figure 44: Summary of steps for model-based parameter estimation and MCMC statistics calculation. The first 4 steps are carried out in this section and the last 2 is completed in the next section

The estimation problem carried out in this section is theoretical in nature. Numerical data are first generated from an original parameter set and random noises are added to mimic experimental conditions. Estimation (or inversion) process is thereafter applied in order to recover the original set (Figure 44).

The estimation process illustrates that it is possible to recover parameters of inter-

est from a single data set, which is a useful capability since performing experiments that can yield the most meaningful information is highly desirable. In addition, this process also stresses the issue of selecting models which adequately describes real data since a bad model returns poor information, no matter how sophisticated the estimation process.

In this section, an automated method based on sensitivity equations is implemented. This choice stems from the fact that Butler-Volmer model is both continuous and analytical. The problem was earlier tackled via Kalman filter approach [169]. The method starts with an initial guess of the parameters and then dynamically updates them as more information (e.g. data points) becomes available. After the data has been taken into account, the final solution is the stationary state. On the other hand, the sensitivity equation is a more holistic approach since all the data are used at each estimation step.

It is also important to note the role of heuristic optimization. Heuristic methods are based on well-known rules-of-thumb that practitioners use to manually adjust system parameters until a reasonable fit is achieved. Although automated approaches are mathematically rigorous and faster, they are not always guaranteed to work with real complex data. Consequently, heuristics still plays an important role when guiding the optimization search.

Parameters	True Value	Units	Comment
D_O	$5.4 * 10^{-6}$	cm^2/s	Assumed known value
D_R	$7.6 * 10^{-6}$	cm^2/s	Assumed known value
k_0	0.001	cm/s	To be estimated
α	0.65	$-$	To be estimated
E_0	0.25	V	To be estimated
R_u	500	Ω	Ignored from the model
C_{dl}	50	$\mu F/cm^2$	Included but not estimated
$\sigma^2_{current}$	10^{-8}	A	Gaussian Noise Variance

Table 10: Parameter values used to generate the synthetic data. Uncompensated resistance is neglected from the model as concluded in Section 3.3. To keep the generality, diffusivities of species R and O are assumed to be different

The parameter set used to generate the synthetic data are summarized in 10. Firstly, the diffusion coefficients for each species are assumed to be known constants. This assumption is reasonable since such information can be predetermined using other electrochemical methods; for example, the single and double potential steps. Secondly,

the solution resistance (or more precisely the Ohmic drop IR_u) is left out of the model because, as previously shown, its presence does not influence the current response. The same electrode size $A = 0.01\,cm^2$ is used in order to maintain the validity of the approximation. Finally, the double layer capacitance is still included, but the aim of the method is to estimate the main Butler-Volmer parameters $[k_0, \alpha, E_0]$ as accurately as possible without considering detailed variations of C_{dl}. This perspective is significant since other work in the literature often need to approximate C_{dl} via empirical-based methods. Furthermore, simple Gaussian noise is added to the simulated data at each voltage or time point, according to Equation 3.26. The synthetic data is shown in Figure 45.

$$I_{synthetic} = I_{simulation} + N(0, \sigma^2_{current}) \tag{3.26}$$

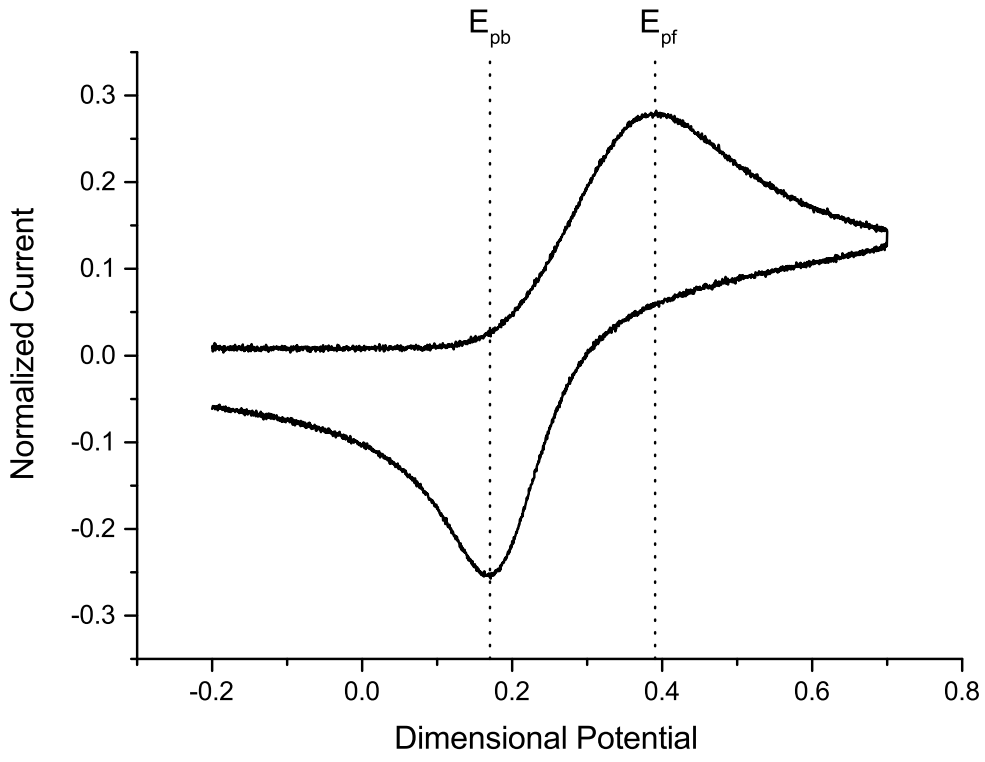

Figure 45: Synthetic cyclic voltammogram used in an estimation process. Gaussian noise is added to the clean data as described in Equation 3.26. The current is normalized by using the expression 2.45 but the voltage is left dimensional (V) to facilitate later discussion

The estimation method is outlined below, starting with the original diffusion equation:

$$\frac{\partial c_i}{\partial t} = D_i \frac{\partial^2 c_i}{\partial x^2} \tag{3.27}$$

and the parameter set is $\theta = [k_0, \alpha, E_0]$ with $\theta_1 = k_0$, $\theta_2 = \alpha$, $\theta_3 = E_0$. In addition, the variables c_i are called the state variables, differentiating the state variables with respect to each parameter θ_i, $i = 1, 2, 3$ which leads to the equation:

$$\frac{\partial s_{R,\theta_i}}{\partial t} = D_i \frac{\partial^2 s_{R,\theta_i}}{\partial x^2} \tag{3.28}$$

$$\frac{\partial s_{O,\theta_i}}{\partial t} = D_i \frac{\partial^2 s_{O,\theta_i}}{\partial x^2} \tag{3.29}$$

with sensitivity variables, defined as follows:

$$s_{c,\theta_i} = \frac{\partial c}{\partial \theta_i} \tag{3.30}$$

Finally, BCs are required for system of Equations 3.28 and 3.29. This is achieved by simply differentiating the Butler-Volmer boundary conditions of Equation 3.27. The gradients of the current with respect to θ_i and used in an optimization procedure at a later time. Explicit calculations are given in Equations 3.31- 3.33:

$$\frac{1}{nFA}\frac{\partial I_f}{\partial k_0} = \frac{k_f}{k_0}(c_R)_{x=0} - \frac{k_b}{k_0}(c_O)_{x=0} + k_f(s_{c_R,k_0})_{x=0} - k_b(s_{c_O,k_0})_{x=0} \tag{3.31}$$

$$\frac{1}{nFA}\frac{\partial I_f}{\partial \alpha} = (k_f(c_R)_{x=0} - k_b(c_O)_{x=0})\frac{-nF(E-E_0)}{RT} + k_f(s_{c_R,\alpha})_{x=0} - k_b(s_{c_O,\alpha})_{x=0} \tag{3.32}$$

$$\frac{1}{nFA}\frac{\partial I_f}{\partial E_0} = (-k_f(c_R)_{x=0}\frac{(1-\alpha)nF}{RT} + k_b(c_O)_{x=0}\frac{\alpha nF}{RT}) + k_f(s_{c_R,E_0})_{x=0} - k_b(s_{c_O,E_0})_{x=0} \tag{3.33}$$

and because the state variables are constant in the bulk term, then Equation 3.34 applies for each c_i:

$$(s_{c,\theta_i})_{x\to\infty} = 0,\ i = 1, 2, 3 \tag{3.34}$$

Since the total current is the sum of I_f, I_c and I_c which is independent of θ:

$$\frac{\partial I}{\partial \theta_i} = \frac{\partial I_f}{\partial \theta_i}$$

which are already calculated. Finally, for the sake of completion, the gradient w.r.t C_{dl} is written as 3.35 though it is not used in the subsequent calculations:

$$\frac{\partial I}{\partial C_{dl}} = \frac{\partial I_c}{\partial C_{dl}} = v_{scan} A \tag{3.35}$$

once the derivatives are calculated and grouped together to form the corresponding Jacobian J. Each corresponding row of J contains the derivatives with respect to θ. Then the Levenberg-Marquardt formula is used to calculate the correction vector, namely:

$$\triangle\theta = (J^T J + \lambda I)^{-1} J^T (Y^* - Y) \tag{3.36}$$

and the parameters are updated as follows:

$$\theta = \theta + \kappa \triangle\theta \tag{3.37}$$

In the formula 3.36, $Y*$ and Y are respectively the column vectors containing the synthetic data and numerical values, which are calculated using the current parameter set. In addition, the dimensions of J and vectors Y^*, Y should be compatible so that the matrix operations in 3.36 work. The constant κ serves as an adjustment factor so as to keep θ physically bounds. Exact values are problem-dependent, but a conservative value of 0.01 is found to be adequate for this work.

When $\lambda = 0$, Levenberg-Marquardt formular reduces to the Newton-Raphson equation described in chapter 2. However, the former is preferred because the inclusion of the term λI generally permits the calculation of $\triangle\theta$ even when J is close to singular. Without such terms, the matrix inversion step could lead to large numerical values in the correction vector and consequently can interfere the updating step 3.37. In addition, Levenberg-Marquardt is computationally economical in the sense that it requires only upto the first order derivative (i.e. the Jacobian J) rather than both J and second order derivatives $Hessian$ as in Newton method. In fact, it is an illustrous example of Gauss-Newton or more generally quasi-Newton optimization.

To speed up the convergence towards the solution, one starts with a large value of λ (say 100). Then after every iteration step, the (non-weighted) sum of square errors

(SSE) are calculated:

$$SSE = (Y^* - Y)^T (Y^* - Y) \tag{3.38}$$

If SSE is smaller after each parameter update, then λ is reduced (e.g. by a fixed constant) and the iteration keeps going until convergence or maximum number of iteration is reached. Figure 46 summarizes the solution process combining the sensitivity equations 3.31-3.33 and optimization procedure 3.36-3.38. Note that since the structures of PDEs for state and sensitivity variables are alike, one might opt to solve them all at once. Consequently, the matrix size in that case would be $(5N_{variables})^2 = 25N_{variables}^2$. On the other hand, if the equations are solved sequentially as in Figure 46, the matrix size is reduced to only $N_{variable}^2$. In this work, the second approach is preferred.

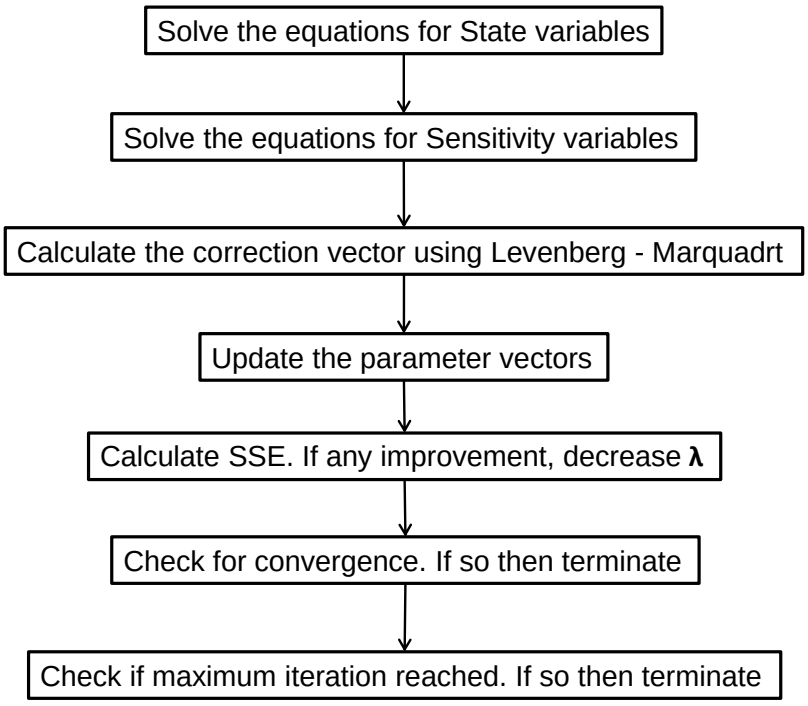

Figure 46: Estimation algorithm using the sensitivity approach as described in Equations 3.31-3.38

Because the estimation process is iterative, a good initial guess is required. Since it

Initial Value	Final Value	Starting SSE	Optimized SSE
$[0.01, 0.5, 0.23]$	$[0.00144, 0.705, 0.234]$	9.27	0.91
$[0.01, 0.5, 0.24]$	$[0.00135, 0.662, 0.245]$	9.70	0.508
$[0.01, 0.5, 0.25]$	$[0.00129, 0.607, 0.257]$	10.17	0.58
$[0.01, 0.5, 0.26]$	$[0.00125, 0.545, 0.268]$	10.69	1.13
$[0.01, 0.5, 0.27]$	$[0.00123, 0.482, 0.278]$	11.34	1.99

Table 11: Initial guesses and final optimal sets. In Levenberg-Marquardt, $\kappa = 0.01$, maximum iteration is set to 200 and λ is decreased by 1.5 everytime SSE is reduced to maintain stability of the updating step 3.37. The orders in each set are $[k_0, \alpha, E_0]$. Since E_0^{guess} is estimated to be about 0.28 from Figure 45 so initial guesses are taken to be smaller than that value. Note that the true values are [0.001, 0.65, 0.25]

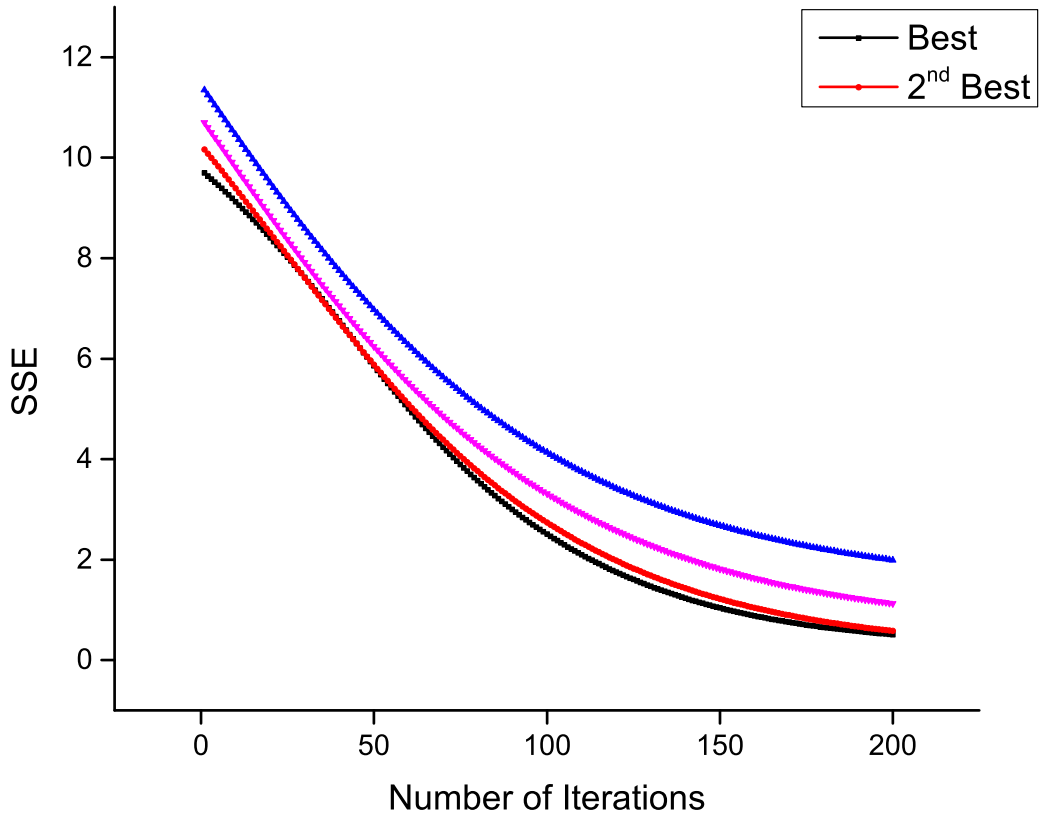

Figure 47: SSE is progressively minimized as the number of iterations increase.At the final iteration, the best two initial sets yield SSE values significantly smaller in comparison to the rest

is not possible to quantify the goodness of a guess, a common method is to use multi-starting points and record the best solution. Furthermore, physical intuition is also useful in constructing these initial guesses. For the current problem, this construction process is described as below.

From Sobol analysis that the initial guess of E_0 influences the outcome of the estimation process most significantly. For fast electrochemical kinetics, E_0 can be approximated by the potential at the mid-point between the two peaks:

$$E_0^{guess} = (E_{pf} + E_{pb})/2 \tag{3.39}$$

however, the wide peak separation (Figure 45) signifies slower kinetics and this mid-point value should therefore be larger than E_0. For k_0, a large value (i.e. fast kinetics) is simply assumed. Furthermore, for the charge transfer coefficient, a symmetrical process is initially chosen , i.e. $\alpha = 0.5$. Table 11 summarizes the initial guesses and results of applying 46 to the synthetic data generated. Figure 47 shows the decrease of SSE as a function of iteration number. Using the original values listed in Table 10, rows 2 and 3 of Table 11 differ from these correct values by $[35\%, 1.85\%, 2\%]$ and $[29\%, 6.61\%, 2.8\%]$ respectively. In addition to SSE, based on the parameter ranking result from Sobol's analysis, row 2 contains the better result because the parameter E_0 is closer to the presummed true value. In practice, the true values of these parameters are rarely known, so a good rule-of-thumb is to average the best 2 results.

In conclusion, the above results show that it is possible theoretically to recover $[k_0, \alpha, E_0]$ to a fair degree of accuracy. This can be accomplished using only a single set of data and neglecting detailed knowledge about the capacitive current. At this point, it is verified that $[k_0, \alpha, E_0]$ parameters are estimable as suggested at beginning of this section. However, due to inherent non-identifiability, all these estimations are obtained with some degree of error. Finally depending on circumstances, one might be interested in parameter C_{dl} but the above analysis emphasizes role of primary parameters in Butler-Volmer model. To complete the experimental design study for a diffusional system, the final section considers the computation of parameter statistics via MCMC Bayesian-framework.

3.5 MCMC Simulations

Section 3.4 shows that it is possible to recover the Butler-Volmer model parameters from a single set of data using optimization approach. The underlying assumption here is that each parameter is a single-valued scalar which minimizes SSE function. Yet most optimization routines only produce point estimates in parameter space, namely a single set of parameters which optimize the error function SSE, where each parameter has an associated distribution or interval. Such information is also more representative and informative than the original point estimate.

In the Levenberg-Marquardt equation, co-variances and standard deviations are determined by using the optimal SSE. If a Jacobian matrix is available, these credible intervals can be constructed via the use of t-distribution[143, 170]. It is noted that these calculations require a linear model, which is usually achievable by linearizing the current non-linear model around the optimum set.

Another popular approach is based on Bayesian inference framework [171]. Equation 1.38 states that:

$$\pi(\theta_i|data) \propto p(data|\theta)\,\pi_i(\theta_i)$$

for each parameter θ_i. If the error $\epsilon = y_i^{data} - y_i^{model}$ is assumed to be normally distributed with constant variance σ^2, the maximum likelihood estimate (MLE) $p(data|\theta)$ is usually expressed as:

$$p(data|\theta) \propto (\sigma^2)^{N_{data}/2}\, exp(-\frac{1}{2\sigma^2}\sum_{1}^{N_{data}}(y_i^{data} - y_i^{model})^2) \tag{3.40}$$

recognizing the summation as the SSE function, this simplifies to:

$$p(data|\theta) \propto exp(-\frac{SSE}{2\sigma^2}) \tag{3.41}$$

The overall objective is to compute $\pi(\theta_i|data)$ given the MLE 3.41 and prior distributions $\pi_i(\theta_i)$. Since no analytical formula is generally available for the posteriors, Monte Carlo calculations is often employed to calculate $p(data|\theta)$. However, there are more options in sampling parameter samples from the priors $\pi_i(\theta_i)$. A reliable methodology is based on Markov Chain sampling [172].

Considering each collection θ as a "state", in Markov Chain theory, $\theta^{(n+1)}$ is dependent only on the previous state $\theta^{(n)}$ where n denotes the time step or sampling

number. Theoretically after sufficient number of sampling steps, θ would converge to a stationary state which can be viewed as the representative of the chain $\theta^{(i)}$. It is computationally efficient to use Markov Chain framework because i) only the most recent state is relevant and ii) the chain is guaranteed (at least in theory) to converge, comparing to the brute-force strategies in which the samples are completely randomized at each iteration n.

Algorithm 3.4 The Random Walk Metropolis Algorithm to calculate the posterior distributions $\pi(\theta|data)$. Markovian property is assumed so that θ_{new} is sampled only from θ_{old} at each step

Initialize the set θ_* which minimizes the SSE. θ_* can be taken directly from the optimization routine
Estimate the variance σ^2
Calculate $SSE_{old} = SSE(\theta_*)$
Calculate the Jacobian J either numerically or analytically. Using the sensitivity approach, J can be taken directly from the final step
Calculate the Covariance Matrix $C = (J^T J)^{-1} * \sigma^2$
Decompose C using Cholesky factorization $C = R^T * R$
for $n = 1 : N_{\text{Chain Length}}$ **do**
  Sample vector $z = [z_i], i = 1, 2, ..., N_{parameter}$ and $z_i \sim N(0, 1)$ ($N(0, 1)$ is the normal distribution with mean 0 and variance 1
  Compute the new parameter set $\theta_{\text{new}} \rightarrow \theta_{\text{new}} + R * z$
  Sample a random variable u from the uniform distribution $U(0, 1)$
  Solve the forward problem using θ_{new}
  Calculate SSE_{new} using data from the forward problem above
  Calcuate Acceptance Probability $P_{\text{accept}} = min(1, exp(-\frac{1}{2}\frac{SSE_{new} - SSE_{old}}{\sigma^2}))$
  if $u < P_{accept}$ **then**
    Set $\theta_{\text{old}} \rightarrow \theta_{\text{new}}$
    Set $SSE_{\text{old}} \rightarrow SSE_{\text{new}}$
    Set $\theta^{\text{n}} \rightarrow \theta_{\text{new}}$
  else
    Set $\theta^{\text{n}} \rightarrow \theta_{\text{old}}$
    Set $SSE_{new} \rightarrow SSE_{old}$
  end if
end for

The basic algorithm is presented in Algorithm 3.4. This algorithm is largely based on reference [152] and often refereed to as the "Random Walk Metropolis". The actual data variance is assumed to be unknown and can be estimated by the following formula:

$$\sigma^2_{est} = \frac{SSE(\theta_*)}{N_{data}}$$

which can be easily seen by differentiating 3.40 with respect to σ^2 and setting the derivative to 0. A slightly different computation is used in this work:

$$\sigma^2_{est} = \frac{SSE(\theta_*)}{N_{data} - N_{parameter}}$$

and when $N_{data} \gg N_{parameter}$ (such as the present case) then the two formulae agree with almost no significant numerical difference.

In Algorithm 3.4, the sampling steps assumes the new sample $\theta^{(n+1)}$ is normally distributed around the previous set $\theta^{(n)}$. This choice implies that each individual parameter has a unimodal distribution. The priors (normal distributions in this case) will consequently lead to posteriors which are also single modes. This fact illustrates the importance of gaining some external knowledge about the parameter before proposing its corresponding prior. For example, a parameter with a potential bi-modal distribution could have its priors constructed from a mixture of two normal distributions 3.42 (p is a scalar factor satisfying $0 < p < 1$):

$$p\, N(\mu_1, \sigma^2) + (1-p)\, N(\mu_2, \sigma^2) \tag{3.42}$$

which signifies that the parameter has two means. However, it is clear that multi-modal cases will struggle to locate a sensible start θ_* in the optimization routine. Furthermore, the physical mechanism for the existence of such multi-mode behaviour must also be explained. The current work opts for single modal distributions for each parameter under consideration.

The Algorithm 3.4 uses a chain length of $N_{Chain\,Length} = 50000$. The bottle neck is probably due to the repetition when solving the diffusion equations with every new set of parameters generated. The starting sample are taken from row 2 of Table 11 along with relevant information of Jacobian matrix and SSE_{old}. An important issue with any post-MCMC calculations is to decide a "burn-in" length. This means a certain number of samples, especially those at the beginning of the chain need to be discarded. This practice reduces the auto-correlation so that later samples are not influenced by earlier ones. Furthermore, by using a burn-in length, the focus is placed on the chain section exhibiting convergent behavior. In the current case, 10% or 5000 samples are discarded. The practice of "chain thinning", which saves every fixed number of samples rather than the whole chain, is not pursued in this study because chain burn-in is believed to be more important.

The computational results are summarized in Figures 48-50. The histogram in each

figure confirms that the convergent parameter sample is significantly closer to their original values. The corresponding means and credible intervals are included in Table 12. In addition, the strength of correlation among parameter pairs is visualized in scatter diagrams 51- 53. While there are weak correlations in pairs (k_0, α) and (k_0, E_0), there is a strong negative correlation between E_0 and α. The observation is confirmed by calculating the corresponding correlation efficient, which is approximately -0.97. Although some of the credible intervals did not contain the true values, the differences between the means and the true values are all within 6%.

Parameter	Mean	2.5% Quantile	97.5% Quantile	95% Credible Interval
k_0	0.00104(6)	0.00103(4)	0.00105(8)	$[0.00103, 0.00106]$
α	0.652(8)	0.652(0)	0.653(7)	$[0.652, 0.654]$
E_0	0.250(4)	0.249(8)	0.250(9)	$[0.250, 0.251]$

Table 12: 95% Credible Intervals for the Butler-Volmer model. Mean values are computed from the burn-in chain. Note that the mean value of each parameter is considerably closer to the true value [0.001, 0.650, 0.25] as listed in Table 10

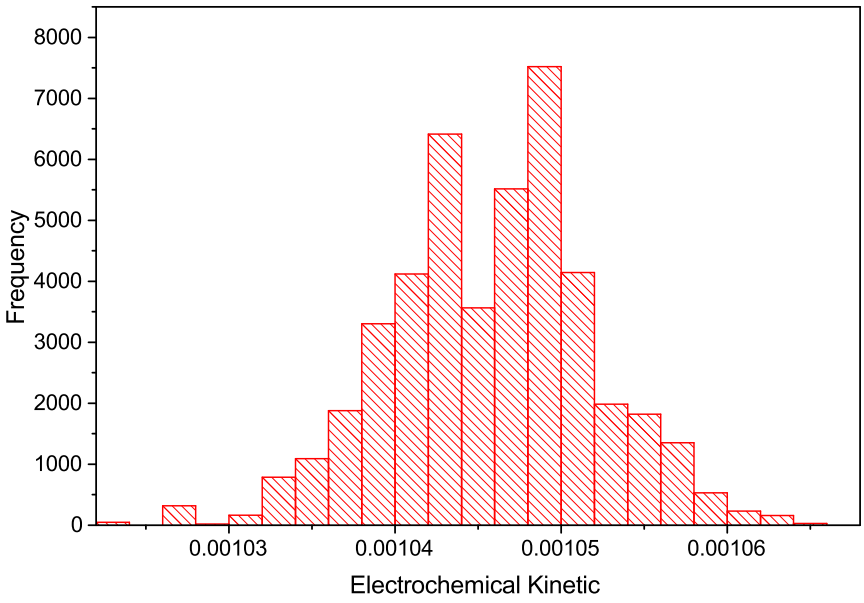

Figure 48: Histogram for k_0. Note that only data from chain no. $5000 - 50000$ are used here. The rest are discarded during burn-in process as described in the text

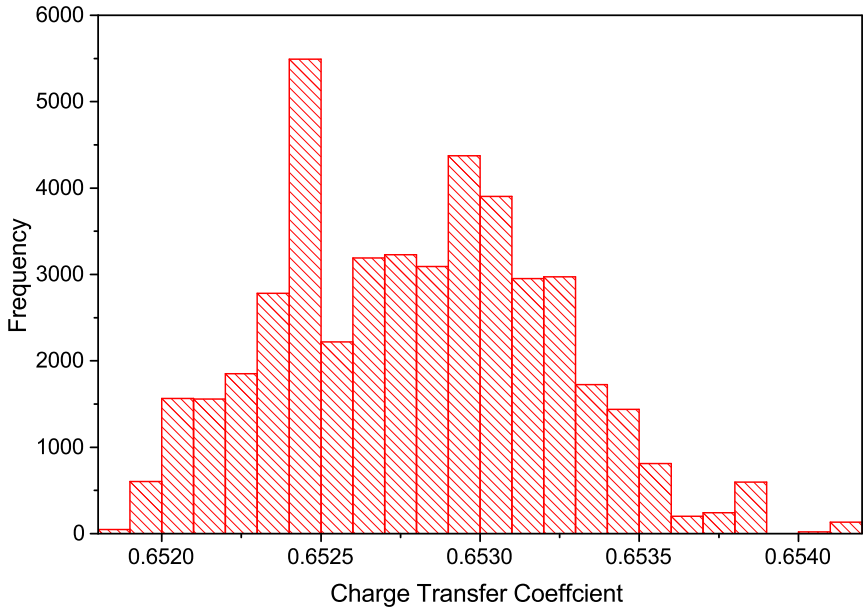

Figure 49: Histogram for α. Data from chain no. $5000 - 50000$ are used

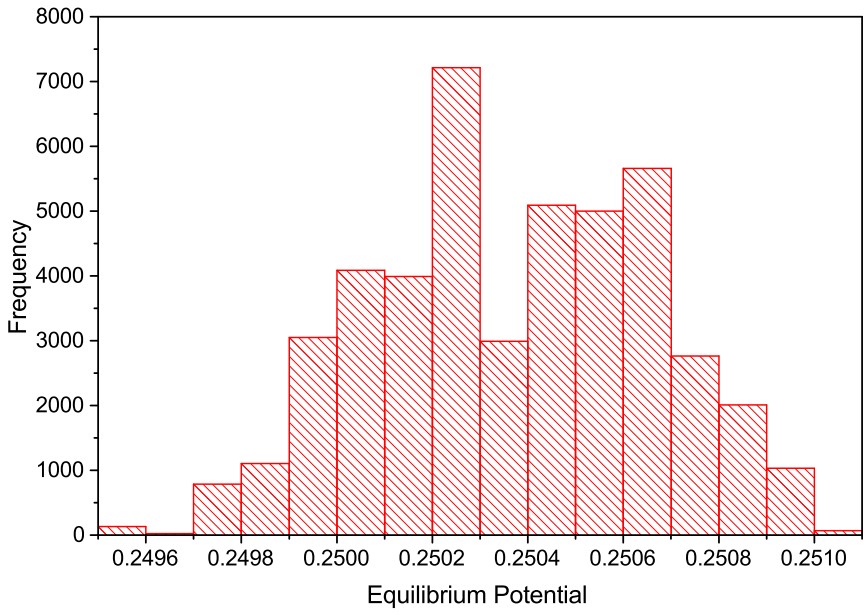

Figure 50: Histogram for E_0. Data from chain no. $5000 - 50000$ are used. The majority of values distribute around 0.25, which is the assumed true value for E_0

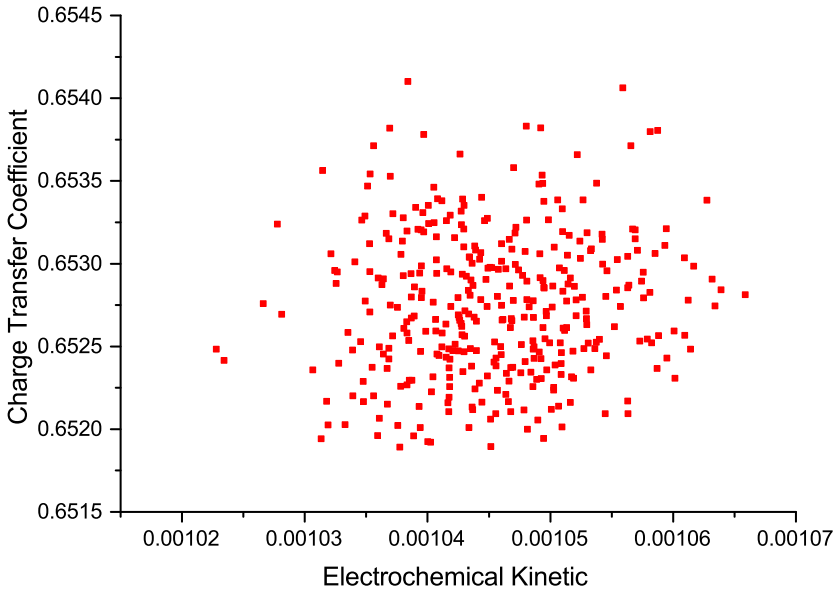

Figure 51: A scattering plot for (k_0, α) shows a weak statistical correlation between the two parameters

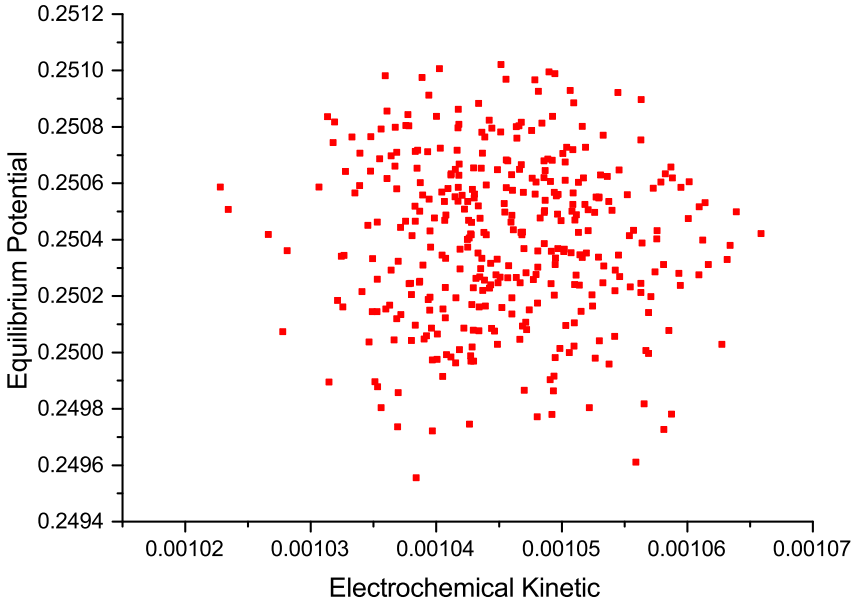

Figure 52: A scattering plot for (k_0, E_0) also indicates a very weak correlation. For non-identifiable situations, higher k_0 should correlate with higher E_0 (i.e. a positive correlation)

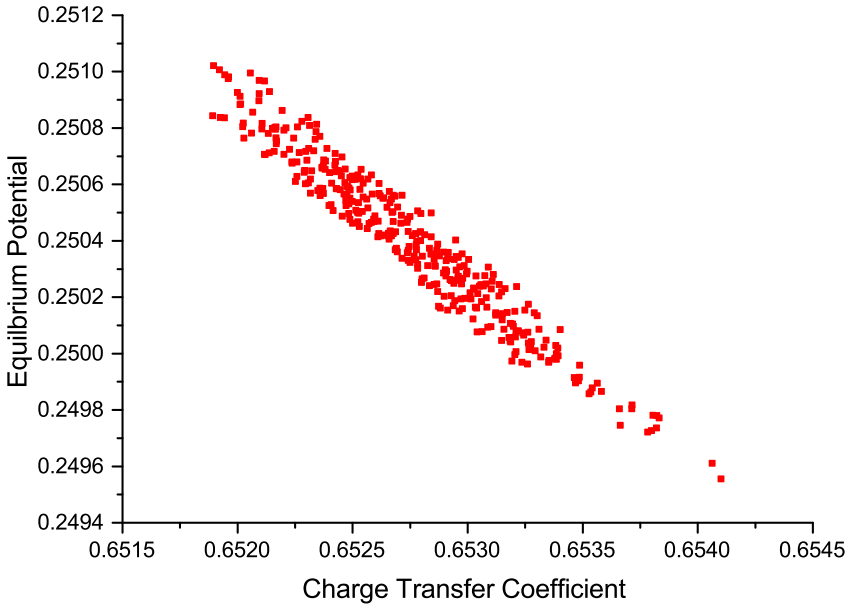

Figure 53: Scatter plot for (α, E_0) indicates a negative correlation

To improve the plain Random Walk Metropolis, other methods have been proposed. For example, the adaptive Metropolis-Hasting MCMC updates its co-variance matrix in the proposal distributions at each iteration in Algorithm 3.4. A potential issue of using the adaptive version is Markovian properties do not apply for the samples, which could result in incorrect convergence towards non-stationary state. For the current problem, the application of adaptive MCMC does not lead to significant improvement. Despite that fact, those methods could lead to better parameter distributions and improve correlations between parameter pair, especially (k_0, E_0) as discussed in Figure 52.

Before closing the discussion, it is noted that Monte Carlo method also provides a possible approach to the problem of model discrimination. Such problems are commonly encountered in the biological area where two models produce similar physical responses and a reasonable question is which one is physically representative. In electrochemistry, the same question was illustrated in [173] to differentiate ECE and $DISP1$ reaction schemes, via comparisons of current responses and exploitation of subtle differences between them. Another criterion to decide this preference is based on Bayesian factor (BF), as demonstrated in [139, 174]. The idea is straightforward, given two competing models M_1 and M_2 along with corresponding parameter sets

θ_1, θ_2 and identical vector outputs y, the BF is defined as:

$$BF = \frac{p(y|M_1)}{p(y|M_2)} = \frac{\int p(y|\theta_1, M_1)p(\theta_1|M_1)d\theta_1}{\int p(y|\theta_2, M_2)p(\theta_2|M_2)d\theta_2}$$

Essentially, BF averages out vector y of each model over the specified parameter space. Under equal prior preference, if $BF \gg 1$ then M_1 is posterior favored and the reverse conclusion applies when $BF \ll 1$. Factor $p(y|\theta_1, M_1)$ is computed from the same likelihood function 3.41. Future work therefore might reconsider ECE and $DISP1$ problem from this approach.

3.6 Chapter Conclusion

This chapter evaluates, from a theoretical perspective, the use of linear signals as an experimental design variable. By fixing the mass transport mode under diffusion control, several aspects of Butler-Volmer kinetics were investigated.

Firstly, the model was extended to include the effects of solution resistance and double layer capacitance. The proposed solution is the combination of the explicit time formulation and a binary search. The identifiability function, η were then defined and optimized by stochastic sampling. The result shows that different sets can often lead to very similar outputs. The large value of η reveals model non-linearity as well as compensating effects among parameter pairs, which in this case involve primarily (k_0, R_u), (E_0, R_u) and (k_0, E_0). Monte Carlo optimization is employed due to its implementation simplicity. The method further avoids the need for calculating complicated derivatives.

To weigh the importance of each parameter, Sobol sensitivity indices were computed. The results indicate that equilibrium potential, kinetic constant and double layer capacitance (in that order) have the most influence on the the current output. Under the designed condition, namely small electrode areas and highly supporting ionic electrolytes, uncompensated solution resistance is the least significant parameter and consequently eliminated from the model. In addition, quasi-Monte Carlo is applied properly in the sample hyper cube of the parameter space and better approximates the integration.

Using the simplified model, a theoretical problem involving parameter regression was proposed. The solution approach is deterministic, based on sensitivity equations and gradients of the error function. Satisfactory results were obtained: the point-estimate was close to the presumed true value. Thus, even though the model is generally non-identifiable, the parameters are still uniquely estimated. A Bayesian framework was then applied to compute relevant statistics such asparameter means and credible intervals. As a result, the plain Metropolis random walk was implemented and yielded improved final estimates. The method also allowed correlations between parameter pairs to be visually displayed.

The chapter results provide theoretical support for the use of a linear sweep as a tool to retrieve the primary set [k_0, α, E_0] in the Butler-Volmer model, and this fact is illustrated in inversion and MCMC computation steps. It is concluded that the application of this simple signal should yield reliable estimates of these parameters.

In addition, the signal's conceptual simplicity, from both an experimental and simulation perspective, explains its popular use in practice. Another implication from these results is that the use of more complicated signals aims to improve the accuracy of parameter estimates and statistics. However, it is emphasized that in reality, the forward model does not often describe data precisely, which undermines the effectiveness of both simple linear and complex waveforms.

Chapter 4 reconsiders the identifiability problem from a different viewpoint. The linear sweep voltammetry is fixed but the mass transport mode is now modified to include forced convective components. Because the identifiability function measures the one-to-one correspondence between the current output and the model parameters, the chapter's goal is to investigate the influence of hydrodynamics on such correspondences.

Chapter 4

Hydrodynamic Tools for Model Identifiability and Kinetics Analysis

In previous chapters, the dominant mass transport mode was static diffusion, induced by a local concentration difference. Hydrodynamic devices have proved popular due to several reasons. Firstly, forced convection is more easily controlled and the convective flux is several times larger than the diffusion component. Furthermore, these conditions often lead to establishment of the Levich equation, which is analytically useful.

There are various configurations of hydrodynamic devices investigated in the literature: most notably the rotating disk (RDE) and channel (CE) electrodes. The selection of a configuration for a research study depends, to a significant degree, on the ability to analyse the resulting flow pattern in such devices. Traditionally, RDE and CE are the most common because fluid mechanics theory for these devices are well developed and analytically tractable [39].

This chapter has two parts. The first part continues the investigation into the identifiability of Butler-Volmer kinetics using a model of rocking disk electrode (RoDE) - a generalized mechanism of the RDE. A major objective is to compare the identifiability values of RoDE and RDE in the experimental design process and consequently illustrate the role of the geometrical/mechanical factor. Model identifiability, as discussed earlier, measures the one-to-one correspondence between the current output and its respective parameter set. A large identifiability value signifies a poor correspondence and implies difficulties with estimations and larger credible intervals. For Butler-Volmer model, though principal parameters (i.e. k_0, α and E_0) can be estimated as shown in Chapter 3, the added value here is to evaluate in advance the reliability of

such parameter estimates.

The second part introduces a new hydrodynamic tool for studying electrochemical transfer under viscous medium - the rotating drum electrode. Recent literature work has paid special attention to unusual solvent environments such as ionic liquids, which are both highly resistive and viscous. CE is not an ideal device choice, since pumping a viscous solution through a micro-sized channel is usually difficult. As we demonstrate later, a rotating drum device offers a convenient experimental mean and the solvent's effect on the model identifiability is straightforwardly eliminated, which forms the basis for an electron transfer kinetic study using various media.

Regarding the computational aspect, this chapter introduces the simulation software *Comsol Multiphysics*®. This PDE engine is specifically designed to solve common equations in physical sciences and engineering. Its strength lies in the user-friendly interface and a wide selection of libraries for different physics-based simulations. The package is based on Finite Element formulation, whose meshing procedure is completely automated and easily fine-tuned according to user requirements. Furthermore, the software possesses up-to-date and powerful linear algebra solvers, which are the "bread and butter" of any numerical technique. Another major motivation for using *Comsol Multiphysics*® is the availability of the Computational Fluid Dynamics (CFD) module. Because solutions of Navier-Stoke equations are required for diffusion-convection transport 1.4, this module is evidently important and useful.

4.1 The Rocking Electrode - An Investigation

4.1.1 Verification of Levich expression for RDE

The rotating disk is a common hydrodynamic device used in electrochemical studies. In this configuration, the electrode casing is rotated at regular rates and the theoretical limiting current is expressed by Equation 1.21:

$$I_{lim}^{RDE} = 1.55\, FAc_{R0} D_R^{2/3} f_{RDE}^{1/2} \nu^{-1/6} \tag{4.1}$$

The theoretical Levich expression is derived in two steps. Firstly, the velocity profile is analytically approximated by von Karman and Cochran treatment. By considering the section of flow near the electrode surface, the convection-diffusion equation is simplified to a 2^{nd} order differential equation [2]. This equation is straightforwardly integrated to obtain the concentration field around the surface, which in turn permits the derivation of the current from Butler-Volmer expression 2.6.

The software *Comsol Multiphysics*® is first used to validate the relation. The aim of this confirmation step is to ensure an adequate set-up of the physics problem and convergence towards Equation 4.1. This test is common practice as it examines the previously developed in-house codes [66, 98]. Assuming sufficient supporting electrolytes are present, a migration flux in Equation1.7 is ignored. The computational scheme using the software is as follows. Firstly, the velocity field is calculated from the incompressible Navier-Stoke equations using a CFD module. The field is then exported to the convection-diffusion equation with electrochemical boundaries implemented in the dedicated Electrochemistry module. Furthermore, because the problem is rotationally symmetric, only a cross-section is considered (Figure 54).

Simulation parameters are summarized in Table 13. Because r_b is much larger than r_e, the electrode is essentially immersed in infinite solution. The respective boundary conditions are listed in the bottom part of Table 13. Figure 55 shows linear sweep voltammograms at different ω_{RDE}'s. At large polarizing potentials, the total current reaches a steady state, which is proportional to $f_{RDE}^{0.5}$ according to Equation 4.1. This is attributed to the hydrodynamic influence which causes the diffusion layer thickness to remain constant. In addition, capacitive current I_c is ignored due to a combination of a small electrode area ($\sim 2\,\mu m^2$) and slow scan rates (e.g. $10\,mV/s$). For the designed conditions, Sobol analysis from Chapter 3 applies, hence the solution resistance R_u can be ignored from the model.

Name	Symbol	Value	Units	Comment
Electrode Radius	r_e	0.8	mm	-
Holder Radius	r_o	4	mm	-
Beaker Radius	r_b	30	mm	-
Kinetic Rate	k_0	0.008	cm/s	Quasi-reversible reaction
Equilibrium Potential	E_{eq}	0.21	V	-

Boundary	Fluid Dynamic	Mass Transport
Beaker Wall/Bottom	Zero Flux	Zero Flux
Symmetric Axis/Solution Interface	No Flux	No Flux
Electrode Holder	Rotating Condition	No Flux
Electrode Surface	-	Butler-Volmer

Table 13: (Top) Parameter settings in rotating disk simulation. Electrochemical values are for the electron transfer reaction $Fe(CN)_6^{4-} \leftrightarrow Fe(CN)_6^{3-} + e^-$. The capacitive effect is ignored. Diffusion coefficients are assumed to be equal at $0.65 * 10^{-9}\, m^2/s$ in aqueous medium. (Bottom) Respective boundary conditions for fluid and mass transport calculations

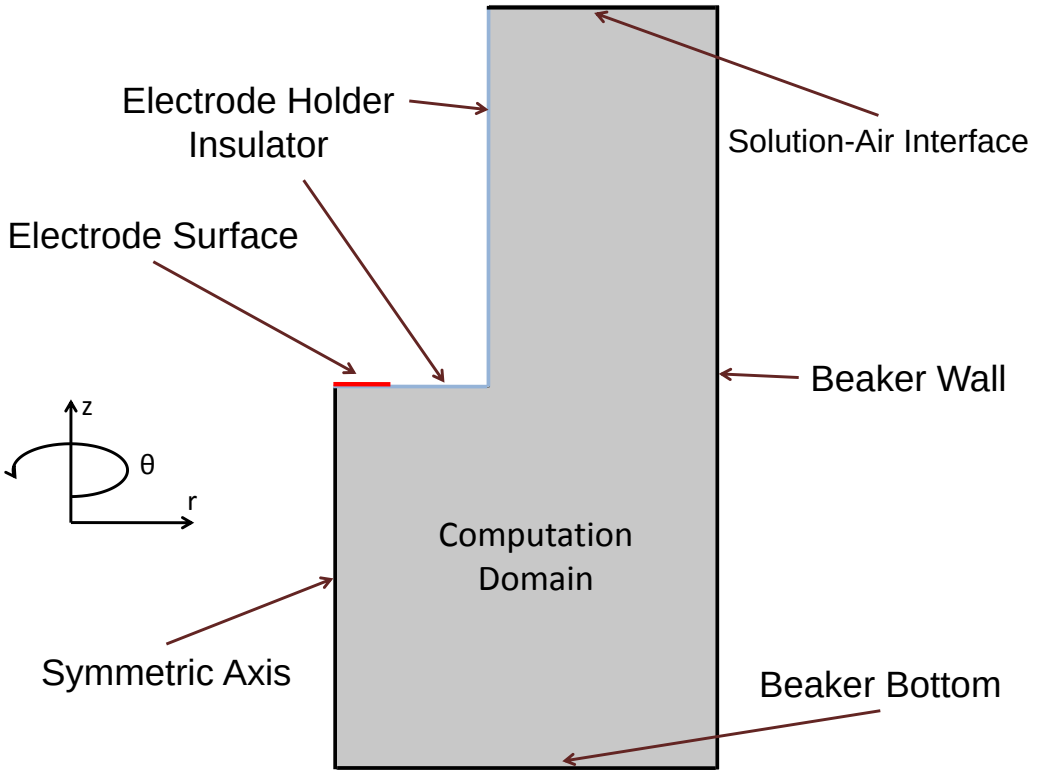

Figure 54: Computational domain for the rotating electrode. The problem is essentially two dimensional due to rotational symmetry around $r = 0$ axis

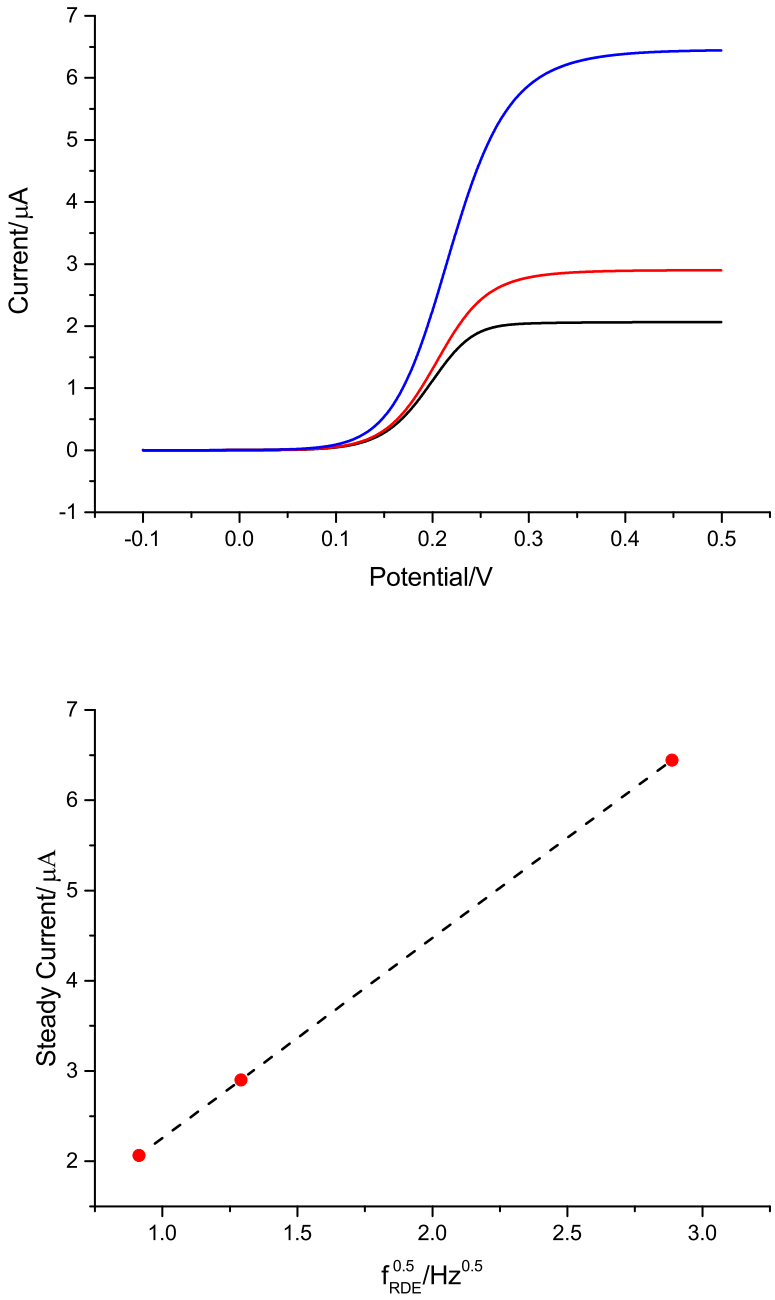

Figure 55: Linear sweep voltammograms for rotating disk electrode at 50 (black), 100 (red) and 500 (blue) rpms under scan rate of $10\,mV/s$ (top) and the steady state currents are proportional to $f_{RDE}^{0.5}$ for rpm in range $50-500$ as confirmed in the Levich relation 4.1

4.1.2 Derivation of Levich expression for the RoDE

The rocking electrode is a generalization of the above configuration. Instead of having a fixed angular speed, the holder's movement is modulated in an approximately harmonical fashion. A schematic drawing of this mechanism is shown in Figure 56. The heart of this construction is the four-bar mechanism [175]. The blue circle is rotated regularly as in the RDE, using the motor assembly. Such motions are then imparted to the red circle via a connecting crank. The red circle then moves back and forth, causing a rocking action. In this representation, the driver crank is L_2 and the rocking driver's crank is L_4. By setting $L_2 = L_4$, crank L_4 motion reduces to the previous regular rotating pattern. Due to the constant acceleration and deceleration of the holder, the flow field is consequently non-steady and time-dependent.

Concept and applications of rocking electrodes were recently introduced into the literature [176, 177].This work focuses on electro-deposition of copper metal and its alloys onto different substrate materials. We demonstrate that such a back-and-forth motion also leads to uniform mass transport effects. Compare this to the rotating electrode, the rocking mechanism does not require the contact brush. In addition, it allows a larger electrode area (to the order of several cm^2) to be used. Thirdly, in electro-deposition, the presence of turbulent flow is noted to help dislodge the air bubbles which impede the deposition process.

This section has two aims. The first goal is to semi-analytically derive the Levich expression for the rocking mechanism. It is evident that this expression is not only useful for analytical purposes but also serves as a first comparison to the rotating disk. In addition, the expression is used as a normalizing factor for computing model identifiability in the following section. This fact is important to ensure the number is completely dimensionless according to Equation 3.11.

Name	Symbol	Value	Units
Distance between supports	L_1	40	mm
Rotating Crank	L_2	7	mm
Connecting Crank	L_3	40	mm
Rocking Crank	L_4	10	mm

Table 14: Geometric lengths used for simulations of rocking mechanism in Figure 56

Because the electrode is now attached to the rocking section of the equipment, it is necessary to derive a relation between the rocking angular speed $\omega_4 = d\theta_4/dt$ and $\omega_{RDE} = \omega_2 = d\theta_2/dt$. Using the vector identity:

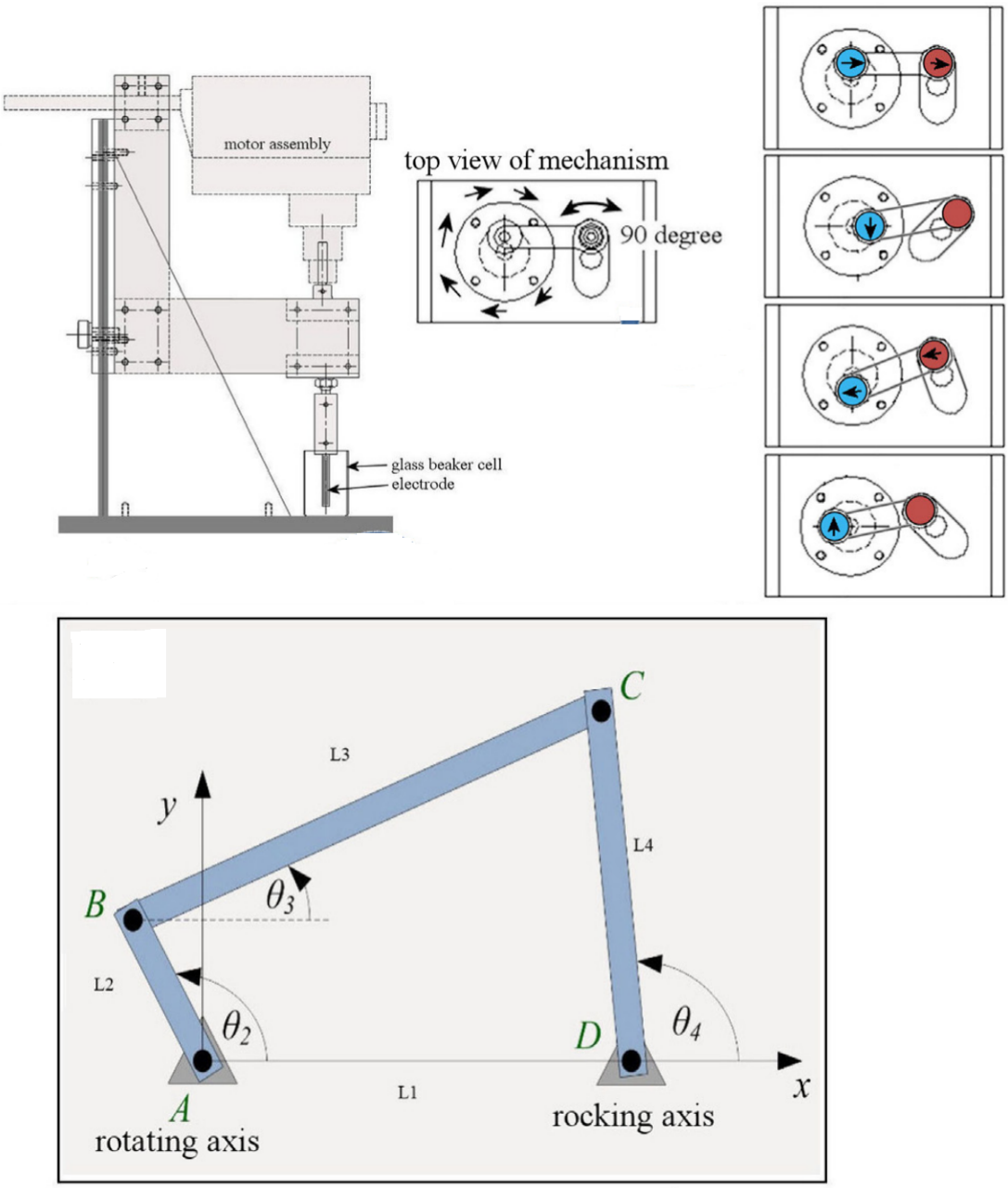

Figure 56: A sketch of the equipment and its rocking mechanism (top right) and the simplified four-bar mechanism used to approximate movements of the cranks (bottom)

$$\overrightarrow{AB} + \overrightarrow{BC} + \overrightarrow{CD} + \overrightarrow{DA} = \overrightarrow{0}$$

and projecting the above equation onto x and y axis respectively, one obtains:

$$L_2 cos\theta_2 + L_3 cos\theta_3 - L_4 cos\theta_4 - L_1 = 0$$

$$L_2 sin\theta_2 + L_3 sin\theta_3 - L_4 sin\theta_4 = 0$$

taking the time derivatives of these equations leading to:

$$-L_2\omega_2 sin\theta_2 - L_3\omega_3 sin\theta_3 + L_4\omega_4 sin\theta_4 = 0$$

$$L_2\omega_2 cos\theta_2 + L_3\omega_3 cos\theta_3 - L_4\omega_4 cos\theta_4 = 0$$

and after simple manipulations, the connecting and rocking angular velocities are:

$$\omega_3 = \frac{d\theta_3}{dt} = \frac{L_2}{L_3}\omega_2 \frac{sin(\theta_2 - \theta_4)}{sin(\theta_4 - \theta_3)} \tag{4.2}$$

$$\omega_4 = \frac{d\theta_4}{dt} = \frac{L_2}{L_4}\omega_2 \frac{sin(\theta_2 - \theta_3)}{sin(\theta_4 - \theta_3)} \tag{4.3}$$

and because L_2 is rotated at a constant speed:

$$\theta_2 = \omega_2 t \tag{4.4}$$

Equations 4.2, 4.3 and 4.4 together with initial conditions for angles θ_2, θ_3 and θ_4 completely describe the four bar mechanism.

Because the flow field is no-longer steady, the computation scheme is modified as follows. Using a global ODE module, differential equations for the rocking mechanism are first solved. As a first approximation, the boundary velocity of the electrode holder is expressed by $\omega_4 r$ and ω_4 values are derived from ODE solutions. Because ω_4 is time-dependent, so is the resulting flow profile. Finally, concentrations and currents are computed from the convection-diffusion equation as in the case of the RDE.

The following calculations are carried out with a 2D axi-symmetric domain as seen earlier in the rotating disk. The implicit assumption is therefore the rocking action, which still retains some symmetric properties. This assumption is clearly not accurate

due to the time-varying nature of both flow and species fields. A proper calculation should be three dimensional. After constructing the full 3D model and implementing several trial runs, it is realized that the computation was too demanding for the current work station. Consequently, the axi-symmetric model is used in subsequent calculations by default despite its theoretical incompleteness.

Geometric lengths for the mechanism are given in Table 14 . Other parameters are kept the same as in Table 13. Figure 57 shows rocking angle θ_4 as a function of time for $\omega_2 = 50\,rpm$. As expected, the angle oscillates around the initial condition of $\pi/2$ in an approximately harmonic fashion. The frequency of the oscillation is not the same as that of the rotating crank because for every full 360^o rotation of L_2, crank L_4 completes the maximum rocking angle approximately twice. The rocking frequency is therefore about twice as large as the rotating frequency. This relationship is discussed in more detail below.

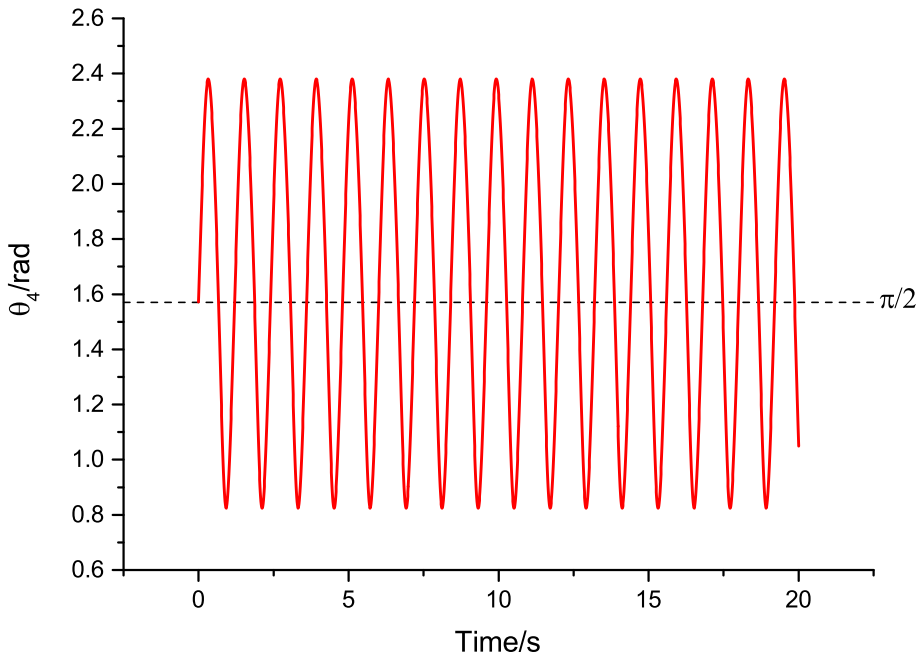

Figure 57: Rocking angle θ_4 as a function of time for $L_2 = 7\,(mm)$,$L_4 = 10\,(mm)$ and $\omega_2 = 50\,rpm$. The initial angle is $\pi/2$ (dotted line). The variation is like a harmonic function. Consequently, the resulting flow field follows in the same manner

Figure 58 demonstrates a good agreement between the computational results and the experimental data at various rotating rates $\omega_2 = 50$, 100 and $500\,rpm$. At large

excess potentials, the currents also become steady. The plot of limiting current versus $f_{RDE}^{1/2}$ confirms a linear correlation. There are two implications following this observation. Firstly, the plot confirms that the structure of mass transport layer under rocking and rotating motions must be similar, at least up to the rotation speed of $500\,rpm$. As a consequence, an approximate expression for $I_{lim,RoDE}$ should differ from Equation 1.21 by only a constant.

To derive $I_{lim,RoDE}$, a semi-empirical form of 1.21 is first assumed:

$$I_{lim,RoDE} = kFAc_{R0}D_R^{2/3} f_{RoDE}^{1/2} \nu^{-1/6} \tag{4.5}$$

whereas f_{RoDE} is the rocking frequency and k is the unknown proportionality constant. The relation $I_{lim,RoDE} \propto \nu^{-1/6}$ and $I_{lim,RoDE} \propto D^{2/3}$ are experimentally confirmed in [178], hence the proposed equation is dimensionally consistent. Between $f_{RoDE} = f_4$ and $f_{RDE} = f_2$, the following relation is used (because each expression is equal to π):

$$\omega_2\, T_2/2 = \omega_4\, T_4$$

where T_2 and T_4 are rotating and rocking periods respectively. Using the relation $f = 1/T$, one obtains:

$$f_4 = 2f_2\,(\omega_4/\omega_2) \tag{4.6}$$

Figure 59 shows the variation of the ratio ω_4/ω_2 at two rotation speeds 50 and 500 rpms. Though there are more variations at higher frequencies, the numerical range remains constant. It therefore means that the average scale of the ratio depends only on the rocking mechanism geometry:

$$\Pi = avg|\omega_4/\omega_2| = f(L_2, L_4) \tag{4.7}$$

Regarding the top graph in Figure 59, the upper and lower sections reach 0.7 and $abs(-0.77) = 0.77$ respectively, yielding an average value of $\Pi = (0.7 + 0.77)/2 = 0.74$. A similar figure is obtained for the bottom graph. It is noted that this scale can also be approximated by simply taking the ratio between rotating and rocking cranks $L_2/L_4 = 0.7$, which further confirms the relation 4.7. Equation 4.6 is more appropriately written using the scale notation $\Pi = \Pi(L_2,\, L_4)$:

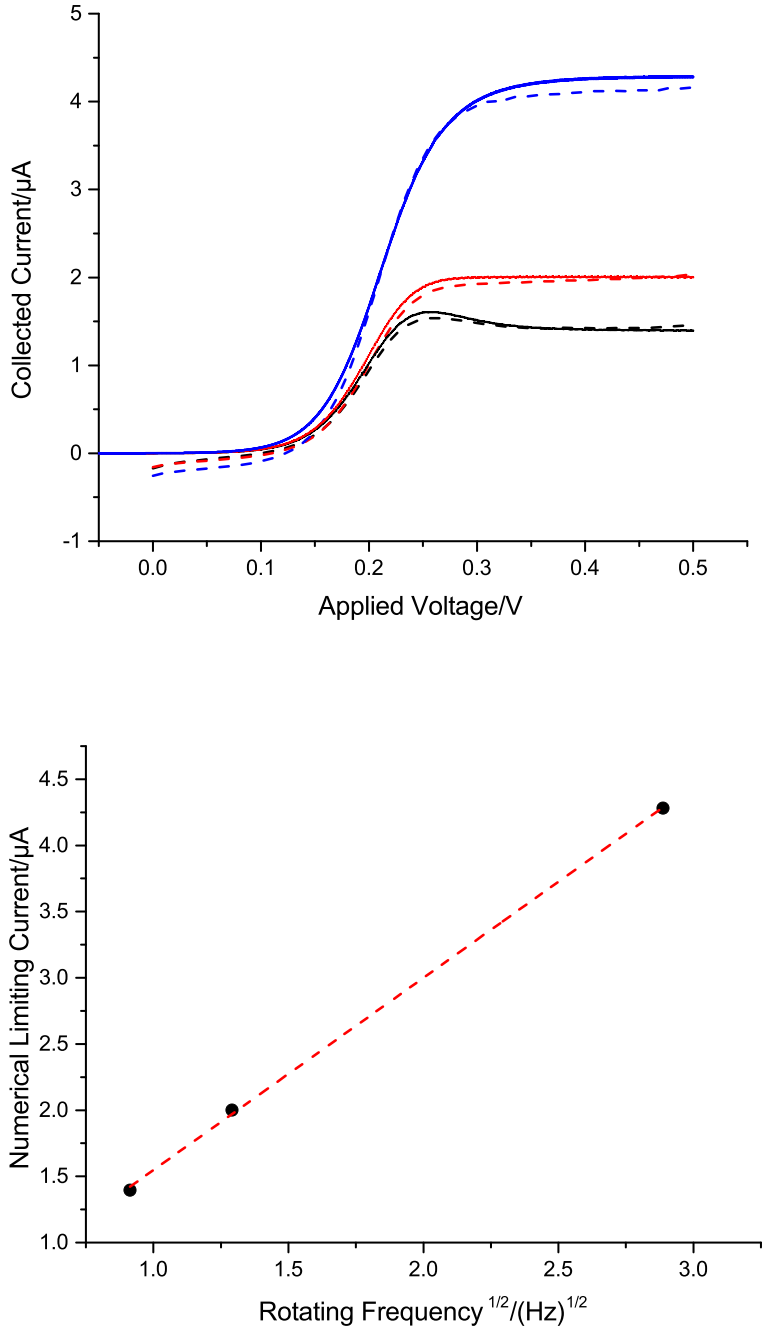

Figure 58: (Top) Numerical (continuous) versus experimental (dashed) linear sweep voltammetries for different regular rotating rates $\omega_2\,(rpm)$: 50 (black), 100 (red) and 500 (blue) at scan rate of $10\,mV/s$. The numerical data are obtained by solving the convective-diffusion equation 1.4 coupled with simple electron transfer reaction. The computational approach is the same as in the case of RDE. (Bottom) Plot of $I_{lim,RoDE}$ against rotating frequencies $f^{1/2}$ showing a linear correlation similar to that of rotating disk (line of best fit (dashed red) has $R^2 = 0.9998$ and slope of $1.451 * 10^{-6}$)

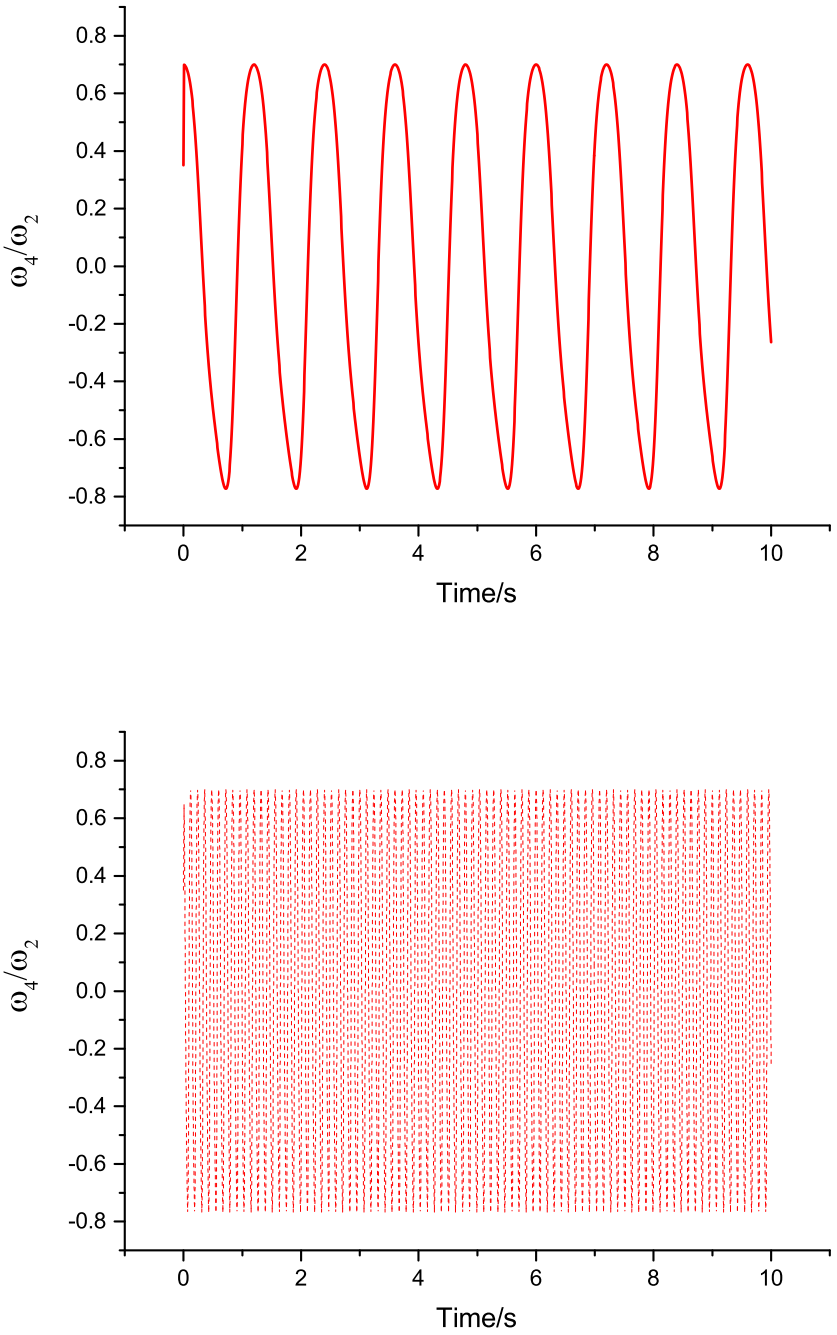

Figure 59: The numerical ratio between rocking and rotating speeds ω_4/ω_2 at 50 (top) and 500 rpm (bottom). Notice that even though the frequency is increased, the ratio scale remains the same. In both cases, they are approximated by L_2/L_4

$$f_{RoDE} = 2\Pi f_{RDE}$$

$$I_{lim,RoDE} = k * (2\Pi)^{1/2} F A c_{R0} D_R^{2/3} f_{RDE}^{1/2} \nu^{-1/6} \tag{4.8}$$

The k value is estimated from the line slope in Figure 58 [179]:

$$k(2\Pi)^{1/2} F A c_{R0} D_R^{2/3} \nu^{-1/6} = 1.451 * 10^{-6}$$

with $A = 2 * 10^{-6}\, m^2$, $c_{R0} = 1mM$, $D_R = 0.65 * 10^{-9}\, m^2/s$ and $\nu = 10^{-6}\, m^2/s$ yielding $k = 0.82$. The Levich-like expression (in terms of rotating frequency) under the current set-up is therefore [178]:

$$I_{lim,RoDE} = F A c_{R0} D_R^{2/3} f_{RDE}^{1/2} \nu^{-1/6} \tag{4.9}$$

It is clear that k is strongly dependent on Π. Furthermore, k can also be treated as a calibration factor from experiments. Because $k = 1 < 1.55$,the limiting current for rocking electrodes is less than that of rotating ones. In terms of analytical sensitivity, the rotating configuration has the advantage. However, a different proportionality constant shows that the rocking system allows for modifications of Levich form, which can be viewed as a benefit.

It is further argued that the constant 1.55 is the upper bound of all possible values for k. If $L_2 < L_4$, then this case follows above calculations, which confirms that $k < 1.55$. On the other hand if $L_2 > L_4$, the rocking angle θ_4 is increased. In this case, a larger slope is expected for the factor $k\,(2\Pi)^{0.5}$. Because $\Pi = L_2/L_4$ is now also larger, the resulting k is again less than 1.55. Another way of reasoning is that when $L_2 > L_4$, rocking crank covers an angle which is complementary (by 2π) to the angle in the case $L_2 < L_4$. However, since the flow field is essentially the derivative of the angle, it should be the same regardless. Because the flow field does not change, the resulting mass transport and Levich equation is the same as before. In conclusion, the rotating disk is the limiting case for all possible configurations of rocking mechanism, as far as Levich relations are concerned.

4.1.3 Comparison of Parameter Identifiability under RDE and RoDE Configurations

The goal of this section is to evaluate the hydrodynamic effect induced in RDE and RoDE configurations on parameter identifiability, specifically the set $\theta = [k_0, \alpha, E_0]$. Because the electrode area is in the micro range and the scan rate is slow, the influence of uncompensated resistance is thus insignificant from the Sobol sensitivity analysis. Furthermore, the magnitude of capacitive current is estimated as:

$$I_c = C_{dl} A v_{scan} \sim 100 \frac{\mu F}{cm^2} \, (2\,10^{-6} cm^2) \, 0.01 \frac{V}{s} = 2 * 10^{-12} (A)$$

which leads to further exclusion of parameter C_{dl}.

From Figure 43, Butler-Volmer parameters consequently remain the most significant. In addition, it is also known from chapter 3 that the total current is mainly influenced by the pair (k_0, E_0). The identifiability calculation is carried out as outlined in Algorithm 3.2. Two samples θ_1 and θ_2 are randomly generated from parameter space. The current response corresponding to each sample is then computed and the result is used to compute the identifiability number (Equation 3.11). Since currents are dimensional, they are non-dimensionalized by the corresponding Levich expressions 4.1 and 4.9. Bounds for each parameter and simulation settings are listed in Table 15. Combinations of slow scan rate $10\,mV/s$, large end voltage E_{end} and rotating rate $100\,rpm$ are to ensure the Levich limiting current is achieved under both RDE and RoDE conditions (Figures 55 and 58).

Parameter Symbol	Upper Bound	Lower Bound	Fixed Value	Unit
k_0	10^{-3}	10^{-6}	-	m/s
α	0.7	0.3	-	-
E_0	0.3	0.1	-	V
E_{start}	-	-	-0.1	V
E_{end}	-	-	0.6	V
v_{scan}	-	-	0.01	V/s
ω_{RDE}	-	-	100	rpm

Table 15: Bounds and simulation settings for Monte Carlo estimation of identifiability numbers $\eta_{transient}$ and η_{steady}. $N_{sample} = 200$ is used in the Algorithm 3.11, which is the same for both RDE and RoDE calculations

A more detailed computational scheme for parameter identifiability is presented in Figure 60. Since fluid and mass transport steps are uncoupled, the fluid dynamic

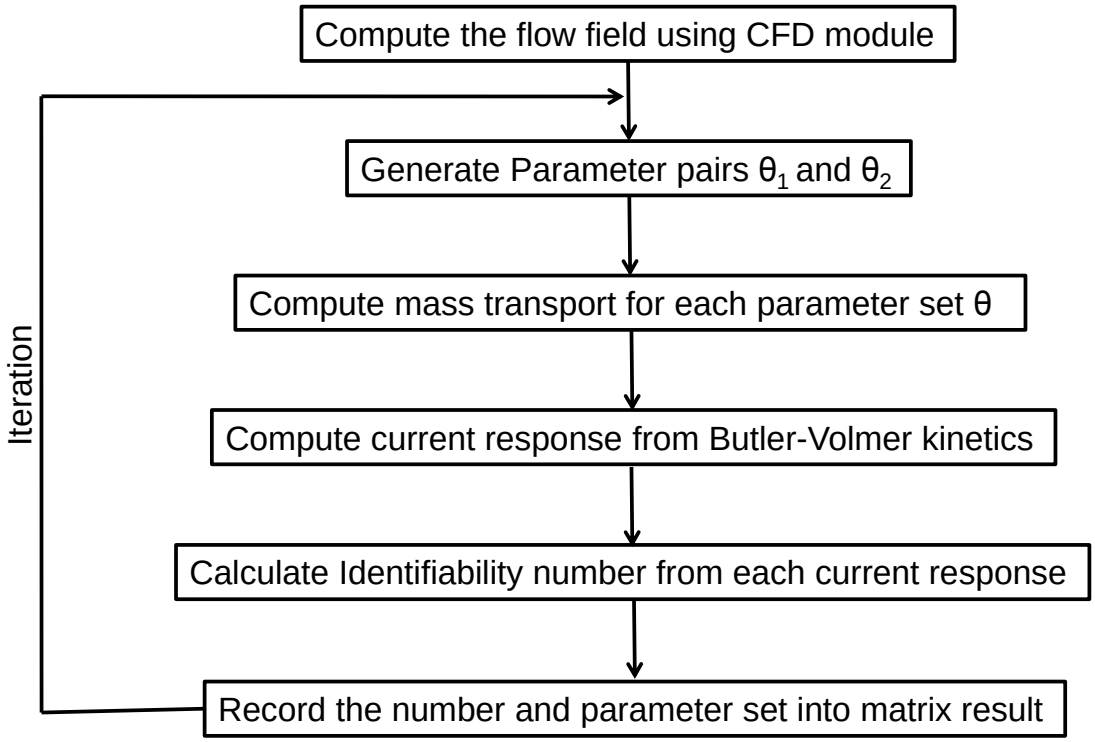

Figure 60: The flow chart for identifiability computation under hydrodynamic conditions. Because fluid dynamics and mass transport steps are independent, the former is carried out outside the iteration loop. The common parameters for both configurations are listed in Table 15. The calculation is implemented in *Comsol Multiphysics*® and *Matlab*® interface environment

part is computed first. This minor change is insignificant for the RDE because the steady state calculation is observed to be fast. On the other hand, for RoDE, the time-dependent calculation requires considerably longer time to complete, hence the modification results in a significantly shorter time for each sample iteration. In addition, two identifiability numbers are computed. The first is the usual number considering the whole current curve. The second number only considers the steady state section at high polarizing potentials. Tables 61 and 62 contain calculation results.

Considering first Table 61, RoDE configuration offers a better identifiability than

Configuration	$\eta_{transient}$	Parameter Sets
RDE	1.90	$[2 * 10^{-4}, 0.367, 0.2724]$
		$[9.3 * 10^{-4}, 0.507, 0.277]$
	0.81	$[2.3 * 10^{-4}, 0.427, 0.207]$
		$[2 * 10^{-6}, 0.345, 0.127]$
	0.53	$[1.2 * 10^{-4}, 0.427, 0.290]$
		$[1.0 * 10^{-6}, 0.476, 0.176]$
	0.51	$[2.8 * 10^{-4}, 0.662, 0.125]$
		$[5.5 * 10^{-4}, 0.553, 0.120]$
	0.49	$[2.0 * 10^{-6}, 0.404, 0.167]$
		$[1.1 * 10^{-4}, 0.355, 0.244]$
	0.26	$[4.0 * 10^{-6}, 0.42, 0.194]$
		$[5.0 * 10^{-6}, 0.64, 0.139]$
	0.16	$[2.6 * 10^{-4}, 0.53, 0.137]$
		$[5.0 * 10^{-6}, 0.65, 0.106]$
RoDE	0.33	$[1.2 * 10^{-4}, 0.427, 0.29]$
		$[1.0 * 10^{-6}, 0.476, 0.176]$
	0.30	$[2.8 * 10^{-4}, 0.662, 0.125]$
		$[5.5 * 10^{-4}, 0.553, 0.120]$
	0.27	$[5.3 * 10^{-5}, 0.638, 0.247]$
		$[5.7 * 10^{-5}, 0.399, 0.233]$
	0.21	$[2.0 * 10^{-6}, 0.460, 0.152]$
		$[2.5 * 10^{-4}, 0.472, 0.282]$
	0.18	$[2.8 * 10^{-4}, 0.617, 0.229]$
		$[1.4 * 10^{-5}, 0.625, 0.207]$
	0.15	$[4.4 * 10^{-5}, 0.418, 0.249]$
		$[4.0 * 10^{-6}, 0.575, 0.137]$
	0.14	$[4.0 * 10^{-6}, 0.420, 0.194]$
		$[5.0 * 10^{-6}, 0.638, 0.139]$

Figure 61: Calculations of $\eta_{transient}$ for RDE (top-half) and RoDE (bottom-half). Parameter values are listed in following columns in the order $[k_0, \alpha, E_0]$. Top 7 values are included

Configuration	η_{steady}	Parameter Sets
RDE	4.26	$[1.1 * 10^{-4}, 0.498, 0.138]$
		$[3.1 * 10^{-5}, 0.359, 0.111]$
	3.04	$[2.8 * 10^{-4}, 0.662, 0.125]$
		$[5.5 * 10^{-4}, 0.553, 0.120]$
	1.92	$[2.0 * 10^{-4}, 0.367, 0.272]$
		$[9.3 * 10^{-4}, 0.506, 0.277]$
	0.81	$[8 * 10^{-6}, 0.473, 0.103]$
		$[9 * 10^{-4}, 0.367, 0.121]$
	0.78	$[5.3 * 10^{-5}, 0.324, 0.147]$
		$[1.1 * 10^{-5}, 0.628, 0.103]$
	0.56	$[1.2 * 10^{-4}, 0.427, 0.290]$
		$[1.0 * 10^{-6}, 0.476, 0.176]$
	0.49	$[2.0 * 10^{-6}, 0.460, 0.152]$
		$[2.5 * 10^{-4}, 0.473, 0.282]$
RoDE	62.7	$[5.6 * 10^{-4}, 0.41, 0.251]$
		$[1.8 * 10^{-4}, 0.45, 0.213]$
	17.5	$[9 * 10^{-6}, 0.51, 0.133]$
		$[6.4 * 10^{-5}, 0.405, 0.23]$
	9.2	$[2 * 10^{-6}, 0.32, 0.210]$
		$[2.1 * 10^{-4}, 0.67, 0.126]$
	8.2	$[1.8 * 10^{-5}, 0.32, 0.280]$
		$[6.8 * 10^{-4}, 0.496, 0.197]$
	6.2	$[2.0 * 10^{-6}, 0.46, 0.152]$
		$[2.5 * 10^{-4}, 0.47, 0.282]$
	4.3	$[1.8 * 10^{-4}, 0.40, 0.201]$
		$[1.2 * 10^{-4}, 0.66, 0.291]$
	3.5	$[4.4 * 10^{-5}, 0.42, 0.290]$
		$[4.0 * 10^{-6}, 0.57, 0.137]$

Figure 62: Calculations of η_{steady} for RDE (top-half) and RoDE (bottom-half). Parameter values are listed in following columns in the order $[k_0, \alpha, E_0]$. Top 7 values are included

its RDE counterpart. This is because the largest $\eta_{transient}$ value corresponding to the former is 0.33, which is significantly less than the maximum (i.e. 1.90) corresponding to the latter. A possible explanation is that the rising section in the voltammogram is very sensitive to the parameter set [k_0, E_0]. In this case, introduction of the rocking flow increases this sensitivity and leads to better differentiation between two similar sets. Therefore, the analysis of electron transfer reactions using RoDE and the whole current-voltage curve should yield a better result than that of RDE. On the other hand, the opposite trend is observed for η_{steady}. From Table 62, it is evident that the determination of Butler-Volmer parameters using the steady section of the voltammogram does not lead to a unique solution. This non-identifiability is demonstrated in rows 2^{nd} and 3^{rd} as even totally different sets cause remarkably similar current responses and consequently very large η_{steady}. In addition, given that overall small identifiability numbers were observed for RDE, this mode of hydrodynamic modulation provides a reliable parameter differentiation and justifies its application in earlier work [65].

4.2 Voltammetric Analysis with Couette flow

This section analyses a new hydrodynamic device which is highly suitable for conducting measurements with viscous media. The outline of the experimental set-up is illustrated in Figure 63. A cylinder is part immersed in a solution and rotated by connecting it to a motor at the back. A frequency controller then changes the rotation rates of the drum cylinder. The drum rotates and drags the solution into the gap between itself and the working electrode. In addition, the gap size can be adjusted by using a piezo-electric positioner. Physical dimensions of the devices are included in Table 16.

This arrangement has several advantages over the rotating or channel electrode. Firstly, it does not require a large amount of solution to be transported during experiments. For solvent such as Polyethylene Glycol (PEG) or ionic liquids, such benefits translate into efficient use of energy. Thanks to the hydrodynamic effect, the current response follows similar behaviour to that of rotating or rocking system, in addition, tunable micro gap facilitates direct transport of electroactive species to and from electrode surface. Finally, as shown below, the current magnitude is sufficiently small and independent of solvent properties. This independence is to be in contrast with rotating configurations (Equations 4.1 and 4.8). Such benefits promise potential use of rotating drum in studies of electron transfer reactions for different redox couples, solvent and electrode materials, which so far has been limited to diffusional regime in previous studies [37, 180].

Parameters	Range of Values	Units	Explanation
h_c	$50 - 500$	μm	Gap between cylinder and electrode
ω	$50 - 500$	rpm	Cylinder rotating frequency
h_d	2	cm	Cylinder Thickness
d_e	250	μm	Electrode Diameter
d_c	4000	μm	Electrode Casing Diameter
d	5	cm	Cylinder Diameter
ρ	1127	kg/m^3	PEG Solution Density
μ	0.043	$Pa * s$	PEG Solution Viscosity
$D_{Fc(CH_2OH)_2}$	$1.4 * 10^{-11}$	m^2/s	Diffusivity of Ferrocene Methanol in PEG

Table 16: List of experimental variables in the rotating drum experiment. The electrode material is Platinum (Pt)

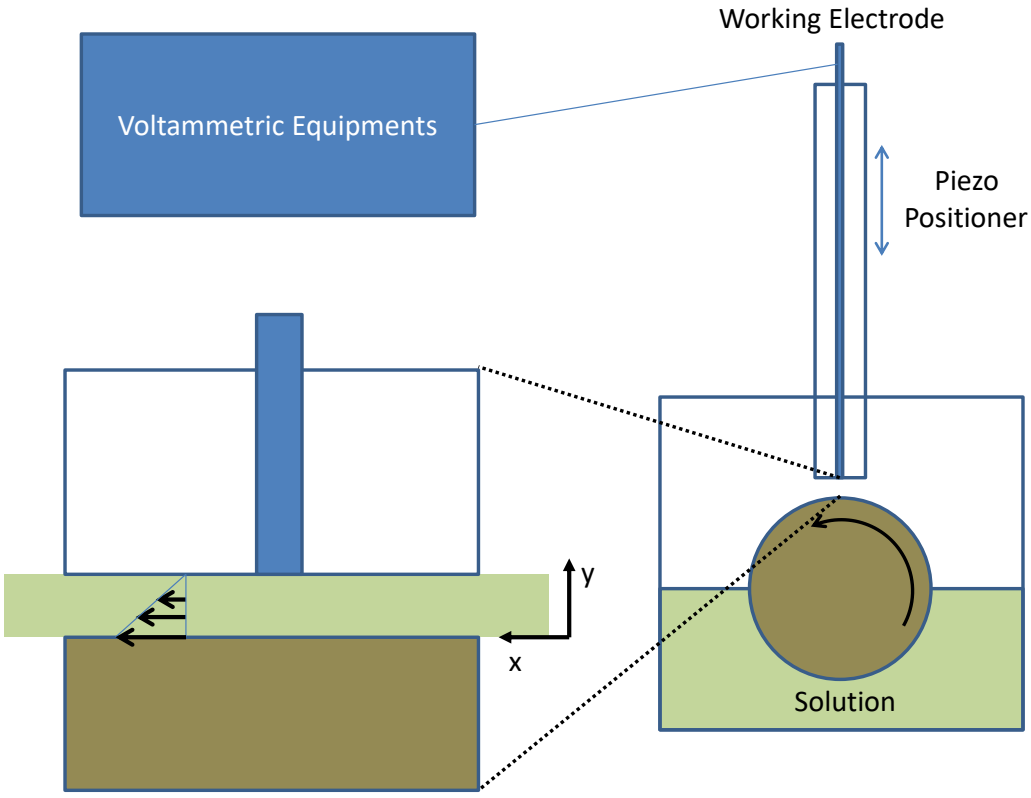

Figure 63: The rotating drum equipment. Schematic end-view (right) and enlargement of the central section with associated linear velocity profile (left). The solution is dragged into the gap via the rotating cylinder

4.2.1 Theoretical Analysis

Because the micro gap h_c is considerably smaller than both casing diameter d_c and cylinder thickness h_d, it is reasonable to simplify the geometry to 2D as shown in Figure 63. Next it is useful to check the induced flow is indeed laminar within the parameter ranges. Comparing to water, PEG solution is highly viscous (about 40 times water's viscosity) while the density is only about 13% higher, this fact thus permits uses of rotation as high as $500\,rpm$. Taking the largest $\omega = 500\,rpm = 52.36\,rad/s$. The maximum velocity at the drum tip is hence $v_{max} = \omega d/2 = 1.3\,m/s$ and Reynold number is estimated to be:

$$Re_{max} = \rho v_{max} h_c/\mu = 1127\,1.3\,(500\,10^{-6})/0.043 = 17$$

which is well below the threshold of 1000 for turbulent regimes and laminar flow is therefore expected under the above parameter ranges. Under Couette flow (enlarged section of Figure 63), the top plane (cylinder) is slid at constant velocity $U\,(m/s)$, whilst the bottom plane (electrode casing) is stationary. This results in a linear flow profile which is expressed as:

$$u = U\,\frac{y}{h_c} \tag{4.10}$$

where the coordinates are as in Figure 13. Although Couette flow is conceptually different from the parabolic profile in CE (Figure 13), they are implicitly related. By linearizing the parabolic profile very close to the electrode plane, one obtains the exact Equation 4.10.

This section first derives an expression for $I_{lim}^{Couette}$ assuming a rectangular geometry and uniform plane width, which can then be extended to other closed geometries. The derivation is essentially based on early works by References [181, 182]. Although such work considers both reversible and quasi-reversible limits, the limiting current is independent of kinetic factors since at sufficiently high voltages, a uniform diffusion layer is always formed. Consequently, the following derivation assumes fast electrochemical reaction and only the voltage range in which mass transport has reached steady-state is considered. Under this assumption, the convective diffusion Equation 4.11-4.14 becomes:

$$U\frac{y}{h_c}\frac{\partial c_i}{\partial x} = D_i\frac{\partial^2 c_i}{\partial y^2} \tag{4.11}$$

$$y \to \infty :\; c_R = c_{R0} > 0,\; c_O = c_{O0} = 0 \tag{4.12}$$

$$y = 0 :\; D_R\frac{\partial c_R}{\partial y} + D_O\frac{\partial c_O}{\partial y} = 0 \tag{4.13}$$

$$y = 0 :\; \frac{c_R}{c_O} = exp(-\frac{nF(E - E_0)}{RT}) = \exp(-\theta) \tag{4.14}$$

Nernst relation (Equation 4.14) is assumed since the electrode kinetics is fast. Applying the variable transformation 4.15 (as suggested in References [181, 182]):

$$\eta = (\frac{U}{xh_c})^{1/3}y \tag{4.15}$$

and calculate each derivation in 4.11 in terms of η:

$$\frac{\partial c}{\partial x} = -\frac{\partial c}{\partial \eta}(\frac{U}{h})^{1/3}\frac{1}{3}y^{-1/3}x^{-4/3}$$

$$\frac{\partial^2 c}{\partial y^2} = \frac{\partial^2 c}{\partial \eta^2}(\frac{U}{h_c x})^{2/3}$$

substituting the above expressions into 4.11 and simplifying:

$$\frac{1}{3D_i}\eta^2\frac{\partial c_i}{\partial \eta} + \frac{\partial^2 c_i}{\partial \eta^2} = 0$$

Each of the above equation can be reduced to ODE by setting $y = \partial c_i/\partial\eta$. Solving these ODEs subjecting to 4.12:

$$\frac{c_R - (c_R)_{y=0}}{c_{R0} - (c_R)_{y=0}} = \frac{\int_0^\eta \exp(-\frac{\eta^3}{9D_R})d\eta}{\int_0^\infty \exp(-\frac{\eta^3}{9D_R})d\eta}$$

and a similar expression for c_O. The integrals in denominator is calculated by changing the variable again $z = \eta^3/9D_i$, $i = R, O$ leading to Gamma function:

$$\int_0^\infty \exp(-\frac{\eta^3}{9D_i})d\eta = (\frac{D_i}{3})^{1/3}\int_0^\infty z^{-2/3}\exp(-z)dz = (\frac{D_i}{3})^{1/3}\Gamma(1/3) = 1.857D_i^{1/3}$$

The numerator can be treated by series-expanding the exponent and integrating term-by-term:

$$\int_0^\eta \exp(-\frac{\eta^3}{9D_R})d\eta = \eta - \frac{\eta^4}{36D_i} + O(\eta^7)$$

Considering only the first order effect, the expressions for c_i finally become:

$$\frac{c_R - (c_R)_{y=0}}{c_{R0} - (c_R)_{y=0}} = \frac{(\frac{U}{xh_c})^{1/3}y}{1.857D_R^{1/3}}$$

$$\frac{c_O - (c_O)_{y=0}}{c_{O0} - (c_O)_{y=0}} = \frac{(\frac{U}{xh_c})^{1/3}y}{1.857D_O^{1/3}}$$

Differentiating the above expression and calculating the flux at $y = 0$:

$$D_R(\frac{\partial c_R}{\partial y})_{y=0} = 0.5384 D_R^{2/3}(\frac{U}{x h_c})^{1/3}(c_{R0} - (c_R)_{y=0})$$

$$D_O(\frac{\partial c_O}{\partial y})_{y=0} = -0.5384 D_O^{2/3}(\frac{U}{x h_c})^{1/3}(c_O)_{y=0}$$

Combining the last two expressions with 4.14:

$$D_R(\frac{\partial c_R}{\partial y})_{y=0} = 0.5384 D_R^{2/3}(\frac{U}{x h_c})^{1/3} c_{R0}\frac{\exp(\theta)}{\exp(\theta) + (D_R/D_O)^{2/3}} \tag{4.16}$$

Finally integrating 4.16 across the electrode surface:

$$I = nFw\int_0^{x_e} D_R(\frac{\partial c_R}{\partial y})_{y=0}dx = 0.8076 nFw D_R^{2/3}U^{1/3}h_c^{-1/3}x_e^{2/3}c_{R0}\frac{\exp(\theta)}{\exp(\theta) + (D_R/D_O)^{2/3}}$$

taking the limit as $exp(\theta) \to \infty$:

$$I_{lim}^{Couette} = 0.8076 nFw D_R^{2/3}U^{1/3}h_c^{-1/3}x_e^{2/3}c_{R0} \tag{4.17}$$

Expression 4.17 applies to the rectangular electrode and *Comsol Multiphysics*® was then used to confirm this relationship. The narrow gap is divided into two sections corresponding to the electrode section and upstream of the flow. These sections are then discretized into rectangular elements with $N_{electrode} = 250$ points to cover the surface and $N_{upstream} = 50$ for the rest. The minimum elemental size is set at $10\,nm$ to adequately resolve the diffusion layer. From Table 16, only the combinations ($50\,rpm$, $50\,\mu m$), ($50\,rpm$, $500\,\mu m$), ($500\,rpm$, $50\,\mu m$), ($500\,rpm$, $500\,\mu m$) need to be simulated and the rest is simply interpolation of these limiting combinations. Table 17 confirms good agreement between numerical and analytical currents. In all four cases, the percentage difference is no more than 2%. Consequently for other combinations of (ω, h_c), these currents do not differ significantly from each other.

For a common geometry such as circles, in order to apply Equation 4.17, the circular shape is divided into many small rectangles as shown in Figure 64. If the diameter is $2r_0$, then the total current would become:

$$I_{lim}^{Couette\,Circle} = 0.8076 nF D_R^{2/3}U^{1/3}h_c^{-1/3}\sum_{N_{rectangle}\to\infty} w x_e^{2/3}$$

where $N_{rectangle}$ denotes the number of rectangles and common factors have been

ω/rpm	$h_c/\mu m$	$I_{lim}^{numerical}$	$I_{lim}^{analytical}$	$I_{lim}^{numerical}/I_{lim}^{analytical}$
50	50	$2.53 * 10^{-4}$	$2.48 * 10^{-4}$	1.02
50	500	$1.15 * 10^{-4}$	$1.15 * 10^{-4}$	1.00
500	50	$5.47 * 10^{-4}$	$5.34 * 10^{-4}$	1.007
500	500	$2.49 * 10^{-4}$	$2.48 * 10^{-4}$	1.004

Table 17: Comparisons of numerical and analytical values for $I_{lim}^{Couette}$. Numbers in the 3^{rd} column are results from $Comsol\,Multiphysics^{®}$ and values in the 4^{th} column are calculated using the expression 4.17. Units of both currents are A/m

moved outside the sum, leaving only the terms which are relevant to the geometry. By normalizing $W = w/r_0$ and $X_e = x_e/r_0$, the above equation is written as:

$$I_{lim}^{Couette\,Circle} = 0.8076nFD_R^{2/3}U^{1/3}h_c^{-1/3}r_0^{5/3}\sum_{n\to\infty} WX_e^{2/3}$$

for a unit circle. By dividing the diameter into an even number of n pieces, this is numerically calculated. Table 18 shows that the convergent value is 2.67 by upto 2 significant figures. The limiting current for a circular disk thus becomes 4.18:

$$I_{lim}^{Couette\,Circle} = 2.156nFD_R^{2/3}U^{1/3}h_c^{-1/3}r_0^{5/3} \tag{4.18}$$

In general, the theoretical limiting current is independent of the medium viscosity but depends on the rotation frequency of the drum via tip speed U.

Number of Rectangular Divisions	Total Sum $\sum WX_e^{2/3}$
1000	2.669
2000	2.670
5000	2.670
10000	2.670

Table 18: Calculating the numerical sums of the form $W\,X_e^{2/3}$ for an unit circle. As expected, the sum quickly converges as the number of divisions are increased

4.2.2 Comparison to Experimental Data

Two main experiments were carried out to verify the theory developed earlier. In the first experiment, the gap is held constant at $500\,\mu m$ and the cylinder had varying rotating rates within the range $50 - 500\,rpm$. The second experiment, on the other hand, fixes the rotation rate at $50\,rpm$ and systematically increases the gap size from

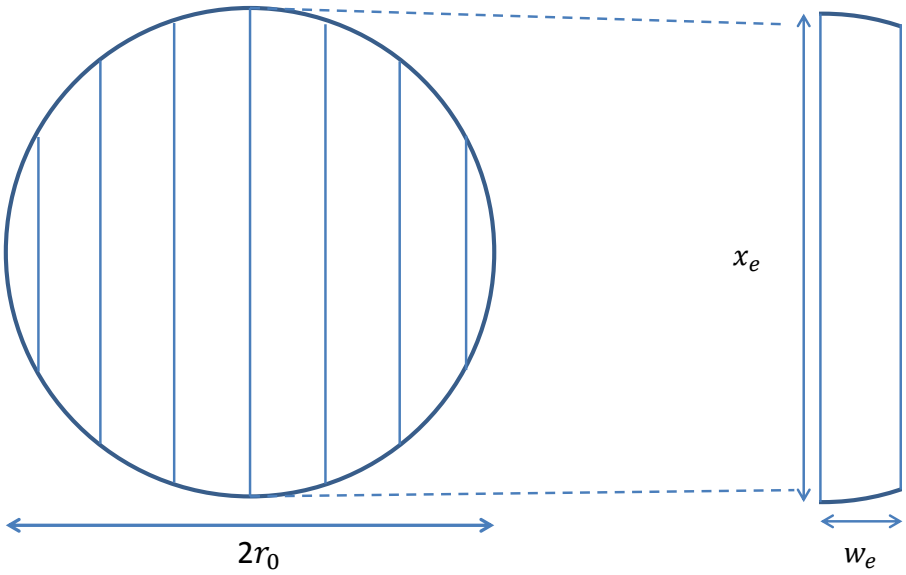

Figure 64: Division of circular disk into many thin rectangles and the relation 4.17 is applied to each element. The approach is generalized to any closed geometrical shape

50 to 500 μm. Equation 4.18 is used to compute theoretical currents. Results for the experiment are shown in Figure 66. Note that both currents shown are the steady state values. In addition, the current's small magnitude is attributed to the fact that the diffusion coefficient in PEG solution is at least two orders of magnitude below that in water. Furthermore the nA scale also implies that the effect of resistance will be essentially ignored. Considering the applied potential including Ohmic resistance:

$$E_{apply} = (E - E_0) - IR_u$$

The magnitude of this loss term for a highly resistive media is estimated as:

$$IR_u \sim 60\,(nA) * 10000(\Omega) = 6 * 10^{-4}\,(V)$$

thus for most of the potential point reasonably far away from E_0, the overpotential $E - E_0 \gg IR_u$ the applied potential is thus effectively the same as in the case of $R_u = 0$. Combining with Equation 4.18, it can be concluded that the voltammogram is not sensitive to solvent choice, apart from sections very close to E_0.

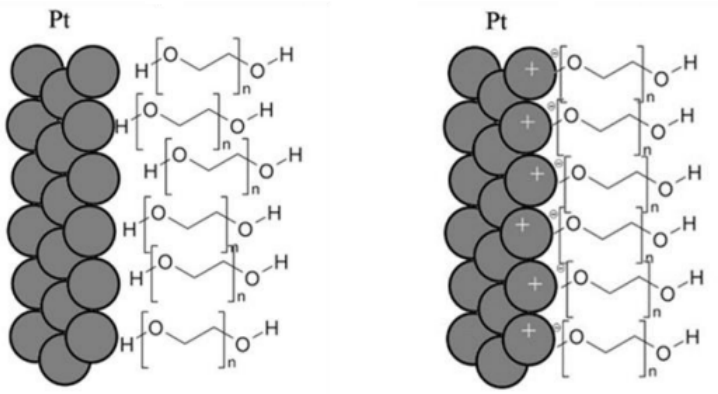

Figure 65: Proposed chemical changes on Pt surface at potetential below $0.45\,(V)$ (left) and above $0.45\,(V)$ (right). At low potential, there is a weak attraction between the surface and PEG molecules. At higher potentials, stronger bonds are formed and result in a more regular structure

It is evident from Figure 66 that theoretical values overestimate actual data by about a factor of 2 [183]. A possible explanation was proposed as follows (Figure 65) [184]. At low potentials, the solution remains a uniformly fluid. At potentials above $0.45\,(V)$, the electrode layer is positively charged, which then forms a bond with the oxygen atom in PEG molecules. Consequently, a thin layer of semi-fluid material is formed and the diffusivity of 1-1 Ferrocene Dimethanol is further reduced inside this layer. Another reason for correction of species diffusivity is as follows. Inside an infinite medium, the diffusion coefficient is $D_{Fc(CH_2OH)_2}$ (Table 16) because diffusion process is three-dimensional. Due to the applied flow, the process now occurs mainly in the direction orthogonal to the electrode surface. Despite this discrepancy, the theoretical result still serves as an upper estimates of the actual data as the two sets follow similar trends. Consequently, the above discussions regarding solvent effects still apply. The device is therefore potentially useful as an alternative hydrodynamic tool beside the traditional diffusion-controlled micro disk.

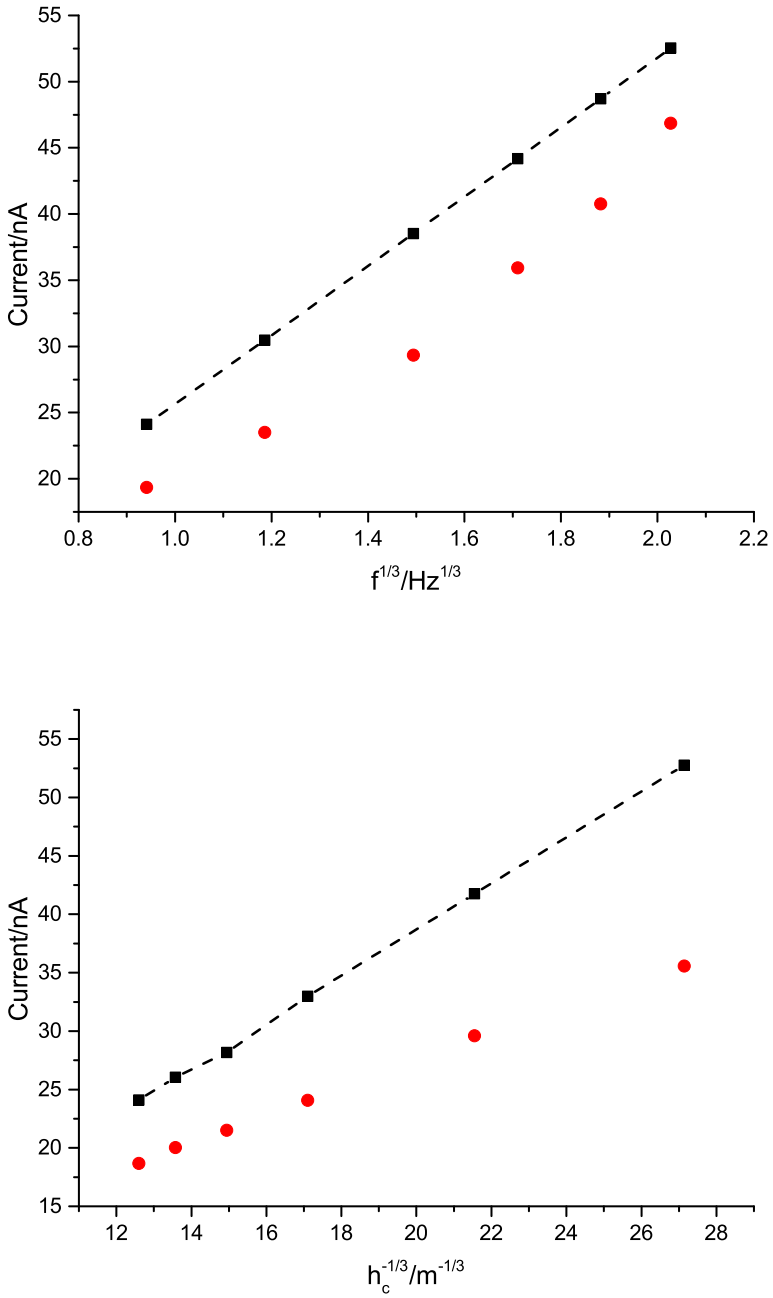

Figure 66: Limiting current versus cube root of frequency at fixed $h_c = 500\,(\mu m)$ (top) and inverse cube root of micro gap at fixed $\omega = 50\,(rpm)$. Black points are calculated using the expression 4.18 and red points are experimental values. Dashed line is the fitted Levich expression

4.3 Chapter Conclusion

This chapter examines the influence of hydrodynamic factors on the identifiability of primary parameters in Butler-Volmer model. First a computational package based on FE formulation, is introduced to verify the theoretical limiting current with RDE. The work then focuses on the analysis of a recent RoDE device, which allows approximate harmonic modulations of the electrode movement. The mechanism was analysed using the well-known 4-bar geometry. Characteristic equation, namely the Levich relation for the configuration, was derived from combinations of simulation and scaling analysis. Furthermore, the result was in good agreement with experimental data, confirming the adequacy of simplified $2D$ axisymmetric model instead of using a full $3D$ construction. However, for higher rpms, the latter is required due to increasing turbulence and the flow dependence on angular positions.

By employing small electrode areas and a slow scan rate, the effects of solution resistance and capacitive currents became negligible. These factors were consequently left out in the model by the same argument from Sobol analysis in Chapter 3. Identifiability values were computed and compared for RDE and RoDE using two numbers $\eta_{transient}$ and η_{steady}. It was evident that RoDE offers a better differentiation of the Butler-Volmer parameter set when the whole current curve is considered. On the other hand, for the steady state section, RoDE's η_{steady} was much bigger than that of RDE, showing the induced non-steady flow field leads to poor identifiability. Therefore, to regress the Butler-Volmer model parameters, RoDE is suitable using the total current response while RDE produces more reliable results for the steady part of the curve.

The last section investigates the rotating drum electrode as an alternative analytical device for highly viscous and resistive media. The Levich equation was derived from first principles using mass transport and simplified Nernstian kinetics. Comparisons were made against experimental results, whilst some discrepancy was observed, the data sets agree qualitatively in terms of trends and magnitudes. The rotating drum is thus a promising tool in experimental design due to two main reasons. Firstly, the current response is theoretically independent of solvent properties, apart from species diffusion coefficient. Secondly the developed flow is also steady state, which shares similar characteristics of RDE. Consequently, the device should perform similarly as RDE regarding the identifiability and estimation aspects. The work here forms a theoretical basis for future studies, especially those involving heterogeneous electron transfers in ionic liquids.

Chapter 5

Elicitation of Electrocatalysis Mechanism via Large amplitude Sinusoidal signals

The work thus far has focused exclusively on experimental design methods to analyse the simple redox reaction. Chapters 3 and 4 covered two major experimental tools, namely the applied potential (i.e. linear sweep and cyclic voltammetries) and control of mass transport (diffusion versus induced mechanical convections). Although E mechanism is often studied, other associated homogeneous reactions can also occur and are useful for analytical purposes.

A special focus of this chapter is the self-catalytic EC' mechanism. There are several motivations for this investigation. The first reason is due to the promising application of the mechanism to detect H_2S in commercial oil wells. This application is valuable when monitoring the crude feed quality, product control as well as rig safety. H_2S is a highly flammable and toxic gas under normal conditions. In addition, concentrations at levels above 1000 parts per million could cause fatal death. Hydrogen sulphide often biologically originates from the decay of organic matter under the presence of anaerobic bacteria. Furthermore, geochemical conditions (i.e. high temperature and pressure) also produce the gas by reactions of methane with calcium sulphate [185]:

$$CaSO_4(s) + CH_4(g) \rightarrow H_2S(g) + CaCO_3(s) + H_2O(l),\ T \sim 285°F$$

Classically, H_2S is often detected using iodometric titration, which proceeds via

the following reaction scheme [186]:

$$H_2S + I_2 \rightarrow 2HI + S$$

$$2S_2O_3^{2-} + I^{3-} \rightarrow S_4O_6^{4-} + 3I^-$$

Modern approaches include kinematic spectroscopy, chromatography [187] and electrochemical techniques. Electrochemical methods have recently become more popular, which is attributed to their sensitivity and reliability. Amperometry and potentiometric are most commonly used for sulphide sensing purposes [188]. Efforts have also been directed towards the modifications of electrode materials as well as careful selection of electrocatalysts to improve reaction kinetics [189, 190]. Because of its molecular structure, H_2S, is generally electro-inactive, hence detections via direct oxidation or reduction (i.e. E mechanism) is not feasible. The EC' scheme offers a simple but elegant route for such a detection that is still based entirely on previous knowledge of electrochemistry.

The second motivation lies in the use of sinusoidal signal as a mean to elicit the effects of catalytic reactions. As in Figure 38, under normal cyclic voltammetry and planar diffusion, a well-known phenomenon termed split-wave is observed and the effect is considered as the signature of catalytic kinetics. Recently, the same phenomenon was reported for square wave [191]. Furthermore, square wave signals can, in theory, be decomposable into the sums of harmonic components. These observations, therefore, lead to a question of whether simple harmonic signal could produce the similar effect. The question implies two interesting points. Firstly, it demonstrates the inclusion of sinusoidal pertubation is a useful analytical complement to the traditional voltammetry. Second, given the fact that AC technique was previously applied to evaluate single electron transfers, EC and similar catalytic mechanisms [58][59], it should also be applicable to EC' mechanism. However, to our best knowledge, no such study was carried out in previous literature.

A series of papers studies general theory of self-catalytic process EC' in great details [192–194]. A notable result is the split polarography waves, which were subsequently confirmed by experiments [195]. The split-wave under micro-fluidic conditions was numerically simulated and current enhancement was confirmed as a result of high catalytic turnovers [196]. Unlike diffusion-limited cases, a "shoulder" is observed and very large homogeneous kinetics are required (Figure 67) [62]. The same mechanism

and responses were again observed for an array of nano-spherical electrodes under a wide range of reaction kinetics, surface coverages and substrate concentrations [168].

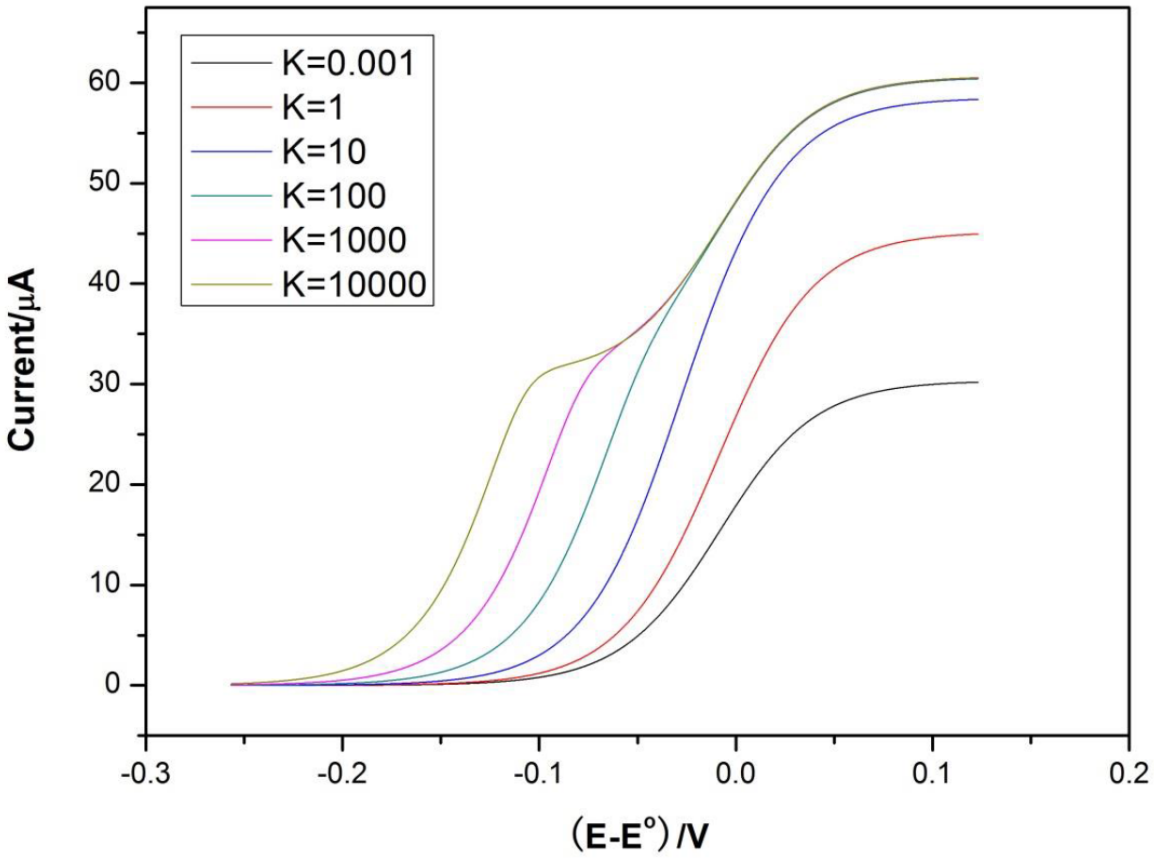

Figure 67: Linear sweep voltammetry at a flow channel for increasing catalytic reaction rates K and a slow scan rate

The chapter is structured as follows. Firstly, additional background on AC voltammetry, based on signal processing concept, is provided. Next the technique is applied to study the basic E reaction. The section explains the fundamentals of the simulation methodology, data analysis and the importance of the FFT algorithm to extract harmonic currents. Subsequent sections focus on the EC' mechanism under large-amplitude AC modulation at different electrode sizes under diffusion control. Finally, the investigation is shifted to hydrodynamic conditions using channel electrodes. To demonstrate the technique's effectiveness under both diffusion and micro-fluidic conditions, relevant experimental data are supplemented to support the simulation results.

5.1 Signal Processing Concept of AC Voltammetry

The work explores the use of the AC voltammetry technique as an experimental design tool. Another less commonly used term is FFT voltammetry, but the two shall be used interchangeably. In the simplest form, FFT voltammetry utilizes a single-frequency sinusoidal-signal as a perturbation, on top of the traditional voltammetric signal. Expressed in time domain, the AC signal is often generated via the following superposition:

$$E_{apply} = E_{dc} + E_{ac} \tag{5.1}$$

$$E_{ac} = \triangle E \sin(2\pi f t) = \triangle E \sin(\omega t) \tag{5.2}$$

$\triangle E$ and f determine the perturbing signal amplitude and frequency respectively. The usual linear voltage, E_{dc}, whose expressions are denoted by Equations 2.40 and 2.42:

$$E_{dc} = E_{start} + v_{scan}t,\ 0 \leq t < t_{scan}$$

$$E_{dc} = E_{vertex} - v_{scan}(t - t_{scan}),\ t_{scan} \leq t < 2t_{scan}$$

The potential E_{dc} serves as a "base-line" signal to drive electrochemical reactions back and forth, and its presence is essential in AC voltammetric technique. Since E_{ac} only varies slightly in comparison to E_{dc}, application of such sinusoidal signal alone cannot significantly affect the electron transfer kinetics and consequently the associated diffusion layer.

Under presence of E_{ac}, the resulting current is considerably altered. The total current now contains the usual current due to E_{dc} (which will be referred to as I_{dc}or DC current) and several sinusoidal varying currents at the same or higher frequencies. The real value of the AC technique is due to the presence of these additional currents, which are commonly referred to as harmonics.

Consider a Single Input Single Output (SISO) black box model of electrochemical system in Figure 68. If the DC signal or E_{dc} is input to the box, one obtains the usual I_{dc} output. Notice that this DC current contains two components: The Faradaic and capacitive currents as remarked in Chapter 1:

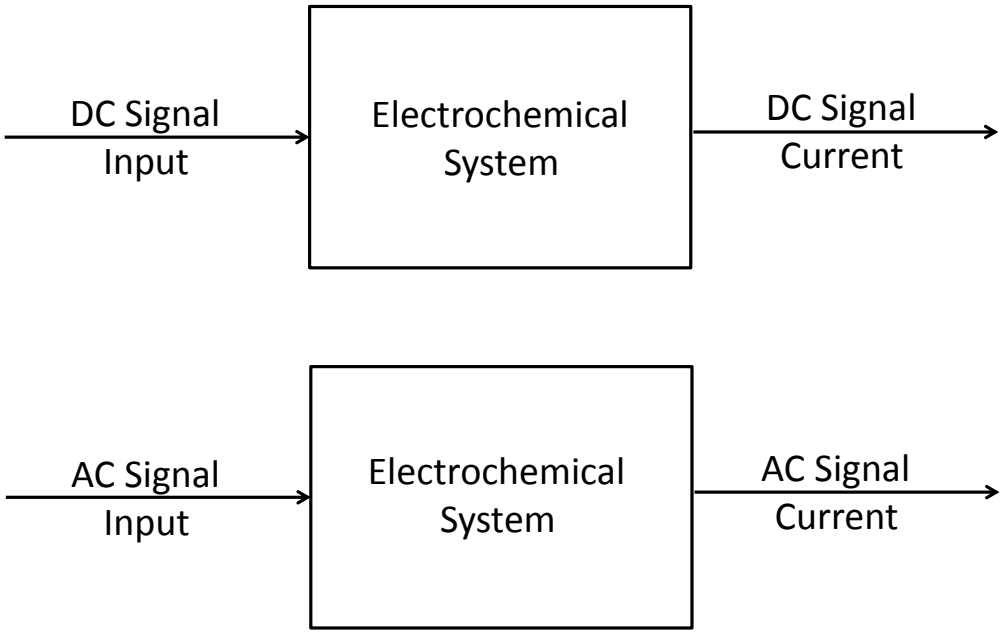

Figure 68: SISO "Black Box"' representation used to demonstrate the general concept of AC voltammetry. When a DC signal is applied, the usual cyclic voltammetry (CV) current is obtained (top). However, the superposition of perturbed AC signals combined with the DC part causes the output to contain and extra sinusoidal varying current, thus the AC current output (bottom)

$$I_{dc} = I_f + I_c$$

The capacitive component is computed from the time derivative of the applied potential as usual:

$$I_c = C_{dl} A \frac{dE_{apply}}{dt} \tag{5.3}$$

The presence of I_c can be viewed as an additional complication beside the main analytical signal I_f. Therefore it is desirable to eliminate as much I_c as possible. If the AC signal E_{ac} is applied, the output becomes I_{ac}. As remarked earlier, this output

can be decomposed component-wise in time domain as follows:

$$I_{ac} = I_{dc} + I_1(\omega t) + I_2(2\omega t) + I_3(3\omega t) + ... \tag{5.4}$$

where the currents $I_1(\omega t)$, $I_2(2\omega t)$, $I_3(3\omega t)$, etc. are called the first, second, third harmonic respectively.Another reason for these names is because I_1, I_2, I_3 has periodical appearance at the principle frequency (f) and then multiple frequencies $2f$, $3f$ and so on. The origin of currents at higher frequencies is worth further elaboration. Suppose that the (black box) electrochemical model is completely linear, then from linear response theorem [197, 198], Equation 5.4 is simplified to:

$$I_{ac} = I_{dc} + I_1(\omega t)$$

because there is only one input E_{ac} at single frequency f and I_{dc} is the same as before. Consequently the second, third and higher harmonic currents must be due to non-linearity of the electrochemical model. This fact is easily verified because the boundary condition (e.g. Butler-Volmer equation) is the source of such non-linearity.

If $E_{ac} = 0$ then all the capacitive current is caused by the gradient of the potential E_{dc}:

$$I_c^{dc} = C_{dl} A \frac{dE_{dc}}{dt}$$

This capacitive current is clearly contained in I_{dc}. Now if E_{ac} is included, additional capacitive current arises due to sinusoidal potentials:

$$I_c^{ac} = C_{dl} A \frac{dE_{ac}}{dt}$$

For a linear system, it is evident that $I_1(\omega t)$ must contain I_c^{ac} since the total current is composed of I_{dc} and $I_1(\omega t)$ while I_{dc} must contain I_c^{dc}. Now if the model becomes non-linear, I_c^{ac} tends to be shared among the harmonics. Numerical and experimental observations show that the current magnitude decreases as the harmonic order increases. Therefore, it is expected that the distributon of I_c^{ac} becomes smaller for higher components. In other words, 2^{nd}, 3^{rd}, 4^{th} etc. harmonics are less influenced by this sinusoidal capacitive current and more Faradaic in nature.

5.2 Single Electron Transfer under Fast Fourier Transform voltammetry

This section lays the theoretical foundation of the technique, which includes the basic simulation methodology and outline of the FFT algorithm to extract the harmonic currents. Calculations are first performed with macro electrode to demonstrate the method before more elaborate cases are considered. The simulation parameters are listed in Table 19 for the generic redox reaction.

From the Table, the reaction is assumed to be reversible (i.e. fast kinetics). Under such conditions, the Butler-Volmer relation is reduced to the Nernstian equation, which is independent of either k_0 or α. In addition, a medium value for the double-layer capacitance is selected, which is typical for the case of aqueous solution. As usual, to minimize the effect of extra resistance, a small electrode area is used. In the sinusoidal perturbation, the work starts with relatively small amplitude $\triangle E$ ($10\,mV$ in this case) and the frequency is set at $3\,Hz$. The simulation scans through a potential window between -0.1 and $0.6\,V$. The ratio between $\triangle E$ and the potential range is therefore about $10 * 10^{-3}/0.7 \approx 1\%$. A larger amplitude might be within $5 - 10\%$ of the scanning potential range.

A typical expanding $1D$ meshing for the simulation is shown in Figure 69. As usual, nodes are concentrated near the left end where the electrode boundary condition is applied. The smallest element size is set to be about $100\,(nm)$ with the expanding coefficient of 1.2. Given the parameters in Table 19, the diffusion layer is estimated to be of the size $6 * 10^{-4}\,(m)$ and thus adequate convergence is ensured with the current settings. In addition, the time stepping scheme is chosen to be "Strict", meaning that the time step is fixed at a constant value. The number of time points are then selected to be power of 2, for example 2^{16} in this case. The reason for this choice is two-fold. First it speeds up the FFT analysis of I_{ac} in the time domain. Secondly, the appropriate number of points need to be sampled for each wave cycle to distinguish between different frequencies. For example, considering two frequencies f_1 and f_2, and one of them is the multiple integral of the other (say $f_2 = 2f_1$), for convergent simulations, more points are required per wave cycle for f_2. This relation can be expressed more precisely as follows. Assuming N_{cycle} is the number of points covering each sinusoidal cycle, then the minimum required number of time points is:

$$N_{simulation\,point} \geq N_{cycle}\, f\, t_{scan} \tag{5.5}$$

From 5.5, by assuming a fixed value for N_{cycle} (e.g. 100), the higher the frequency and/or longer the scanning time, the more points will be needed. This also means that the total computational time also increases. Of course, other factors such as complexity of the governing equations, number of dimensions, non-linear sources etc. also contribute to such an increase.

Parameter Symbol	Value	Units
D_R	$7.6 * 10^{-10}$	m^2/s
D_O	$7.6 * 10^{-10}$	m^2/s
k_0	0.001	m/s
α	0.5	$-$
C_{dl}	50	$\mu F/cm^2$
E_0	0.25	V
v_{scan}	50	mV/s
c_{R0}	1	mM
c_{O0}	0	mM
A	0.01	cm^2
E_{start}	-0.1	V
E_{vertex}	0.6	V
$\triangle E$	10	mV
$f_{fundamental}$	3	Hz

Table 19: Parameters for numerical calculations of the E reaction. The simulation is carried out in *Comsol Multiphysics*® using the dedicated Electrochemistry module

Figure 69: A typical one dimensional finite element meshing for macro electrode calculations

Figure 71 presents the simulated current with the above settings. Algorithm 5.1 presents the detail of extracting individual components from this total current. A critical point in this algorithm is determining the $N_{First\,Harmonic\,Index}$, $N_{Second\,Harmonic\,Index}$ and so on. These indices are found by simply plotting the absolute value (or two-sided power spectrum) of the vector Y after the FFT. Such two-sided spectrum not only reveals the peaks corresponding to current components, but also their relative strengths. The numerical positions of these peaks can then be taken as the harmonic indices (note that DC current has an index of 0). Currently, these numbers are manually read off the spectrum but future work could automate the process, for example

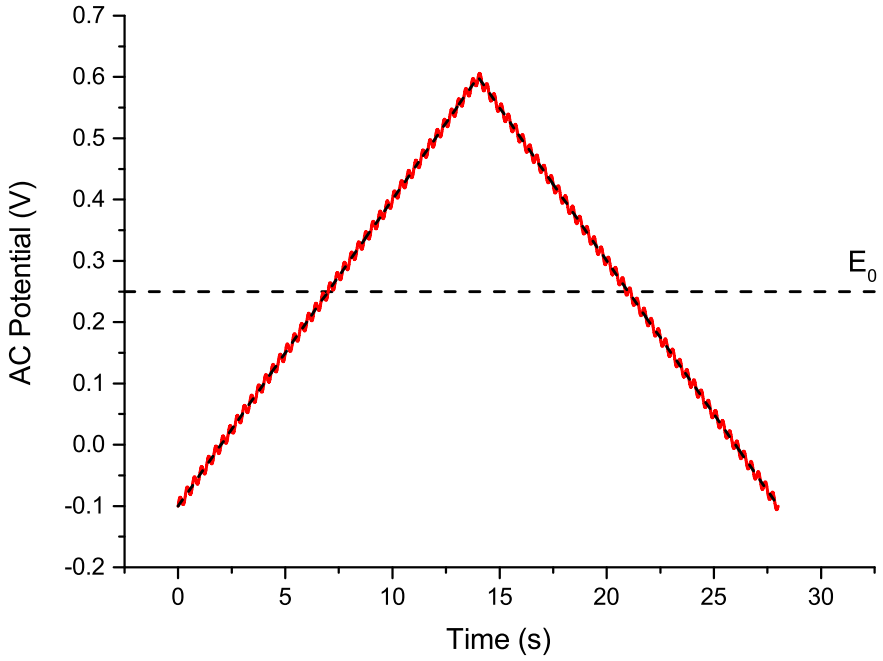

Figure 70: Applied AC Potential under amplitude $\triangle E = 10\,mV$ and $f = 3\,Hz$. The base-line (CV) potential is plotted as the dark dash line. The equilibrium potential E_0 is also included. Whilst the CV potential fundamentally drives the reaction, AC signal perturbs the process around a given potential and enhances the harmonics

via peak detection algorithm in time series [199].

The numbers N_{dc}, N_{First}, N_{Second}, etc. are simply heuristic choices. They are selected so that all the elements corresponding to respective harmonics are completely covered. The current work uses the following settings: $N_{dc} = 20$ and other Ns are set at 40. Although retrieval of only up to 4^{th} harmonic is shown in the code, the same procedure can be repeated to extract higher harmonics. Furthermore, the FFT and iFFT computations are extremely fast if the lengths L of the respective vectors are powers of 2. In that case, the numerical computation is easily carried out via the binary "dividing and conquer" approach [200, 201]. It should be noted that FFT computations are also available when the vector length is product of other prime numbers, but the power of 2 is the simplest and most intuitive case.

Figure 72 shows the single-sided spectrum obtaining from the FFT of the total current from Figure 71. By scaling the indices of the two-sided power spectrum, the one-sided power plot is easily obtained. In Figure 72, the first cluster at around 0

Algorithm 5.1 Harmonic Current extraction using FFT and inverse FFT (iFFT) functions. The algorithm is implemented in $Matlab^{®}$, which already has the built-in routines for FFT and iFFT. Variable L denotes the length of the current vector. Harmonic up to the 4^{th} is extracted but the methodology is easily extended to any harmonic number

Extract the current vector from storage file
Apply the FFT function $Y \rightarrow fft(current)$
Set $Y_{\text{dc}} = Y$
Set the elements between N_{dc} and $L - N_{\text{dc}}$ to 0
Apply the iFFT function $I_{\text{dc}} \rightarrow ifft(Y_{\text{dc}})$
Set $Y_{\text{First Harmonic}} = Y$
Set the elements of $Y_{\text{First Harmonic}}$ in the following intervals to 0: $[1, N_{\text{First Harmonic Index}} - N_{\text{First}}]$, $[N_{\text{First Harmonic Index}} + N_{\text{First}}, L - N_{\text{First Harmonic Index}} - N_{\text{First}}]$ and $[L - N_{\text{First Harmonic Index}} + N_{\text{First}}, L]$
Apply the iFFT function $I_{\text{First Harmonic}} \rightarrow ifft(Y_{\text{First Harmonic}})$
Set $Y_{\text{Second Harmonic}} = Y$
Set the elements of $Y_{\text{Second Harmonic}}$ in the following intervals to 0: $[1, N_{\text{Second Harmonic Index}} - N_{\text{Second}}]$, $[N_{\text{Second Harmonic Index}} + N_{\text{Second}}, L - N_{\text{Second Harmonic Index}} - N_{\text{Second}}]$ and $[L - N_{\text{Second Harmonic Index}} + N_{\text{Second}}, L]$
Apply the iFFT function $I_{\text{Second Harmonic}} \rightarrow ifft(Y_{\text{Second Harmonic}})$
Set $Y_{\text{Third Harmonic}} = Y$
Set the elements of $Y_{\text{Third Harmonic}}$ in the following intervals to 0: $[1, N_{\text{Third Harmonic Index}} - N_{\text{Third}}]$, $[N_{\text{Third Harmonic Index}} + N_{\text{Third}}, L - N_{\text{Third Harmonic Index}} - N_{\text{Third}}]$ and $[L - N_{\text{Third Harmonic Index}} + N_{\text{Third}}, L]$
Apply the iFFT function $I_{\text{Third Harmonic}} \rightarrow ifft(Y_{\text{Third Harmonic}})$
Set $Y_{\text{Fourth Harmonic}} = Y$
Set the elements of $Y_{\text{Fourth Harmonic}}$ in the following intervals to 0: $[1, N_{\text{Fourth Harmonic Index}} - N_{\text{Fourth}}]$, $[N_{\text{Fourth Harmonic Index}} + N_{\text{Fourth}}, L - N_{\text{Fourth Harmonic Index}} - N_{\text{Fourth}}]$ and $[L - N_{\text{Fourth Harmonic Index}} + N_{\text{Fourth}}, L]$
Apply the iFFT function $I_{\text{Fourth Harmonic}} \rightarrow ifft(Y_{\text{Fourth Harmonic}})$
Post-processing the data and plot the harmonics from I_{dc} to $I_{\text{Fourth Harmonic}}$ in time domain
Convert the harmonics in envelope format using Hilbert and Absolute functions and replot them

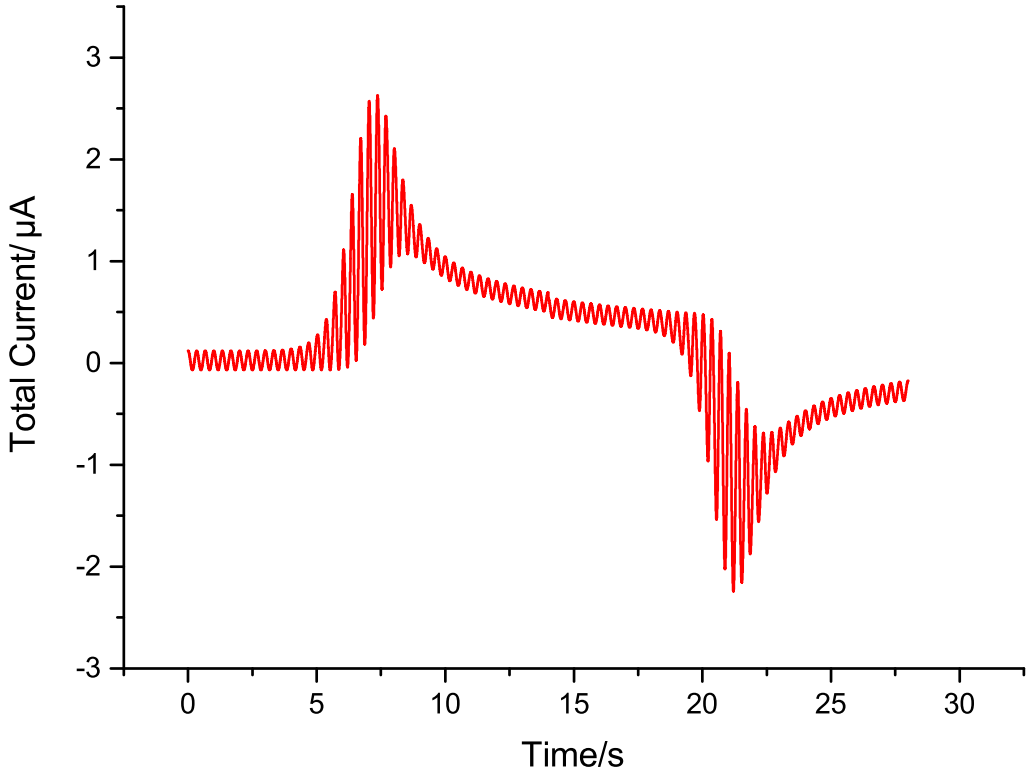

Figure 71: Simulated total current in time domain using the settings from Table 19

frequency evidently corresponds to the DC component. In addition, there are signals at the applied fundamental frequency of $3\,Hz$ and the secondary (due to non-linear effects) at $6\,Hz$. The secondary frequency is evidently very weak relative to the rest.

Closer inspection of Figure 72 reveals that the frequency peaks are not sharp but instead spread over a narrow neighborhood of each frequency. These clusters of frequencies do not overlap, implying that harmonic currents are distinct and exclusive of each other. Considering the principle $f = 3\,Hz$, the signal power axis shows that frequencies in range $2.5 - 3.5\,Hz$ are also present albeit at smaller magnitudes. Hence to be rigorous, the first harmonic $I_1(\omega t)$ is not composed of a single frequency, but a sum of many waves with frequencies close to each other $f \pm \triangle f$ ($\triangle f = 0.5\,Hz$). Physically, this phenomenon results in acoustics beat and I_1 is essentially a beat rather than a pure sinusoidal wave. However to keep the context simple, this complication is not considered further.

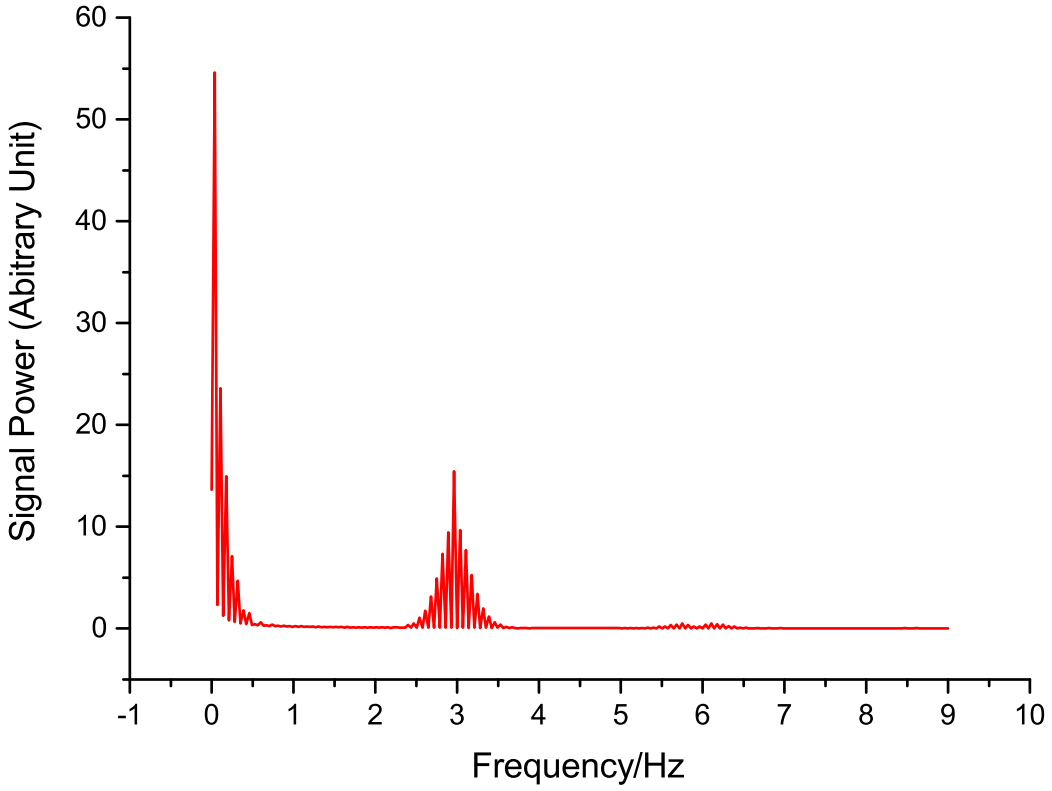

Figure 72: Single Sided Power spectrum of the simulated current above. This one-sided spectrum is derived directly from the two-sided counter-part by scaling with respect to the frequency

By separating each element corresponding to the currents and applying iFFT function as outlined in algorithm above, these harmonics are recovered and plotted out in Figures 73, 74 and 75. As noted earlier, the signal magnitude for the 2^{nd} harmonic is considerably smaller than that of the 1^{st} harmonic. There is a negligible peak at the 3^{rd} harmonic so the current is essentially 0. The fundamental harmonic possesses 1 peak for the forward sweep between 0 and 14 (s) and an extra peak in the backward scan (between 14 and 28 (s)). For the 2^{nd} harmonic, the forward wave contains 2 peaks and so does the backward wave.

Figures 74 and 75 above are usually referred to as the full plots. Another way of representing these currents is to plot out just the envelope. A main advantage of the envelope plots is the simplicity in information representation by retaining only the

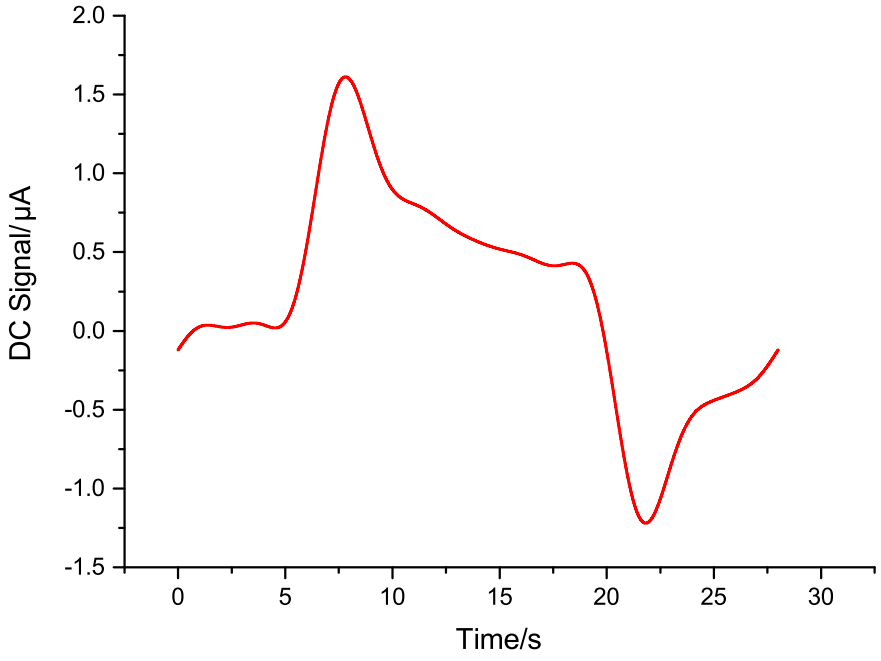

Figure 73: Recovered DC signal from the AC current in Figure 71

main feature of the graphs. For a sinusoidal function, an envelope can be constructed by simply joining its local extremes [202]. In the current case, the *hilbert* function is applied to the sinusoidal function in order to calculate the corresponding envelope. Furthermore, it is visible that the upper and lower parts of each harmonic figure are completely symmetrical. Consequently, it is more economical to only plot the positive section (i.e. upper part) of each envelope. By applying the above operations to the harmonic currents, Figures 76 and 77 are obtained. From this section onwards, all the harmonics will be plotted in envelopes instead of full formats.

The base line of 1^{st} harmonic is above 0. This characteristic can be attributed to the sinusoidal capacitive current. The size of such current can be calculated by the following expression:

$$I_c^{ac} = AC_{dl}\frac{dE_{ac}}{dt} = AC_{dl}\triangle E\omega cos(\omega t) \tag{5.6}$$

thus the maximum value of I_c^{ac} is attained when $cos(\omega t) = 1$ which is the base-line

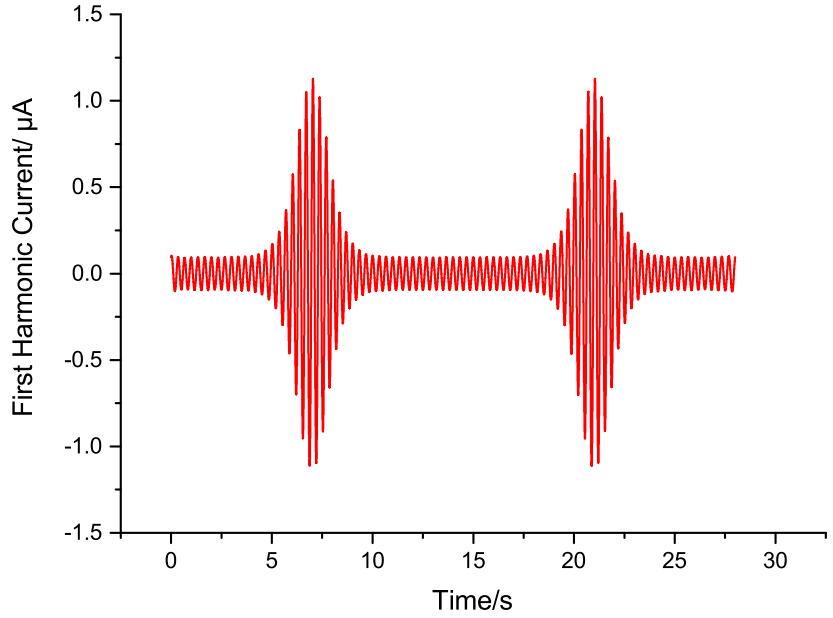

Figure 74: Recovered 1^{st} harmonic signal from the AC current

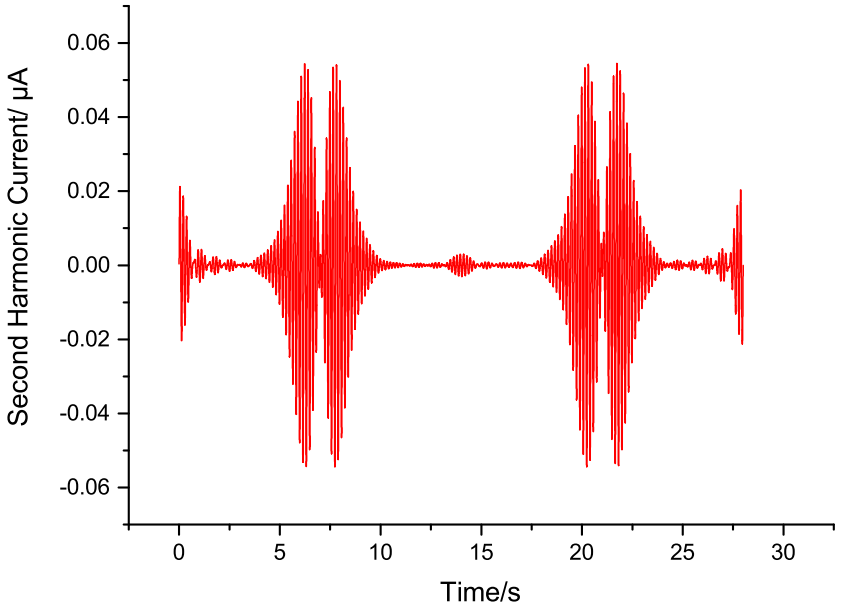

Figure 75: Recovered 2^{nd} harmonic signal from the AC current

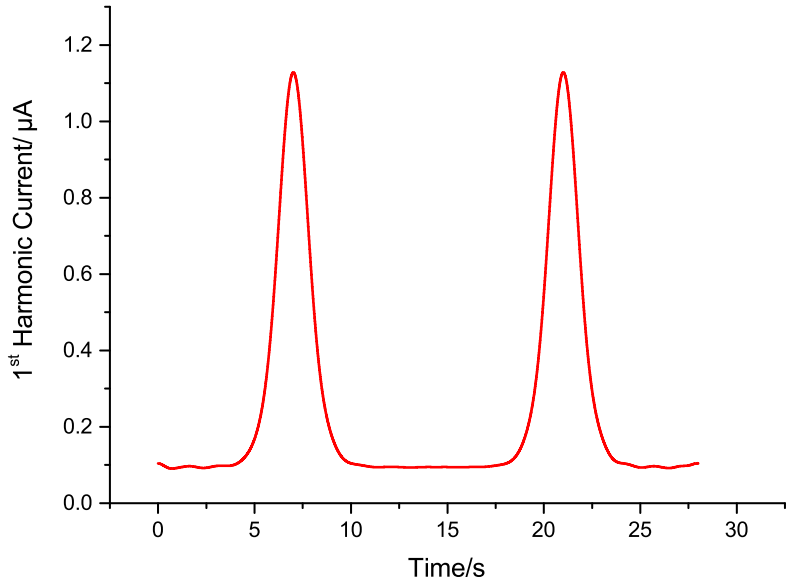

Figure 76: 1^{st} harmonic in Figure 74 plotted in the envelope format

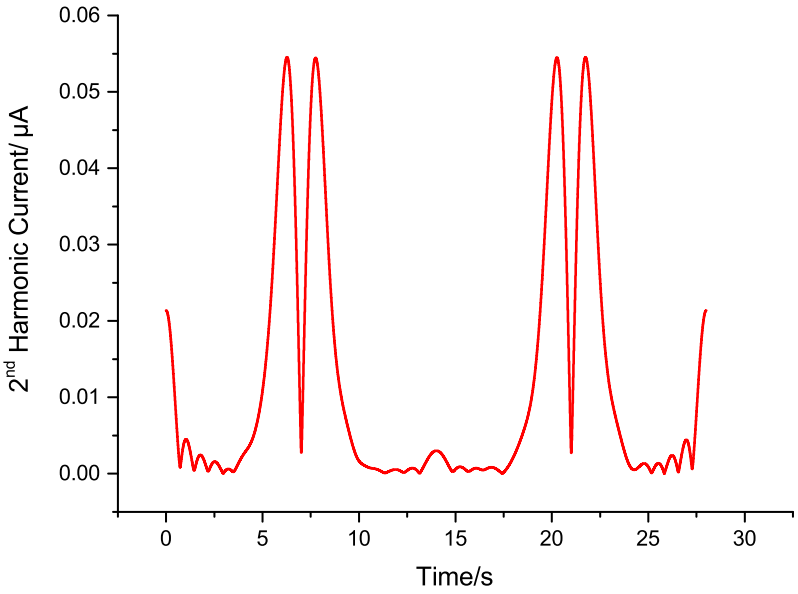

Figure 77: 2^{nd} harmonic in Figure 75 plotted in the envelope format. Notice large fringes at the beginning and end of the voltammogram

in the Figure 76:

$$max\, I_c^{ac} = AC_{dl} \triangle E \omega = AC_{dl} \triangle E\, (2\pi f) \tag{5.7}$$

Using the parameters in Table 19, Equation 5.7 is estimated to be:

$$0.01\, cm^2 * 50.10^{-6}\, \frac{F}{cm^2}\, 10\, 10^{-3}\, (V) * 2\pi\, 3\, (Hz) \sim 9.2 * 10^{-8}\, (A)$$

which is in good agreement with the reading from the Figure 76 (about $0.1\, \mu A$). On the other hand, the 2^{nd} or higher harmonics are essentially free of the capacitive current, hence the base line for these currents should be at $0\, (A)$. However, this appears not to be the case from Figure 75. The main reason for this unexpected behavior is due to inverse transform of the vector $Y_{Second\, Harmonic}$. Since this vector contains very small numbers, the procedure introduces some numerical errors. Furthermore, such errors are not negligible when being compared to the peak current in the 2^{nd} harmonic (almost 40% of the maximum value). The next section shows that by simply increasing the amplitude $\triangle E$, this problem is effectively eliminated.

5.3 Effect of Large Amplitude on Harmonics

The last section concludes that under small AC amplitude, the 2^{nd} harmonic current becomes very small. When this occurs, it could become difficult to separate the actual harmonics from the background current. In real experiments, such problem can complicate data analysis step. Furthermore, numerical errors can arise during the inverse FFT step and the base-line for higher harmonics are not well defined. Effects such as fringes at the beginning, end and middle of the AC voltammograms are indicative signs of such problem.

To eliminate the fringe effects, a general strategy is to increase $\triangle E$. Such change enhances the signal strength of the 2^{nd} harmonic. However, the signal power spectrum still follows the decreasing pattern as shown in Figure 72. Thus at some high frequencies, the harmonic becomes small enough that the fringe effect becomes significant again. To extract these higher harmonics, one can simply increase the amplitude even further. In literature and practice, up to 7^{th} harmonic has been reported. In this work, however, attention here is restricted upto the 4^{th} harmonic.

Figure 80 shows the single sided power spectrum under the increased amplitude $\triangle E = 40\,mV$. Under this new circumstance, signal power of the 1^{st} harmonic is now larger than that of the DC component. This is to be contrasted with Figure 72, in which DC current has larger power magnitude. A possible explanation is that when the amplitude of the perturbing signal is increased, signal strength enhancement distributes mainly to the harmonics and little to the DC current. The conclusion is self-evident, given the fact that the DC current corresponding only to the DC signal input and it should therefore be the same regardless of $\triangle E$ being 10 or $40\,mV$.

Figures 78 and 79 show the effect of larger amplitude on harmonic currents. For the 1^{st} harmonic, notice that both the peak and the baseline shift upwards. The base-line shifting can again be explained by using Equation 5.7. Because $\triangle E$ is increased by 4 times, the magnitude of the base line should also increase by the same amount, from about $0.09\,\mu A$ to about $0.36\,\mu A$ as shown in the Figure 78. In the 2^{nd} harmonic, the peak becomes much larger than the fringes caused by the numerical computation and the base-line is considered to be well-defined at 0. In addition, the voltammograms for 3^{rd} and 4^{th} harmonics are also included. The 3^{rd} component is fairly well recovered with minor fringe effects. On the other hand, the last harmonic is not well resolved and thus requires a further increase in $\triangle E$.

As an additional note, when $\triangle E$ is increased, the perturbation signal around a

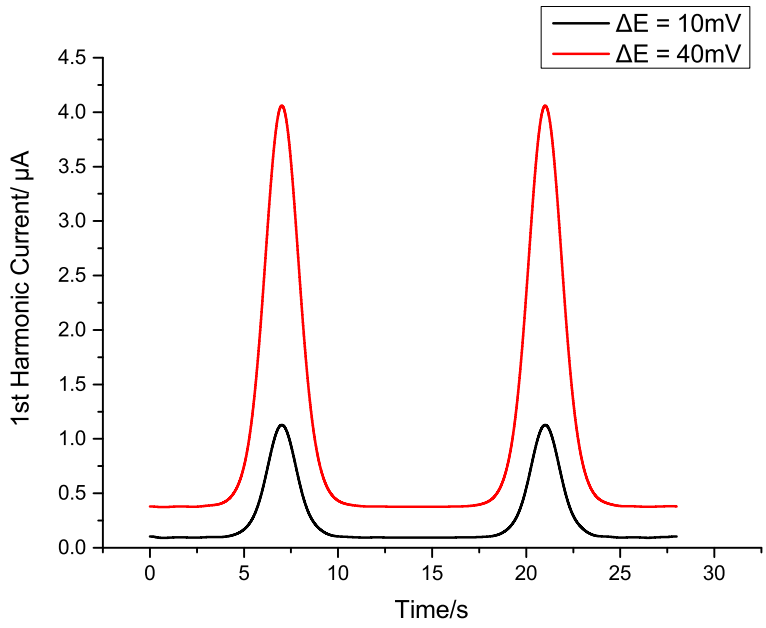

Figure 78: Comparison of 1^{st} harmonic current under $10\,mV$ (black line) and $40\,mV$ (red line). Notice that the base line shift upwards as the amplitude is increased

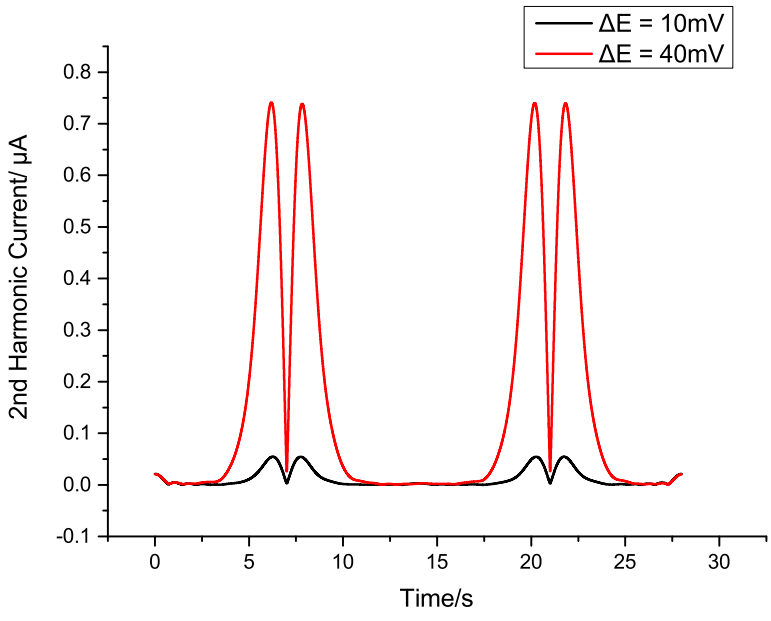

Figure 79: Comparison of 2^{nd} harmonic current under $10\,mV$ (black) and $40\,mV$ (red)

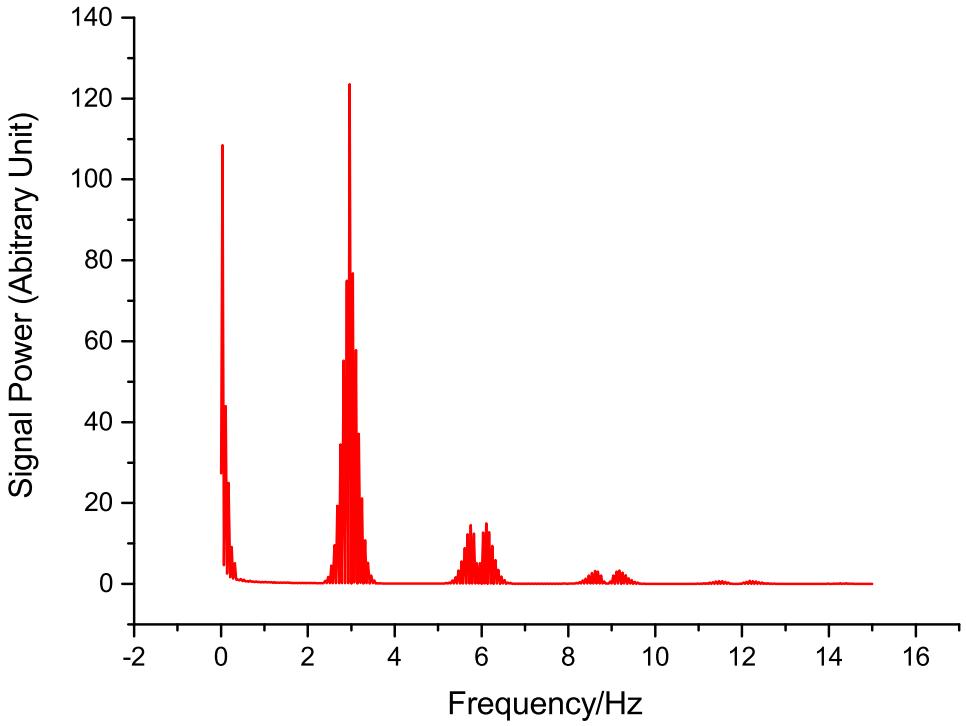

Figure 80: Power spectrum for harmonic signal at $\triangle E = 40\,mV$. Note that under larger sinusoidal amplitude, higher frequencies start to appear. In this case, even the 4^{th} harmonic (i.e. $f_4 = 12\,Hz$) is weakly visible on the spectrum

given potential is also larger. Therefore, in order to converge the PDEs solutions, either smaller time steps or extra iterations is required. In this study, the former approach is preferred. Usually this process can be done via trial-and-error. One usually starts with a reasonably large number of time points and small amplitude first. The amplitude is then increased and the simulation is performed again. The number of time points are afterwards doubled and the run is repeated, often with slight improvements in convergence. The procedure is reiterated until satisfactory convergence level is achieved.

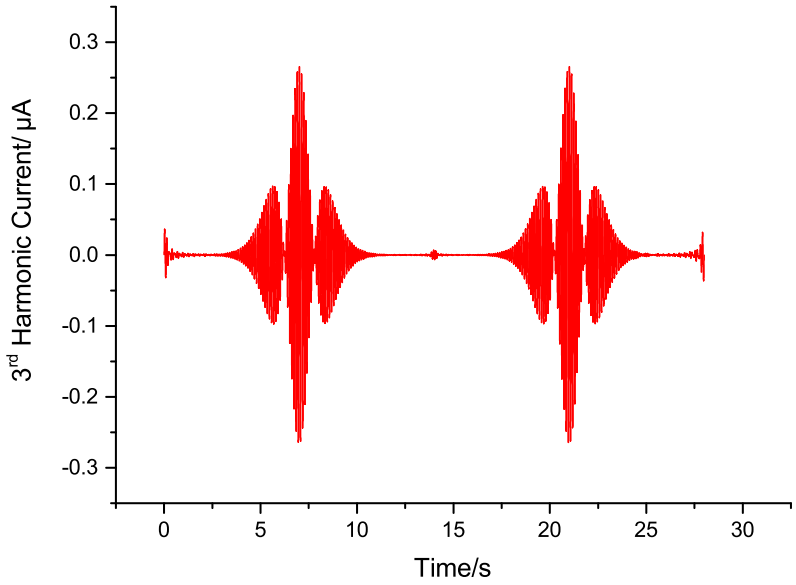

Figure 81: 3^{rd} harmonic current (full form) under $\triangle E = 40\,mV$. There are 3 peaks in both forward and backward scans

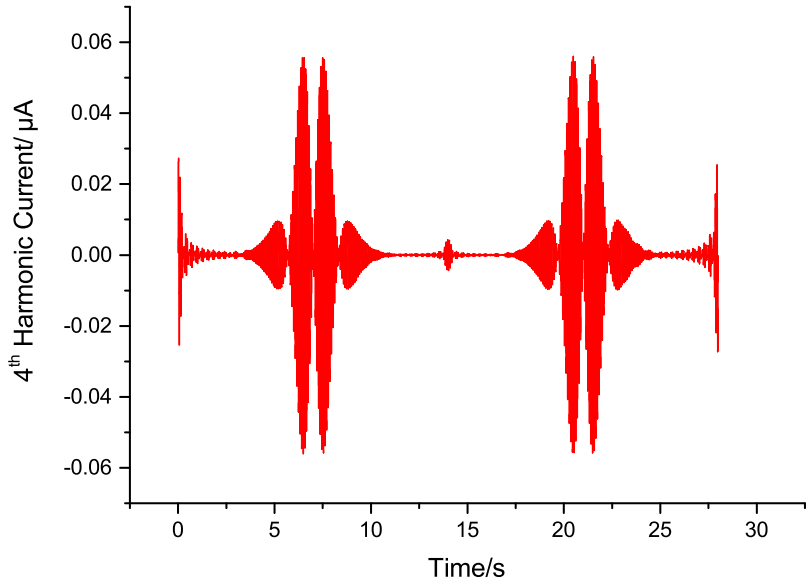

Figure 82: 4^{th}harmonic current (full form) with 4 peaks in each direction of scan

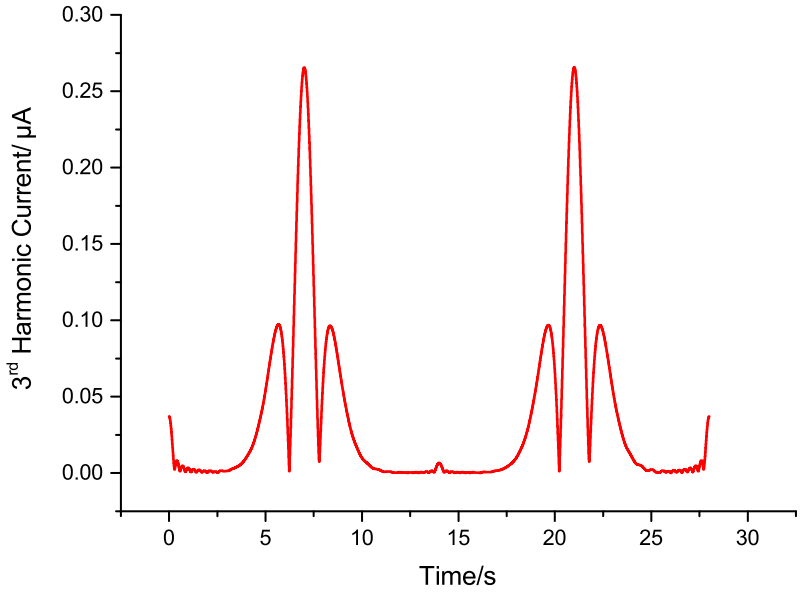

Figure 83: 3^{rd} harmonic in envelope format

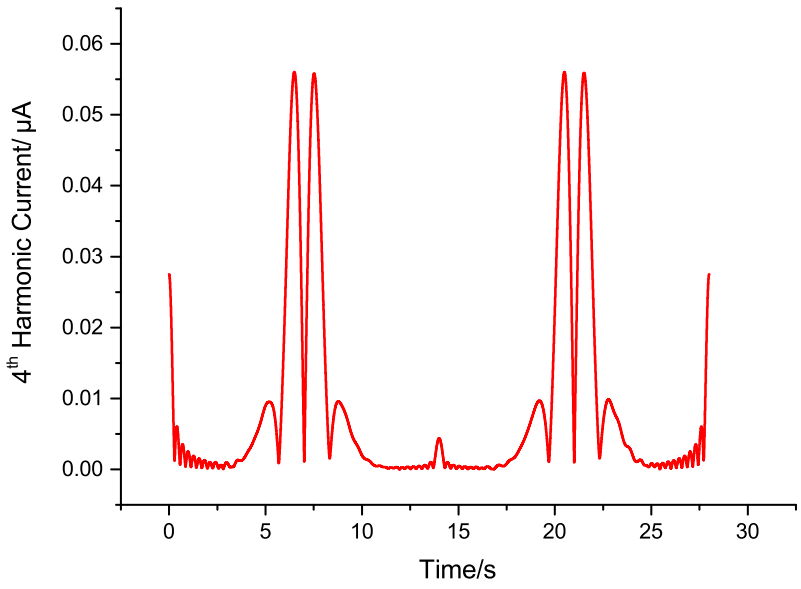

Figure 84: 4^{th} harmonic in envelope format

5.4 EC' Mechanism under Fourier Transform AC voltammetry

The self-catalytic EC' mechanism is introduced earlier in Chapter 2. The reaction scheme is repeated here for the sake of clarity:

$$R \leftrightarrow O + e^{-} \, (E) \tag{5.8}$$

$$O + S \rightarrow R + P \, (C') \tag{5.9}$$

Species S is often referred to as the substrate. In experiments, a similar compounded called L-cysteine is often used to mimic the sulphide molecule. L-cysteine is a crystalline compound and has good solubility in water. Due to its bulky molecular structure, a representative value of $6 * 10^{-6} \, m^2/s$ is assumed for the substrate diffusivity. Additional parameter settings for simulations in this section are summarized in Table 20.

Parameter Symbol	(Range of) Value	Units
v_{scan}	10	mV/s
c_{S0}	$1 - 4$	mM
D_S	$6 * 10^{-10}$	m^2/s
$\triangle E$	$40 - 50$	mV
$k_{EC'}$	1000	$(Ms)^{-1}$
$f_{fundamental}$	$1 - 6$	Hz

Table 20: Additional parameters for the EC' mechanism. The rest of parameters are the same as in the Table 19. Reaction constant $k_{EC'}$ of the homogenous reaction 5.9 is assumed to be sufficiently large

The reaction-diffusion PDEs corresponding to the above mechanism are as follows (assuming negligible migration flux):

$$\frac{\partial c_R}{\partial t} = D_R \nabla^2 c_R + k_{EC'} c_O c_S$$

$$\frac{\partial c_O}{\partial t} = D_O \nabla^2 c_O - k_{EC'} c_O c_S$$

$$\frac{\partial c_S}{\partial t} = D_S \nabla^2 c_S - k_{EC'} c_O c_S \tag{5.10}$$

For a macro electrode, a typical linear cyclic voltammetry at slow scan rates is presented in Figure 85. An interesting phenomenon is the pre-wave during forward scan of the voltammogram. In order to the pre-wave to manifest, it requires a fast C' step, a slow scan rate and a reasonably fast E reaction. The first and third conditions ensure maximum regeneration (and re-oxidization) of species R at early potential and therefore more current is generated in comparison to the non-catalytic cases. In addition, fast C' kinetics exhausts substrate near the electrode surface and the current becomes limited by substrate diffusion from the bulk, thus forming the pre-wave. In addition, if a larger scan rate is used and the applied potential varies more quickly, the current has less time to become substrate-limited. Under such circumstance, the pre-wave does not appear in the voltammogram. Finally, it was demonstrated that there is a linear relation between the pre-wave peak and the substrate concentration (Figure 39).

In general, the pre-wave phenomenon occurs under a special circumstance called total catalysis (Figure 86) [203]. The vertical axis represents homogenous reaction kinetics (C') step while the horizontal axis denotes the substrate concentration ratio c_{S0}/c_{R0}. Restricted conditions are required for the phenomenon, namely the large C' kinetics and the right-level substrate ratio. Because λ is defined as:

$$\lambda = \frac{RT}{F}\frac{k_{EC'}c_{R0}}{\upsilon_{scan}}$$

hence a slow scan rate is required to compensate for possibly slow kinetics $k_{EC'}$. Since pre-wave contains useful analytical information, a great deal of experimental effort is invested in finding the right chemicals to increase λ and consequently shifting the electrochemical responses towards zone $KT2$.

The above discussion demonstrates that a simple E_{dc} signal can be used to evoke the effect of EC' reaction, i.e. the pre-wave phenomenon as seen in the aperiodic I_{dc} component. Under Nernstian reactions, the AC components are dependent on the diffusion layer. Consequently, a similar phenomenon is expected for the harmonics if the sinusoidal component 5.2 is included.

The subsequent sections focus on the applications of AC voltammetry to examine the pre-wave effects in harmonic currents. To compare the effects of mass transport, macro and micro electrodes are used. Whilst diffusion limit control is easily attained using the former device, the enhanced mass transport under micro electrodes would possibly lead to different current responses.

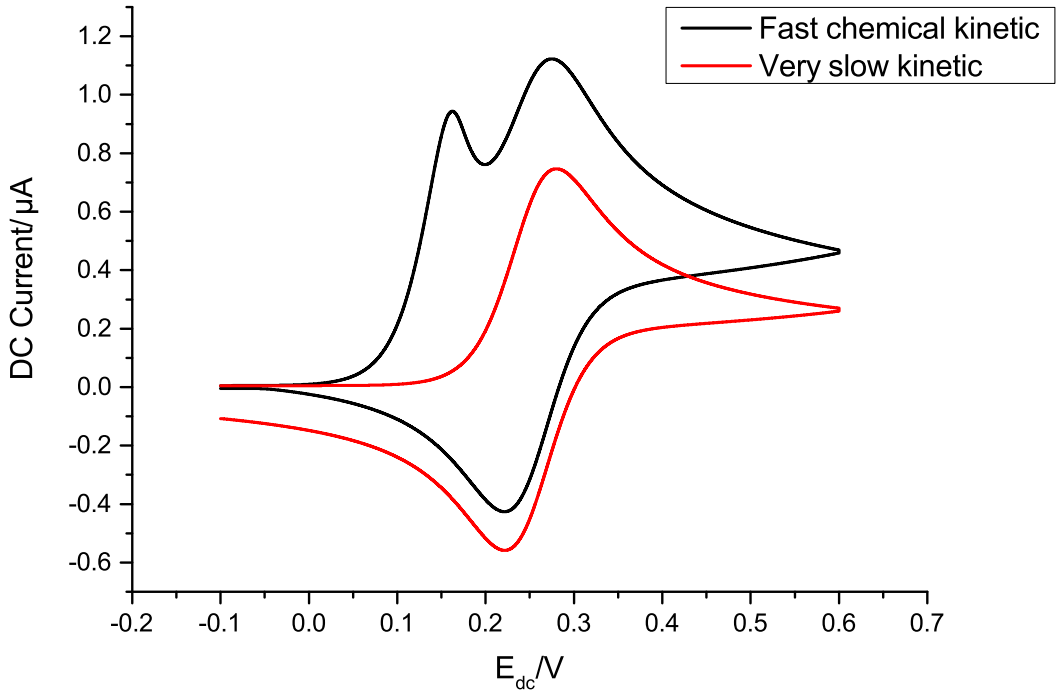

Figure 85: The pre-wave phenomenon under DC signal (black) for a macro electrode. The first peak is due to the substrate diffusion limitation and the second peak corresponds to the usual E reaction. The overall current increases substantially in comparison to the lower kinetic case (red). The scan rate is $10\,mV/s$ and the substrate concentration is $c_{S0} = 1.0\,mM$ (or substrate concentration ratio $c_{S0}/c_{R0} = 1.0$)

5.4.1 Macro Planar Electrode

The first calculation aims to investigate whether total catalysis is observable with AC signals. A large amplitude of $\triangle E = 50\,mV$ is used to enhance the harmonics. The scan rate is fixed at $10\,mV/s$ and given the voltage window between -0.1 and $0.6\,V$ the total scanning time is now $2\,t_{scan} = 140\,(s)$. From Equation 5.5, the total points $N_{simulation\,points}$ should be higher to maintain the solution convergence. For the current case, $N_{simulation\,point} = 2^{17}$ (compared to 2^{16} for the simple E reaction) is selected. To ensure concentration convergence, the reaction layer zone (Figure 36) is estimated to be:

$$L_{rxn} = (\frac{D_R}{k_{EC'}c_{R0}})^{1/2} \tag{5.11}$$

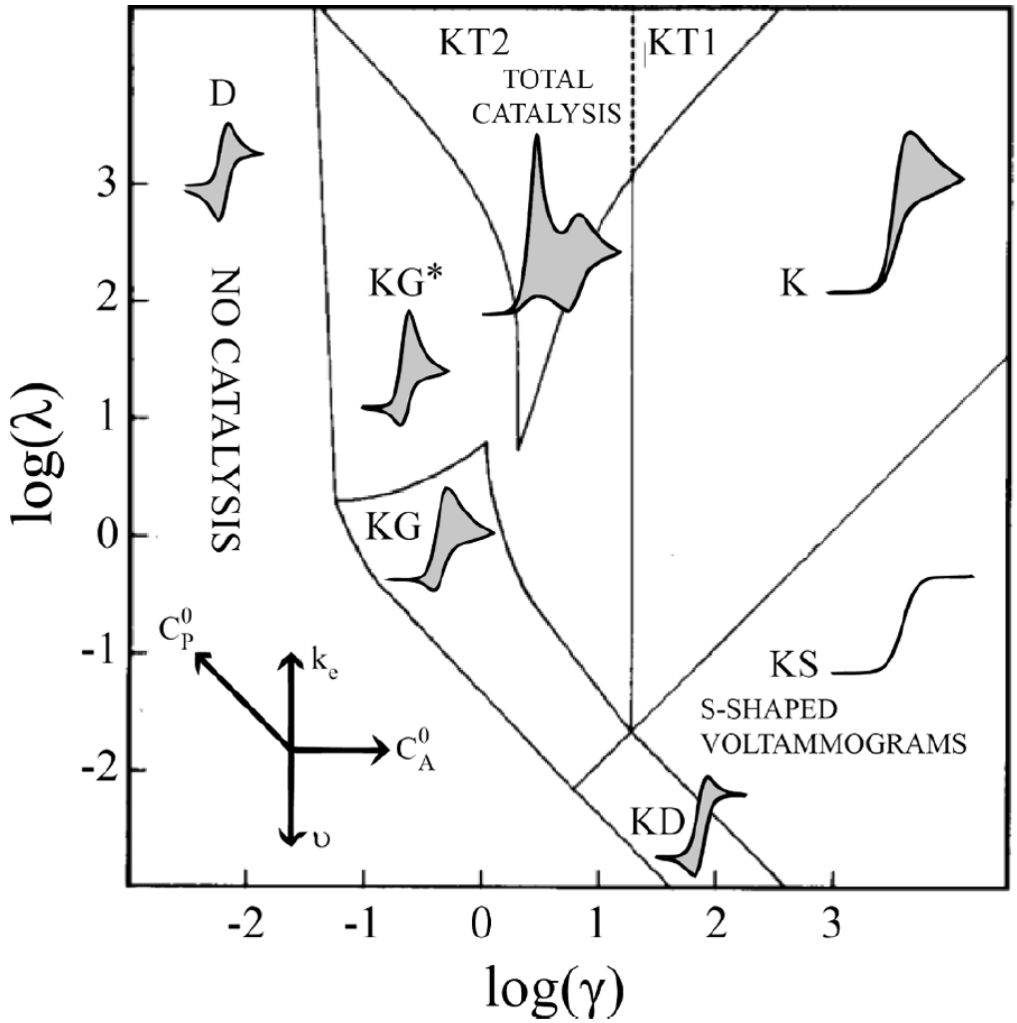

Figure 86: The CV diagrams for EC' mechanism under various combinations of reaction kinetic (vertical axis) and concentration ratio (horizontal axis) factors

From Equation 5.11, the layer size is about $6 * 10^{-7}\,(m)$. Thus in generating the mesh, the smallest element is set at $100\,(nm)$ with the exponential growth rate of 1.2. Different substrate ratios c_{S0}/c_{R0} are used, ranging between 0.5 and 4. Because c_{R0} is fixed at $1\,mM$, the setting corresponds to c_{S0} between 0.5 and $4\,mM$. The results are presented in two sets of Figures 87, 88 and 89, 90 below.

Two observations are evident from the above set of figures. Firstly, the split-wave is present in all harmonics. In addition, the split-wave is clearest at low frequencies ($f = 1$ and $2\,Hz$) and only a single peak is present at higher frequencies. However, the effect is sustained at substrate ratio as high as $c_{S0}/c_{R0} = 4.0$ at all frequencies. Thanks to the use of large amplitude, all the harmonics from 2^{nd} onwards are well resolved with

base-lines of 0. Therfore in order to manifest the pre-wave, slow modulation of AC signal is recommended. Another interpretation is suggested as follows. Considering the scan rate corresponding to sinusoidal current, which is computed from E_{ac} as:

$$v_{scan}^{ac} = \triangle E\, \omega = 2\pi f \triangle E \tag{5.12}$$

thus increasing f leads to a larger v_{scan}^{ac} and this has the same effect of larger v_{scan} as discussed from Figure 85, which is to dampen the pre-wave current.

It was also shown in Chapter 2 that under the DC signal, the pre-wave peak current is proportional to the substrate ratio (Figure 39). This information is analytically useful as it can be used to calibrate sensors for the substrate. To investigate the similar correlation, the 1^{st} and 2^{nd} harmonics under frequencies of 1 and $2\,Hz$ are first plotted out (Figures 91 and 92). Correlation between the peak currents and substrate concentrations are plotted in Figures respectively. Similar to the pre-wave in DC current, there is a strong linear correlation between the pre-wave peaks in the 1^{st} and 2^{nd} harmonics and the substrate levels (all the unadjusted Pearson R^2 are all around 0.999). For the 1^{st} harmonic since the frequency is fixed, the value of the base-line does not affect the shown correlations.

When the substrate ratio falls below 0.5, the pre-wave diminish, thus making substrate calibration using the harmonics difficult. The effect of increasing $\triangle E$ is investigated for substrate ratio of 0.5 as shown in Figure 95. The pre-wave does not become more distinct at higher amplitudes (e.g. $80\,mV$). This observation indicates that it may not be possible to express the fundamental chemistry just by amplifying the amplitude. Finally, though similar analytical correlations can be derived for the 3^{rd} and 4^{th} harmonics, the first two harmonics are adequate to demonstrate the principle. More importantly for the 2^{nd} harmonic, the confirmed linear relationship is evidently useful because the current is less influenced by the electrical double layer.

Selected experimental results are also included to illustrate the design choice above. The experiments first use Ferrocene Carboxylic Acid (FCA) as electroactive species. A primary reason for using FCA is because the electrochemical behavior of the species was known to be close to reversible and is therefore suitable for EC' reaction. The raw data are first collected and a simple procedure is then implemented in $Matlab$® to decimate sections of data points which helps reduce the file size.

Figures 97 and 98 confirm important features of the harmonics shown in simulations. Firstly, the pre-waves increase with the substrate ratio and becomes subdued

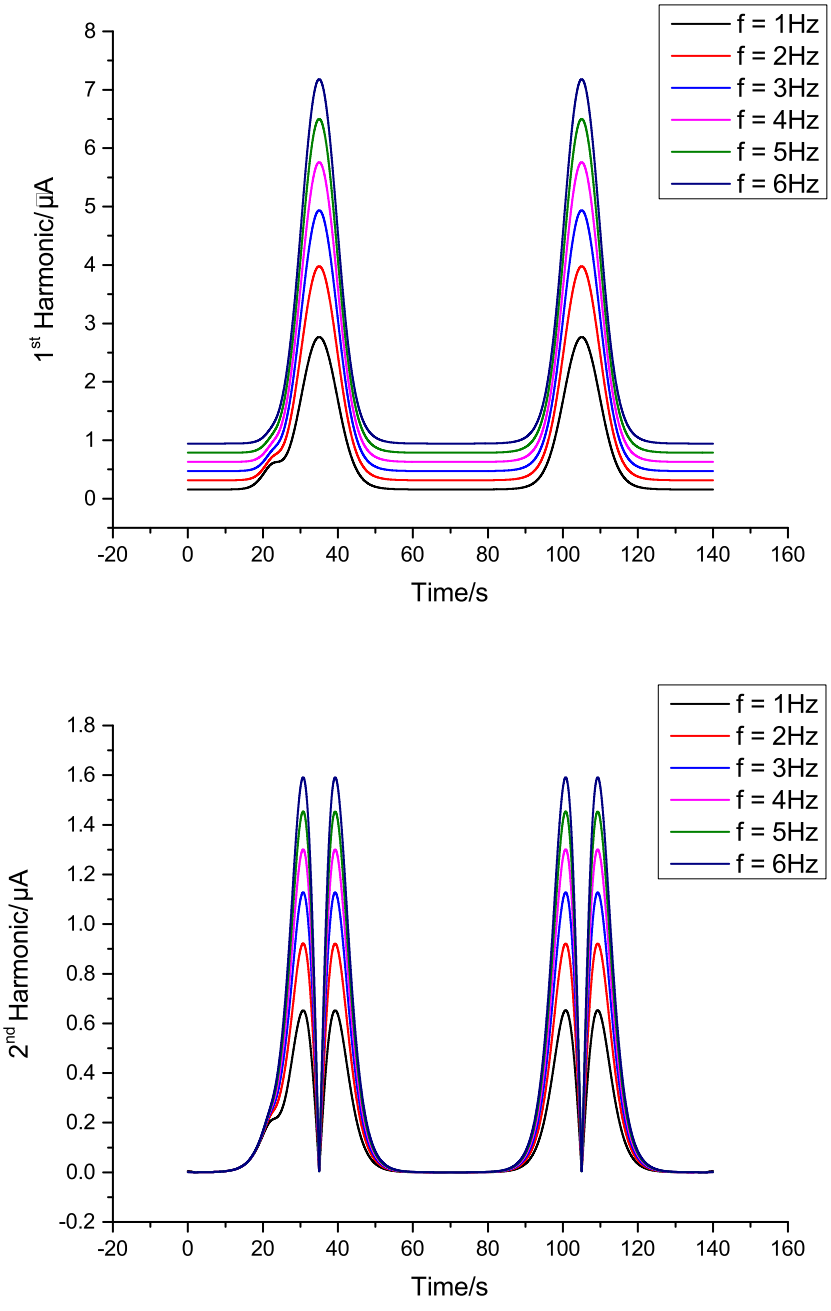

Figure 87: 1^{st} (top) and 2^{nd} (bottom) harmonics at at $c_{S0} = 0.5\,mM$ or substrate ratio $c_{S0}/c_{R0} = 0.5$ at various frequencies between $f = 1$ and $6\,Hz$

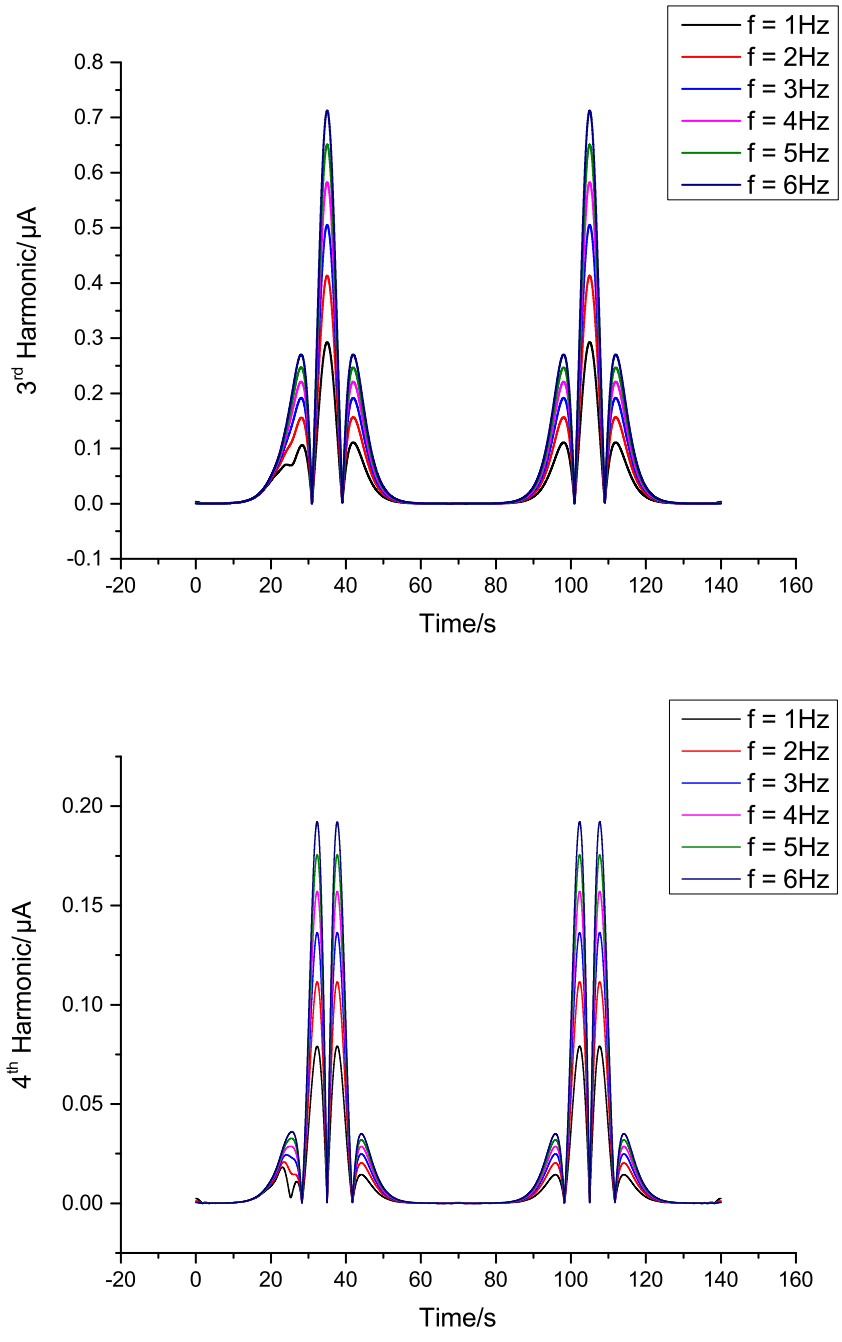

Figure 88: 3^{rd} (top) and 4^{th} (bottom) harmonics at at $c_{S0} = 0.5\,mM$ or substrate ratio $c_{S0}/c_{R0} = 0.5$ at various frequencies between $f = 1$ and $6\,Hz$

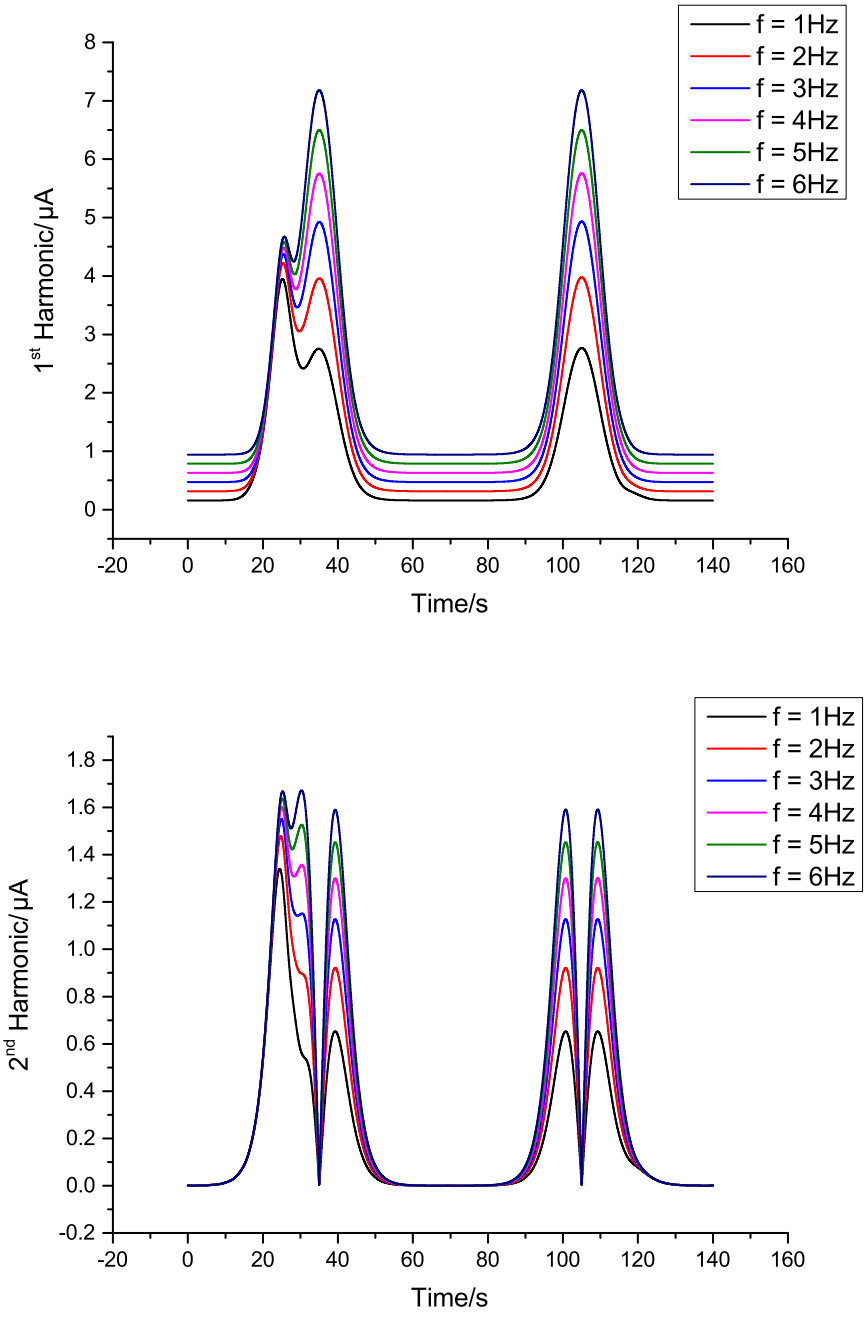

Figure 89: 1^{st} (top) and 2^{nd} (bottom) harmonics at at $c_{S0} = 4\,mM$ or substrate ratio $c_{S0}/c_{R0} = 4$ at various frequencies between $f = 1$ and $6\,Hz$

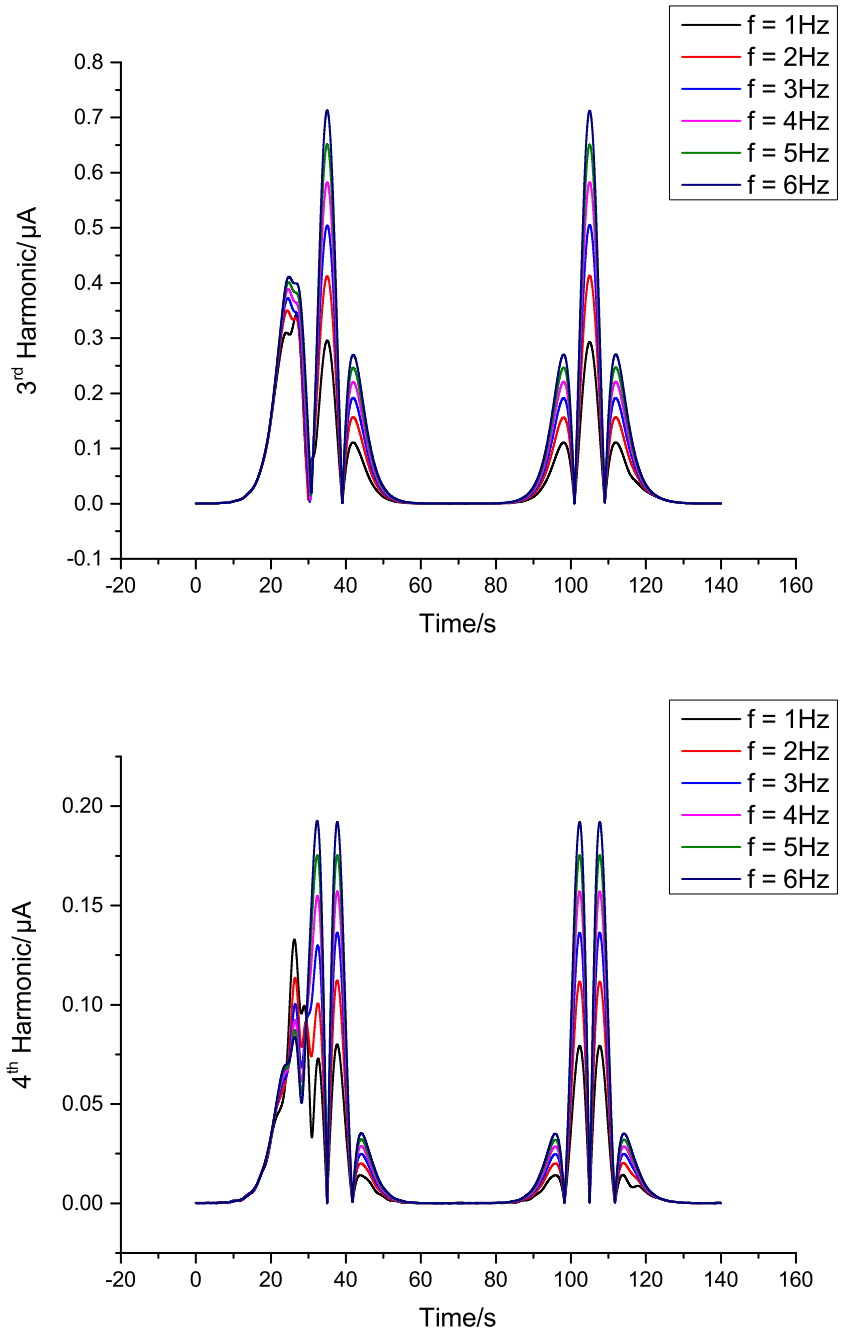

Figure 90: 3^{rd} (top) and 4^{th} (bottom) harmonics at at $c_{S0} = 4\,mM$ or substrate ratio $c_{S0}/c_{R0} = 4$ at various frequencies between $f = 1$ and $6\,Hz$

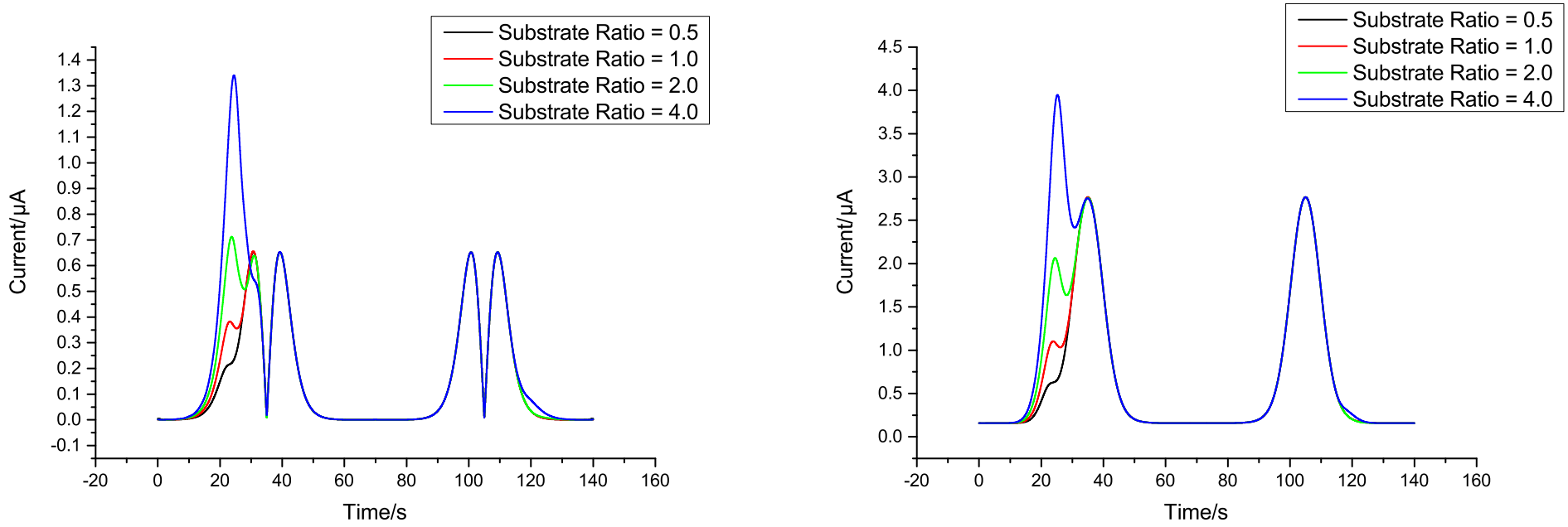

Figure 91: 1^{st} (right) and 2^{nd} (left) harmonics at different substrate ratios 0.5, 1.0, 2.0 and 4.0 (the frequency is fixed at $1\,Hz$)

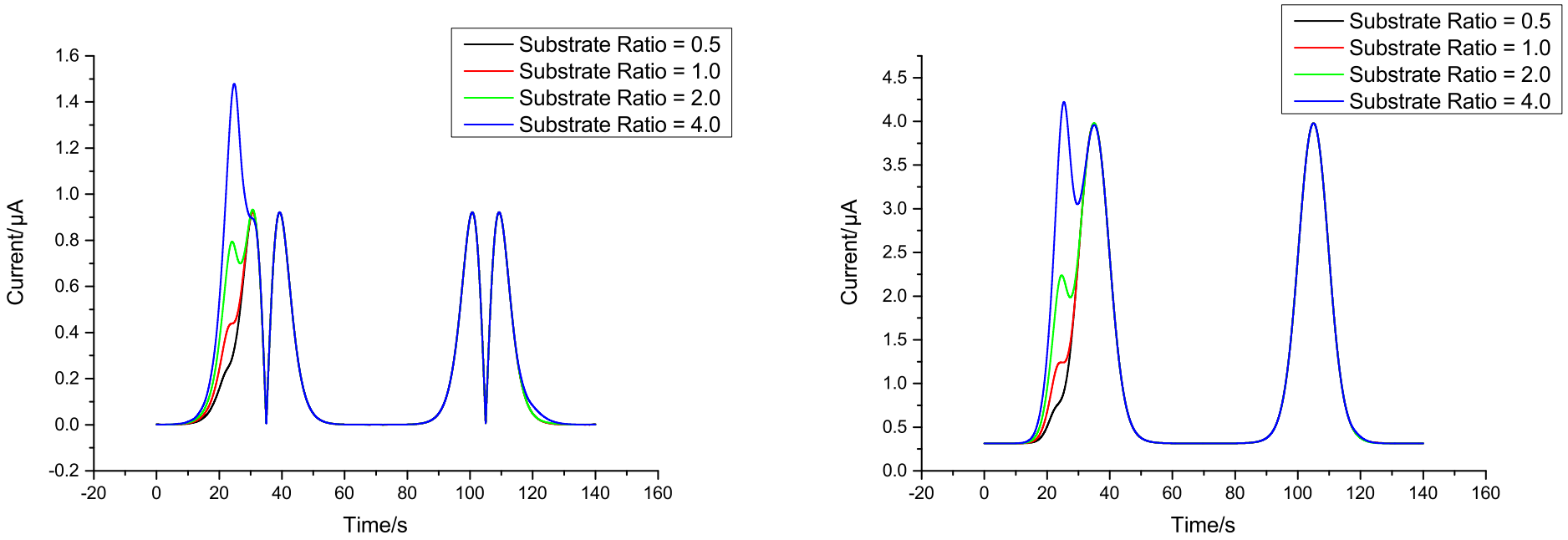

Figure 92: 1^{st} (right) and 2^{nd} (left) harmonics at different substrate ratios 0.5, 1.0, 2.0 and 4.0 (the frequency is fixed at $2\,Hz$)

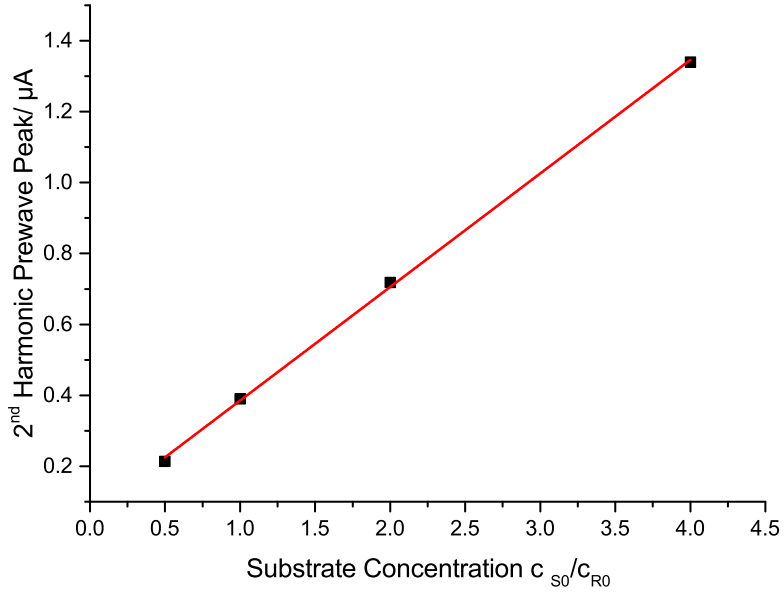

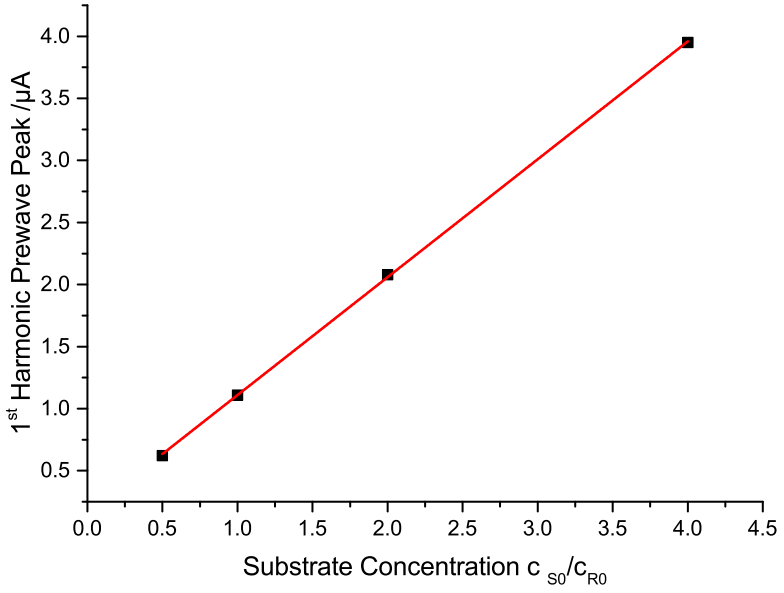

Figure 93: Plots of the pre-wave peak currents in the 1^{st} (right) and 2^{nd} (left) harmonics versus the substrate concentrations for $f = 1\,Hz$. The Pearson (unadjusted) R^2 coefficients are 0.9999 and 0.9997 respectively. The calculations are done with *Origin Lab*® (version 9.1)

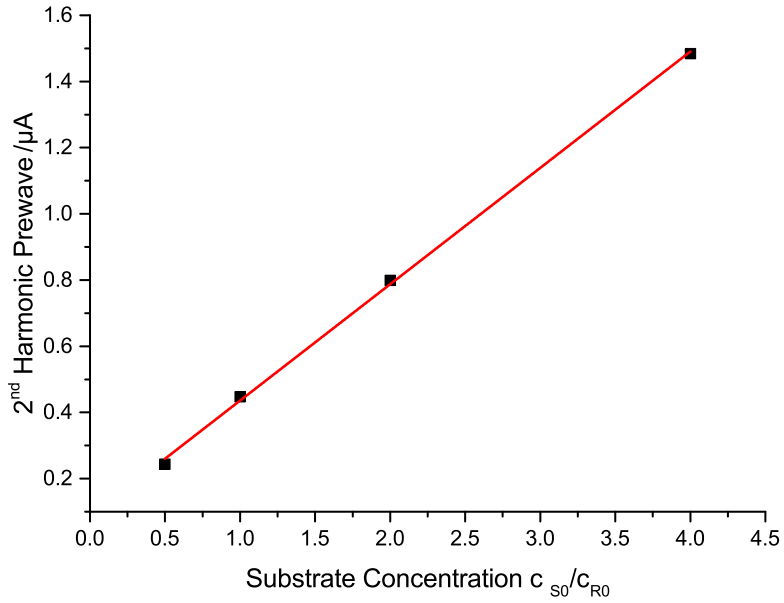

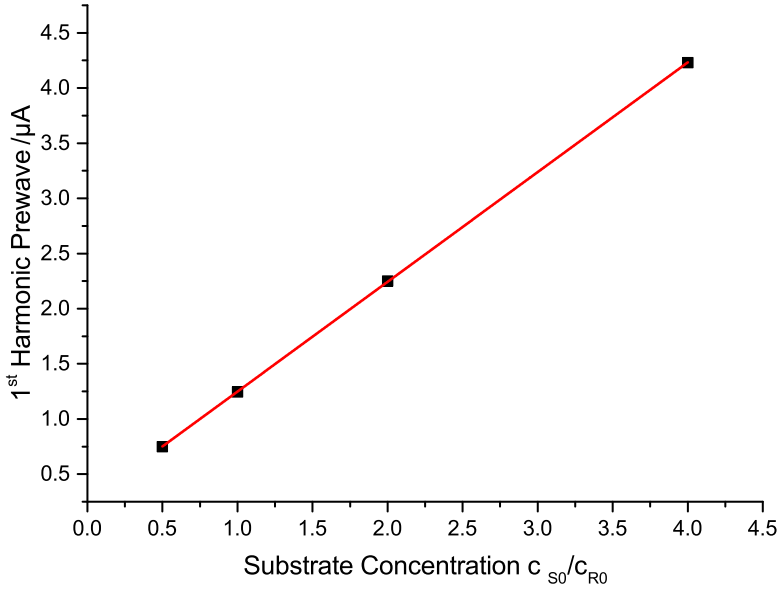

Figure 94: Plots of the pre-wave peak currents in the 1^{st} (right) and 2^{nd} (left) harmonics versus the substrate concentrations for $f = 2\,Hz$. The Pearson (unadjusted) R^2 coefficients are 0.9999 and 0.9991 respectively. The calculations are done with *Origin Lab*® (version 9.1)

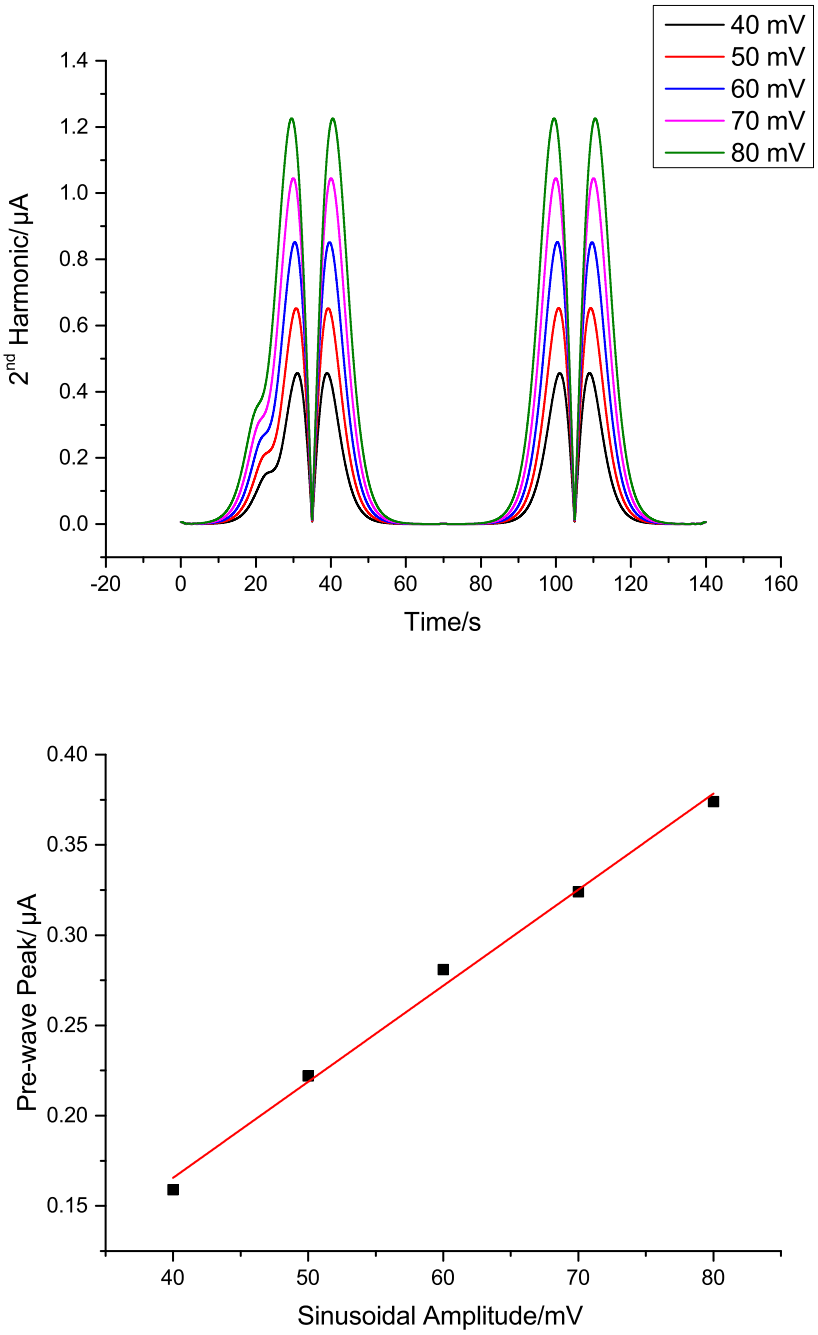

Figure 95: 2^{nd} harmonic current under different sinusoidal amplitudes (top) and plot of pre-wave peak currents versus the sinusoidal amplitude (bottom). At higher amplitudes, the pre-waves becomes less distinct and difficult to find within the current. Consequently, the linear fit (red line) is not very good

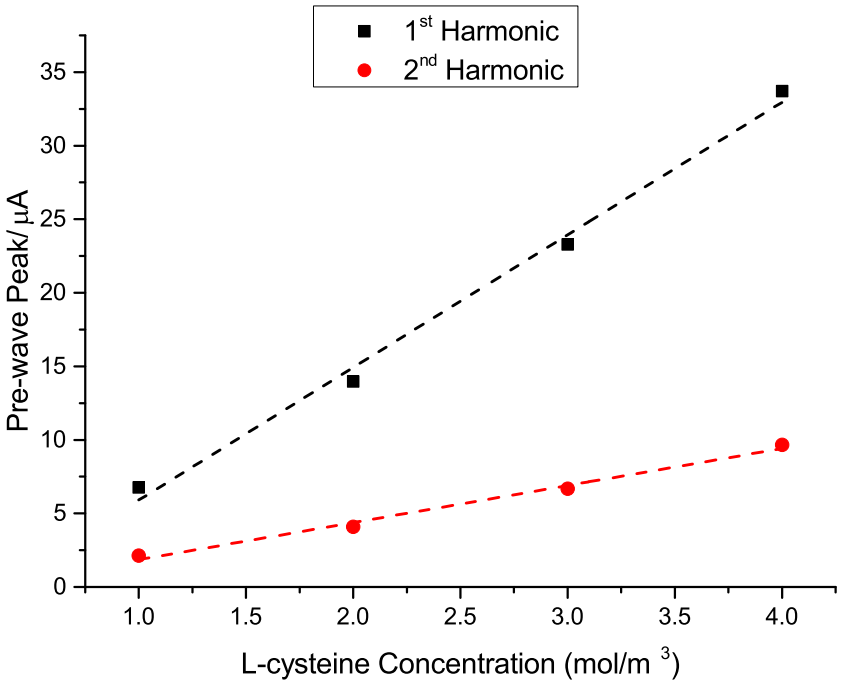

Figure 96: Extract of pre-wave currents in the harmonics from Figure 99 (dots) and relatively good linear fits (dash lines) are confirmed

with increasing frequency. For larger substrate ratio, split-wave is maintained at $6\,Hz$ at higher frequencies (not shown). Additionally, it was also observed that higher amplitudes cause the pre-wave to become less distinguishable from the normal oxidation peak (Figure 95).

By fixing the frequency at $1\,Hz$ and varying L-cysteine concentrations, Figure99 shows the increase in pre-wave current with rising substrate levels. This variation is in line with prediction from Figure 91. The linear correlation from simulation results (Figure 93) is also confirmed in Figure 96 for both the first and second harmonics. Therefore the proposed diffusion model is adequate to describe the trend in real data.

Overall, the above results demonstrate a simple design of the potential signal to express the effect of the EC' mechanism (i.e. the pre-wave phenomenon). Such phenomenon is previously observed in only aperiodic component, but it is now extended for multiple harmonics (e.g. 1^{st} and 2^{nd}). The phenomenon is mainly attributed to the mass transport limitation of the substrate around electrode surface. In addition, the relation between pre-wave peaks and substrate concentrations is confirmed to be

linear, thus demonstrating the potential value for sensing or analytical applications. Finally, preliminary experimental data have shown qualitative agreement with the simulations, which reaffirms the efficacy of this voltage design in both theoretical and practical settings.

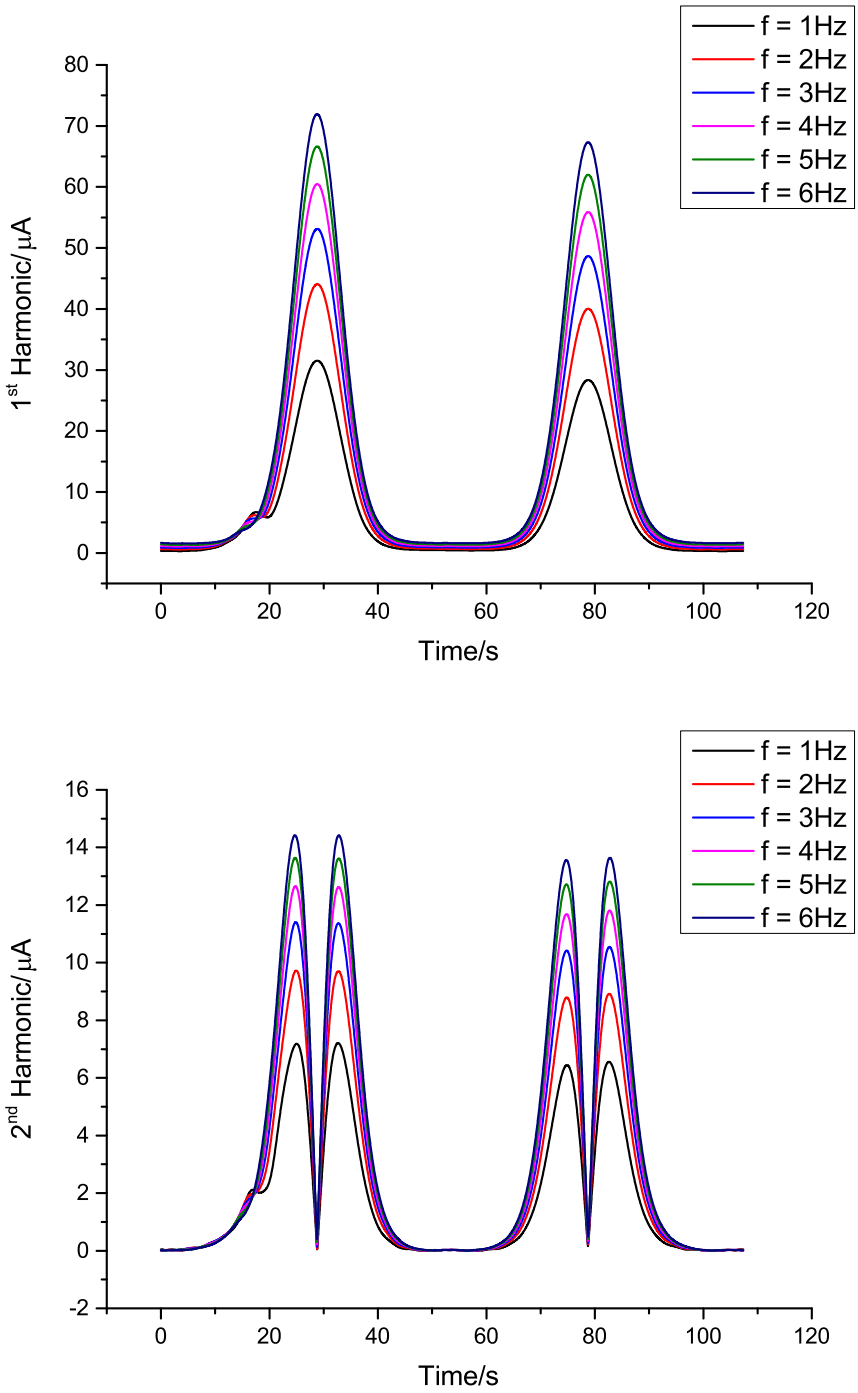

Figure 97: Experimental data for first and second harmonics using FCA ($c_{R0} = 2\,mM$) and L-cysteine ($c_{S0} = 0.5\,mM$) (excess factor is $0.5/2 = 0.25$). Scan rate: $11.8\,mV/s$, $\triangle E = 50\,mV$ and glassy carbon (GC) electrode of diameter $3\,mm$

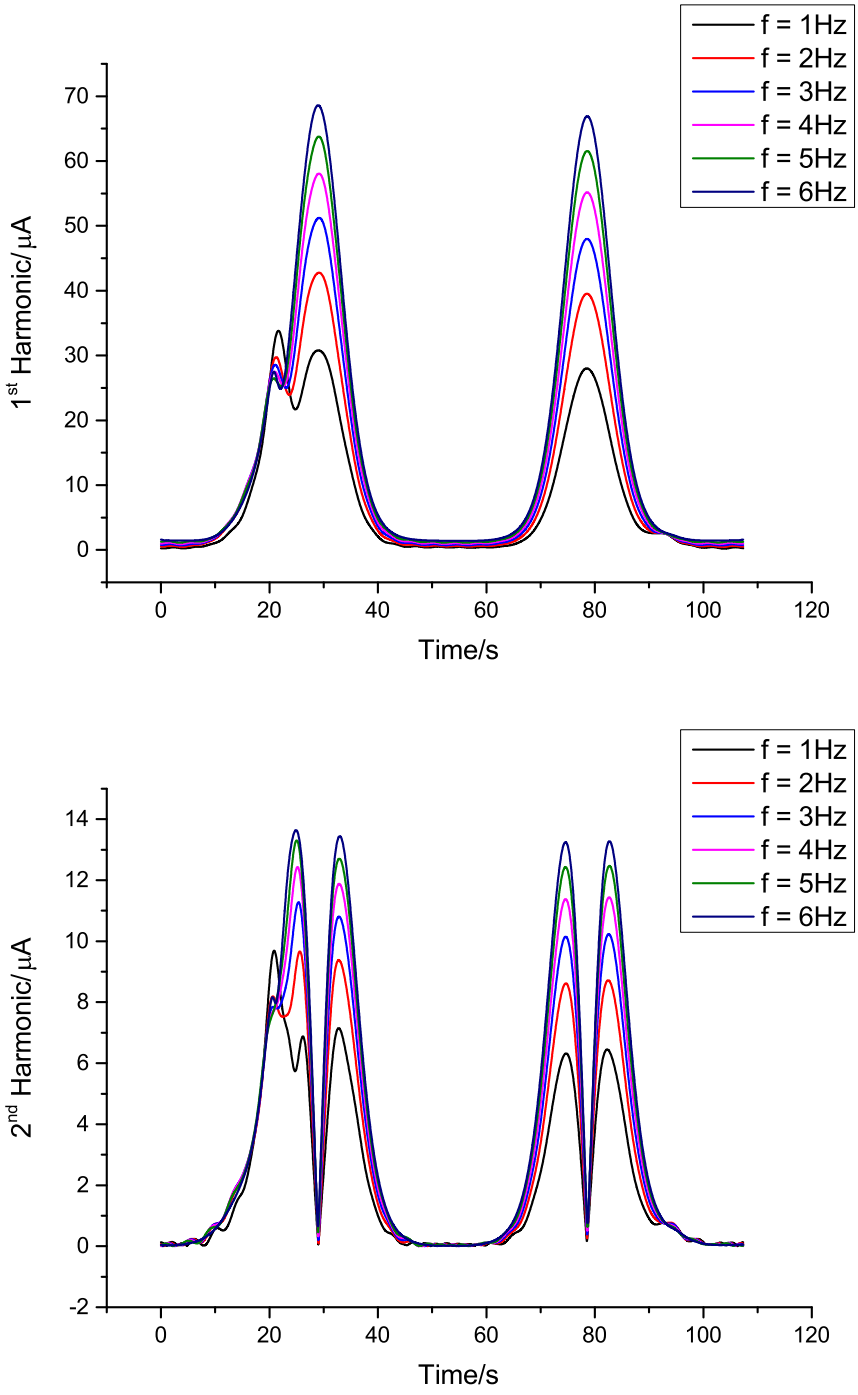

Figure 98: Experimental data for 1^{st} and 2^{nd} harmonics with FCA ($c_{R0} = 2\,mM$) and L-cysteine ($c_{S0} = 4\,mM$) (excess factor is now $4/2 = 2$). Scan rate $11.8\,mV/s$, amplitude $50\,mV$ and $3\,mm$ GC electrode

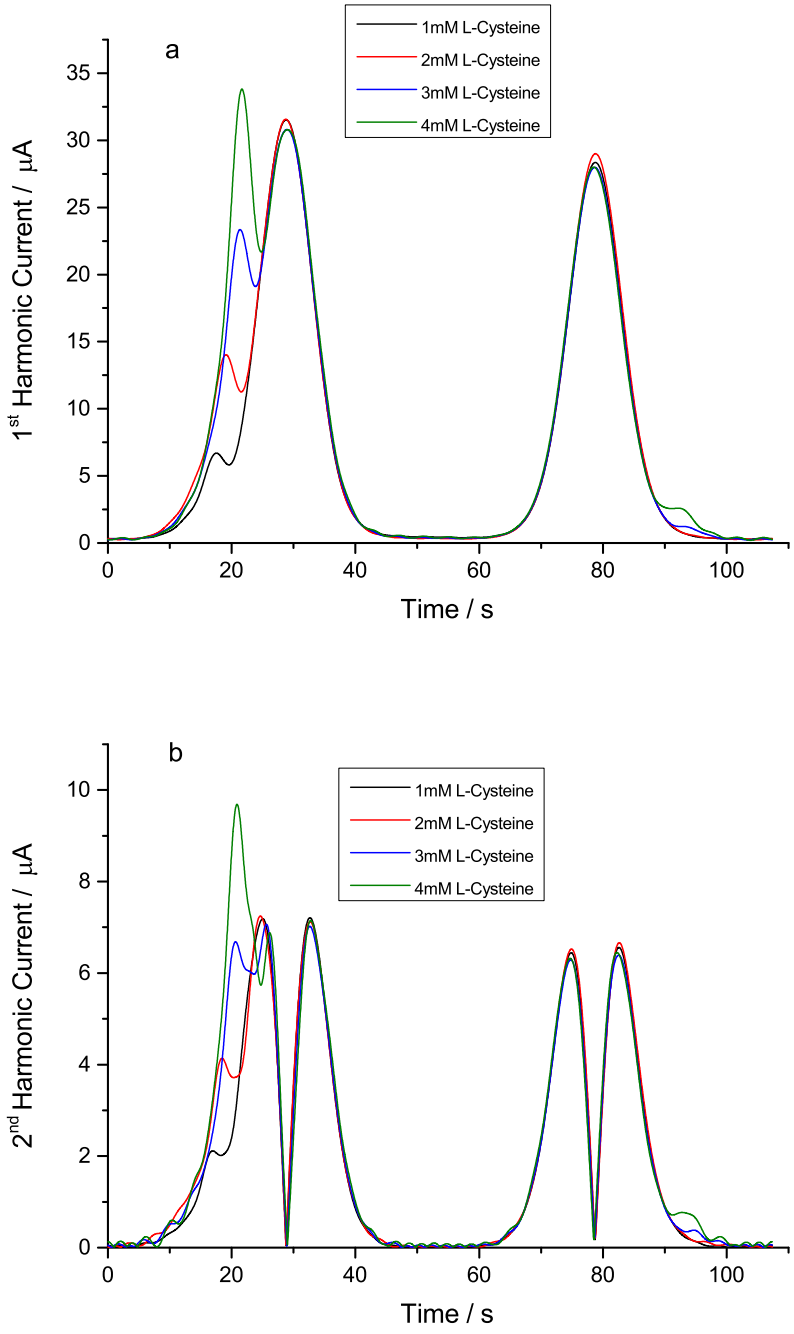

Figure 99: Experiment results for 1^{st} and 2^{nd} harmonics with different L-cysteine levels $1-4\,mM$. The pre-wave current increases along with the substrate concentration (scan rate $11.8\,mV/s$, sinusoidal amplitude $50\,mV$, frequency $1\,Hz$ and FCA concentration $c_{R0} = 2\,mM$, GC electrode $3\,mm$ diameter)

5.4.2 Micro Disk Electrode

The previous section shows that the pre-wave phenomenon are observable in harmonic currents using large amplitude AC voltammetry. The underlying reason for such effect is i) the dependence of harmonics on the diffusion and reaction layers and ii) the substrate's mass transport limitation. This section reinvestigates this result for a 2D axisymmetric micro disk. The disk radius is set to be $r_0 = 30\,\mu m$, which a typical value in laboratory experiments. The structure of the mesh used for the simulation is shown in Figure 102. Exponentially expanding mesh is applied at the interface between the electrode and insulator. Smallest element size and expanding factor are kept the same as before. Towards the bulk, the mesh is composed of tetrahedral instead of triangular elements. Such choice is made to decrease the number of degree of freedoms. Finally, the mesh is composed of two parts: the unstructured (inner section of tetrahedral segments) and structured parts [204].

Algorithm 5.1 is first tested by setting $K_{EC'} = 0$, which reduces EC' to the familiar E mechanism. The first to fourth harmonics are presented in Figures 100 and 101. For the first harmonic, since the electrode area is shrunk considerably in comparison to the previous section, the capacitive currents become much smaller and thus the base-line is effectively 0 for all harmonics. As a consequence, all harmonics are extracted and insignificantly influenced by the double layer capacitance.

The same calculations are then repeated for different substrate ratios of 0.5, 1.0, 2.0 and 4.0 and the same $K_{EC'}$ as in the case of macro electrode. Due to additional dimension, the average computing time is now considerably larger than for the one-dimensional situation. $N_{simulation\,point}$ is set to be 2^{16}, which is observed to yield satisfactory convergence in trial runs. The sinusoidal amplitude is set at $50\,mV$ and frequencies are also varied between 1 and $6\,Hz$. Results are shown in Figures 103 - 110 respectively.

Comparing to the data on macro electrode, there are several significant differences. Firstly, for the 1^{st} and 2^{nd} harmonics, the split-wave effect is only observed at low substrate concentration ratios (i.e. 0.5 and 1.0) in Figures 103 and 105, while the phenomenon completely disappears at higher ratios (Figures 107 and 109). Such disappearance can be explained as follows. With micro electrodes, diffusion transport is now multi-directional and therefore considerably enhanced in comparison to macro electrode conditions. Because the pre-wave is primarily attributed to the mass transport limit of substrate S, the effect is consequently not expected at high concentration

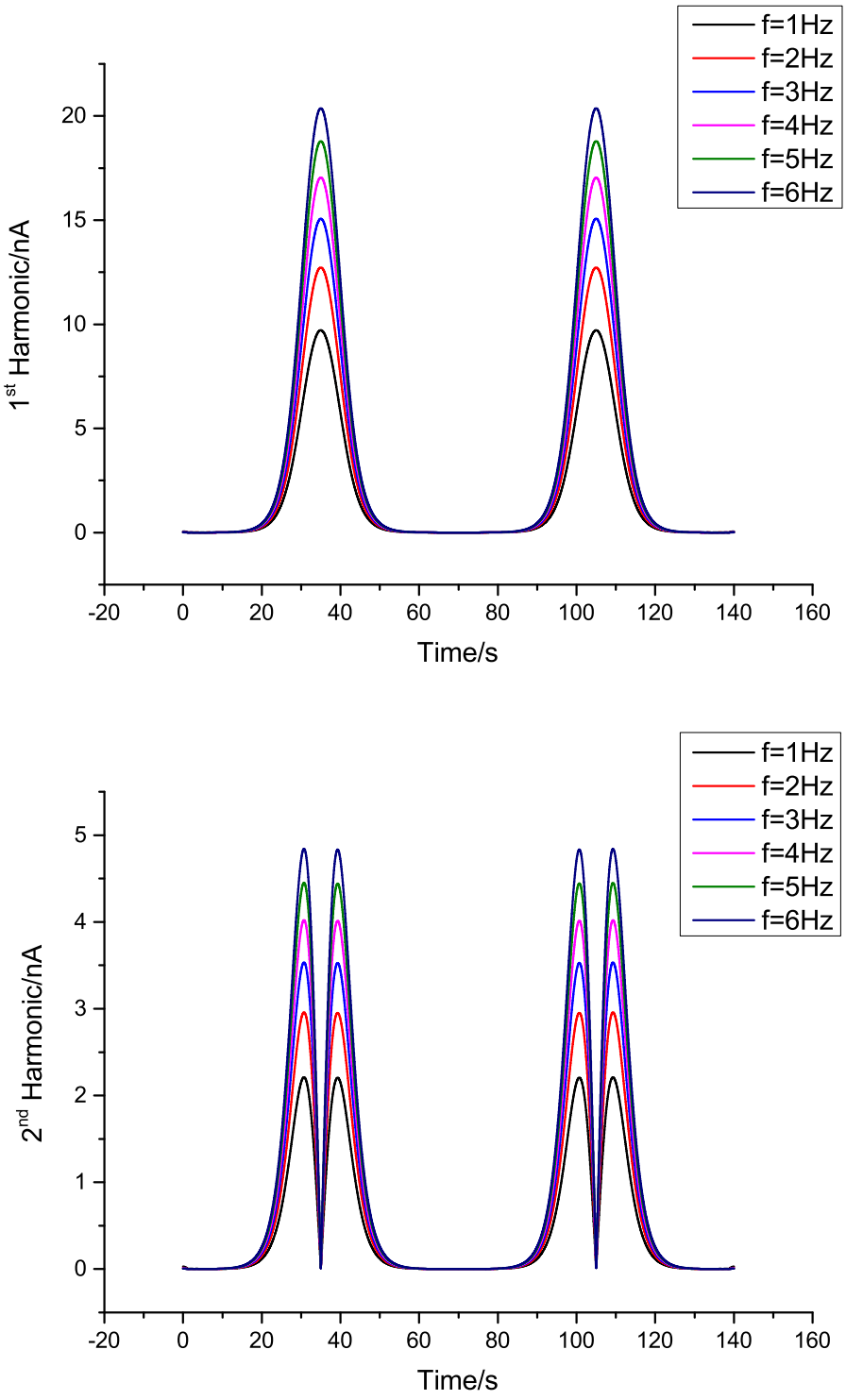

Figure 100: 1^{st} and 2^{nd} harmonics for a micro disk under simple E reaction

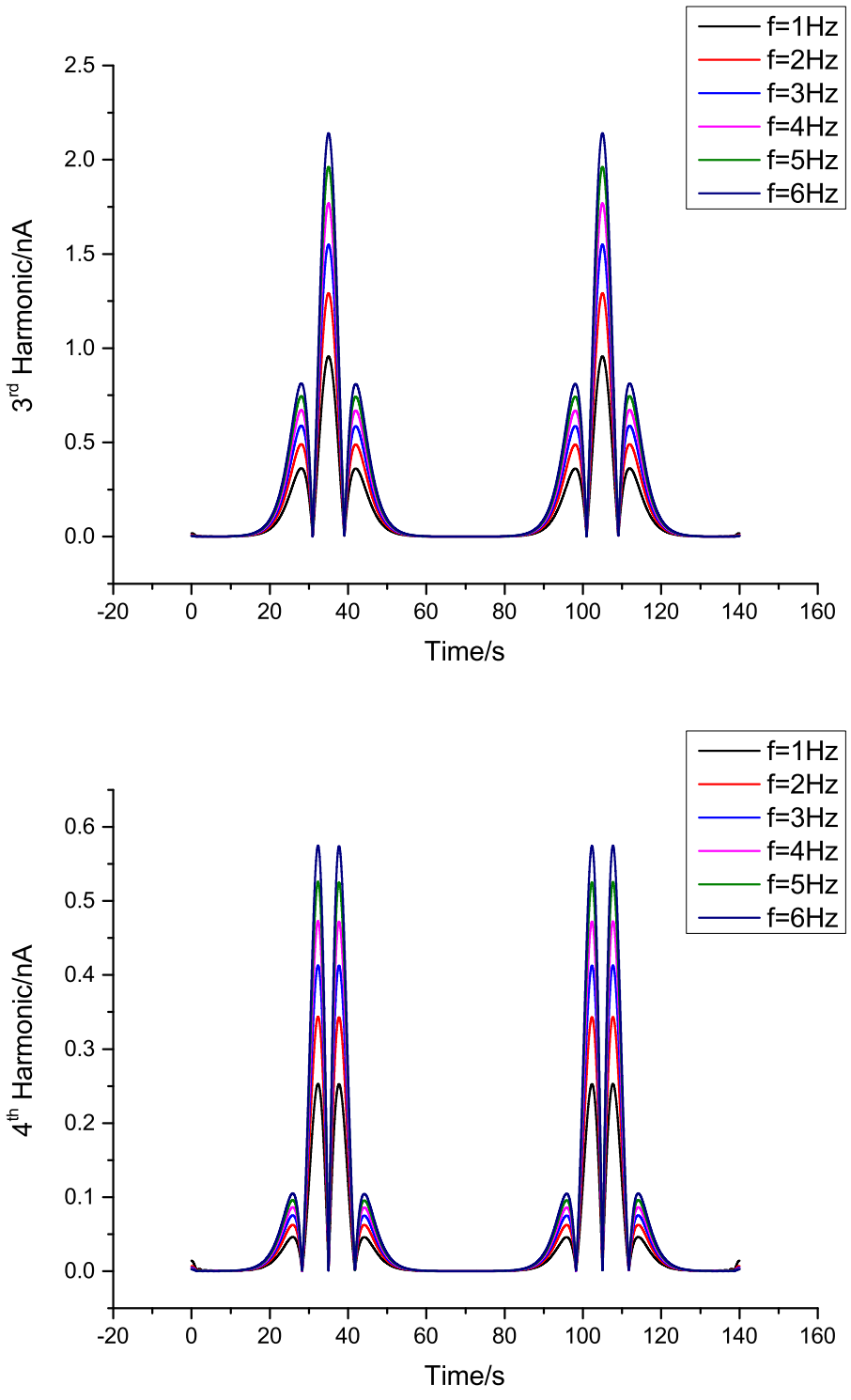

Figure 101: 3^{rd} and 4^{th} harmonics for a micro disk under simple E reaction

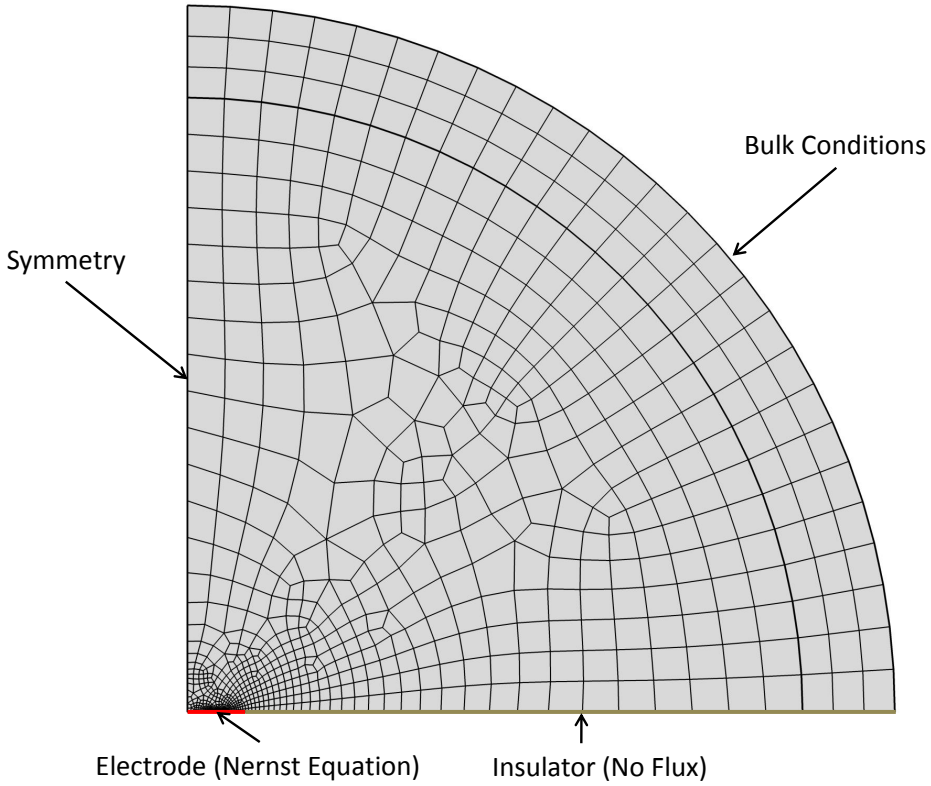

Figure 102: Finite element mesh used for the calculations. Tetrahedral shape is applied instead of triangular ones in order to save some degree of freedoms. Respective boundary conditions are also included. Towards the bulk, a more regular mesh is used

limits. As a consequence, the split-wave is only possible at low concentration conditions, although due to the efficient mass transfer mechanism it is weakly observed. In addition, it is therefore not possible to calibrate correlations for peak currents and concentrations using 1^{st} and 2^{nd} harmonics. Another salient feature is at high substrate ratios, only single peaks corresponding to the E reaction are present but with increasing magnitude. Such increase in current is attributed to the catalytic step C' in the mechanism. Furthermore, the increase is considerably larger in the forward scan than the backward scan. Such asymmetrical difference is explained by the fact that during the backward scan, there is less of species O present in EC' in comparison to E, thus the reductive current is less than the oxidative counterpart.

Regarding the 3^{rd} and 4^{th} harmonic, the split-wave re-appears at higher substrate ratios. At ratio of 0.5, there is no pre-wave and only a weak shoulder emerges at ratio

1.0 (Figures 104 and 106). At 2.0 and 4.0 ratios, the very first E peak (top Figure 101) is split into two smaller waves (Figures 108 and 110). It is further noted that the splitting occurs both in forward and backward sections of the voltammograms (although the effect is again asymmetrical). This observation is to be contrasted with the results from macro case, in which the splitting only occurs in the first half of the voltammograms. It is thus inferred that the increased mass transport effect becomes less significant in higher harmonics due to re-emergence of split-waves. As a consequence, the phenomenon is expected for 5^{th} or later harmonics, though this might be very difficult to discern due to complex variations in time domain representations.

In conclusion, this section demonstrates interesting insights into the EC' mechanism under enhanced mass transport. The split-wave phenomenon appears only at low substrate ratios in 1^{st} and 2^{nd} harmonics, which somehow limits their analytical values. In addition, at even lower substrate ratios, the pre-wave is expected to disappear due to transition from zone $KT2$ to zones KG^*/KG (Figure 86), thus severaly limiting the applications for substrate sensoring. Secondly, higher harmonics are observed to be less influenced by the mass transfer effects since pre-waves are noticed in their voltammograms. The analytical applications of these higher harmonics should be used critically because it is not straightforward to extract simple information from their time domain representations. They are however, still valuable as comparisons to real data and serve as an indicator of model adequacy. In the next section, the split-wave phenomenon is examined under a similarly enhanced but more controllable mass transport environment, namely the channel electrode.

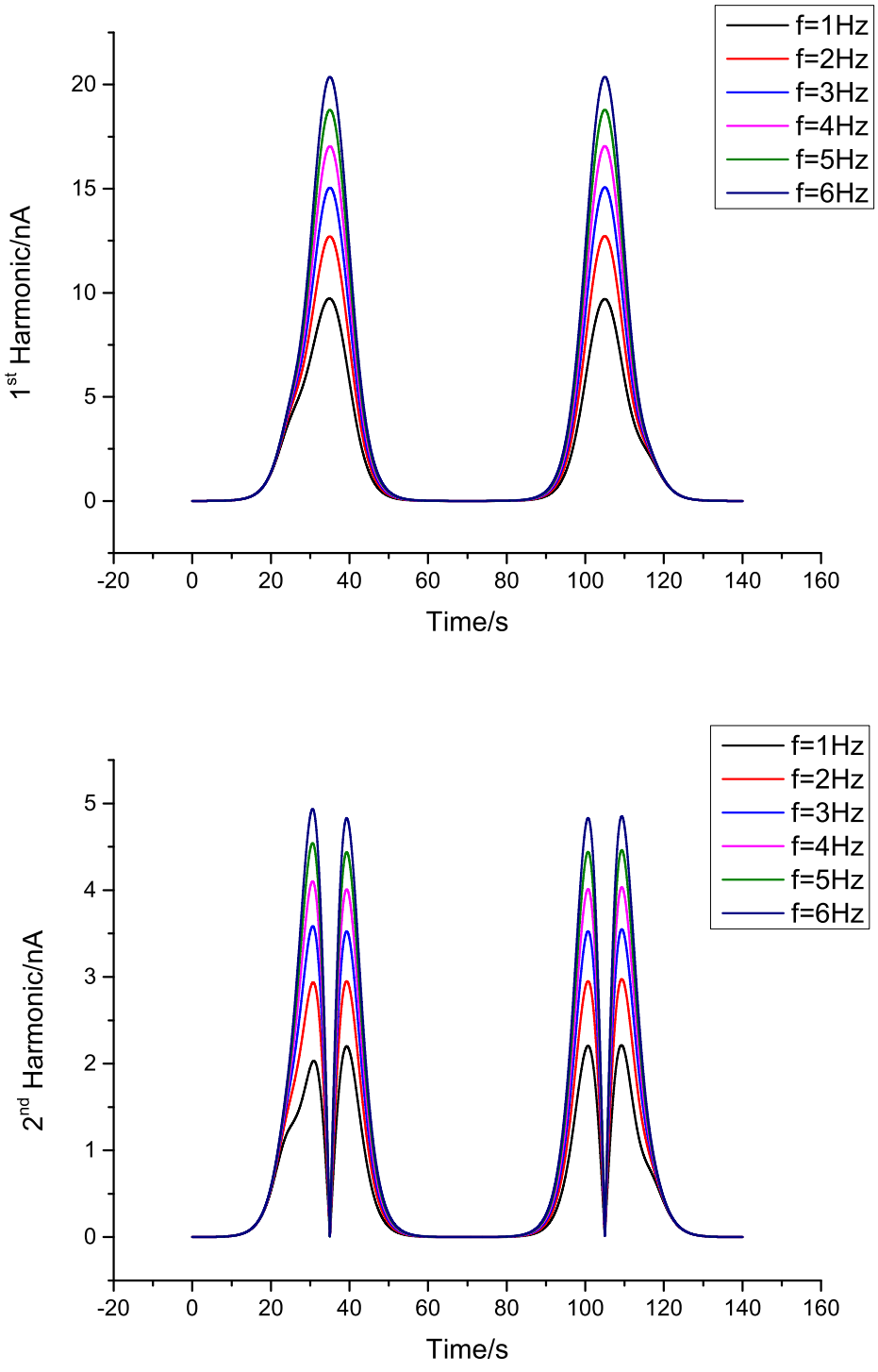

Figure 103: 1^{st} and 2^{nd} harmonics under EC' reaction and substrate ratio of 0.5 for a micro electrode

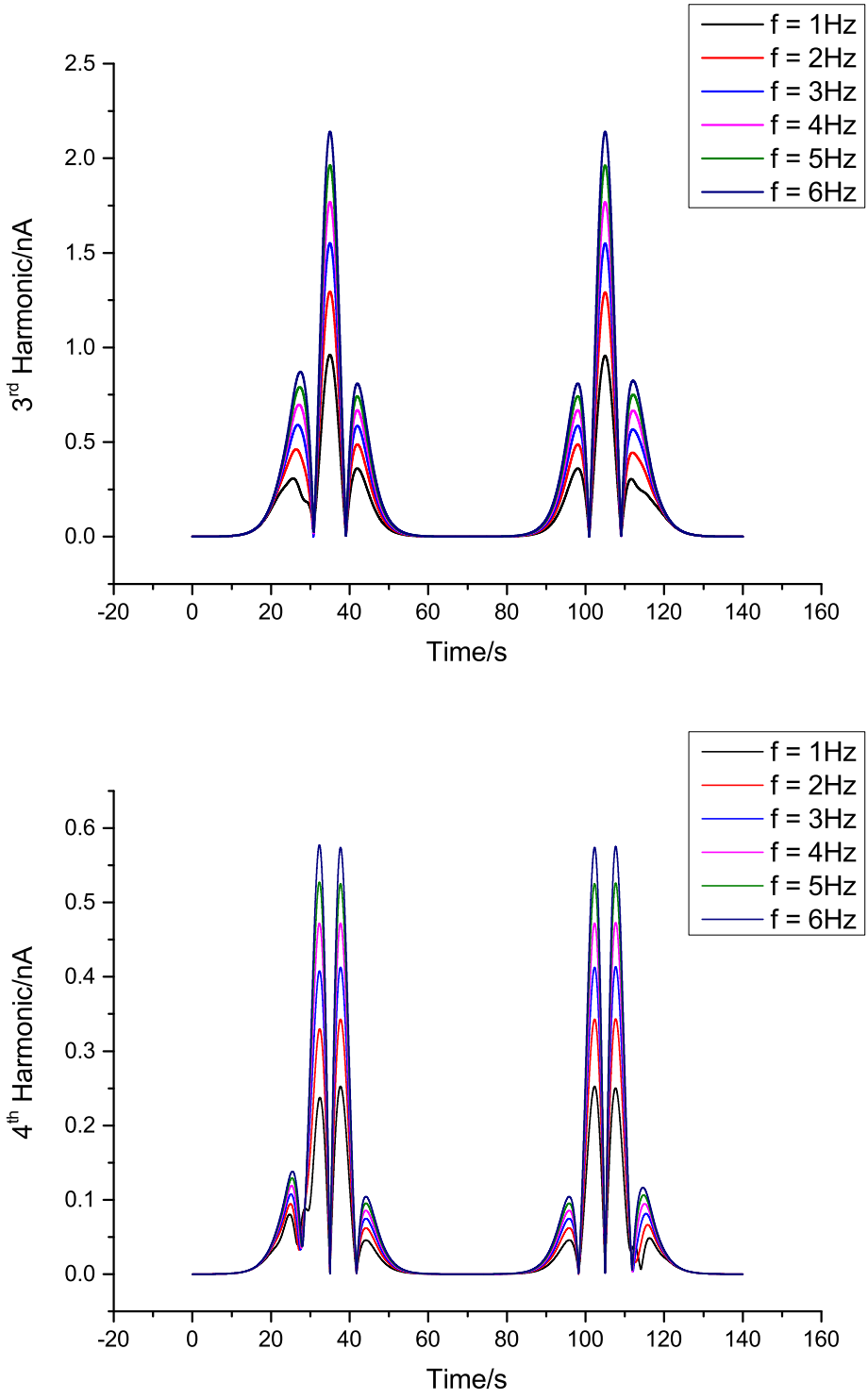

Figure 104: 3^{rd} and 4^{th} harmonics under EC' reaction and substrate ratio of 0.5 for a micro electrode

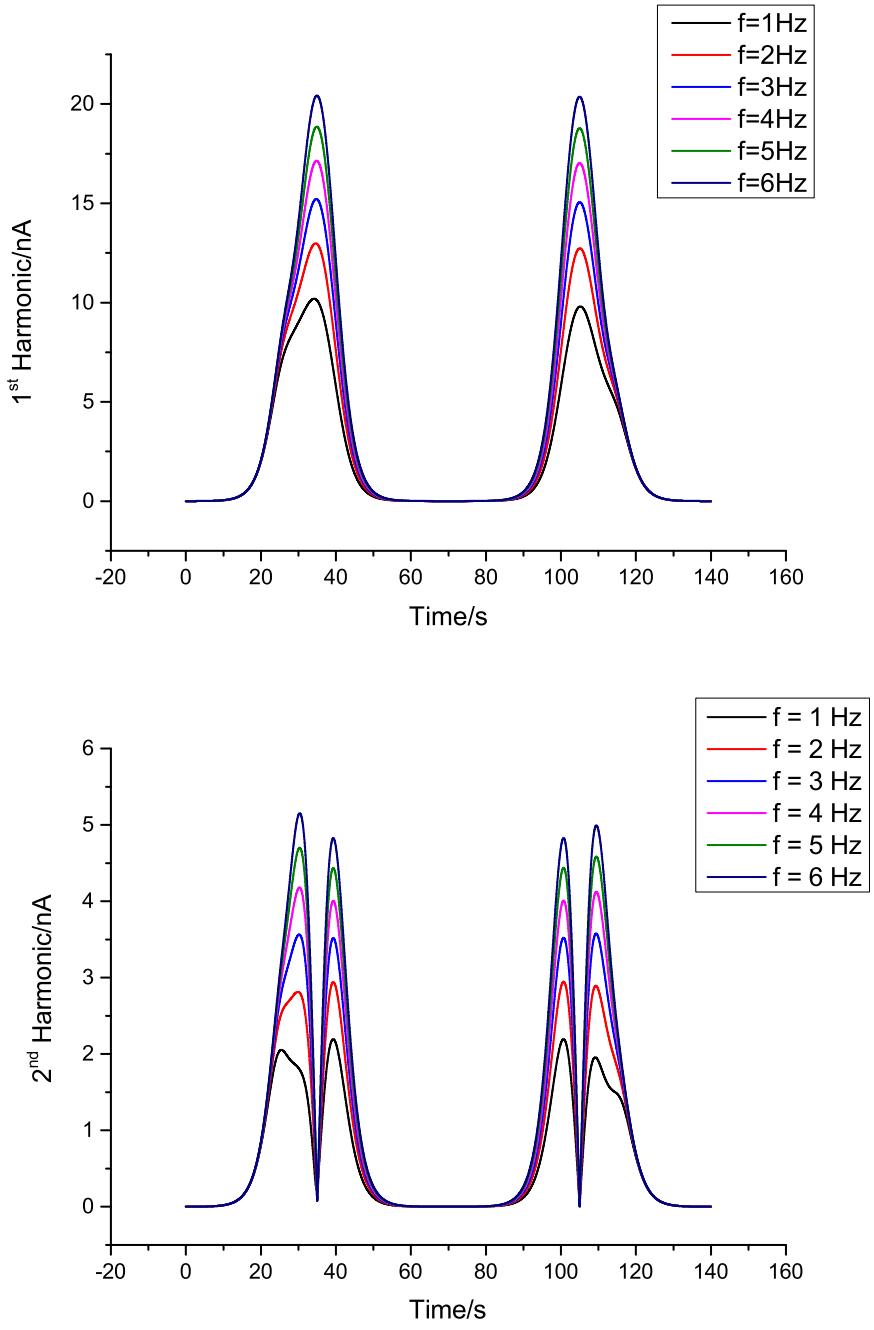

Figure 105: 1^{st} and 2^{nd} harmonics under EC' reaction and substrate ratio of 1.0 for a micro electrode

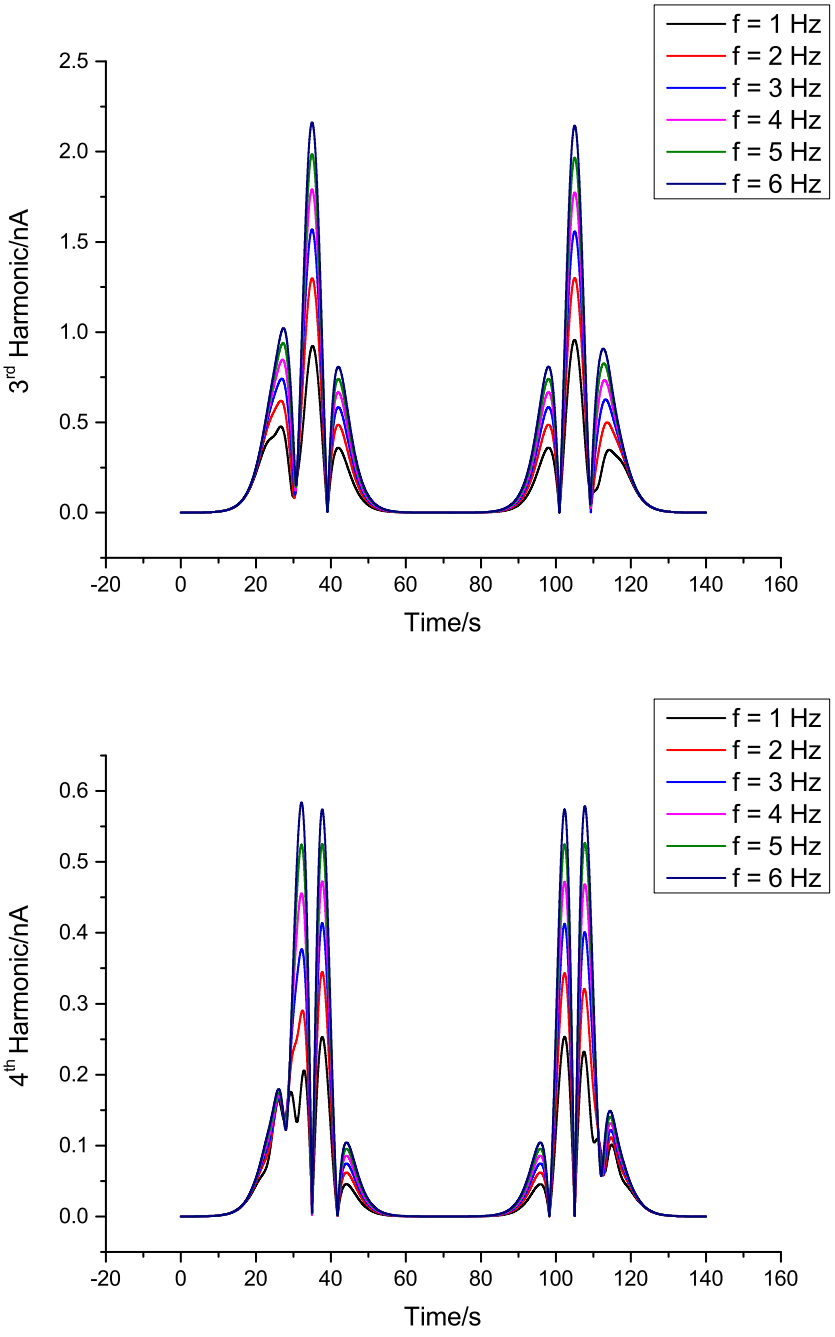

Figure 106: 3^{rd} and 4^{th} harmonics under EC' reaction and substrate ratio of 1.0 for a micro electrode

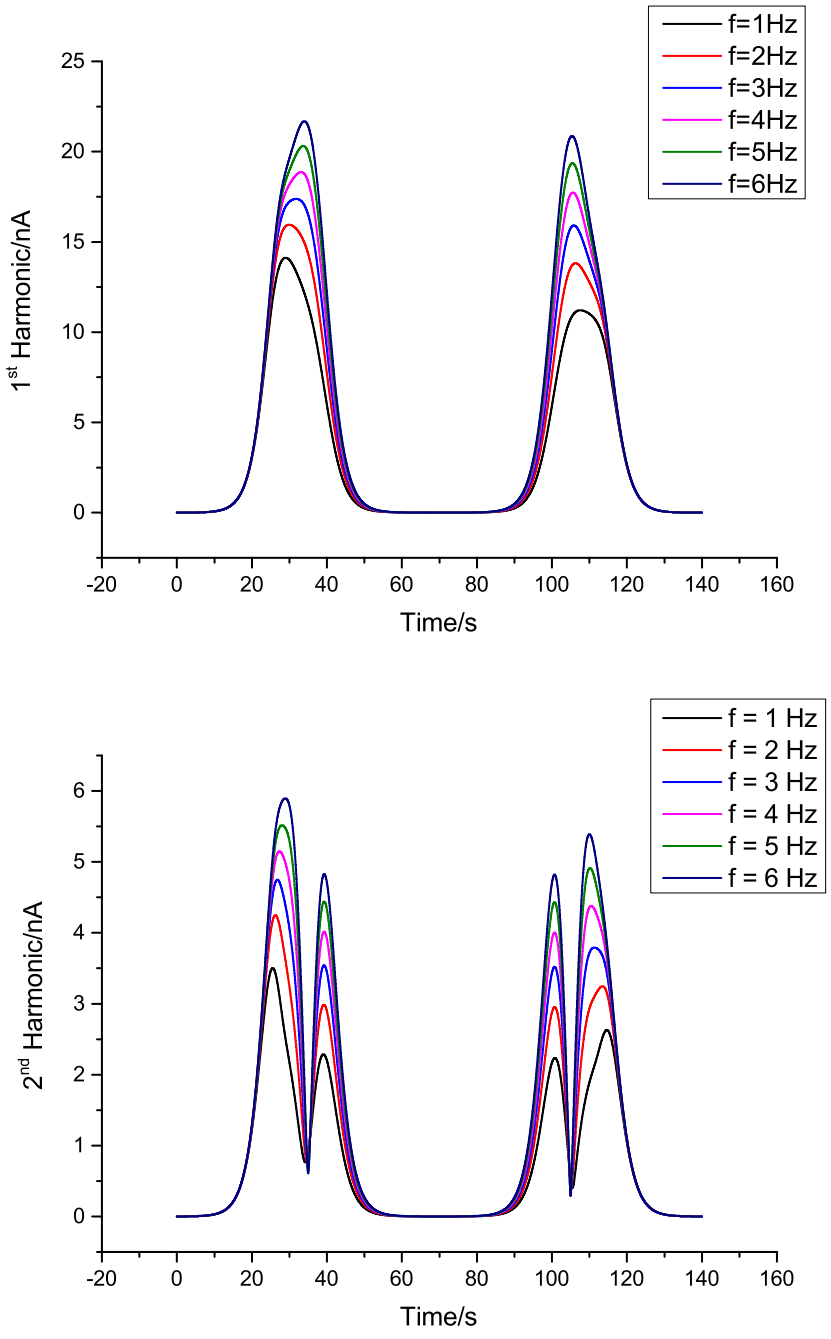

Figure 107: 1^{st} and 2^{nd} harmonics under EC' reaction and substrate ratio of 2.0 for a micro electrode

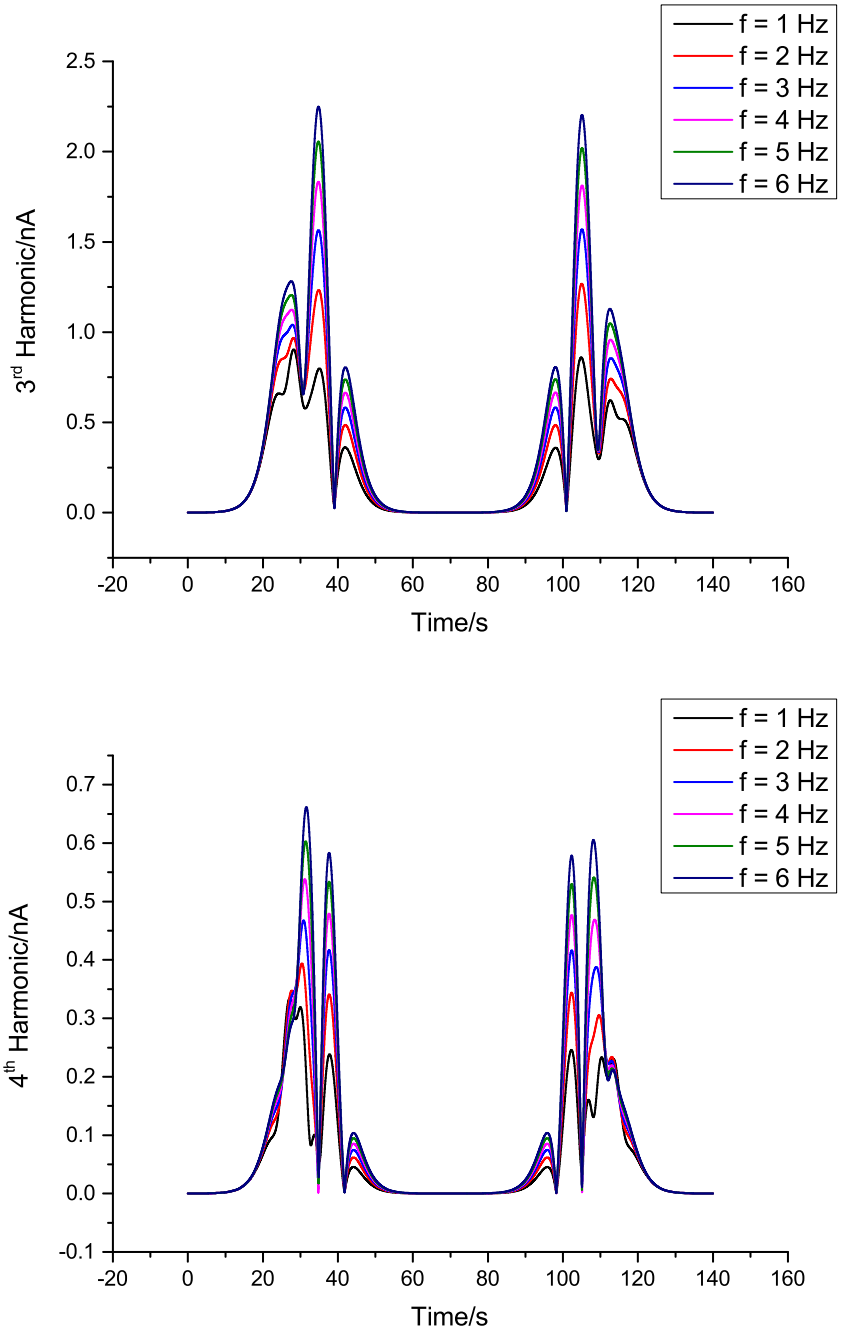

Figure 108: 3^{rd} and 4^{th} harmonics under EC' reaction and substrate ratio of 2.0 for a micro electrode

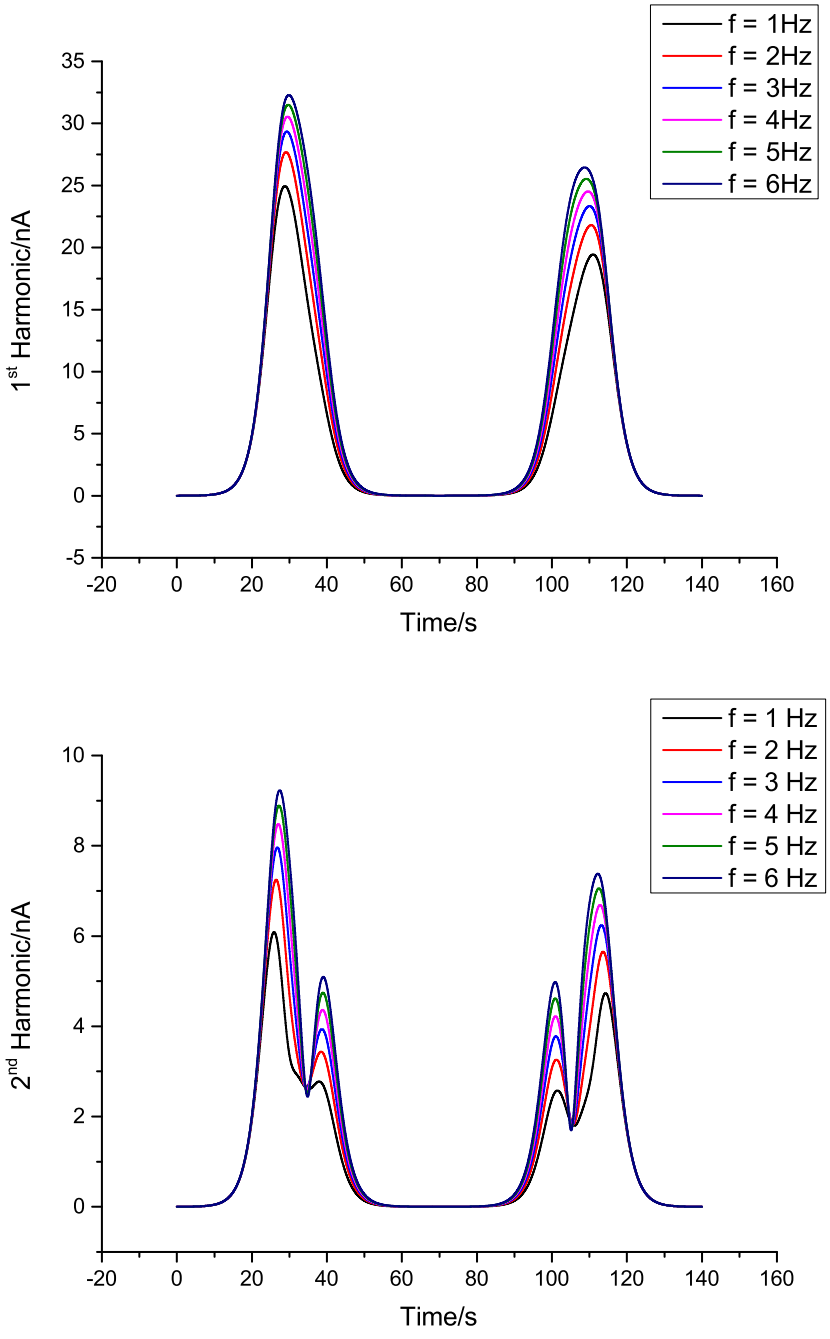

Figure 109: 1^{st} and 2^{nd} harmonics under EC' reaction and substrate ratio of 4.0 for a micro electrode

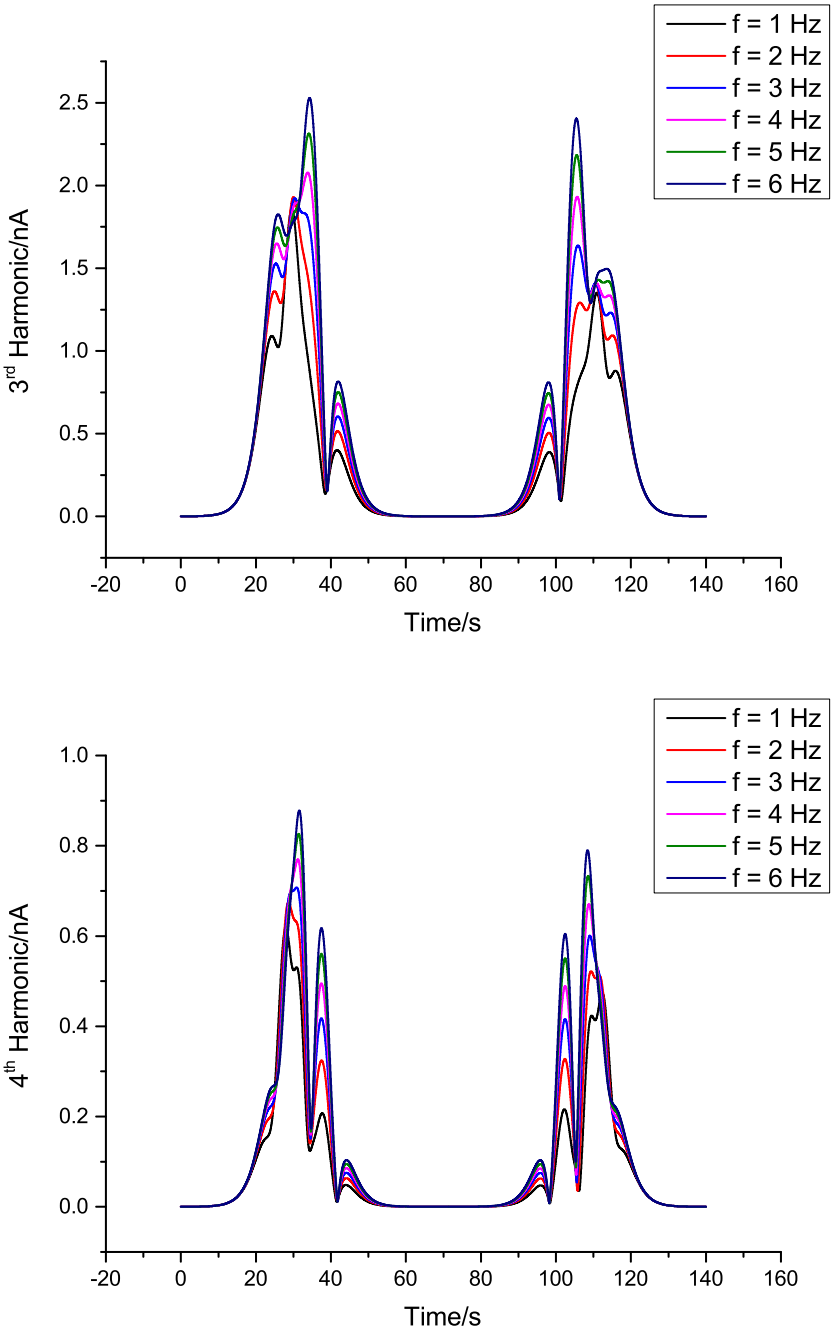

Figure 110: 3^{rd} and 4^{th} harmonics under EC' reaction and substrate ratio of 4.0 for a micro electrode

5.5 Self-Catalytic Reaction with Micro Fluidic Flow

Section 5.4 demonstrate two interesting points. Firstly, the characteristic pre-wave is elicited via the use of slowly modulating signals for macro electrode. Secondly under enhanced transport conditions with micro disk, the split-wave disappears at early harmonics and then re-emerge at higher components - a behaviour similar to that at a planar electrode. Thus in order to observe such behavior, it is important to control the mass transport factor.

Early investigation using micro fluidic channel has suggested that experimentally extracted harmonics follow the same behavior as discussed above [64]. That is, these components are essentially unchanged under both diffusion and flow conditions. This observation suggests that micro fluidic is a possible tool to express the split-wave behavior because mass transport conditions are now controllable by varying flow rate.

This section is divided into two sub-parts. The first part numerically verifies Levich equation for channel flow. The goal is to set up a reliable framework for subsequent calculations including the EC' catalysis. As before, large amplitude AC voltammetry is introduced and the extraction algorithm 5.1 is applied extensively. A major aim here is to observe whether pre-wave appears in early harmonics, rather than at higher components as seen in micro disk calculations.

5.5.1 Levich equation for embedded channel electrode

Considering the 2D cross-section of the channel and assuming uniformity across the electrode in z direction (Figure 13). This assumption only applies if $d \gg w$. Two implied consequences are i) the flow is parabolic at every cross-section of the electrode and ii) diffusion is z direction can be ignord due to translational symmetry. In addition, since the flow is uni-directional (i.e. in x direction). These results lead to the simplified version of Equation 1.4:

$$\frac{\partial c}{\partial t} = D(\frac{\partial^2 c}{\partial x^2} + \frac{\partial^2 c}{\partial y^2}) - v_x \frac{\partial c}{\partial x} \tag{5.13}$$

where the velocity field is dominantly in x direction with parabolic profile:

$$v_x = 4v_0(\frac{y}{h_c} - (\frac{y}{h_c})^2) \tag{5.14}$$

$$v_0 = \frac{3}{2}\frac{V_f}{d_c h_c}$$

Since the top and bottom surfaces of the channel are impermeable to the solution, this condition leads to zero-flux conditions. At the electrode surface, since the bottom plane is stationary, the velocity diminishes to 0 and the applied Butler-Volmer equation only has the diffusion component and assumes the form 1.8 as before.

Under special conditions, equation 5.13 can be further simplified. By analyzing the scales of the diffusion and convection terms in x direction:

$$D\frac{\partial^2 c}{\partial x^2} \sim D\frac{c}{l_x^2} \tag{5.15}$$

$$v_x\frac{\partial c}{\partial x} \sim v_x\frac{c}{l_x} \tag{5.16}$$

and the velocity component can be scaled as:

$$v_x \sim v_0 = \frac{V_f}{dh_c}$$

taking $l_x \sim l$ then the diffusion term in the x-direction can be ignored (relative to the convection term) if:

$$\frac{V_f l}{dh_c D} \gg 1 \tag{5.17}$$

At fairly slow flow rates, diffusion process is multi-directional while at larger flows, the contribution primarily comes from direction orthogonal to the electrode surface. However for all calculations in this section, diffusion components in x and y directions are both included, which also accounts for the effects of Taylor dispersion at large flow rates [205].

The parameters for simulation are listed in Table 21. It is also important to keep track of the laminarity of the flow, which is expressed via the Reynold's number:

$$Re = \frac{v_0 h_c}{\nu} = \frac{V_f}{d\nu} \tag{5.18}$$

If $Re < 10^3$ then it is usually safe to assume that the flow is laminar and the velocity field has a parabolic profile. It is also important to discuss FE meshing and relevant numerical aspects for the current case. First , a structured rectangular mesh is used (Figure 111). Similar to FD, the mesh is exponentially expanded away from the

bottom plane where the electrode is located. The simulation domain can be divided into three rectangles. The first rectangle corresponds to up-stream flow, the second part contains the electrode and the final corresponds to the down-stream. Finer mesh is put at the edge between the 1^{st} and 2^{nd} rectangles, whilst such condition is not required for the interface between 2^{nd} and 3^{rd} domains since the concentration field already becomes steady at that position. Finally, an estimate of the diffusion layer size under flow condition is:

$$l_{dif} \sim (D_R h_c x_e / v_0)^{1/3} \tag{5.19}$$

which clearly depends on V_f. In simulation practice, the smallest spacing is typically at least 10 times smaller than l_{diff} to ensure adequate resolution of the layer.

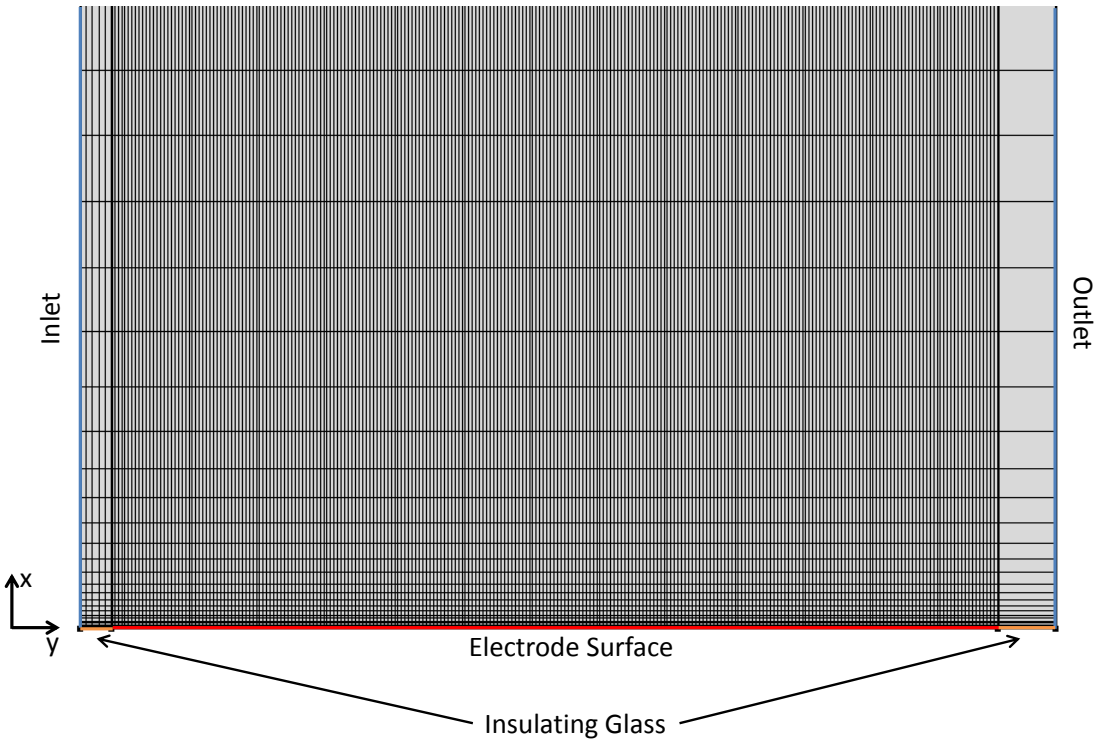

Figure 111: Structured rectangular mesh used for channel electrode calculations. Edge, distribution and mapping operations in *Comsol Multiphysics*® are combined to produce this mesh

The time-dependent Equation 5.13 can be solved in *Comsol Multiphysics*® in two

Symbol	Value	Units	Comment
D_R, D_O	10^{-5}	cm^2/s	Oxidative species diffusivity
x_e	500	μm	Electrode Length
l	1000	μm	Channel Length
h_c	200	μm	Channel Height
d_c	0.6	cm	Channel Width
w_e	0.04	cm	Electrode Width
c_{R0}, c_{O0}	$1, 0$	mM	Species Bulk Concentrations
k_0	10^{-4}	m/s	Reversible electrode kinetics
E_0	0.25	V	Equilibrium Potential for the oxidation reaction
α	0.6	-	Charge Transfer Number
ρ	1000	kg/m^3	Solution density (assumed water)
ν	10^{-6}	m^2/s	Solution dynamic viscosity (assumed water)

Table 21: Parameters used in verification of Levich expression for channel electrode

ways. The first and most general approach is using the Time-Dependent solver, which is based on the backward implicit formulation. However, if the electrochemical kinetics is fast, there is another approach called Parameter Sweep which is more convenient and produces solutions at similar level of accuracy. Parameter Sweep is particularly useful for problems having multiple steady states. The method is as follows: the voltage range is first divided into discrete points as before. The limiting current is then calculated at each of these fixed potentials. Thus the current-voltage curve of the original problem becomes a collection of the points (I_{lim}, E_{apply}) in which E_{apply} is the applied potential and I_{lim} is the corresponding steady state current. In this section, the usual time-dependent solver is however used because of its generality.

Different flow rates between 0.001 and $1\,cm^3/s$ are used for the calculations. The maximum Re numbers are 250 which are well below the turbulent condition. Comparison between limiting currents and Levich expressions are shown in Figure 112. It should be noted here that the flow rates between $0.1 - 1\,cm^3/s$ are fairly large (the average velocity v_0 in the order of cm/s) and are therefore not so commonly used in practice due to high possibility of solution leakage. However, numerical observations show that the higher the flow rates, the smaller the percentage differences between numerical values and the Levich expression 1.20. Figure 113 shows the effect of solution flow rate on concentration profiles across electrode surface. At very small flow rate (e.g. $10^{-6}\,cm^3/s$), the profile is almost symmetrical akin to that of a micro disk. As higher volummetric rates are applied, the contour is distorted and skewed in the same direction of flow and the diffusion layer's thickness decreases.

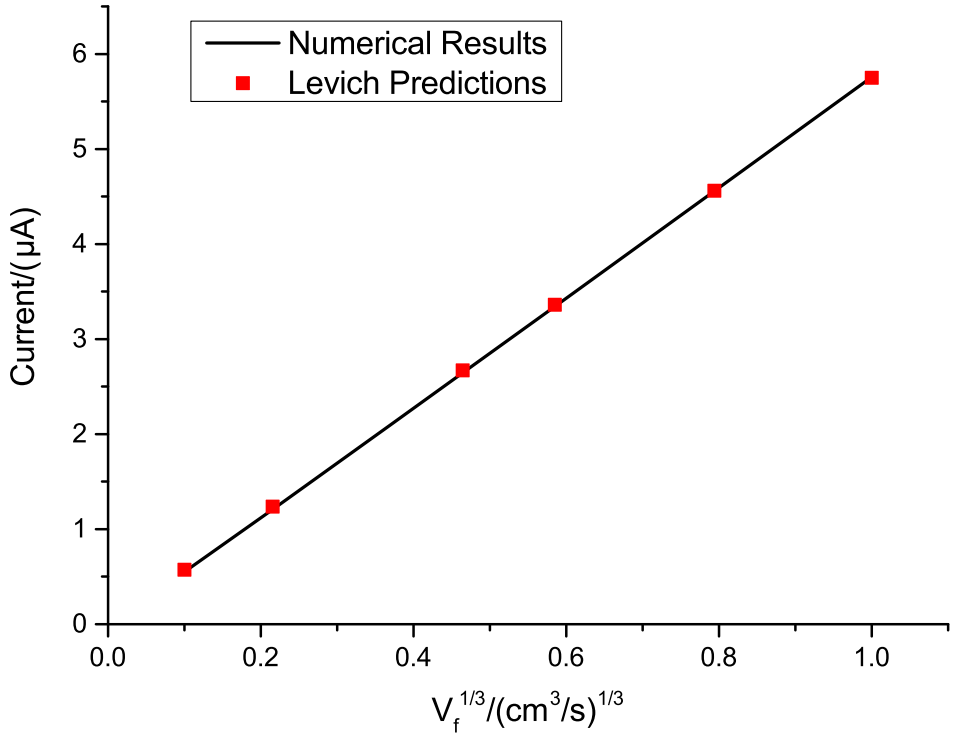

Figure 112: Comparison between numerical values and the Levich prediction $I_{lim}^{CE} = 0.925nFc_{R0}w_e x_e^{2/3} D_R^{2/3} (4V_f/h_c^2 d)^{1/3}$ for the channel electrode at various flow rates V_f. There is a good convergence between simulation and theory. Numerical differences are largest at small flow rates (e.g. $0.001\,cm^3/s$) and decrease as V_f is increased

5.5.2 Effects of large AC amplitude and catalysis

This section investigates the EC' mechanism via the use of channel electrode. Based on results from section 5.4, $f = 1\,Hz$ is chosen for all following simulations. This choice stems from the observation that the wave-splitting phenomenon is most clearly shown under the slowest sinusoidal modulation. For the micro fluidic calculations, the electroactive species concentration is raised to $c_{R0} = 2\,mM$. Such choice is purposely made for later comparisons with experiments. The parameter setting is summarized in Table 22.

Under channel flow, Equation 5.10 is modified to include the convective component:

$$\frac{\partial c_R}{\partial t} = D_R \frac{\partial^2 c_R}{\partial y^2} - v_x \frac{\partial c_R}{\partial x} + k_{EC'} c_O c_S$$

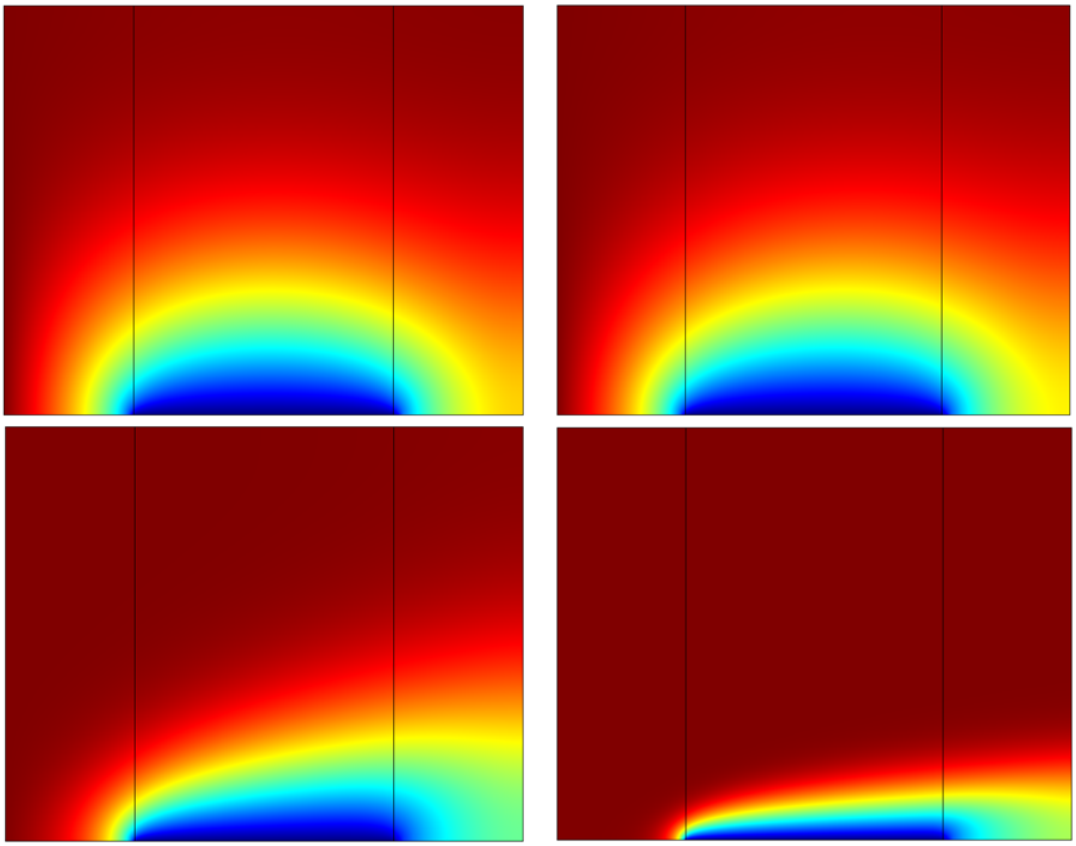

Figure 113: Cross sectional concentration profile at large over potential and various flow rates $V_f = 10^{-6}$, 10^{-5}, 10^{-4} and $10^{-3}\, cm^3/s$ (direction: left to right, top to bottom). Red colour indicates high concentrations whilst blue colour is $0\,(mM)$. The contour is sharp near the leading edge of the electrode and becomes flatter downstream. As a consequence, the current flux peaks at the front and then tends to a lower constant value

$$\frac{\partial c_O}{\partial t} = D_O \frac{\partial^2 c_O}{\partial y^2} - v_x \frac{\partial c_O}{\partial x} - k_{EC'} c_O c_S$$

$$\frac{\partial c_S}{\partial t} = D_S \frac{\partial^2 c_S}{\partial y^2} - v_x \frac{\partial c_S}{\partial x} - k_{EC'} c_O c_S \tag{5.20}$$

In arriving at Equation 5.20, the diffusion component in x and convective term in y directions are ignored. In earlier analysis, Equation 5.17 shows that this assumption applies at sufficiently large flow rate V_f. Using the criteria and the above dimensional values:

Parameter Symbol	Value	Units
D_R	$0.76 * 10^{-9}$	m^2/s
D_O	$0.76 * 10^{-9}$	m^2/s
k_0	0.001	m/s
α	0.5	$-$
C_{dl}	50	$\mu F/cm^2$
E_0	0.25	V
v_{scan}	10	mV/s
c_{R0}	2	mM
c_{O0}	0	mM
c_{S0}	$0.1 - 1$	mM
D_S	$6 * 10^{-10}$	m^2/s
$k_{EC'}$	10^6	$M^{-1}s^{-1}$
d_e	100	μm
w_e	600	μm
h_c	1000	μm
d_c	670	μm
$\triangle E$	50	mV
V_f	$0.1 - 0.6$	mL/min
$f_{fundamental}$	1	Hz

Table 22: Simulation parameters for micro fluidic channel. A small scan rate and sinusoidal frequency are employed to manifest the split-wave effect. Electrode size is length d_e and width w_e with a channel height h_c and width d_c)

$$\frac{V_f d_e}{d_c h_c D_R} \sim \frac{(0.1\,10^{-6}/60)\,(100\,10^{-6})}{(670\,10^{-6})\,(1000\,10^{-6})\,(10^{-9})} \sim 250$$

which is well above 1 and therefore justifies the above assumption. Another way of checking is to estimate the average speed v_0, which comes out to be:

$$v_0 \sim \frac{0.1\,10^{-6}/60}{(670\,10^{-6})\,(1000\,10^{-6})} \sim 2500\,\frac{\mu m}{s}$$

and considering the channel length is $x_e = 100\,\mu m$, the fluid dynamic time scale is $100/2500 = 0.04\,(s)$ and the flow is thus very fast compared to the time scale of mass transport process. Consequently, the steady-state flow profile 5.14 is assumed to be uniform across electrode width.

Figure 111 illustrates the structured mesh for the simulation. Regarding the boundary conditions, Nernstian relation 1.13 is applied at electrode level and at insulating glass, zero flux is imposed. For the inlet condition, fresh (i.e. bulk concentration)

species are supplied. Finally, at the outlet, diffusion term along the channel is assumed to be negligible because the convective term is much more dominant.

Calculations are first carried out with simple E reaction. The aim is to ensure adequate convergence from the solver and test the harmonic extraction algorithm. Results for different flow rates are shown in the set of Figures 114 - 116. Under micro fluidic condition, the DC current reaches a steady state which is theoretically proportional to $V_f^{1/3}$ according to Equation 1.20. This relationship is verified in bottom Figure 114. Interestingly, by analyzing the 1^{st} harmonics, it was empirically found that the peak currents are proportional to approximately $V_f^{0.286}$. The correlation is illustrated in Figure 117. The smaller exponent of V_f implies that the harmonics become less dependent on the flow rates in comparison to the DC current. This fact is neatly shown in 3^{rd} and 4^{th} harmonics, in which despite an increase of 6 fold in flow rate the current rise is clearly much less significant.

Considering that the homogeneous reaction term $K_{EC'}c_O c_S$ is introduced into the domain. For this simulation, $c_{R0} = 2\,mM$ and $c_{S0} = 0.3\,mM$ (the substrate ratio is hence $r_S = 0.3/2 = 0.15$). A simple relation between steady currents under E and EC' reactions is stated in Equation 5.21:

$$I_{ss}^{EC'} = I_{ss}^{E}\,\frac{c_{R0}}{c_0}\,(1 + \frac{c_{S0}}{c_{R0}}) = I_{ss}^{E}\,\frac{c_{R0}}{c_0}(1 + r_S) \tag{5.21}$$

where c_0 is the normalized concentration of $1\,mM$ and I_{ss}^{E} corresponds to the steady current at that concentration. The table in Figure 118 compares the two currents and reveals a good agreement between them. The agreement becomes better as the flow rate increases. The term $1 + r_S$ is sometimes referred to as the efficiency factor:

$$N_{eff} = 1 + r_S \tag{5.22}$$

N_{eff} measures the electrochemical current enhancement due to catalytic effects relative to the case of single electron transfer. Note that this concept is not restricted to just EC' but extendable to other common mechanisms such as EC, ECE [206]. Factor 5.22 can also be considered as the maximum turn-over efficiency. For example, if the kinetic constant $K_{EC'}$ is considerably smaller, then species R is not regenerated quickly enough and the turn-over efficiency becomes smaller. Another possible reason for reducing N_{eff} is species O is quickly transported away from the electrode by means of stronger convection at large flow rates. Under such circumstances, the rate of catalytic step C' is hindered, leading to lower regeneration of R and the current.

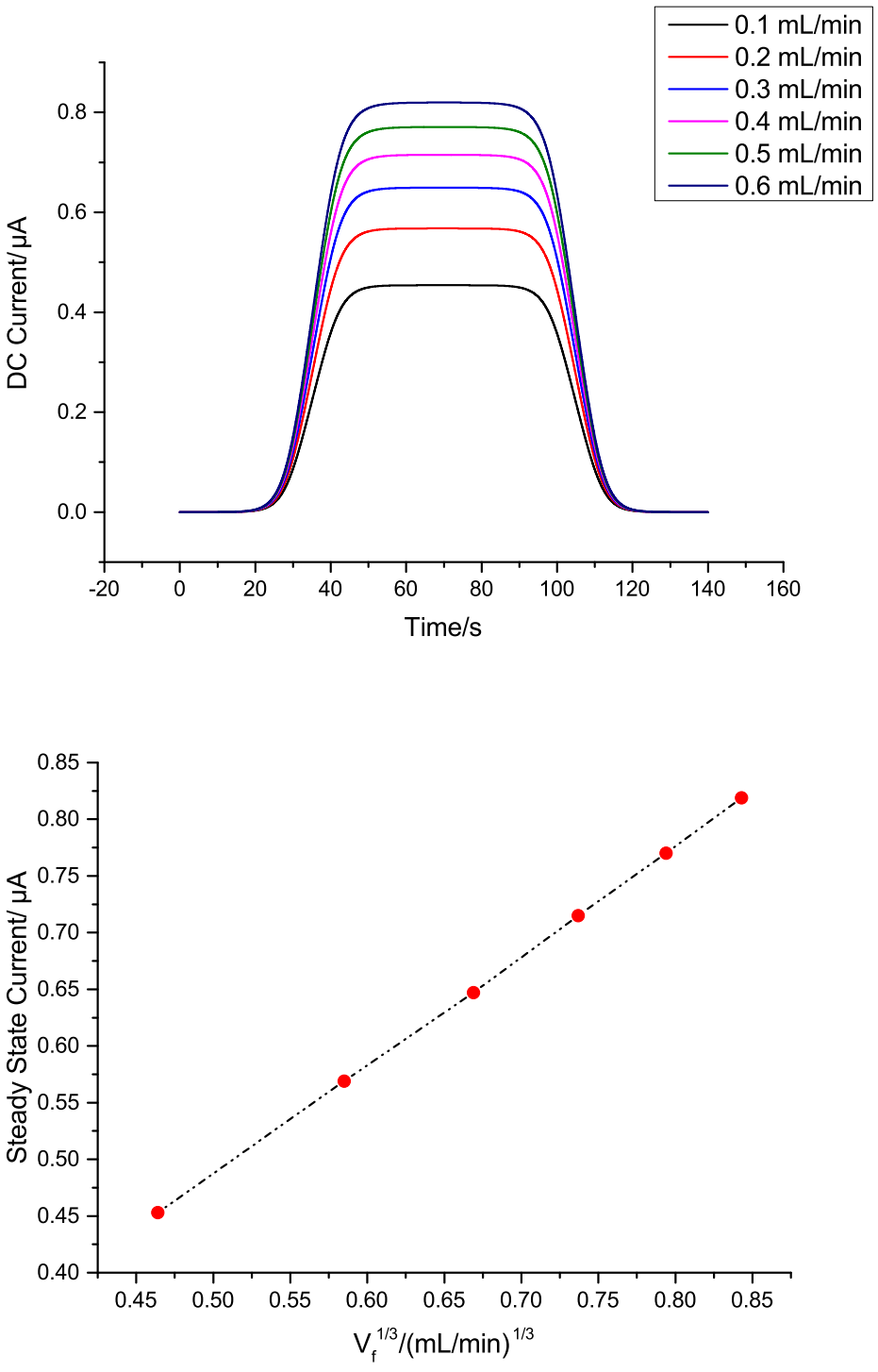

Figure 114: Extracted DC current in time domain at various flow rates between 0.1 and 0.6 mL/min (top). The Levich relation is confirmed in the bottom figure

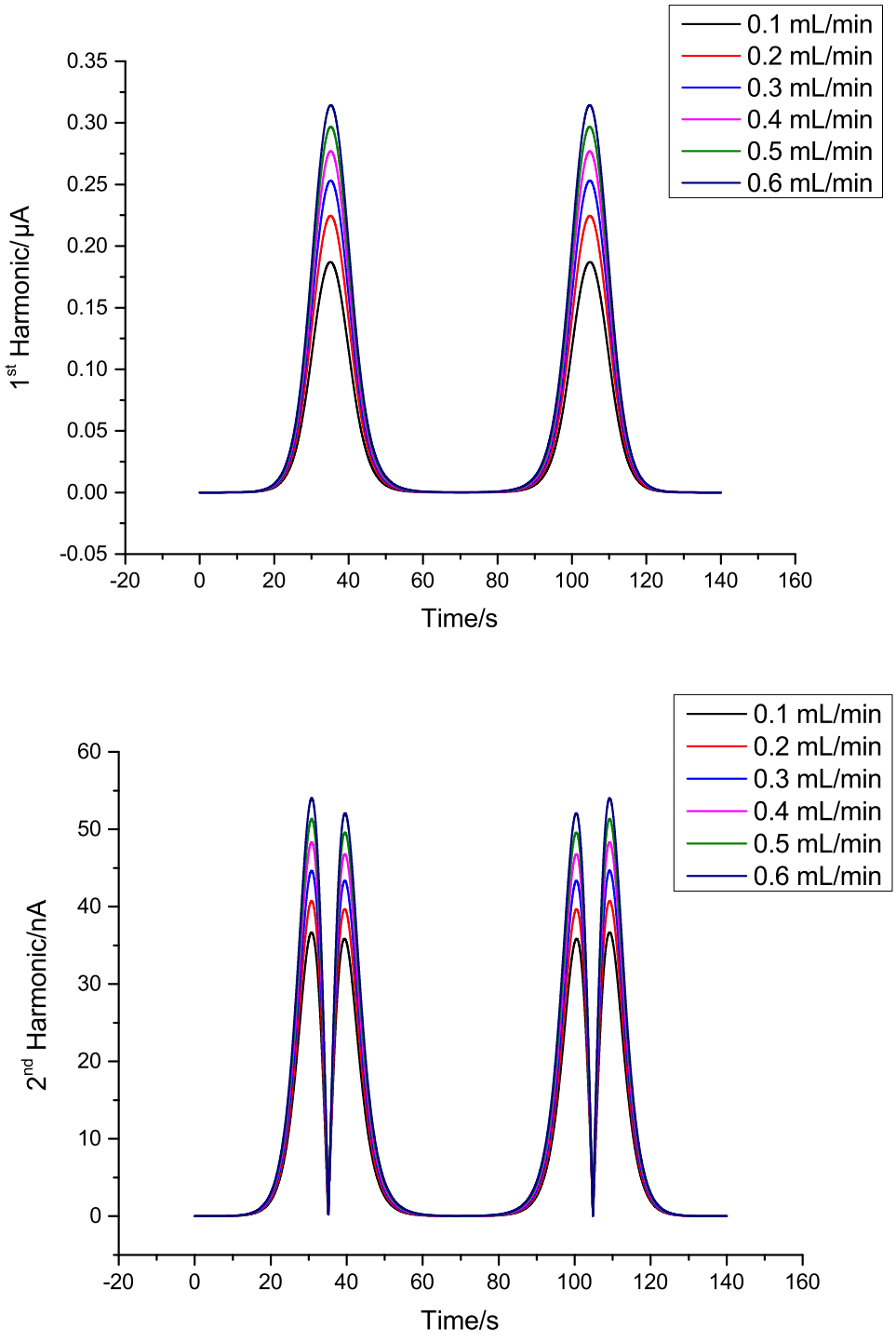

Figure 115: Extracted 1^{st} (top) and 2^{nd} (bottom) harmonics for the same range of flow rates as in Figure114

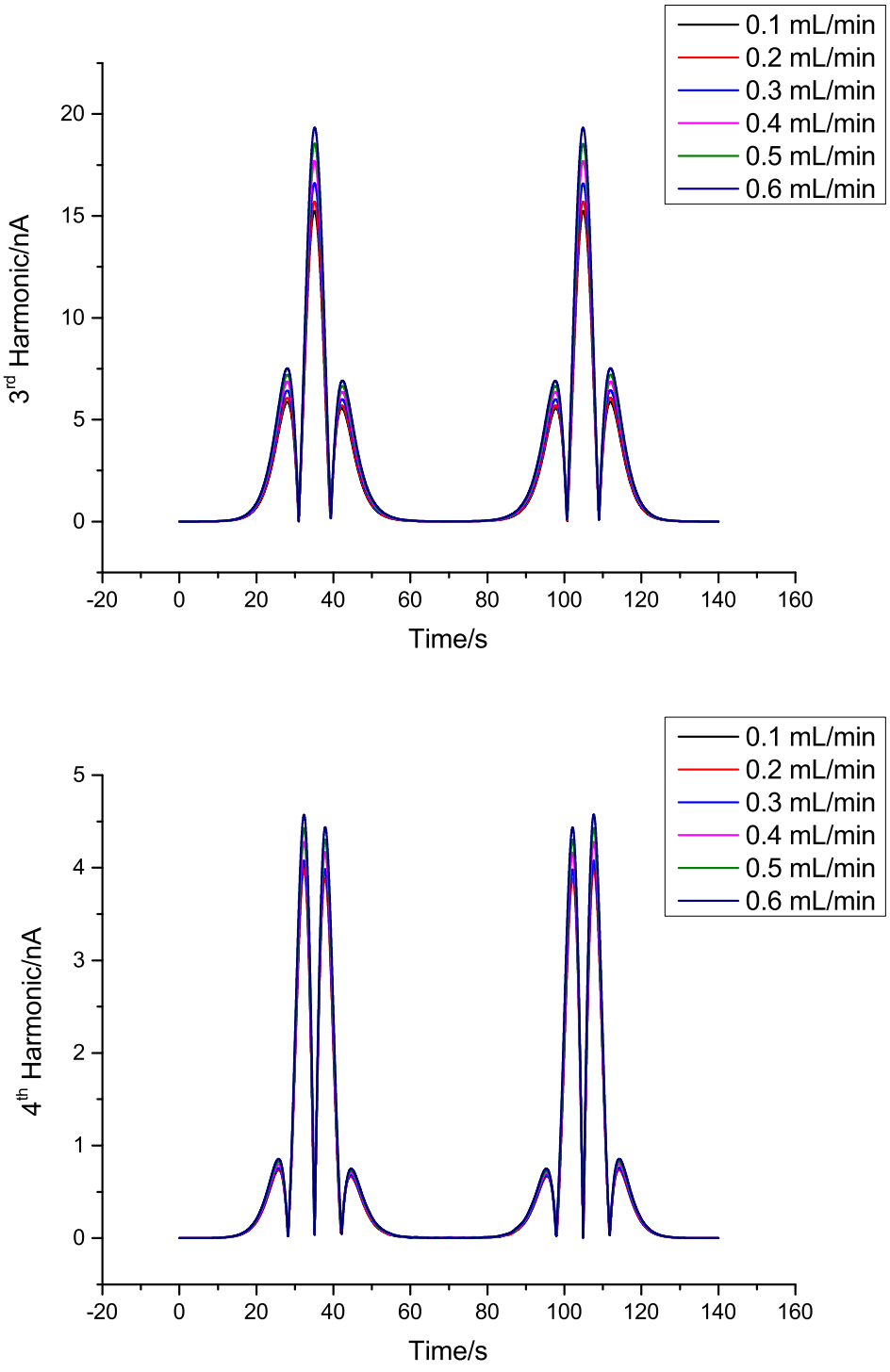

Figure 116: Extracted 3^{rd} (top) and 4^{th} (bottom) harmonics for the same range of flow rates as in Figure 114

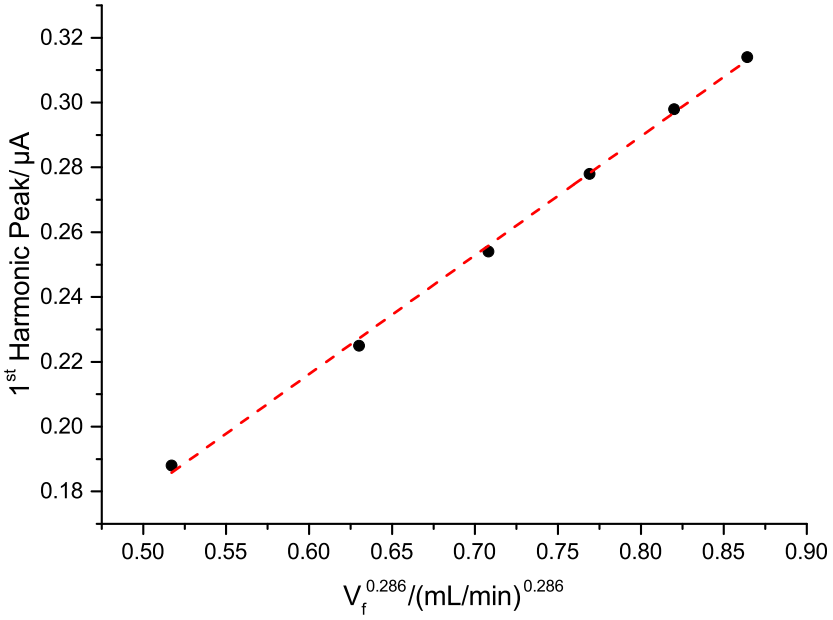

Figure 117: Empirical correlation between 1^{st} harmonic peaks and $V_f^{0.286}$. The exponent 0.286 is less than that of Levich expression (0.333), implying that the harmonic currents are less flow-rate dependent than the DC component

From Figure 119, no split-wave effect is evident in the first harmonic. This behaviour resembles that of the micro electrode. However, there is a weak shoulder in second harmonic at the slowest flow rate. This phenomenon can be explained as follows. Under diffusion control and macro electrodes, the split-wave is present in harmonics. Assuming that the flow is very small (which mimics the diffusion condition), a pre-wave is expected on this channel electrode. At higher flow rates, the mass transport effect is enhanced to an extent that the condition now is closer to that of a micro electrode and the effect consequently is subdued. Thus the behaviour at the channel electrode can be viewed as an intermediate between the macro and micro limits. The biggest advantage of using channel is the ability to control the flow rate, which is a factor in manifesting the split-wave. Consequently, the channel electrode should exhibit similar behavior to that of macro electrodes if the volumetric flow is not too high. In addition, because subsequent harmonics are less flow-rate dependent than the DC and 1^{st} harmonic, the pre-wave is therefore expected from 2^{nd} components onwards.

The discussion implies that the flow-rate should be set large enough so that steady DC current is reached, but not so high that the pre-wave disappears in the 2^{nd} har-

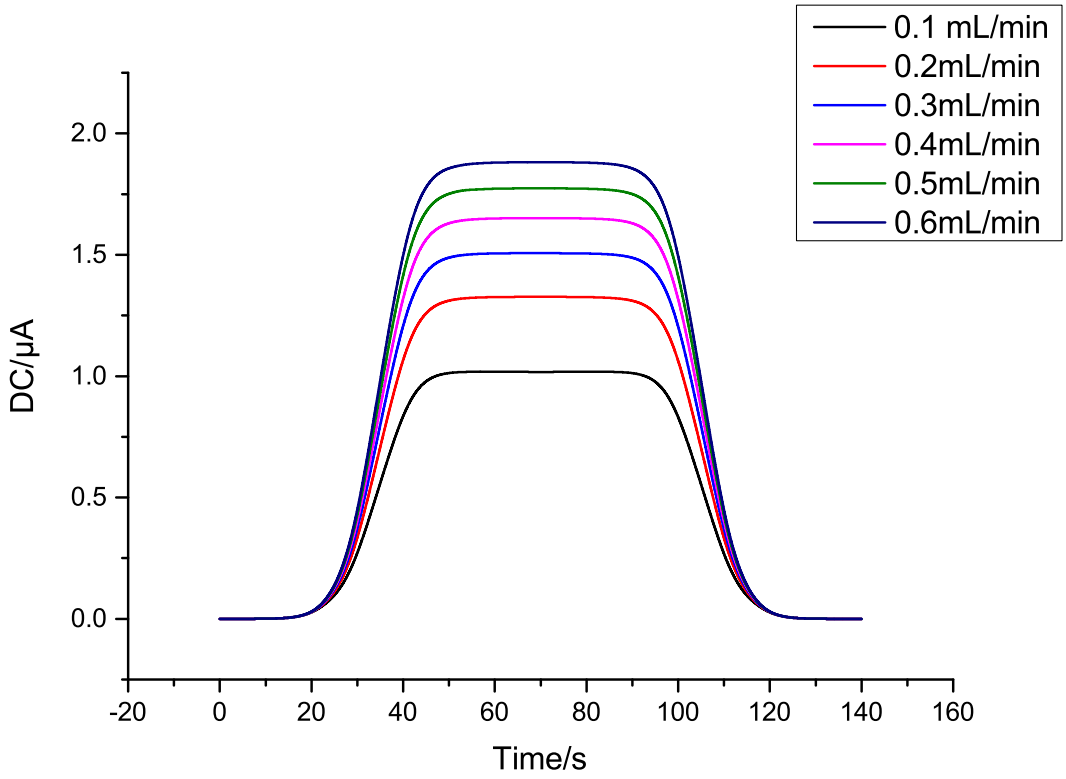

Flow Rate (mL/min)	Relation 5.21	Figure 118	Percentage Difference
0.1	1.041	1.022	1.8
0.2	1.311	1.322	0.8
0.3	1.494	1.506	0.8
0.4	1.647	1.655	0.5
0.5	1.776	1.778	0.1
0.6	1.888	1.890	0.1

Figure 118: The DC Current for a EC' reaction with $c_{R0} = 2\,mM$ and $c_{S0} = 0.3\,mM$ between flow rate 0.1 and $0.6\,mL/min$ (top). Comparison of steady currents using the Equation 5.21 and direct data from Figure 118. From Equation 5.21, the efficiency factor is fixed and the steady currents therefore follow the Levich relation 112

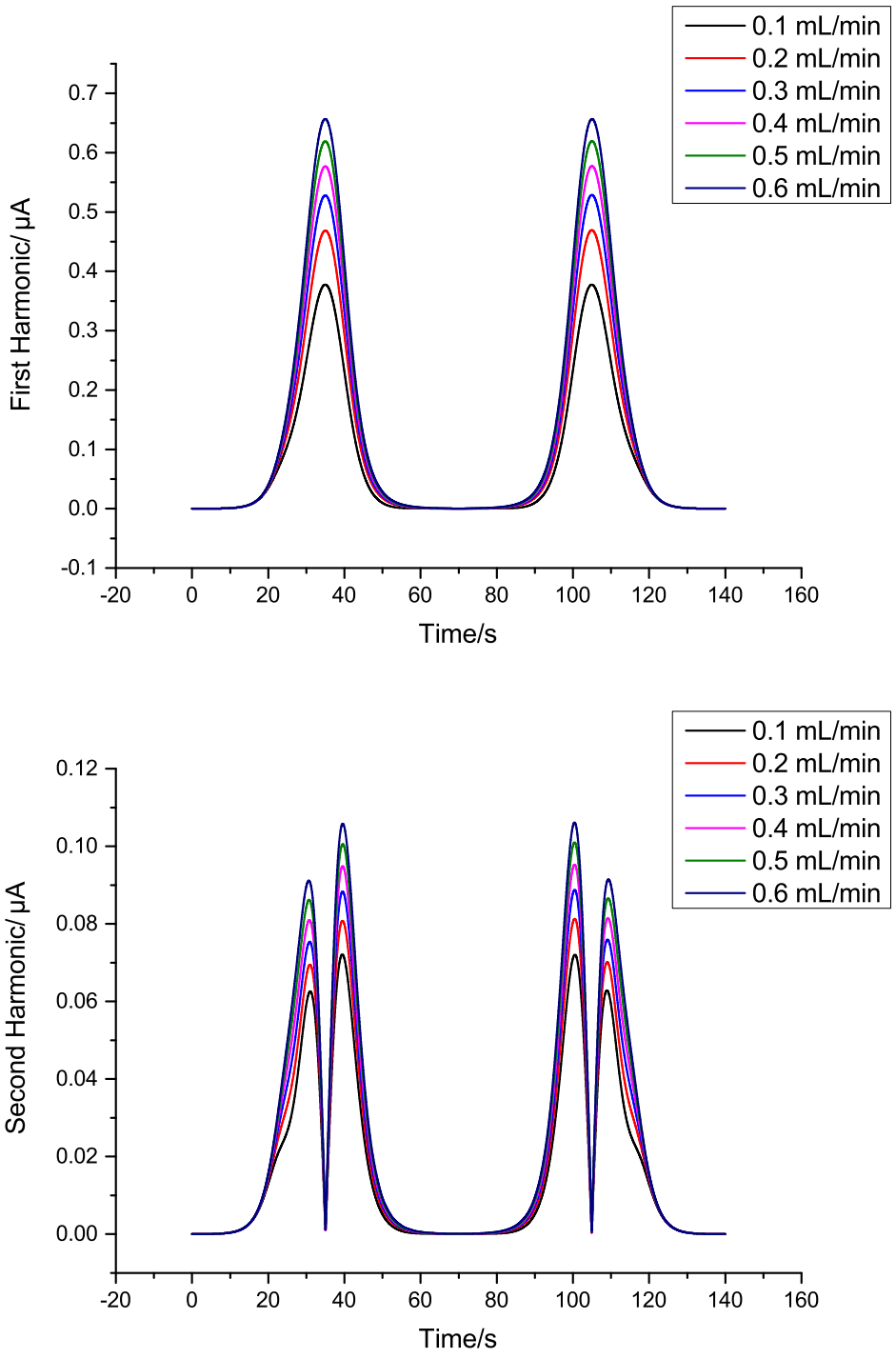

Figure 119: 1^{st}(top) and 2^{nd} (bottom) harmonics for EC' reaction with $c_{R0} = 2\,mM$ and $c_{S0} = 0.3\,mM$. Notice the relatively weak shoulder in 2^{nd} harmonics under the smallest flow rate $V_f = 0.1\,mL/min$

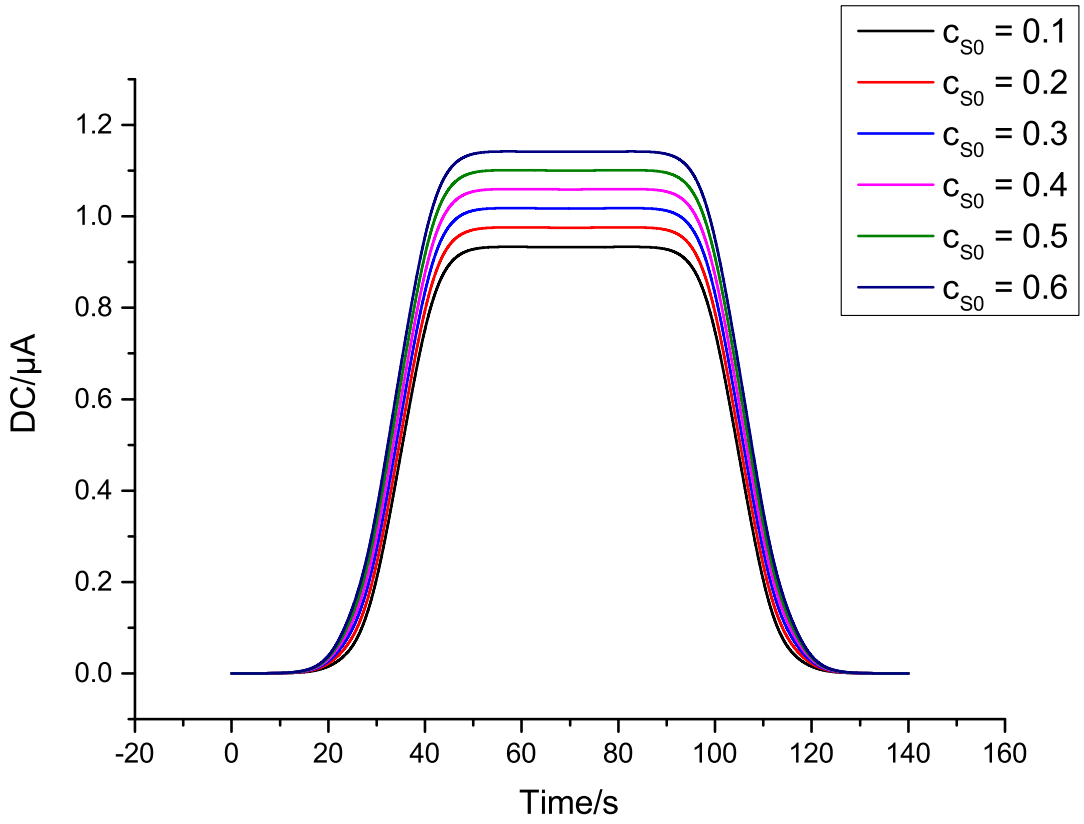

Substrate Concentration	Charge Count in (0, 35)	Charge Count in (35, 70)
0.1	1.135(9)	1.135(6)
0.2	1.141(0)	1.140(0)
0.3	1.147(7)	1.146(9)
0.4	1.156(0)	1.154(9)
0.5	1.165(6)	1.164(2)
0.6	1.176(6)	1.175(0)

Figure 120: (Top) DC current for various substrate concentrations $c_{S0} = 0.1 - 0.6\,mM$ (corresponding to r_S between 5% and 30%). The flow rate is fixed at $V_f = 0.1\,mL/min$ and inlet electroactive concentration is $c_{R0} = 2\,mM$. (Bottom) Counting the charge for the 2^{nd} harmonic at each substrate concentration in Figure 121. The unit of charge is μC. Numerical values are included up to 3 decimal places. It is clear that the same amount of charge is transferred during both time periods

monic. For the current situation, $V_f = 0.1\,mL/min$ is a sensible choice. The flow rate is then fixed at this level and computations are performed for different substrate concentrations. Figure 120 illustrates that as the substrate concentration increases, so does the steady current (by Equation 5.21). In addition, the split-wave effect is clearly seen in the 2^{nd} harmonic (top Figure 121) at sufficiently high substrate concentrations $c_{S0} = 0.6\,mM$ (or ratios $r_s = 30\%$). Note that at $c_{S0} = 0.3\,mM$ ($r_S = 15\%$), the shoulder is fairly apparent and therefore can be taken as the lower detection limit under the current set-up.

The voltammograms for micro fluidic channel are highly symmetric. The first reason is convection is a much faster mean of mass transport than diffusion. In addition, a slow scan rate means that a quasi-steady diffusion layer is formed at each applied potential. Finally, since the forward and backward potentials are approximately symmetrical, the diffusion layer profile should also be symmetrical and consequently so is the current. This feature is to be contrasted with results for macro electrodes in which the current profiles are strongly asymmetric favouring the forward current.

For the 2^{nd} harmonic, as soon as the pre-wave is formed, the associated E peak decreases in magnitude in comparison to the second E peak (Figure 121). However, the total amount of charge under each portion of the diagram should be equal. The cumulative charge is expressed as the area under the current-time graph:

$$Q(t_1, t_2) = \int_{t_1}^{t_2} I * dt \tag{5.23}$$

where (t_1, t_2) is the time interval. For each concentration level in Figure 121, the expression 5.23 is calculated for intervals (0, 35) and (35, 70) respectively. The computation is conveniently carried out using the simple trapezoidal rule to numerically integrate the current. The table in Figure 120 shows that charge balance is maintained at all concentration levels.

As before, it is analytically useful to check the correlation between the pre-wave peaks in the 2^{nd} harmonics and the substrate concentrations. A linear relation is indeed confirmed in bottom Figure 122. Statistical analysis further shows that the line does not strictly pass through the (0, 0) coordinate. However, because current magnitude is smaller in this case (order $\sim 10\,nA$) than that of macro electrode (order $\sim 100\,nA$), the mentioned anomaly is not a critical issue. Experimental results also show that the pre-wave phenomenon is present in the 2^{nd} but not the 1^{st} harmonic (Figure 123). In accordance with the simulation (Figure 119), a slight shoulder is present

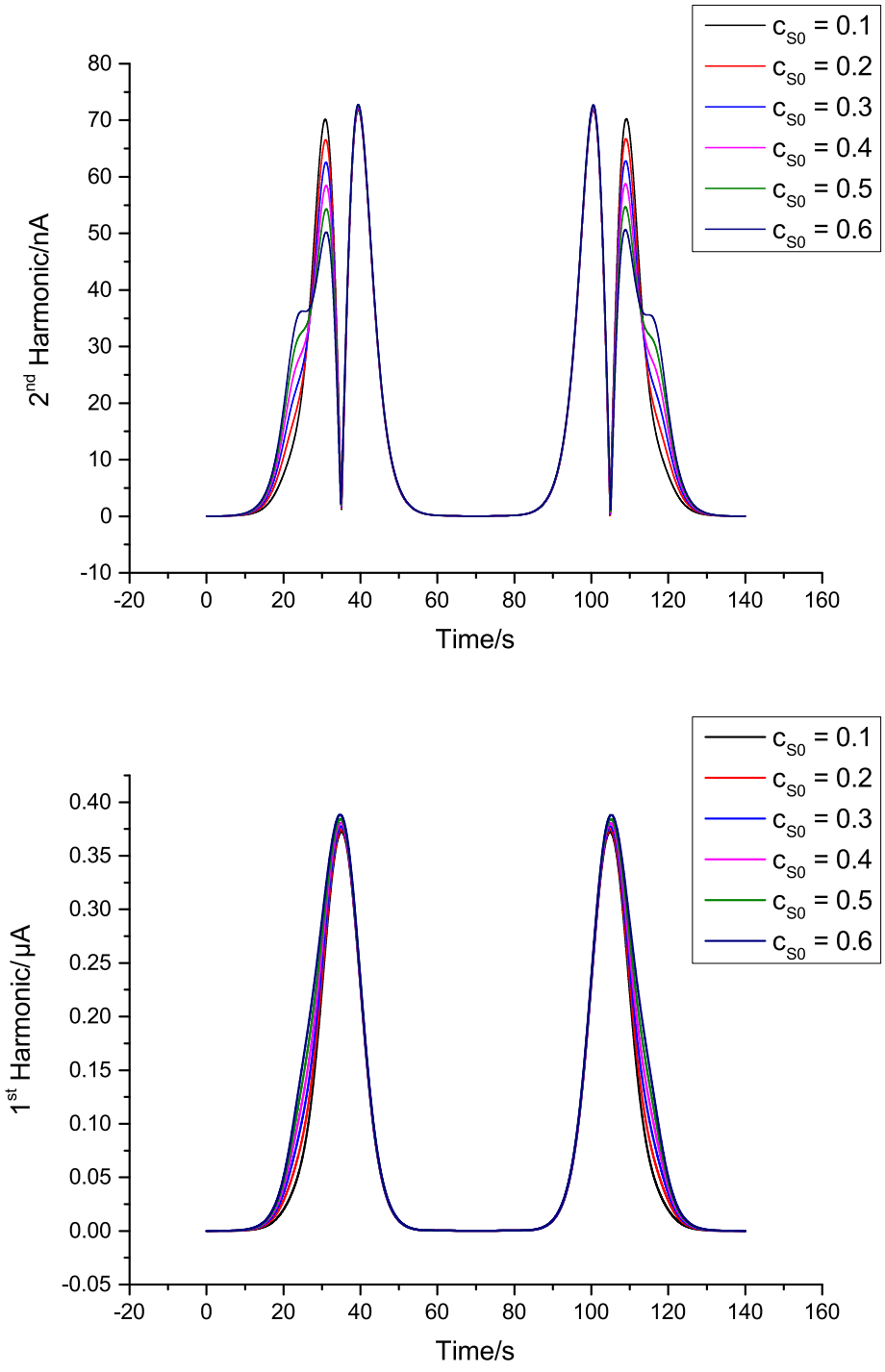

Figure 121: 2^{nd}(top) and 1^{st} (bottom) harmonics for different substrate concentrations $(0.1 - 0.6\,mM)$ and $c_{R0} = 2\,mM$, $V_f = 0.1\,mL/min$ and $\nu_{scan} = 10\,mV/s$. There is an evolution of split-wave in second harmonic but this is not observed in the first

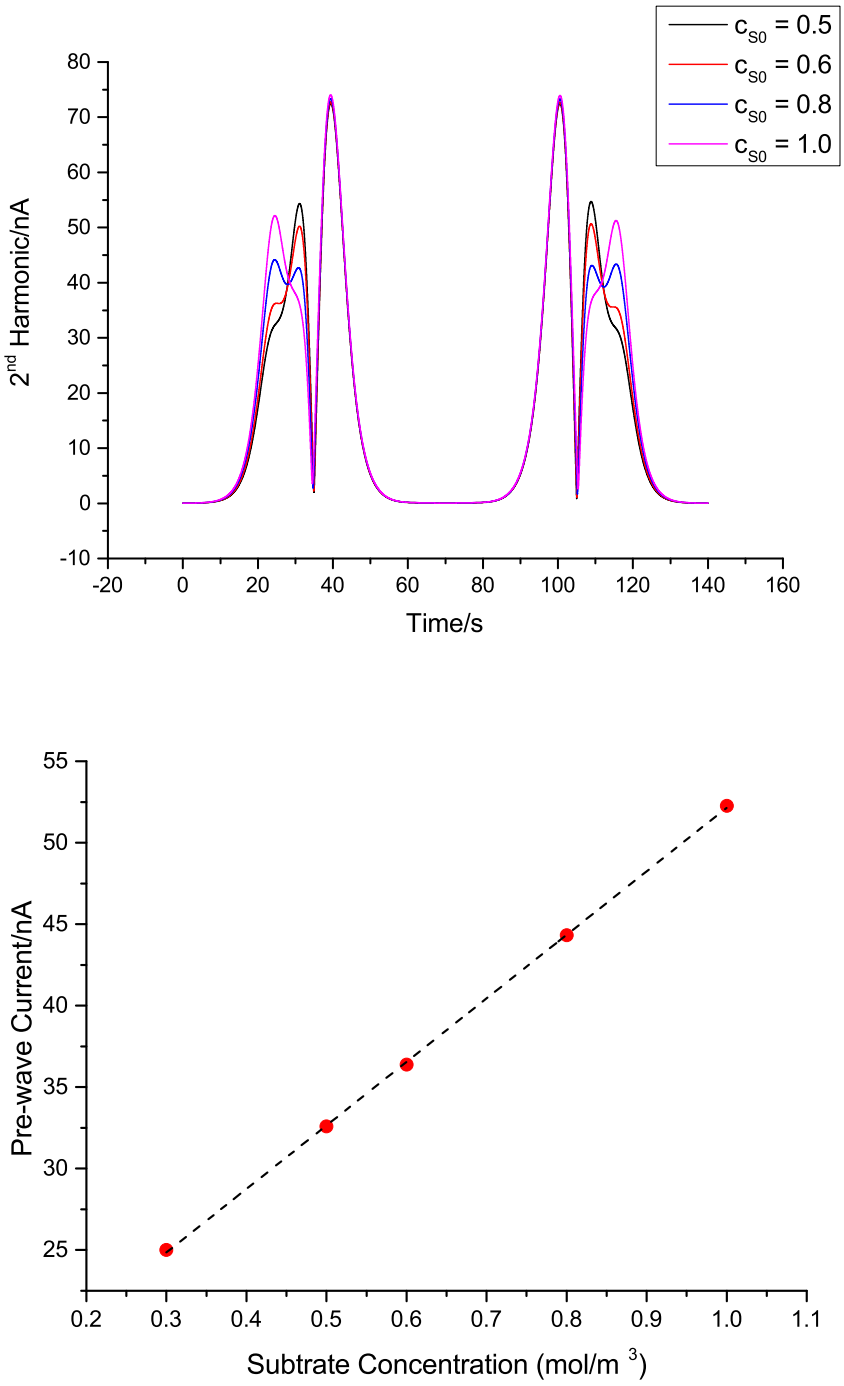

Figure 122: Comparison of 2^{nd} harmonics (top) and plot of the pre-wave peak versus the substrate concentrations (bottom). Linear correlation (black dash) is fitted with Pearson coefficient of 0.9999

at $c_{S0} = 0.3\,mM$ and disappears completely at $0.1\,mM$. In terms of magnitude, it is observed that currents are smaller in experiments than in simulations for both harmonics. One possible reason is because species diffusivities R, S in Table 22 was set larger than their actual values inside the channel.

In addition, it is acknowledged that acquiring reliable data under flow conditions has been very challenging. A frequently observed issue is the gold electrode surface is turns black and consequently corrupts the measurement signals. It is therefore speculated that the fabricated gold layer is unstable, slowly oxidized and worn off as the flow is applied over a period of time. This problem is traced back to dirty glass surface on which the gold crystals grows and thus a possible solution is to improve conditions inside the fabrication room.

To summarize, this section illustrates a novel combination between sinusoidal signal and forced convection to manifest the split-wave phenomenon in the 2^{nd} harmonics. As in the case of micro disk, strong mass transport inside the channel leads to disappearance of the split-wave in the 1^{st} component. The study also reaffirms the fact that harmonic components tend to be less flow-rate dependent and resemble those harmonics under diffusion control. The results also reveal the linear relationship between the pre-wave currents and concentration ratios, which is useful for analytical calibrations. More interestingly, for the current set-up, both theoretical and observable detection limits were shown to be around $0.3\,mM$.

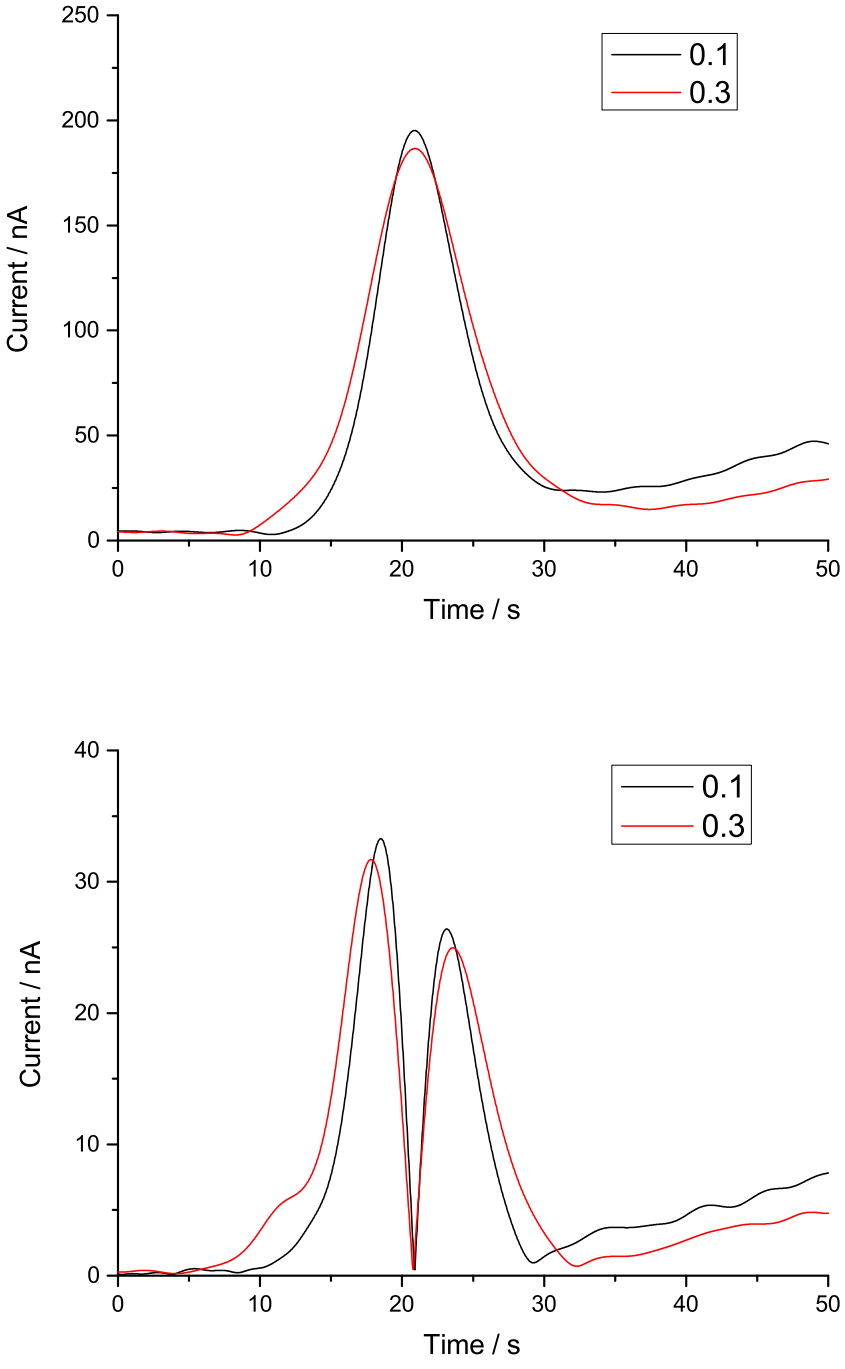

Figure 123: Experimental data for 1^{st} (top) and 2^{nd} (bottom) harmonic under L-cysteine concentrations of 0.1 (black) and $0.3\,mM$ (red) respectively (scan rate: $14.9\,mV/s$, amplitude $50\,mV$, volumetric flow rate $0.1\,mL/min$, gold electrode of length $100\,\mu m$). Note that only half of the voltammograms is shown in each figure

5.6 Chapter Conclusion

This chapter studies the design of fundamental harmonic signals and their application to elicit the effects of electro-catalysis, namely the EC' mechanism. The primary motivation was due to earlier investigations on similar mechanisms and uses of more complex voltammetry, but none considered the basic sinusoidal as a tool to achieve similar results. The work then proceeds to build up the background of the FFT (or AC) voltammetric technique as well as simulation methodology. Two major outcomes from this development are the algorithm to extract any harmonic component and the recognition of large amplitude sinusoidal as a convenient mean to improve signal to noise ratio. Simulation was then carried for diffusion-limit situation for macro and micro disks. For the former case, it was evident that the characteristic split-wave due to catalytic reaction was present in all harmonics. The effect is however frequency-dependent, as higher frequencies tend to subdue the pre-wave. In addition, the current magnitude also forms a linear correlation with substrate levels - a relationship confirmed in earlier chapter for the anharmonic or DC component. In addition, experimental measurements show a good agreement with simulation findings. These results illustrate an example for the use of AC perturbation to study effects of chemical catalysis. Finally, since any periodic signal can be decomposed into the sum of harmonics, the result here is theoretically more fundamental.

The same chemistry was re-examined under the enhanced mass transport condition with micro disk and rather different results were obtained. Firstly, the split-wave is no-longer observed in the first two harmonics both for low and high substrate levels. However, the effect is manifested weakly in subsequent higher harmonics. These observations lead to the conclusion that effect of mass transport was reduced for higher components and a proper control of such effect could reproduce the pre-wave behaviour in lower harmonics. The above hypothesis was then studied via the application of micro-fluidic devices. Using a combination of reasonably slow flow rates and large amplitude AC voltammetry, simulation study predicts the split-wave in 2^{nd} component as well as the same linear correlation observed for macro electrode. The former result was confirmed by experiments whilst the latter has not been checked due to technical difficulties in obtaining data and stabilizing electrode surface conditions. Furthermore, the fact that higher harmonics were weakly flow-rate dependent was supported by numerical data.

Chapter 6

Conclusions

This thesis applies a experimental design framework to the analysis of electron transfer kinetics and self-catalytic mechanism. The classical Butler-Volmer model is assumed to describe the fundamental electrochemical reaction. Though more sophisticated models, such as the Marcus-Hush-Chidsey, is available, Butler-Volmer model is preferred due to its simplicity and known effectiveness for describing the majority of redox reactions.

Since the work favours the model-based approach, numerical solutions to the forward problem were emphasized and thoroughly developed. Chapter 2 details FD method for solution of electron transfer processes. This is motivated by the fact that most experiments in electrochemistry are still conducted under diffusion-limited conditions. The chapter's results show good agreement between simulated data and the theory , thus confirming the reliability of FD in solving this forward problem. Based on the foundation in chapter 2, chapter 3 examines the use of linear sweep voltammetry as an experimental design variable to regress primary parameters in the Butler-Volmer model: the kinetic constant, charge transfer coefficient and the equilibrium voltage. By fixing the mass transport mode as diffusion control, a sequence of investigations concerning model parameters (identifiability, Sobol ranking, inversion and statistics computations) were carried out. From the identifiability test, potential compensating effects and correlations among the parameters were noticed. By employing reasonably small electrode areas as an additional design variable, solution resistance factors were shown to be insignificant and were subsequently excluded from the generalized formulation. Finally, a theoretical inversion under a quasi-reversible regime proves primary parameters can be recovered with a satisfactory degree of accuracy. Furthermore, a MCMC simulation was observed to improve the point estimate statistics as well as

detail correlations among parameter pairs. A major conclusion from this chapter is a simple linear signal that is adequate for parameter estimation purposes, which is in line with previous results stating that more complex waveforms only yield minor improvement in parameter identification. A possible research direction is the synthesis of voltage signal which improves the identifiability number. Though such work was partially undertaken, a complete answer is yet to be reached.

Because hydrodynamic devices have become common in electrochemistry, chapter 4 investigates the role of mechanical convection in model identifiability. The signal factor was fixed by employing only linear sweep voltammetry. The recent RoDE device, was studied because it is a generalized configuration of the well-known rotating disk. The rocking mechanism was approximated by the four-bar geometry and yielded good agreement with experimental data, despite the over-simplified 2D axisymmetric model for both fluid and mass transports. In addition, the limiting Levich expression was derived from numerical considerations, showing RDE is the limiting case for all possible combination of RoDE. Identifiability calculation was carried out to further compare the two configurations. An important result is RoDE provides a better differentiation of the parameter set when the whole current response was considered. On the other hand, if only the limiting responses were concerned, then RDE is a much better choice to determine these parameters. The final section introduces the rotating drum as a potential device to study electrochemical reaction in viscous media such as PEG and ionic liquids and future considerations should pursue these studies. Due to the time constraint, comparison of model identifiability between a rotating drum and rotating disk was not undertaken, though similar results, especially the number η_{steady} for these configurations are expected. In addition, future work should consider the reduced effective diffusivity under flow driven conditions.

Chapter 5 explores the application of large amplitude harmonic disturbances to probe the effects of homogeneous catalytic reactions. The EC' mechanism was selected due to promising chemical applications in detecting sulphide compounds. The AC voltammetry relies on the combination of the common linear sweep (to drive the fundamental electron transfer reaction) and a single sinusoidal term. This term then produces extra currents, called the harmonics, in addition to the usual aperiodic current. Algorithms based on FFT and iFFT operations were implemented to automatically extract harmonics from the total current response. The calculation was first carried out for diffusion control conditions. For a large planar electrode, the signature split-wave was observed in all harmonics as well as in the DC current. In addition,

the pre-wave current peak shows a linear relationship with the species concentrations, thus confirming analytical values of the method. For micro electrode, because of strong mass-transport enhancement, these pre-waves were prominent in only higher (e.g. 3^{rd}, 4^{th}) harmonics. Consequently, to control the transport factor, micro-fluidic channel was used because the flow rate is more easily controlled than in the diffusion mode. By carefully adjusting the flow rate, both the split-wave phenomenon and linear correlation were again confirmed for the 2^{nd} harmonics, though it was not the case for the 1^{st} harmonics due to large residues of mass-transport effect. Overall, harmonic pertubations prove to be a useful tool to extract additional information on chemical kinetics. A potential future direction is to re-evaluate the above mechanism using the combination of rocking condition and FFT voltammetry to compare the results with channel electrode. Electro-catalysis under hydro dynamic conditions is a relatively new topic and recent work only experimentally studies alcohol oxidations using TEMPO as the mediator [207]. Though the harmonic currents are not expected to be significantly different among these devices, their characteristic fluid dynamic effects might give rise to subtle and potentially useful differences.

References

[1] J. C. Myland et al. An analytical expression for the current-voltage relationship during reversible cyclic voltammetry. *Journal of Electroanalytical Chemistry*, 153:43–54, 1983.

[2] A. J. Bard and L. R. Faulkner. *Electrochemical Methods, Fundamentals and Applications*. Wiley-Interscience, 2001.

[3] D. Shoup and A. Szabo. Chronoamperometric current at finite disk electrodes. *Journal of Electroanalytical Chemistry*, 14:237–245, 1984.

[4] V. Maheshwari et al. Multiobjective framework for model-based design of experiments to improve parameter precision and minimize parameter correlation. *Industrial and Engineering Chemistry Research*, 52:8289–8304, 2013.

[5] G. Grundmeier et al. Corrosion protection by organic coatings: electrochemical mechanism and novel methods of investigation. *Electrochimica Acta*, 45:2515–2533, 2000.

[6] J. B. Goodenough et al. The Li-Ion rechargable battery: A perspective review. *Journal of the American Chemical Society*, 135:1167–1176, 2013.

[7] G. Wang et al. A review of electrode materials for electrochemical supercapacitors. *Chem. Soc. Rev*, 41:797–828, 2012.

[8] A. Kirubakaran et al. A review on fuel cell technologies and power electronic interface. *Renewable and Sustainable Energy Reviews*, 13:2430–2440, 2009.

[9] Z. Li et al. Photoelectrochemical cells for solar hydrogen production: current state of promising photoelectrodes, methods to improve their properties and outlook. *Energy and Environmental Science*, 6:347–370, 2013.

[10] B. Privett et al. Electrochemical sensors. *Anal. Chem.*, 80:4499–4517, 2008.

[11] E. Bakker. Electrochemical sensors. *Anal. Chem.*, 76:3285–3298, 2004.

[12] J. Janata. *Principles of Chemical Sensors, 2nd Edition*. Springer, 2009.

[13] R. F. Taylor and J. S. Schultz. *Handbook of Chemical and Biological Sensors*. IoP Publishing, 1996.

[14] M. Pumera et al. Graphene for electrochemical sensing and biosensing. *TrAC Trends in Analytical Chemistry*, 29:954–965, 2010.

[15] H. E. Zittel and F. J. Miller. A glassy carbon electrode for voltammetry. *Anal. Chem.*, 37:200–202, 1965.

[16] A. C. Fisher. *Electrode Dynamics*. Oxford University Press, 1996.

[17] P. Atkins. *Physical Chemistry*. Oxford University Press, 2006.

[18] R. B. Bird et al. *Transport Phenomena*. Wiley Inter-Science, 2007.

[19] R. Fox et al. *Introduction to Fluid Mechanics*. John Wiley and Sons, 2003.

[20] B. R. Munson. *Fundamentals of Fluid Mechanics, 7th Edition*. Wiley Science, 2013.

[21] Southampton Electrochemistry Group. *Instrumental Methods in Electrochemistry*. Horwood Publishing Chichester, 1985.

[22] C. M. A. Brett and A. M. O. Brett. *Electrochemistry: Principles, Methods and Applications*. Oxford University Press, 1994.

[23] E. J. F. Dickinson and R. G. Compton. How much supporting electrolytes is required to make a cyclic voltammetry experiment quantitatively diffusional? a theoretical and experimental investigation. *J. Phys. Chem. C*, 113:11157–11171, 2009.

[24] E. J. F. Dickinson and R. G. Compton. The zero-field approximation for weakly supported voltammetry: A critical evaluation. *Chemistry Physical Letter*, 497: 173–183, 2010.

[25] S. Schofer. Numerical solution of the Poisson-Nernst-Planck equation system. Master's thesis, Friederich-Alexander-University, 2013.

[26] M. Lyons. Molecular thermodynamics and kinetics lecture 6: Phenomenological electrode kinetics, 2013.

[27] R. A. Marcus. On the theory of electrochemical and chemical electron transfer processes. *Can. J. Chem.*, 37:155–163, 1959.

[28] H. Girault. *Analytical and Physical Electrochemistry*. E P F L Press, 2004.

[29] L. M. Torres et al. Understanding the difference between inner- and outer-sphere mechanisms: An electrochemical experiment. *Journal Of Chemical Education*, 73, 1996.

[30] R. G. Compton, E. Larboda, and K. R. Ward. *Understanding Voltammetry:Simulation of Electrode Processes*. Imperial College Press, 2013.

[31] E. Larboda et al. Asymmetric marcus-hush theory for voltammetry. *Chem. Soc. Rev.*, 42:4894–4905, 2013.

[32] F. Marken. Basics in electrode kinetics, advanced electrochemistry summer course, 2016.

[33] E. Laborda et al. A comparison of Marcus-Hush versus Butler-Volmer electrode kinetics using potential pulse voltammetric techniques. *Journal of Electroanalytical Chemistry*, 660:169–177, 2011.

[34] Y. Wang et al. The use of differential pulse voltammetries to discriminate between the Butler-Volmer and the simple Marcus-Hush models for heterogeneous electron transfer: The electro-reduction of europium (iii) in aqueous solution. *Journal of Electroanalytical Chemistry*, 668:7–12, 2012.

[35] M. C. Henstridge et al. Marcus-hush-chidsey theory of electron transfer applied to voltammetry: A review. *Electrochimica Acta*, 84:12–20, 2012.

[36] E. Larboda et al. Asymmetric marcus theory: Application to electrode kinetics. *Journal of Electroanalytical Chemistry*, 67:48–53, 2012.

[37] E. L. Tanner et al. One-electron reduction of 2-nitrotoluene, nitrocyclopentane, and 1-nitrobutane in room temperature ionic liquids: A comparative study of Butler-Volmer and Marcus-Hush theories using microdisk electrodes. *J. Phys. Chem. C*, 119:2716–2726, 2014.

[38] V. G. Levich. *Physicochemical Hydrodynamics*. Prentice-Hall, Inc., Englewood Cliffs, 1962.

[39] J. Alden. *Computational Electrochemistry*. PhD thesis, University of Oxford, 1998.

[40] J. Newman and K. E. T. Alyea. *Electrochemical Systems*. Wiley-Interscience, 2004.

[41] G. C. Barker et al. Square-wave polarography. *Analyst*, 77:685–696, 1952.

[42] B. A. Brookes et al. Simulation of square wave voltammetry: Reversible electrode processes. *Journal of Physical Chemistry B*, 103:5289–5295, 1999.

[43] L. Ramaley et al. Theory of square wave voltammetry. *Analytical Chemistry*, 41:1362–1365, 1969.

[44] A. Chen and B. Shah. Electrochemical sensing and biosensing based on square wave voltammetry. *Anal. Methods*, 37:2158–2173, 2013.

[45] V. Mirceski et al. Square-wave voltammetry: A review on the recent progress. *Electroanalysis*, 25:2411–2422, 2013.

[46] D. J. Gavaghan and A. M. Bond. A complete numerical simulation of the techniques of alternating current linear sweep and cyclic voltammetry: analysis of a reversible process by conventional and fast fourier transform methods. *Journal of Electroanalytical Chemistry*, 480:133–149, 2000.

[47] A. M. Bond et al. Changing the look of voltammetry: Can ft revolutionize voltammetric techniques as it did for NMR. *Analytical Chemistry*, 77:186–195, 2005.

[48] M. K. Hobson. *Mathematical Methods for Physics and Engineering*. Cambridge University Press, 1997.

[49] D. J. Gavaghan et al. A comparison of sinusoidal, square wave, sawtooth, and staircase forms of transient ramped voltammetry when a reversible process is analysed in the frequency domain. *Journal of Electroanalytical Chemistry*, 513: 73–86, 2001.

[50] S. O. Engblom et al. Large amplitude AC voltammetry: A comparison between theory and experiment. *Electroanalysis*, 13:626–630, 2001.

[51] J. Zhang and A. M. Bond. Discrimination and evaluation of the effects of uncompensated resistance and slow electrode kinetics from the higher harmonic components of a fourier transformed large-amplitude alternating current voltammogram. *Anal. Chem.*, 57:2276–2288, 2007.

[52] A. Sher et al. Resistance, capacitance and electrode kinetic effects in fourier-transformed large-amplitude sinusoidal voltammetry: Emergence of powerful and intuitively obvious tools for recognition of patterns of behavior. *Analytical chemistry*, 76:6214–6228, 2004.

[53] A. Sher et al. Fourier transformed large amplitude square-wave voltammetry as an alternative to impedance spectroscopy: Evaluation of resistance, capacitance and electrode kinetic effects via an heuristic approach. *Electroanalysis*, 17:1450–1462, 2005.

[54] E. Mashkina and A. M. Bond. Implementation of a statistically supported heuristic approach to alternating current voltammetric harmonic component analysis: Re-evaluation of the macrodisk glassy carbon electrode kinetics for oxidation of ferrocene in acetonitrile. *Analytical Chemistry*, 83:1791–1799, 2011.

[55] K. Bano et al. Investigations of fast electrode kinetics for reduction of 2,3,5,6-tetrafluoro-7,7,8,8-tetracyanoquinodimethane in conventional solvents and ionic liquids using fourier transformed large amplitude alternating current voltammetry. *J. Phys. Chem. C*, 118:9560–9569, 2014.

[56] A. M. Bond et al. An integrated instrumental and theoretical approach to quantitative electrode kinetic studies based on large amplitude fourier transformed AC voltammetry: A mini review. *Electrochemistry Communications*, 57:78–83, 2015.

[57] E. Mashkina et al. Estimation of electrode kinetic and uncompensated resistance parameters and insights into their significance using fourier transformed AC voltammetry and e-science software tools. *Journal of Electroanalytical Chemistry*, 690:104–110, 2013.

[58] C. Y. Lee et al. Effects of coupled homogeneous chemical reactions on the response of large-amplitude AC voltammetry: Extraction of kinetic and mechanistic information by fourier transform analysis of higher harmonic data. *J. Phys. Chem. A*, 114:10122–10134, 2010.

[59] B. Lertanantawong et al. Investigation of mediated oxidation of ascorbic acid by ferrocenemethanol using large-amplitude fourier transformed AC voltammetry under quasi-reversible electron-transfer conditions at an indium tin oxide electrode. *Anal. Chem.*, 80:6515–6525, 2008.

[60] A. C. Fisher. Fundamentals of electrochemical engineering: Lecture notes, ceb part iib, 2013.

[61] K. Yokoyama and Y. Kayanuma. Cyclic voltammetric simulation for electrochemically mediated enzyme reaction and determination of enzyme kinetic constants. *Anal. Chem.*, 70:3368–3376, 1998.

[62] S. Peng. *Microengineered Electrochemical Reactors*. PhD thesis, University of Cambridge, 2015.

[63] J. Cooper. Energy harvesting from sulphurous environment, master thesis. Master's thesis, University of Hull, 2013.

[64] S. M. Matthews et al. Attributes of direct current aperiodic and alternating current harmonic components derived from large amplitude fourier transformed voltammetry under microfluidic control in a channel electrode. *Analytical Chemistry*, 84:6686–6692, 2012.

[65] K. Bano et al. Large amplitude fourier transformed AC voltammetry at a rotating disc electrode: a versatile technique for covering levich and flow rate insensitive regimes in a single experiment. *Phys. Chem. Chem. Phys*, 14:4742–4752, 2012.

[66] I. Henley. *Computational Electrochemistry*. PhD thesis, University of Bath, 2004.

[67] G. D. Smith. *Numerical Solution of Partial Differential Equations: Finite Difference Methods 3rd Edition.* Oxford University Press, 1985.

[68] H. A. Obaid et al. An unconditionally stable nonstandard finite difference method applied to a mathematical model of hiv infection. *Int. J. Appl. Math. Comput. Sci.*, 23:357–372, 2013.

[69] J. Zhao. *A highly accurate compact finite difference method and its applications in financial mathematics and computational biology.* PhD thesis, University of Western Ontario, 2006.

[70] M. Rudolph. A fast implicit finite difference algorithm for the digital simulation of electrochemical processes. *Journal of Electroanalytical Chemistry and Interfacial Electrochemistry*, 314:13–22, 1991.

[71] M. Rudolph. A fast implicit finite difference algorithm for the digital simulation of electrochemical processes, part ii. an improved treatment of electrochemical mechanisms with second-order reactions. *Journal of Electroanalytical Chemistry*, 338:85–98, 1992.

[72] S. W. Feldberg. A fast quasi-explicit finite difference method for simulating electrochemical phenomena Part I. Application to cyclic voltammetric problems. *Journal of Electroanalytical Chemistry*, 290:49–65, 1990.

[73] K. Aoki et al. Linear sweep voltammetry at very small stationary disk electrode. *Journal of Electroanalytical Chemistry and Interfacial Electrochemistry*, 171:219–230, 1984.

[74] K. Aoki, K. Tokuda, and H. Matsuda. Theory of chronoamperometric curves at microband electrodes. *Journal of Electroanalytical Chemistry*, 225:19–32, 1987.

[75] J. Heinze. Diffusion processes at finite (micro) disk electrodes solved by digital simulation. *Journal of Electroanalytical Chemistry and Interfacial Electrochemistry*, 124:73–86, 1981.

[76] D.J. Gavaghan. An exponentially expanding mesh ideally suited to the fast and efficient simulation of diffusion processes at microdisc electrodes. 2. application to chronoamperometry. *Journal of Electroanalytical Chemistry*, 456:13–23, 1998.

[77] D.J. Gavaghan. An exponentially expanding mesh ideally suited to the fast and efficient simulation of diffusion processes at microdisc electrodes. 3. application to voltammetry. *Journal of Electroanalytical Chemistry*, 456:25–35, 1998.

[78] J. G. L. Peterson et al. Cyclic voltammetry in weakly supported media: The stripping of thallium from a hemispherical amalgam drop. *J. Phys. Chem. C*, 112:17175–17182, 2008.

[79] K. Aoki et al. Chronoamperometry of strong acids without supporting electrolyte. *Journal of Electroanalytical Chemistry*, 472:1–6, 1999.

[80] C. C. Dai. *Fabrications and Applications of pH Sensors*. PhD thesis, University of Cambridge, 2015.

[81] S. Iijima. Helical microtubules of graphitic carbon. *Nature*, 354:56–58, 1991.

[82] K. R. Ward et al. The theory of cyclic voltammetry of electrochemically heterogeneous surfaces: comparison of different models for surface geometry and applications to highly ordered pyrolytic graphite. *Phys. Chem. Chem. Phys.*, 14:7264–7275, 2012.

[83] B. A. Brookes et al. A computational and experimental study of cyclic voltammetry response of partially blocked electrodes part i: Non overlapping uniformly distributed blocking systems. *J. Phys. Chem. B*, 107:6431–6444, 2003.

[84] T. J. Davies et al. A computational and experimental study of cyclic voltammetry response of partially blocked electrodes part ii: Randomly distributed and overlapping blocking systems. *J. Phys. Chem. B*, 107:6431–6444, 2003.

[85] E. O. Barnes et al. Voltammetry at porous electrodes: A theoretical study. *Journal of Electroanalytical Chemistry*, 720-721:92–100, 2014.

[86] F. Qiu. *Numerical Methods in Electrochemistry*. PhD thesis, University of Bath, 1999.

[87] F. Hecht. New development in freefem++. *J. Numer. Math.*, 20(3-4):251–265, 2012.

[88] M. Penczek and Z. Stojek. Current distribution at a submicrodisc electrode. *Journal of Electroanalytical Chemistry*, 227:271–274, 1987.

[89] J. Galceran et al. Voltammetric currents for any ligand-to-metal concentration ratio in fully labile metal-macromolecular complexation. *Journal of Electroanalytical Chemistry*, 472:42–52, 1999.

[90] R. Ferrigno et al. Finite element simulation of the chronoamperometric response of recessed and protruding microdisc electrodes. *Electrochimica Acta*, 42:1895–1903, 1997.

[91] R. Ferrigno et al. Finite element simulation of electrochemical ac diffusional impedance. Application to recessed microdiscs. *Journal of Electroanalytical Chemistry*, 492:1–6, 2000.

[92] D. J. Gavaghan et al. Adaptive finite element methods in electrochemistry. *Langmuir*, 22:10666–10682, 2006.

[93] K. Harriman et al. Adaptative finite element simulation of currents at microelectrodes to a guaranteed accuracy. Application to a simple model problem. *Electrochemistry Communication*, 2:150–156, 2000.

[94] K. Harriman et al. Adaptative finite element simulation of currents at microelectrodes to a guaranteed accuracy. first-order EC' mechanism at inlaid and recessed discs. *Electrochemistry Communication*, 2:163–170, 2000.

[95] K. Harriman et al. Adaptive finite element simulation of currents at microelectrodes to a guaranteed accuracy. ECE and EC2E mechanisms at channel microband electrodes. *Electrochemistry Communication*, 2:576–585, 2000.

[96] N. P. C. Stevens, K. E. Gooch, and A. C. Fisher. Computational electrochemstry: Simulation of homogeneous chemical reactions in the confluence reactor and channel flow cell. *Journal of Physical Chemistry*, 104:1241–1248, 2000.

[97] N. P. C. Stevens et al. Finite element simulations in electrochemistry. Hydrodynamic Voltammetry. *J. Phys. Chem. B*, 101:8259–8263, 1997.

[98] K. A. Gooch. *Numerical Electrochemistry*. PhD thesis, University of Cambridge, 2003.

[99] S. W. Feldberg and C. I. Goldstein. Examination of the behavior of the fully implicit finite-difference algorithm with the richtmyer modification: Behaviour

with an exponentially expanding time grid. *Journal of Electroanalytical Chemistry*, 397:1–10, 1995.

[100] S. V. Patankar. *Numerical Heat Transfer and Fluid Flow*. McGraw-Hill Book Company, 1980.

[101] G. Q. Du, S. M. Matthews, M. L. Johns, and A. C. Fisher. Computational electrochemistry: Lattice boltzmann simulation of voltammetry at microelectrodes. *Electrochemistry Communication*, 9:2519–2524, 2007.

[102] G. Q. Du. *Lattice Boltzmann Approach in Numerical Electrochemistry*. PhD thesis, University of Cambridge, 2007.

[103] N. Fietkau et al. Voltammetric sizing and locating of spherical particles via cyclic voltammetry. *J. Phys. Chem. C*, 111:13905–13911, 2007.

[104] J. A. Jacquez et al. Numerical parameter identifiability and estimability: Integrating identifiability, estimability and optimal sampling design. *Mathematical Biosciences*, 77:201–227, 1985.

[105] R. Bellman et al. On structural identifiability. *Mathematical Biosciences*, 7: 329–339, 1970.

[106] S. P. Asprey et al. Statistical tools for optimal dynamic model building. *Computer and Chemical Engineering*, 24:1261–1267, 2000.

[107] A. P. M. Kevin et al. Mathematical modelling of chemical processes, obtaining the best model predictions and parameter estimates using identifiability and estimability procedures. *Canadian Journal of Chemical Engineering*, 90:351–366, 2012.

[108] A. Ben-Zvi et al. Identifiability of linear time-invariant differential-algebraic systems. i. the generalized markov parameter approach. *Ind. Eng. Chem. Res.*, 42:6607–6618, 2003.

[109] E. August and A. Papachristodoulou. A new computational tool for establishing model parameter identifiability. *Journal of Computational Biology*, 16:875–885, 2009.

[110] B. K. Petersen et al. Practical identifiability of model parameters by combined respirometric-titrimetric measurements. *Water Sci. Technol*, 43:347–355, 2001.

[111] D. Dochain and P. A. Vanrolleghem. *Dynamical Modelling and Estimation in Wastewater Treatment Processes*. IWA Publishing, 2001.

[112] S. P. Asprey and S. Macchietto. Designing robust optimal dynamic experiments. *Journal of Process Control*, 12:545–556, 2002.

[113] G. Franceschini et al. Model-based design of experiments for parameter precision: State of the art. *Chemical Engineering Science*, 63:4846–4872, 2008.

[114] K. Z. Yao et al. Modeling ethylene/butene copolymerisation with multi-site catalysts: Parameter estimability and experimental design. *Polym. React. Eng.*, 11:563–588, 2003.

[115] S. K. Wu et al. Selection of optimal parameter set using estimability analysis and mse-based model-selection criterion. *Int. J. Adv. Mechatronic Syst.*, 3:188–197, 2011.

[116] Z. Chu, Y. et al. Improving prediction capabilities of complex dynamic models via parameter selection and estimation. *Chem. Eng. Sci.*, 64:4178–4185, 2009.

[117] I. M. Sobol. Global sensitivity indices for nonlinear mathematical models and their monte carlo estimates. *Mathematics and Computers in Simulation*, 55: 271–280, 2001.

[118] B. Iooss et al. A review on global sensitivity analysis methods, 2015.

[119] X. Y. Zhang et al. Sobol sensitivity analysis: A tool to guide the development and evaluation of systems pharmacology models, 2015.

[120] M. Rodriguez-Fernandez et al. Novel global sensitivity analysis methodology accounting for the crucial role of the distribution of input parameters: application to systems biology models. *International Journal of Robust and Nonlinear Control*, 22:1082–1102, 2012.

[121] X. Zhang. *Multiscale Modeling of Li-ion Cells: Mechanics, Heat Generation and Electrochemical Kinetics*. PhD thesis, University of Michigan, 2009.

[122] N. Bilal. Implementation of sobol's method of global sensitivity analysis to a compressor simulation model. Master's thesis, Purdue University, 2014.

[123] A. Vikhansky et al. Numerical analysis of alternating current voltammetry: Identifiability, parameter selection and experimental design. *Industrial and Engineering Chemistry Research*, 50:2831–2838, 2011.

[124] A. Vikhansky. Numerical analysis of the global identifiability of reaction and diffusion systems. *Computers and Chemical Engineering*, 35:1978–1982, 2011.

[125] F. Berthier et al. Identifiability and distinguishability concepts in electrochemistry. *International Journal of Robust and Nonlinear Control*, 32:973–984, 1996.

[126] L. T. Biegler. *Nonlinear Programming Concepts, Algorithms, and Applications to Chemical Processes*. Society for Industrial and Applied Mathematics Philadelphia, 2010.

[127] E. T. Dowling. *Schaum's Outline of Introduction to Mathematical Economics, 3rd Edition*. Schaum's Outline Series, 2012.

[128] T. F. Edgar, D. M. Himmelblau, and L. S. Lasdon. *Optimization of Chemical Process*. McGraw-Hill Higher Education, 2001.

[129] S. Boyd and L. Vandenberghe. *Convex Optimization*. Cambridge University Press, 2004.

[130] M. J. D. Powell. A method for nonlinear constraints in minimization problems. *Optimization*, 257:283–298, 1969.

[131] M. J. D. Powell. On search directions for minimization algorithms. *Mathematical Programming*, 4:193–201, 1973.

[132] J. A. Nelder and R. Mead. A simplex method for function minimization. *The Computer Journal*, 4:308–313, 1965.

[133] G. B. Dantzig. *Maximization of a linear function of variables subject to linear inequalities*. Wiley and Chapman-Hall, 1951.

[134] V. S. Vassiliadis. Linear and non-linear optimization: Lecture notes, ceb part iib, 2013.

[135] X. H. Yang. *Engineering Optimization: An Introduction with Metaheuristic Application*. Wiley Inter-Science, 2010.

[136] S. Kirkpatrick et al. Optimization by simulated annealing. *Science*, 220:671–680, 1983.

[137] D. Bertsimas and J. Tsitsiklis. Simulated annealing. *Statistical Science*, 8:10–15, 1993.

[138] L. Sergio et al. *Simulated Annealing Evolution*. INTECH, 2012.

[139] K. J. Beers. *Numerical Methods for Chemical Engineering with Applications in Matlab*. Cambridge University Press, 2007.

[140] J. R. Leis and M. A. Krame. The simultaneous solution and sensitivity analysis of systems described by ordinary differential equations. *ACM Transactions on Mathematical Software*, 14:45–60, 1988.

[141] Y. Bard. *Nonlinear Parameter Estimation*. Academic Press, New York, 1974.

[142] W. H. Chen. *Estimation of Parameters in Partial Differential Equations-With Applications to Petroleum Reservoir Description*. PhD thesis, California Institute of Technology, 1973.

[143] Q. Guo et al. Parameter estimates for a pemfc cathode. *Journal of The Electrochemical Society*, 151:983–993, 2004.

[144] S. Santhanagopalan et al. Parameter estimation and model discrimination for a lithium-ion cell. *Journal of The Electrochemical Society*, 154:198–206, 2007.

[145] H. P. Gavin. The levenberg-marquardt method for nonlinear least squares curve-fitting problems, 2013.

[146] A. Gelman et al. *Bayesian Data Analysis 3rd Edition*. Chapman and Hall, 2014.

[147] C. E. Rasmussen and C. K. I. Williams. *Gaussian Processes for Machine Learning*. MIT Press, 2006.

[148] C. P. Robert and G. Casella. *Monte Carlo Statistical Method*. Springer Texts in Statistics, 2004.

[149] R. Bardenet. Lecture note on monte carlo methods, 2012.

[150] J. Lee et al. Metamodel for efficient estimation of capacity-fade uncertainty in li-ion batteries for electric vehicles. *Energies*, 8:5538–5554, 2015.

[151] H. Wei et al. Prognostics of Li-Ion batteries based on dempster-shafer theory and the bayesian monte carlo method. *Journal of Power Sources*, 196:10314–10321, 2011.

[152] A. Solonen. Monte carlo methods in parameter estimation of nonlinear models. Master's thesis, Lappeenrante University of Technology, 2006.

[153] R. H. Johnstone et al. Uncertainty and variability in models of the cardiac action potential: Can we build trustworthy models? *Journal of Molecular and Cellular Cardiology*, 96:49–62, 2015.

[154] L. Lapidus and G. F. Pinder. *Numerical Solution of Partial Differential Equations in Science and Engineering*. John Wiley and Sons, 1982.

[155] K. Morton and D. Mayer. *Numerical Solutions of Partial Differential Equations - An Introduction*. Cambridge University Press, 2005.

[156] D. Britz. *Digital Simulation in Electrochemistry, 3rd Edition*. Springer, 2009.

[157] H. Matsuda et al. The theory of the cathode-ray polarography of randles-sevcik. *Zeitschrift fuer Elektrochmie and Angewandte Physikalische Chemie*, 59:494–503, 1955.

[158] R. S. Nicholson et al. Theory of stationary electrode polarography. single scan and cyclic methods applied to reversible, irreversible, and kinetic systems. *Anal. Chem.*, 36:706–723, 1964.

[159] D. Britz, K. Poulsen, and J. Strutwolf. Reference values of the diffusion-limited chronoamperometric current at a microband electrode. *Electrochimica Acta*, 51: 333–339, 2005.

[160] J. Mocak and S. W. Feldberg. The richtmyer modification of the fully implicit finite difference algorithm for simulations of electrochemical problems. *Journal of Electroanalytical Chemistry*, 378:31–37, 1994.

[161] S. W. Feldberg and C. I. Goldstein. Examination of the behavior of the fully implicit finite-difference algorithm with the richtmyer modification: Behaviour with an exponentially expanding time grid. *Journal of Electroanalytical Chemistry*, 397:1–10, 1995.

[162] W. H. Press et al. *Numerical Recipes The Art of Scientific Computing*. Cambridge University Press, 2007.

[163] J. Kiusalaas. *Numerical Methods in Engineering with MATLAB*. Cambridge University Press, 2007.

[164] G. Strang. *Linear Algebra and Its Applications, 4th Edition*. Cengage Learning, 2006.

[165] P. Delgado. Operator splitting methods for Partial Differential Equations, 2013.

[166] D. Kuzmin. Lecture 11: Operator splitting techniques, introduction to cfd, 2010.

[167] R. L. Burden and J. D. Faires. *Numerical Analysis 9th Edition*. Brooks Cole CENGAGE Learning, 2010.

[168] K. R. Ward, L. Nathan, R. S. Harthshone, and R. G. Compton. Cyclic voltammetry of the ec' mechanism at hemispherical particles and their arrays: The split wave. *The Journal of Physical Chemistry C*, 115:11204–11215, 2011.

[169] T. F. Brown et al. Estimation of electrochemical charge transfer parameters with the kalman filter. *Analytical Chemistry*, 56:1214–1221, 1984.

[170] A. Constantinides and N. Mostoufi. *Numerical Methods for Chemical Engineers with MATLAB Applications*. Prentice Hall, 1999.

[171] D. S. Sivia. *Data Analysis: A Bayesian Tutorial*. Oxford University Press, 2006.

[172] Cambridge Mathematics Tripos Part IB. Markov chain lecture notes, 2010.

[173] E. O. Barnes et al. Electrochemical reactions where the variation of supporting electrolyte concentration is mechanistically revealing: ECE-DISP1 processes in which the chemical step is an isomerisation. *Journal of Electroanalytical Chemistry*, 660:185–194, 2011.

[174] J. Kim et al. Model discrimination in dynamic molecular systems: Application to parotid de-differentiation network. *Journal of Computational Biology*, 20: 524–539, 2013.

[175] P. E. Nikravesh. Analytical kinetimatics, aerospace and mechanical engineering course notes, 2014.

[176] C. Y. Cummings, P. E. Frith, G. Zoppi, I. Forbes, K. D. Rogers, D. W. Lane, and F. Marken. Rocking disc electro-deposition of copper films on Mo and MoSe2 substrates. *Thin Solid Films*, 519:7458–7463, 2011.

[177] C. Y. Cummings, G. Zoppi, I. Forbes, D. Colombara, L. M. Peter, and F. Marken. Rocking disc electro-deposition of CuIn alloys, selenisation and pinhole effect minimisation in CISe solar absorber layers. *Electrochimica Acta*, 79:141–147, 2012.

[178] S. D. Ahn. *Carbon Based Nano-Composite Interfaces for Electro-Catalysis*. PhD thesis, University of Bath, 2016.

[179] S. D. Ahn et al. Hydrodynamic voltammetry at a rocking disc electrode: Theory versus experiment. *Electrochimica Acta*, 188:837–844, 2016.

[180] C. L. Bentley et al. Mass-transport and heterogeneous electron-transfer kinetics associated with the ferrocene/ferrocenium process in ionic liquids. *Journal of Physical Chemistry C*, 120:16516–16525, 2016.

[181] W. J. Blaedel and L. N. Klatt. Reversible charge transfer at the tubular platinum electrode. *Analytical Chemistry*, 38:879–883, 1966.

[182] W. J. Blaedel and L. N. Klatt. Quasi-reversible and irreversible charge transfer at the turbular electrode. *Analytical Chemistry*, 39:1065–1072, 1967.

[183] C. E. Hotchen. Hydrodynamic microgap voltammetry under couette flow conditions: Electrochemistry at a rotating drum in viscous poly-ethylene glycol. *ChemPhysChem*, 16:2789–2796, 2015.

[184] C. E. Hotchen. *Electrochemical methods for processes in polymer solvents, PhD Thesis Submitted*. PhD thesis, University of Bath, 2015.

[185] J. Gaspar et al. Biogenic versus thermogenic h2s source determination in bakken wells: Considerations for biocide application. 3:127–132, 2016.

[186] Z. Pawlak and A. S. Pawlak. Modification of iodometric determination of total and reactive sulfide in environmental samples. *Talanta*, 48:347–353, 1999.

[187] P. R. Haddad and A. L. Heckenberg. Trace determination of sulfide by reversed-phase ion-interaction chromatography using pre-column derivatization. *Journal of Chromatography*, 447:415–420, 1988.

[188] N. S. Lawrence, J. Davis, and R. G. Compton. Analytical strategies for the detection of sulfide: a review. *Talanta*, 52:771–784, 2000.

[189] J. B. Raoof, R. Ojani, and H. Beitollahi. L-cysteine voltammetry at a carbon paste electrode bulk-modified with ferrocenedicarboxylic acid. *Electroanalysis*, 19:1822–1830, 2007.

[190] K. I. Ozoemena and T. Nyokong. Electrocatalytic oxidation and detection of hydrazine at gold electrode modified with iron phthalocyanine complex linked to mercaptopyridine self-assembled monolayer. *Talanta*, 67:162–168, 2005.

[191] S. Peng et al. A mechanistic study of the ec prime mechanism - the split wave in cyclic voltammetry and square wave voltammetry. *RSC Advances*, 6:70237–70242, 2016.

[192] C. P. Andrieux et al. Homogeneous redox catalysis of electrochemical reactions: Part i. *Journal of Electroanalytical Chemistry and Interfacial Electrochemistry*, 87:39–53, 1978.

[193] C. P. Andrieux et al. Homogeneous redox catalysis of electrochemical reactions: Part ii. *Journal of Electroanalytical Chemistry and Interfacial Electrochemistry*, 87:55–65, 1978.

[194] C. P. Andrieux et al. Homogeneous redox catalysis of electrochemical reactions: Part iii. *Journal of Electroanalytical Chemistry and Interfacial Electrochemistry*, 88:43–48, 1978.

[195] C. P. Andrieux et al. Homogeneous redox catalysis of electrochemical reactions: Part iv. cyclic voltammetry. *Journal of Electroanalytical Chemistry and Interfacial Electrochemistry*, 113:1–18, 1980.

[196] A. C. Fisher and R. G. Compton. The EC' mechanism: Split waves at the channel electrode. *Electroanalysis*, 4:311–315, 1992.

[197] D. G. Manolakis and V. K. Ingle. *Applied Digital Signal Processing*. Cambridge University Press, 2011.

[198] V. K. Ingle and J. G. Proakis. *Digital Signal Processing Using Matlab*. CENGAGE Leaning, 2012.

[199] G. Palshikar. Simple algorithms for peak detection in time series, 2009.

[200] J. W. Cooley and J. W. Tukey. An algorithm for the machine calculation of complex fourier series. 19:297–301, 1965.

[201] T. Cormen et al. *Introduction to Algorithms*. The MIT Press, 2009.

[202] https://en.wikipedia.org/wiki/envelope waves, 2016.

[203] E. S. Rountree, B. D. McCarthy, T. T. Eisenhart, and J. L. Dempsey. Evaluation of homogeneous electrocatalysts by cyclic voltammetry. *Inorganic Chemistry*, 53: 9983–10002, 2014.

[204] D. Trinh et al. Numerical simulation of the far-field boundaries onto a microdisc electrode by using the infinite element. *Journal of Electroanalytical Chemistry*, 729:1–8, 2014.

[205] University of Michigan. Models for nonideal reactors, 2015.

[206] A. M. Bond. *Broadening Electrochemical Horizons*. Oxford University Press, 2002.

[207] S. D. Ahn et al. Hydrodynamic rocking disc electrode study of the tempo-mediated catalytic oxidation of primary alcohols. *Electroanalysis*, 28:2093–2103, 2016.